RIBONUCLEASE P CATALYSIS:
METAL ION INTERACTION AND CONFORMATIONAL DYNAMICS

by

Yu Chen

A dissertation submitted in partial fulfillment
of the requirements for the degree of
Doctor of Philosophy
(Chemistry)
in the University of Michigan
2015

Doctoral Committee:

Professor Hashim M. Al-Hashimi, Co-Chair
Professor Carol A. Fierke, Co-Chair
Professor David R. Engelke
Professor Bruce A. Palfey
Professor Nils G. Walter

DEDICATION

To my mother and father

You believe in me and give me confidence to accomplish my goals.

Thank you for your endless love and support.

ACKNOWLEDGMENTS

This work would have been impossible without help and support from mentors, families and friends. I thank my advisor **Dr. Carol Fierke** for her guidance and encouragement throughout the Ph. D process. Carol has been a role model for me as an extraordinary scientist and wonderful mentor. Without her essential suggestions and inspiration, I would not have been able to learn such a great range of experimental methods and developed the critical thinking tools to finish this dissertation. I want to thank my advisor **Dr. Hashim Al-Hashimi** for his support and continual help. His passion in research and insightful ideas drove me to explore challenging questions and pushed me to strive for a higher standard in research. He also taught me to be persistent in accomplishing my goals.

Thank you to my committee members who have been so very patient and helpful. The monthly RNase P meeting with **Dr. David Engelke** and members from his group has provided me with a wealth of useful feedback and helpful discussions on my research. As an RNA expert, **Dr. Nils Water** provided me with thoughtful ideas on ribozyme catalysis that informed my research. I also advanced my knowledge of RNA through him and his group members (**Visha Krishnan**, **Sethu Pitchiaya** and **Wendy Tay**) by doing a rotation in his lab. I learned enzyme kinetics in **Dr. Bruce Palfey's** class: the best enzyme kinetics class in the nation. He has helped me to interpret my kinetics data and understand the results more clearly.

I want to thank my master advisor, **Dr. Leif Kirsebom**. He opened the world of ribozymes to me and taught me how to ask questions and express my ideas. I also want to thank my undergraduate research advisor **Dr. Yali Cui**. She gave me the chance to do research in her lab and brought me into the biochemistry field. Without her support, I would not have started down my science career path.

I also want to extend my acknowledgement to my mentors, all past and current lab-mates of the Fierke lab and the Al-Hashimi lab and collaborators. **Dr. Wanhsin Lim** showed me experimental procedures and she is also a great friend since my first day in the lab. **Dr. Elaina Zverina** is a great source of inspiration, particularly her enthusiasm and insightful ideas on careers and life. I want to thank **Dr. Noah Wolfson** for his support and career advice. He is also the person I always ask for help when I have issues on lab instruments. **Andrea Stoddard** has graciously helped me in the lab countless times. I want to thank her for support and encouragement during my graduate school years. I want to express my special thanks to **Dr. Xin Liu** who has been a great mentor - teaching me assays, analytical methods and instruments. She has provided excellent ideas and thoughtful suggestions on my research. As a friend, she brings happiness in my life and support during hard times. I have learned things from her not only in science, but also about our career path and life. **Dr. Michael Howard** for his insightful questions and suggestions on my project and being an inspiring friend. **Nancy Wu** is a colleague and friend. I thank her for the critical discussion and reading my chapters and manuscripts, as well as the happy times in the lab. I also want to acknowledge all members of the RNase P subgroup for insightful discussions on research, including **Dr. Wanhsin Lim, Dr. Xin Liu, Dr. Michael Howard, Bradley**

Klemm, Nancy Wu and Kipchumba Kaitany. I want to thank **Dr. Katja Petzold** for teaching me NMR techniques and data analysis, and sharing critical discussions on my research. She has been a great mentor and colleague. **Huiqing Zhou** is a helpful colleague and friend. I thank her for collaborating with me on my project and helping me with the data analysis. I want to thank **Dr. Aaron Frank** for the collaborations and insightful discussions on my research. His expertise on computational chemistry helped me to understand my results more clearly. I thank **Dr. Janghyun Lee** for his time and patience,teaching me how to use the spectrometer and analyze data. I want to express my thanks to **Dr. Carol Ann Pitcairn** for her positivity and encouragement, for being **a** great colleague and friend, through challenging and happy times in graduate school. My thanks also go to **Elia Wright** for support and encouragement during hard times.

I would like to thank my dear friends and family whom I have not yet mentioned. I thank my supportive friend **Dr. Shiying Wu** for her long phone calls, encouragement, and endless patience. I must thank **Dr. Jing Chen**, **Dr. Chenxi Shen**, **Dr Ningkun Wang**, **Dr. Xiao Liu**, **Dr. Wenjing Chen**, **Dr. Bo Peng**, **Dr. Yipei Wang**, **Dr. Yaru Zhang**, **Dr. Lyra Chang** for valuable friendships, smile, understanding and support. I also thank **Dr. Wencheng Ge**, **Dr. Ping Guo**, **Jing Yan**, **Shuai Niu**, **Dr. Yi Liao**, **Shusheng Lv**, **Shi Jin**, **Yuanyuan Zhang** for the happy times we spent together since the first day in Ann Arbor.

I want to express my special thanks to **Carl Duke** for his patience, support, understanding and being caring to me all these years. I would like to thank my uncle **Letian Wang** and my aunt **Weihong Lang** for their emotional support and the joyful family times. They have been taking care of me since the first day I arrived in US. Their

love makes me feel I have never been away from home. I want to express my utmost gratitude to **my parents**, who raised me up with unconditional love. I would have not been able to get to this point without their love, support and encouragement. **爸爸，妈妈**，谢谢你们养育我长大，无条件地相信我，支持我的决定和我想做的事情。没有你们的爱和支持，我是不会有今天的成果的。 谢谢你们！我爱你们！

TABLE OF CONTENTS

DEDICATION ..... **ii**

ACKNOWLEDGMENTS ..... **iii**

LIST OF FIGURES ..... **xiv**

LIST OF TABLES ..... **xx**

LIST OF EQUATIONS ..... **xxiii**

LIST OF APPENDICES ..... **xxiv**

ABSTRACT ..... **xxvi**

CHAPTER 1 INTRODUCTION: IMPORTANCE OF METAL ION INTERACTION AND CONFORMATIONAL DYNAMICS FOR THE FUNCTION OF RNASE P **1**

1.1 Introduction 1

1.2 RNase P Enzyme: Function and Variations 2

1.2.1 RNA-based RNase P 5

1.2.2 Protein-only RNase P 9

1.3 Catalytic Mechanism of RNase P 11

1.3.1 Structure of Bacterial RNase P 11

1.3.2 Substrate Recognition by RNase P 16

1.3.3 Divalent Metal Ions and RNase P Catalysis 17

1.3.4 Conformational Change in RNase P Catalysis 23

1.4 Charactering RNA Structure and Dynamics by Nuclear Magnetic Resonance ... 27

1.4.1 Studying RNA Structure by NMR 27

1.4.2 Probing RNA Dynamics by NMR 29

1.5 Objectives of this Research 32

1.6 References 34

CHAPTER 2 PROBING METAL ION BINDING SITES IN THE P4 HELIX OF *BACILLUS SUBTILIS* RNASE P 44

2.1 Abstract 44

2.2 Background 45

2.3 Results 52

2.3.1 Preparation of PRNA with Atom Modifications in the P4 Helix 52

2.3.2 Modifications at G378 and G379 Affect Metal Dependent Pre-tRNA binding affinity 54

2.3.3 Modifications at G378 and G379 Do Not Affect the Global structure of PRNA at High Concentrations of Mg^{2+} ion 57

2.3.4 O6 at G379 Is Important for Pre-tRNA Cleavage Catalyzed by RNase P 59

2.3.5 The Base of G379 Is Important for the Conformational Change Step of RNase P Catalysis 63

2.3.6 G379 Modifications Affect Pre-tRNA Cleavage Catalyzed by PRNA Without Altering the Cooperativity of the Apparent Affinity of Mg^{2+} to PRNA 67

2.3.7 Cd^{2+} Ion Does Not Rescue G379-6SG Holoenzyme Activity 68

2.4 Discussion 70
2.4.1 G378 and G379 Are Important for Metal Ion Dependent Substrate Binding 71
2.4.2 G379 Coordinates a Co-catalytic Metal Ion through Outer-sphere Coordination 72
2.4.3 The Base of G379 Participates in the Conformational Change of RNase P Catalysis 75
2.5 Conclusion 76
2.6 Materials and Methods 77
2.6.1 Materials and Reagents 77
2.6.2 Preparation of P Protein, Substrate and WT PRNA 78
2.6.3 Preparation of Circularly Permuted 366P and 386-365P RNA 79
2.6.4 Preparation of Modified PRNA by Ligation 80
2.6.5 Determination of Pre-tRNA Dissociation Constant by Spin Column 81
2.6.6 PRNA Folding Measured by Ultraviolet Absorbance (UV) and Circular Dichrosm (CD) Spectroscopy 82
2.6.7 Single-turnover Kinetic Experiments 83
2.6.8 Fluorescence Stopped-flow Kinetics Experiments 85
2.7 References 87

CHAPTER 3 VISUALIZING THE TRANSIENT STATE OF THE P4 HELIX FROM *BACILLUS SUBTILIS* RNASE P 91

3.1 Abstract 91
3.2 Background 92
3.3 Results 96

3.3.1 Secondary Structure of the P4 Helix Mimic 97
3.3.2 Relaxation Dispersion Reveals a Shared Transient, Low Populated State of the P4 Helix Mimic 101
3.3.3 A-tract Stabilizes the Transient State of the P4 Helix Mimic 104
3.3.4 Probing the Structure of Transient State of the P4 Helix Mimic 107
3.3.5 The individual transient state of bulged U7 observed in the presence of Mg^{2+} 126
3.3.6 Building a 3D model of the TS of the P4 helix mimic 133
3.4 Discussion 136
3.4.1 The Shared Transient State of the P4 Helix Mimic 137
3.4.2 The Flexible Helical Formation of the P4 Helix Mimic is Important for the Transition between the GS and the TS 144
3.4.3 Base Flipping of the Bulged U7 Contributes the TS 145
3.4.4 Mg^{2+} Decreases the Population and Exchange Rate Constant of the TS 148
3.5 Conclusion 149
3.6 Materials and Methods 150
3.6.1 Materials and Reagents 150
3.6.2 Sample Preparation and Purification for NMR 151
3.6.3 Carbon and Nitrogen $R_{1\rho}$ Relaxation Dispersion 153
3.6.4 Experiments in the presence of Mg^{2+} 155
3.6.5 Thermodynamics Analysis 155
3.6.6 UV Thermal Melting Experiments 156
3.6.7 MCSYM-LARMOR 3D RNA Structure Modeling 156

3.6.8 Electrostatic Potential Calculations. 157

3.7 References 159

CHAPTER 4 CHARACTERIZING the role of P4 HELIX in *BACILLUS SUBTILIS* RNASE P catalysis 165

4.1 Abstract 165

4.2 Background 166

4.3 Results 170

4.3.1 Preparation of PRNA with Atom Modifications in the P4 Helix 170

4.3.2 Modification on A-tract Affects Pre-tRNA Cleavage Catalyzed by RNase P 171

4.3.3 The Structure of G50 Is important for RNase P catalysis 173

4.3.4 Modifications in the A-tract and G50 alter Mg2+ affinity for pre-tRNA cleavage by RNase P 176

4.3.5 Modifications on Universal Conserved Uridine affect RNase P catalysis ... 178

4.3.6 Double Deletion Results in Inactive RNase P 180

4.3.7 Modifications on the 3' Side of the P4 Helix Have Little Effect on Pre-tRNA Cleavage by RNase P 181

4.4 Discussion 183

4.4.1 A-tract Facilitates the Conformational Change of RNase P - pre-tRNA Complex 184

4.4.2 Nucleobase of G50 Stabilizes the Active Conformation of RNase P - pre-tRNA Complex 187

4.4.3 Bulged U51 Contributes to the Conformational Change of RNase P Catalysis 191
4.4.4 Flexible Helix Is Required for RNase P catalysis 192
4.4.5 Implications of the Conformational Change 194
4.5 Conclusion 194
4.6 Materials and Methods 195
4.6.1 Materials and Reagents 195
4.6.2 Preparation of P Protein, Substrate, PRNA and PRNA mutant 196
4.6.3 Preparation of Circularly Permuted RNA 196
4.6.4 Preparation of Modified PRNA by Ligation 197
4.6.5 Single-turnover Kinetics Experiments 197
4.7 References 198

CHAPTER 5 CONCLUSIONS AND FUTURE DIRECTIONS 201
5.1 Conclusions 201
5.1.1 An Outer-Sphere Metal Ion Binding Site in the P4 Helix Enhances RNase P Catalysis 201
5.1.2 The Transient State of the P4 Helix Mimic 203
5.1.3 Conformational Change of the P4 Helix Facilitates the Binding Affinity of Catalytic Metal Ions 204
5.2 Future Directions 206
5.2.1 Probing the functional ligands associated with the metal ions stabilizing the conformational change of RNase P - pre-tRNA complex 206
5.2.2 Examining the Conformational change of RNase P 207

5.2.3 Characterizing the P4 helix in Full-length PRNA by NMR spectroscopy 209

5.2.4 Characterizing RNase P and Pre-tRNA Interaction by NMR spectroscopy 212

5.3 References 215

APPENDICES 216

LIST OF FIGURES

Figure 1-1: Model of tRNA maturation pathway 3

Figure 1-2: RNase P catalyzed 5'-end maturation of tRNA 4

Figure 1-3: Minimum consensus secondary structure of RNase P RNAs 7

Figure 1-4: Secondary structure of *T. maritima* RNase P RNA 13

Figure 1-5: Crystal structure of *T. maritima* RNase P 14

Figure 1-6: Structure of *T. maritima* RNase P active site 15

Figure 1-7: Kinetic mechanism of *B. subtilis* RNase P 19

Figure 1-8: Catalytic mechanism of RNase P proposed from the crystal structure of the *T. maritima* RNase P ternary complex 20

Figure 1-9: Proposed metal ion binding sites in the P4 helix of RNase P RNA identified by structural and biochemical studies 22

Figure 1-10: A cartoon showing the sequential connectivities in a nonexchangeable NOESY 29

Figure 1-11: Measurement of chemical exchange by $R_{1\rho}$ relaxation dispersion 31

Figure 2-1: Secondary structure of the *B. subtilis* PRNA and proposed metal ion binding sites 50

Figure 2-2: Chemical structures of guanosine and substituted bases 51

Figure 2-3: Kinetic mechanism of bacterial RNase P 52

Figure 2-4: Incorporation of modifications into *B. subtilis* PRNA by using circularly permuted PRNA (cpPRNA) 53

Figure 2-5: 386-365P does not bind to pre-tRNA substrate or catalyze pre-tRNA cleavage 54

Figure 2-6: Modifications at G378 and G379 affect metal dependent pre-tRNA substrate binding affinity for *B. subtilis* RNase P 56

Figure 2-7: Equilibrium folding of WT and modified *B. subtilis* PRNA 59

Figure 2-8: Modifications at G379, but not G378, affect catalysis of pre-tRNA cleavage by *B. subtilis* RNase P 62

Figure 2-9: Biphasic stopped-flow kinetics of Fl-pre-tRNA^{Asp} binding to *B. subtilis* RNase P under pseudo-first-order conditions 65

Figure 2-10: Stopped-flow fluorescence trace after mixing 10 nM of Fl-pre-tRNA^{Asp} with 360 nM of WT (red), 366P (orange), 366P ligation (pink), G378-2AP (green) and G379-2AP (blue) *B. subtilis* RNase P reveals three phases 66

Figure 2-11: Mg^{2+} dependence of WT (●), 366P (O), G378-2AP (□), G379-2AP (■) and G379-abG (+) *B. subtilis* PRNA STO cleavage for Fl-pre-tRNA^{Asp} 68

Figure 2-12: Cd^{2+} dependence of STO cleavage catalyzed by WT and modified *B. subtilis* RNase P in the presence of 20 mM of Mg^{2+} 69

Figure 2-13: Model of effects of G379 modifications on co-catalytic metal ion coordination 75

Figure 3-1: Comparison of the secondary structures between previous reported P4 helix mimic (mutant P4) and the construct used in this study (WT P4) 97

Figure 3-2: Resonance assignments of the P4 helix mimic from *B. subtilis* PRNA 101

Figure 3-3: Observation of the shared transient state in and around U7 and A-tract of the P4 helix mimic from *B. subtilis* PRNA at the condition of 15 mM NaH_2PO_4, 25 mM NaCl and 0.1 mM EDTA under pH 6.8 at 25°C with 2.3 mM of the P4 WT 103

Figure 3-4: Resonance assignments of DelA4 P4 mutant from *B. subtilis* PRNA..... 106

Figure 3-5: DelA4 mutant eliminates relaxation dispersion observed for the P4 WT in and around U7 and A-tract regions 107

Figure 3-6: Hypothesized transient state of the P4 helix mimic caused by helix melting at bulge U7 and A-tract regions. 108

Figure 3-7: Temperature dependence of on- and off-resonance of $R_{1\rho}$ relaxation dispersion profiles for selected residues of the P4 WT and best fits (solid lines) to a two-state exchange model 109

Figure 3-8: Thermodynamics analysis for the transition between the GS and the TS of the P4 helix mimic 112

Figure 3-9: Temperature dependence of on- and off-resonance of $R_{1\rho}$ relaxation dispersion profiles for selected residues of DelA4 and best fits (solid lines) to a two-state exchange model 113

Figure 3-10: Resonance assignments and chemical shifts of single-strand RNA containing G2 to U11 of the P4 helix mimic from *B. subtilis* PRNA..... 116

Figure 3-11: Hypothesized transient state of the P4 helix mimic involving in A-tract flipping out 117

Figure 3-12: Chemical shifts of P4 WT titrated with saturating paromomycin..... 118

Figure 3-13: Chemical structures of the guanosine with *anti* conformation and 8-bromoguanosine with restricting *syn* conformation, wherein the nucleobase is positioned over the ribose sugar 119

Figure 3-14: Resonance assignments of G6-8BrG P4 helix mimic construct from *B. subtilis* PRNA 122

Figure 3-15: Chemical structures for Watson-Crick G6-C24 and hypothesized Hoogsteen G6-$C24^{+}$ base pairs. 123

Figure 3-16: pH dependence of $R_{1\rho}$ relaxation dispersion for the P4 helix mimic from *B. subtilis* PRNA. 124

Figure 3-17: Chemical shifts of P4 WT titrated $MgCl_2$ 130

Figure 3-18: $R_{1\rho}$ relaxation dispersion for the P4 WT (2.3 mM) and DelA4 mutant (2.5 mM) from *B. subtilis* PRNA in the presence of Mg^{2+} 132

Figure 3-19: Two different views showing 3D models of the GS (blue) and TS (purple) of the P4 helix mimic form *B. subtilis* PRNA predicted by MCSYM-LARMORD method 134

Figure 3-20: Determining the chemical shift data responsible for selecting the TS model with the kink formation between A5 and G6 136

Figure 3-21: Secondary structures of the GS and the TS of the P4 helix mimic from *B. subtilis* PRNA 138

Figure 3-22: Surface electrostatic potential for the GS (left) and the TS (right) of the P4 helix mimic from *B. subtilis* PRNA 142

Figure 3-23: U7 in the P4 helix mimic (U51 in RNase P, *B. subtilis* numbering) adopts two different conformations between the GS and the TS 148

Figure 4-1: Secondary structure of the P4 helix (black) and P4 helix stem-loop mimic (black and grey) 168

Figure 4-2: Chemical structures of adenosine, guanosine, uridine and substitutions . 169

Figure 4-3: Modification at A-tract decreases pre-tRNA cleavage catalyzed by *B. subtilis* RNase P 173

Figure 4-4: The structure of G50 affects pre-tRNA cleavage catalyzed for *B. subtilis* RNase P 176

Figure 4-5: Deletion of one adenosine on A-tract and modifications on G50 affect Mg^{2+} affinity for pre-tRNA cleavage catalyzed by *B. subtilis* RNase P 178

Figure 4-6: Modifications on the universal conserved U51 affect pre-tRNA cleavage catalyzed by *B. subtilis* RNase P 180

Figure 4-7: Double deletion of one adenosine in the A-tract and U51 results in inactive RNase P 181

Figure 4-8: Modifications on the residues on 3' side of the P4 helix have minimal effect on pre-tRNA cleavage catalyzed by *B. subtilis* RNase P. 183

Figure 4-9: Two possible conformations of A-tract in the P4 helix of *B. subtilis* PRNA. 186

Figure 5-1: Chemical structures of adenosine, guanosine and substitutions 207

Figure 5-2: Chemical structures of guanosine, uridine and fluorescent analogs 208

Figure 5-3: The strategy of selectively labeling half of the P4 helix in *B. subtilis* PRNA 211

Figure 5-4: 2D ^{13}C-^{1}H and ^{15}N-^{1}H spectra of $^{13}C/^{15}N$ uniformly labeled *B. subtilis* $tRNA^{Asp}$ 214

Figure A-1: Examples of ligation efficiency of 20-mer ribo-oligonucleotides containing (A) 2-amonipurine (2AP) and (B) abasic (abG) of G379 determined by primer extension analysis 216

Figure A-2: Modified *B. subtilis* RNase P enzymes catalyze cleavage of Fl-pre-tRNA^{Asp} substrate at correct site 217

Figure B-1: Normalized resonance intensities as a function of residue in P4 WT 226

Figure B-2: Observation of the TS in and around U7 and A-tract of the P4 helix mimic from *B. subtilis* PRNA at the condition of 15 mM NaH_2PO_4, 25 mM NaCl and 0.1 mM EDTA under pH 5.4, 6.8 and 7.6 at 15°C, 25°C and 37°C with 2.3 mM of the P4 WT 233

Figure B-3: DelA4 mutant eliminates the shared TS observed for the P4 WT in and around U7 and A-tract regions but retains the separated TS at U7 238

Figure B-4: ^{1}H NMR chemical shift of G6-1mG P4 helix mimic construct from *B. subtilis* PRNA 241

Figure B-5: Resonance assignments of G6-1mG P4 helix mimic construct from *B. subtilis* PRNA 243

LIST OF TABLES

Table 2-1: Pre-tRNA^{Asp} substrate binding affinity for WT and modified *B. subtilis* RNase P at low and saturating Mg^{2+} 56

Table 2-2: $K_{1/2}^{Mg^{2+}}$ (mM) for stabilization of folded WT and modified *B. subtilis* PRNA 58

Table 2-3: Single-turnover observed rate constants for cleavage of Fl-pre-tRNA^{Asp} catalyzed by *B. subtilis* WT and modified RNase P 62

Table 2-4: Biphasic kinetics parameters of Fl-pre-tRNA^{Asp} catalyzed by WT and modified *B. subtilis* RNase P 64

Table 2-5: Three-phase kinetics parameters of Fl-pre-tRNA^{Asp} catalyzed by WT and modified *B. subtilis* RNase P 66

Table 2-6: Mg^{2+} dependence of WT and modified *B. subtilis* PRNA catalyzed STO cleavage 68

Table 3-1: Global fits of off-resonance $R_{1\rho}$ relaxation dispersion of the P4 helix mimic at 15°C, 25°C and 37°C 109

Table 3-2: Thermodynamics parameters for the transition between GS and TS of the P4 helix mimic 111

Table 3-3: Global fits of off-resonance $R_{1\rho}$ relaxation dispersion of the P4 helix mimic at pH 5.4 and pH 7.6 125

Table 3-4: Global fits of off-resonance $R_{1\rho}$ relaxation dispersion of the P4 helix mimic in the presence of 5 mM Mg^{2+} 132

Table 3-5: $R_{1\rho}$ relaxation dispersion off-resonance analysis for U7C1' and U7C6 of P4 WT and DelA4 mutant in the presence of 44 mM Mg^{2+} 132

Table 4-1: Single-turnover rate constants for cleavage of Fl-pre-tRNA^{Asp} catalyzed by *B. subtilis* WT and A-tract modified RNase P 172

Table 4-2: Single-turnover rate constants for cleavage of Fl-pre-tRNA^{Asp} catalyzed by *B. subtilis* WT and G50 modified RNase P 175

Table 4-3: Mg^{2+} dependence of WT and modified *B. subtilis* PRNA catalyzed STO cleavage 177

Table 4-4: Single-turnover rate constants for cleavage of Fl-pre-tRNA^{Asp} catalyzed by *B. subtilis* WT and U51 modified RNase P 179

Table 4-5: Single-turnover rate constants for cleavage of Fl-pre-tRNA^{Asp} catalyzed by *B. subtilis* WT and 3' side of the P4 helix modified RNase P 182

Table B-1: Parameter sets for P4 WT in 15 mM NaH_2PO_4, 25 mM NaCl and 0.1 mM EDTA 218

Table B-2: Parameter sets for DelA4 in 15 mM NaH_2PO_4, 25 mM NaCl and 0.1 mM EDTA at pH 6.8 221

Table B-3: Parameter sets for WT in 15 mM NaH_2PO_4, 25 mM NaCl, 5 mM or 44 mM $MgCl_2$ and 0.1 mM EDTA under pH 6.8 at 25 °C 223

Table B-4: Parameter sets for DelA4 in 15 mM NaH_2PO_4, 25 mM NaCl, 44 mM of $MgCl_2$ and 0.1 mM EDTA under pH 6.8 at 25 °C 225

Table B-5: Temperature dependence of P4 WT off-resonance $R_{1\rho}$ relaxation dispersion in 15 mM NaH_2PO_4, 25 mM NaCl and 0.1 mM EDTA at pH 6.8 239

Table B-6: pH dependence of P4 WT off-resonance $R_{1\rho}$ relaxation dispersion in 15 mM NaH_2PO_4, 25 mM NaCl and 0.1 mM EDTA at 25 °C 240

Table B-7: P4 WT off-resonance $R_{1\rho}$ relaxation dispersion in 15 mM NaH_2PO_4, 25 mM NaCl, 5 mM $MgCl_2$ and 0.1 mM EDTA under pH 6.8 at 25 °C 241

Table B-8: Sugar pucker and glycosidic angle designation for residues from G2 to U11 and C19 to C27 in the GS and the TS of the P4 helix mimic from *B. subtilis* PRNA[a] .. 244

Table C-1: STO rate constants for cleavage of Fl-pre-tRNA^{Asp} catalyzed by *B. subtilis* WT and modified RNase Ps 245

Table C-2: Mg^{2+} dependence of WT and modified *B. subtilis* PRNA catalyzed STO cleavage 249

LIST OF EQUATIONS

Equation 1 82

Equation 2 82

Equation 3 83

Equation 4 83

Equation 5 84

Equation 6 85

Equation 7 85

Equation 8 85

Equation 9 86

Equation 10 86

Equation 11 86

Equation 12 154

Equation 13 155

Equation 14 156

Equation 15 157

Equation 16 157

LIST OF APPENDICES

APPENDIX A 216

A.1 Ligation Efficiency Determination by Primer Extension 216

A.2 Both RNase P Holoenzyme and PRNA with Modifications at G378/G379 Catalyze Cleavage of Fl-pre-tRNA^{Asp} at Correct Site 217

APPENDIX B 218

B.1 Parameter Sets for On- and Off-Resonance $R_{1\rho}$ Relaxation Dispersion Profiles of P4 WT and DelA4 Measured at Different Conditions 218

B.2 U7 Is the Only Bulged Residue in the P4 Helix Mimic 226

B.3 On- and Off-Resonance of $R_{1\rho}$ Relaxation Dispersion Profiles 227

B.3.1 $R_{1\rho}$ relaxation dispersion profiles of P4 WT under different conditions 227

B.3.2 $R_{1\rho}$ relaxation dispersion profiles of DelA4 under different conditions 234

B.4 Individual Fits of P4 WT Off-Resonance $R_{1\rho}$ Relaxation Dispersion under Different Conditions 239

B.5 G6-8BrG sample has high purity and without contaminations 241

B.6 G6-m1G Modification Is Unable to Provide Evidence for Hoogsteen Base Pair in the TS of the P4 Helix Mimic 242

B.7 Structural Comparison between the TS and the ES 244

B.8 References 244

APPENDIX C 245

C.1 STO rate constants for cleavage of Fl-pre-tRNA^{Asp} catalyzed by *B. subtilis* WT and modified RNase Ps 245

C.2 Mg^{2+} dependence of WT and modified *B. subtilis* PRNA catalyzed STO cleavage 249

ABSTRACT

RNase P is a divalent metal ion dependent ribonucleoprotein that catalyzes the hydrolysis of a specific phosphodiester bond in all precursor tRNAs (pre-tRNAs), generating mature tRNAs with a phosphate at the 5'-end. The conserved catalytic RNA subunit of bacterial RNase P is essential for activity. Bound divalent metal ions and conformational dynamics in RNase P are important for enhancing the substrate affinity and contributing to the catalytic function of RNase P.

In this dissertation research, first a putative metal ion binding site at G378 and G379 of *Bacillus subtilis* RNase P RNA (PRNA) was examined using atom substitutions. The data suggest that the carbonyl oxygen at O6 position of G379 in PRNA functions as a hydrogen bond acceptor and likely forms an outer-sphere contact with a metal-bound water that is important for substrate affinity and efficient catalysis. The guanosine base of this nucleotide also contributes to stabilization of an active conformer of RNase P.

Secondly, ^{13}C and ^{15}N $R_{1\rho}$ relaxation dispersion NMR experiments were used to probe the existence of alternate conformers in a P4 helix stem-loop mimic. A two-state off-resonance analysis of the data revealed a shared transient state (TS) for bases and sugars in the helix and an independent TS for U7 (U51 in *B. subtilis* PRNA). Based on the chemical shift changes, a computational MCSYM-LARMORD approach predicted a 3D model of the TS. In the shared TS, the A-tract region unwinds and G6 (G50 in *B. subtilis* PRNA) changes from *anti* conformation to *syn* that is coupled to the formation of

a kink in the backbone between A5 and G6 (A49 and G50 in *B. subtilis* PRNA) that creates an electrostatic patch favorable for metal ion association. Additionally, the bulged U7 flips in and out of the helix with a motion that is faster than the dynamics of the shared TS.

To investigate whether the alternative conformer detected in the P4 helix mimic is related to the conformational change observed in the RNase P catalytic cycle, mutants and nucleoside modifications were incorporated into the P4 helix in the full-length *B. subtilis* PRNA. The kinetic data show strong correlations with the NMR results demonstrating that the TS observed in the P4 stem-loop model mimics the P4 helix conformational change in RNase P. The likely functional role of the structural rearrangement in the P4 helix is the formation of an electrostatic site at the backbone between A49 and G50, which is favorable for Mg^{2+} ion binding to RNase P and activating catalysis.

Overall, this work provides structural information about the metal ion binding sites and conformational change in the P4 helix during RNase P catalysis, and enhances our understanding of the functional roles of metal ion binding and conformational dynamics in RNA.

CHAPTER 1
INTRODUCTION: IMPORTANCE OF METAL ION INTERACTION AND CONFORMATIONAL DYNAMICS FOR THE FUNCTION OF RNASE P

1.1 Introduction

The correlation between RNA and protein synthesis was originally suggested by Brachet and Casperson in the late 1930s [1]. In 1958, Francis Crick proposed the sequence hypothesis and the central role of RNA in protein synthesis was established [2]. However, RNA is not only a messenger operating between DNA and protein. RNA is also known to be involved in many aspects of cellular physiology and to influence all steps of gene expression and regulation [3]. In addition to storing and relaying genetic information, RNA participates in transcription and translation regulation, RNA splicing and modification, gene silencing and catalyzing chemical reactions [4-10]. The centrality of RNA in cellular function led to the speculation of an RNA world early in evolution, where RNA was both the genetic material and biological reaction catalyst [11]. With the discovery of ribozymes, such as self-splicing introns [12] and ribonuclease P (RNase P) [13], and the demonstration that the ribosome is an RNA enzyme [14], the concept of RNA as a catalyst became firmly established.

Just like protein enzymes, metal ion binding is crucial to both structure and function of many ribozymes [5, 15-17]. Ribozymes also exploit structural rearrangements to guide the catalytic process similar to protein enzymes [18-22]. Since RNA contains mainly four

types of nucleobases, the function of RNA is amplified by its conformational dynamics. Unlike self-cleaving ribozymes, RNase P is one of two known natural ribozymes that catalyze multiple-turnover reactions and remain unchanged after catalysis (the other one is the ribosome). RNase P is a divalent metal ion dependent endonuclease that requires conformational changes to catalyze 5' maturation of precursor tRNA (pre-tRNA). Here, I'll describe the current picture of RNase P catalysis and recent advances in elucidating the important roles of metal ions and conformational changes in RNase P. I'll also discuss applying nuclear magnetic resonance (NMR) spectroscopy as a tool to characterize RNA structure and dynamics.

1.2 RNase P Enzyme: Function and Variations

The tRNA genes are transcribed as precursors, which are further processed by various enzymes to generate mature and functional tRNA molecules (Figure 1-1). Maturation of tRNA is typically initiated by cleavage of the 5′ leader (Figure 1-2), followed by removal of the extra 3' nucleotides by varied nucleases, including endonuclease RNase Z and exonucleases such as RNase II, D, PH, BN, and T [23-25]. Further post-transcriptional processing can include the addition of a 3' CCA sequence, splicing, and base modifications [26]. The maturation of the 5'-end of tRNA is the result of cleavage catalyzed by ribonuclease P (RNase P). With only one exception [27], this enzyme is found in all cells in all domains of life and is crucial to maintaining cell viability [28-31].

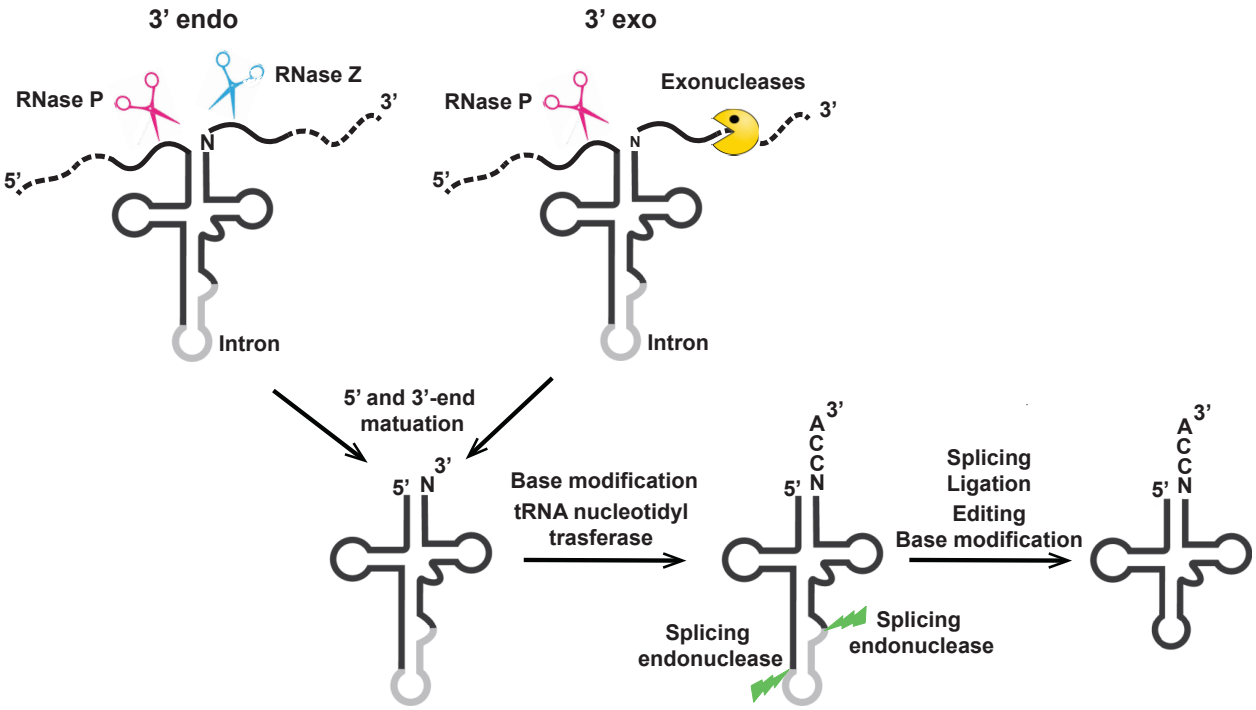

Figure 1-1: Model of tRNA maturation pathway [23]. In Both pathways, RNase P is responsible for catalyzing tRNA 5'-end maturation. 3'-end maturation is processed either by endonuclease RNase Z (left) or various exonucleases (right). After 5' and 3' maturation, the CCA triplet is added to tRNA by nucleotidyl transferase. Some tRNAs are also transcribed with Introns (in grey), which are removed by splicing endonuclease. N represents the discriminator nucleotide.

RNase P is a divalent metal ion dependent ribonucleoprotein enzyme that is responsible for the hydrolysis of the specific phosphodiester bond between the N(-1) and N(+1) bases in precursor-tRNAs (pre-tRNAs) and generating mature tRNAs with a phosphate at their 5'-end (Figure 1-2) [32-35]. Beside pre-tRNA substrate, RNase P also processes various other substrates in cells [36], such as 4.5S RNA [37, 38], tmRNA [39, 40], mRNAs [41, 42], riboswitches [43], lactose operon [44], non-coding OLE RNA [45] and several phage-induced regulatory RNAs [46].

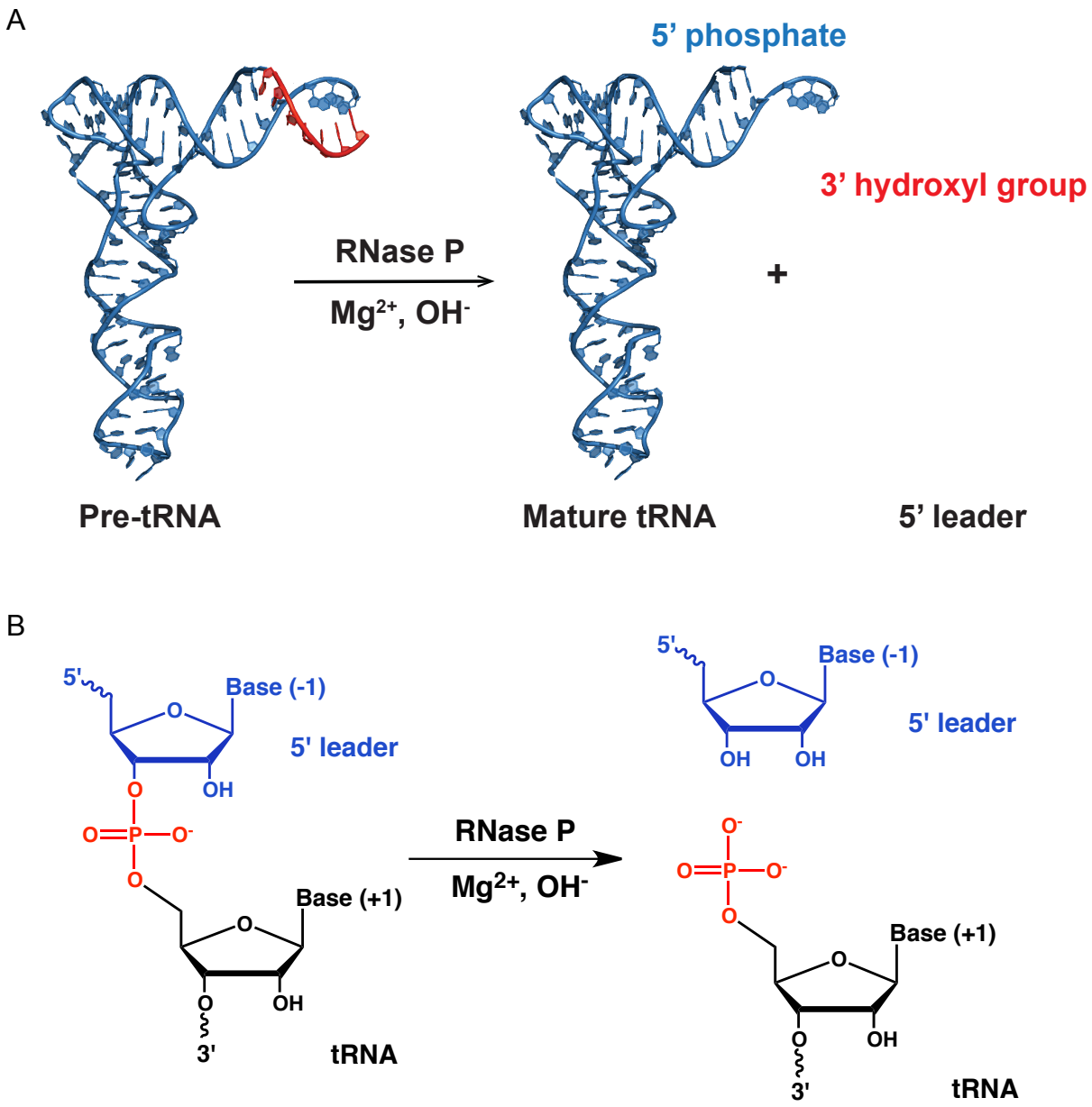

Figure 1-2: RNase P catalyzed 5’-end maturation of tRNA. **(A)** A cartoon showing RNase P generates mature tRNA with a phosphate at the 5’-end and a 5’ leader product with a 3’ hydroxyl group [32]. **(B)** Reaction of RNase P catalyzing hydrolysis of a phosphodiester bond in pre-tRNA generating a 5’ monophosphate on tRNA.

In most organisms, RNase P is ribonucleoprotein complex which is composed of one conserved catalytic RNA subunit and a varying number of protein subunits depending on the organisms (1 in bacteria, 4-5 in archaea and 9-10 in eukarya nuclei) [28, 33, 47-

51], with the exception of the RNase P from plant mitochondria and chloroplast and human mitochondria. In these organelles, RNase P is proposed to consist exclusively of protein [52-54]. Therefore, RNase P could be an antimicrobial target or used for gene-therapy [55-59] due to the differences between bacterial and human enzymes. In RNA-based RNase P, the RNA subunit of RNase P mediates pre-tRNA 5'-end cleavage at the correct position in the absence of protein subunit [13, 60, 61]. However *in vivo*, both the RNA and protein subunits are necessary for function [33, 62-64].

1.2.1 RNA-based RNase P

1.2.1.1 The RNA Subunit of RNase P

The RNase P RNA subunit, the catalytic subunit of the enzyme, is present in all three domains of life (bacteria, archaea, and eukarya), and in some mitochondria and plastids [65-68]. The sequences of RNase P RNA are highly variable and recognize a variety of substrates [69]. However, a core consensus sequence with conserved secondary structure is shared among bacterial, archaeal and eukaryotic nuclear RNase P RNAs [70]. While the eukaryotic nuclear RNase P RNA has diverse secondary structures, in bacteria and archaea there are five major distinct types of secondary structures [63, 69, 71-74] including type A (ancestral), B (*Bacillus*), C (Chloroflexi), M (Methanococci) and P (*Pyrobaculum*).

Phylogenetic analysis classified the structure of bacterial RNase P RNA into three types [69, 75-78]. Type A RNAs are the most common form found in bacteria, represented by *Escherichia coli* RNase P RNA, and type B RNAs are found in most low-GC gram-positive bacteria and RNase P RNA of *Bacillus subtilis* is the model example

[69, 79]. Type C RNAs are found in some Chloroflexi and they appear intermediate between types A and B [69, 72]. Even though the secondary structures of types A and B are significantly different, the alterations are not in the region directly involved in substrate recognition or catalysis. The regions shared between types A and B contain the sequences and structures required for catalytic function *in vitro* [80]. The structures of these P RNAs can be divided into two domains, the catalytic domain, which is sufficient for catalyzing pre-tRNA cleavage, and the specificity domain that enhances substrate affinity [70, 81, 82].

In archaeal RNase P RNAs the most common type of the RNA structure is type A, resembling the ancestral bacterial type but lacking P13/P14 and P18. Another type in archaea is M-type RNAs, which are found in *Methanococci* and *Archaeoglobus*. They are similar to archaeal A-type RNAs but lack P8, P16, P6 pseudoknot and the CCA recognition loop in P15 that enhances substrate recognition [83]. The type P RNase P RNAs are found in *Pyrobaculum*. These RNase P RNAs contain only the catalytic domain, lacking nearly the entire specificity domain seen in other bacterial and archaeal RNase P RNAs [84].

The sequences of eukaryal RNase P RNAs are highly variable and diverse [71, 74]. In some primitive mitochondria and plastids, secondary structures of RNase P RNA are similar to their bacterial ancestors [71]. In yeast mitochondria, the sequence length of RNase P RNA varies between 140 and 490 nt in different species [85]. However, the eukaryotic RNase P RNA sequences can also be described by a minimal consensus secondary structure with the bacterial and archaeal RNase P RNA [86]. Several conserved regions and helical elements have been identified that are present in all of

these RNAs [70, 83, 86]. The universally conserved structural core consists of five sequence-conserved regions, CR1 to CRV, and several helical elements, P1-P4 and P7-P10/11, which are variable in sequence but occur at the same position in the different RNAs (Figure 1-3) [31, 70, 87]. Only 21 nucleotides in the universal core are conserved in nucleotide identity and 11 of them are located in helix P4 and adjacent sequences, which forms an essential part of the catalytic center of RNase P and plays crucial roles in structure and function [31, 70, 88, 89].

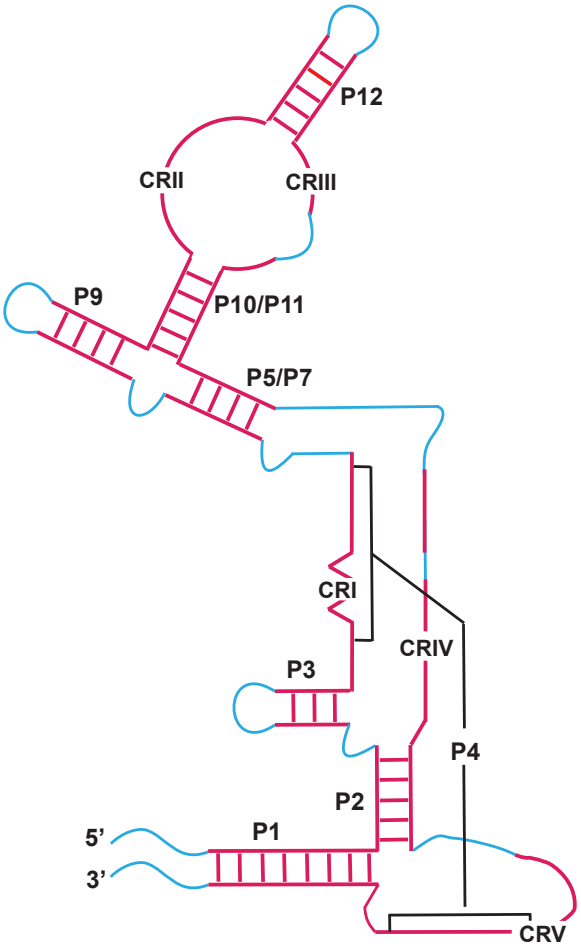

Figure 1-3: Minimum consensus secondary structure of RNase P RNAs [90]. Blue lines indicate connections that vary in structure between conserved elements. CR: conserved region; P: paired region (i.e. helical).

1.2.1.2 The Protein Subunit(s) of RNase P

While the RNase RNAs are fully catalytic *in vitro* at high cation concentrations [13, 60, 61], the RNase P proteins are required *in vivo* [33, 62-64]. The main role of the protein subunits is to enhance substrate and metal ion binding affinity as well as alter substrate selectivity [13, 60, 61, 91, 92].

In bacteria, RNase P contains one single protein of about 14 kDa. The sequences of bacterial RNase P proteins have little similarity, but they are structurally homologous [93, 94]. They share a fold and structure with overall αββββαβα topology and two RNA binding regions, a central cleft and RNR motif [95-97]. Bacterial RNase P proteins are functionally interchangeable; the RNA and protein subunits from one species can complement subunits from the other species with variable reactivity [13, 58, 98].

Archaeal RNase P presents an interesting montage made up of an RNA, which bears striking resemblance to the bacterial counterpart, and at least four proteins, which share sequence homology with yeast and human RNase P proteins, but not the bacterial protein [99, 100]. The four archaeal RNase P proteins have significant similarity to four of nine RNase P proteins from yeast nucleus, POP4, POP5, RPP1 and RPP2 [100, 101]. In *Pyrococcus furiosus*, RNase P proteins function as two binary complexes, POP5 - RPP30 and RPP21 - RPP29 (using the nomenclature for human RNase P protein subunits), to enhance substrate recognition and affect cleavage site selection [102].

In eukarya, nuclear RNase P usually contains nine to ten proteins and most of them are shared with the related endonuclease MRP (mitochondrial RNA processing) [103, 104]. Conservatively estimate, at least four of the human proteins are homologs of

proteins from yeast RNase P, but none has clear homology to the bacterial protein subunit [103]. In the mitochondria of *Saccharomyces cerevisiae*, RNase P contains one protein with no homology with any other RNase P proteins [67, 105]. Compared to their bacterial and archaeal counterparts, eukaryal RNase P enzymes are not as well characterized structurally and biochemically.

1.2.2 Protein-only RNase P

In plant chloroplast, it has long been suggested that RNase P lacks an RNA subunit based on its different density from ribonucleoprotein [106]. Biochemical studies of RNase P activity suggested protein-only enzymatic activity in both plant chloroplast and human mitochondria [52, 107].

Catalytic activity of an RNase P deriving entirely from proteins was first time demonstrated by the identification of components from human mitochondrial RNase P [54]. Human mitochondrial RNase P is a complex of three proteins, MRPP1, 2 and 3 and mitochondrial RNase P activity can be reconstituted *in vitro* by using only recombinant MRPP1, MRPP2 and MRPP3 [54]. MRPP1 is a SAM dependent tRNA N1-methylguanosine and N1-methyladenosine methyltransferase [108, 109]. MRPP2 is a NAD^+-dependent short-chain dehydrogenase/reductase (SDR) that forms a stable sub-complex with MRPP1 [110, 111]. MRPP3 contains an NYN (Nedd4-BP1, YacP nucleases) metallonuclease domain and catalyzes endonucleolytic cleavage of pre-tRNA and possibly other substrates. MRPP3 also contains 5-6 pentatricopeptide repeat (PPR) helix-turn-helix structural motifs, which are important for RNA binding [112-114]. While MRPP1 and MRPP2 are tightly associated with each other, MRPP3 does not

form a stable association with the MPRR1/2 complex [54]. The MRPP1/2 complex activates MRPP3 by an unknown mechanism, although the catalytic activities of MRPP1 and MRPP2 are not required [108]. Numerous questions about this newly identified enzyme remain unanswered, such as cellular location, structural characterization and biological function.

Different from human mitochondrial RNase P, in most plants, RNase P is a single subunit protein-only RNase P (PRORP). It was first identified in *Arabidopsis thaliana*, which contains three PRORP isoforms, PRORP1, PRORP2, and PRORP3 [53]. PRORP1 localizes to the mitochondria and chloroplasts, whereas PRORP2 and 3 localize to the nucleus [53, 115]. All three PRORPs are homologous to human MRPP3 [53]. In contrast to human mitochondrial RNase P, the PRORPs of plants are capable of processing pre-tRNA without the assistance of other subunits [53, 115, 116]. Structural studies of PRORP1 show that the NYN metallonuclease and PPR domains are linked by a structural zinc domain [114]. Like RNA-based RNase P, PRORP1 activity is dependent on divalent metal ions and the metal-bound structure reveals an active site with conserved aspartate residues that bind two manganese ions [114, 117]. The PPR domain of *A. thaliana* PRORP1 enhances pre-tRNA affinity and is important for cleavage activity [114, 117, 118].

The crystal structure reveals that nature pieced together three distinct protein domains to replace the ancient RNA enzyme [114]. None of the domains shows significant sequence homology to any previously identified RNase P protein components. RNA based RNase P is an extremely efficient enzyme. At 37°C, k_{cat}/K_M for pre-tRNA cleavage of the yeast nuclear RNase P holoenzyme is ~10^8 $M^{-1}s^{-1}$ [119] and ~4×10^6

$M^{-1}s^{-1}$ for bacterial RNase P [92]. In contrast, the activities for PRORP1 and PRORP3 are much slower (~10^5 $M^{-1}s^{-1}$) [114, 115, 120, 121]. These data indicate that the driving force for evolving a protein-only RNase P is unlikely to be enhanced catalytic efficiency. It has been speculated that it might be due to the difficulty of importing large RNA into mitochondria and/or to enhance the substrate specificity. Furthermore, the high pH and free radicals in organelles decrease the stability of RNA [121].

1.3 Catalytic Mechanism of RNase P

RNase P catalytic activity is dependent on divalent metal ions, for both RNA-based and protein-only RNase P [13, 53, 114, 122]. The kinetic studies suggest a conformational change step, which is essential for RNA-based bacterial RNase P catalysis, occurs after substrate binding and before hydrolytic cleavage [123]. Biochemical data of protein-only RNase P, PRORP1, show a dependence on pH and metal ions that mirrors that observed for the RNA-based RNase P, suggesting similar catalytic mechanisms [116]. Here I'll describe the catalytic mechanism of RNase P using the RNA-based bacterial enzyme as example, including a discussion of the importance of metal ions and conformational dynamics in RNase P catalysis.

1.3.1 Structure of Bacterial RNase P

Bacterial RNase P is the simplest ribonucleoprotein RNase P, composed of one 300-400 nt RNA (100-130 kDa) and a small protein (14 kDa). Under high ionic strength and divalent metal ion conditions, bacterial RNase P RNA alone can catalyze cleavage of 5'

leaders of pre-tRNA correctly *in vitro* [13]. But *in vivo*, both RNA and protein subunits are essential [57].

X-ray crystal structures of both the type A (from *Thermotoga maritima*) [124] and B (from *Bacillus stearothermophilus*) [125] RNase P RNAs have been solved. RNase P RNA has a highly conserved core structure including two independently folding domains, catalytic domain (C-domain), which contains conserved regions CR-I, IV and V, and specificity domain (S-domain), which contains CR-II and III (Figure 1-4) [70, 81, 82]. The C-domain alone and in the presence of RNase P protein is catalytically active, although cleavage is slower than intact RNase P RNA, but the largest effect is that the pre-tRNA substrate affinity is decreased. These data indicate that the C-domain contains the catalytic site [126-128]. The S-domain interacts with the D- and TψC-domains of pre-tRNA and increases substrate binding affinity and specificity [129-131]. The P4 helix is the most highly conserved region in the C-domain of RNase P RNA, possessing 11 of the 21 universally conserved nucleotides (Figure 1-4) [31, 70], suggesting that the conserved nucleotides in the P4 helix play important structural and functional roles in RNase P catalysis.

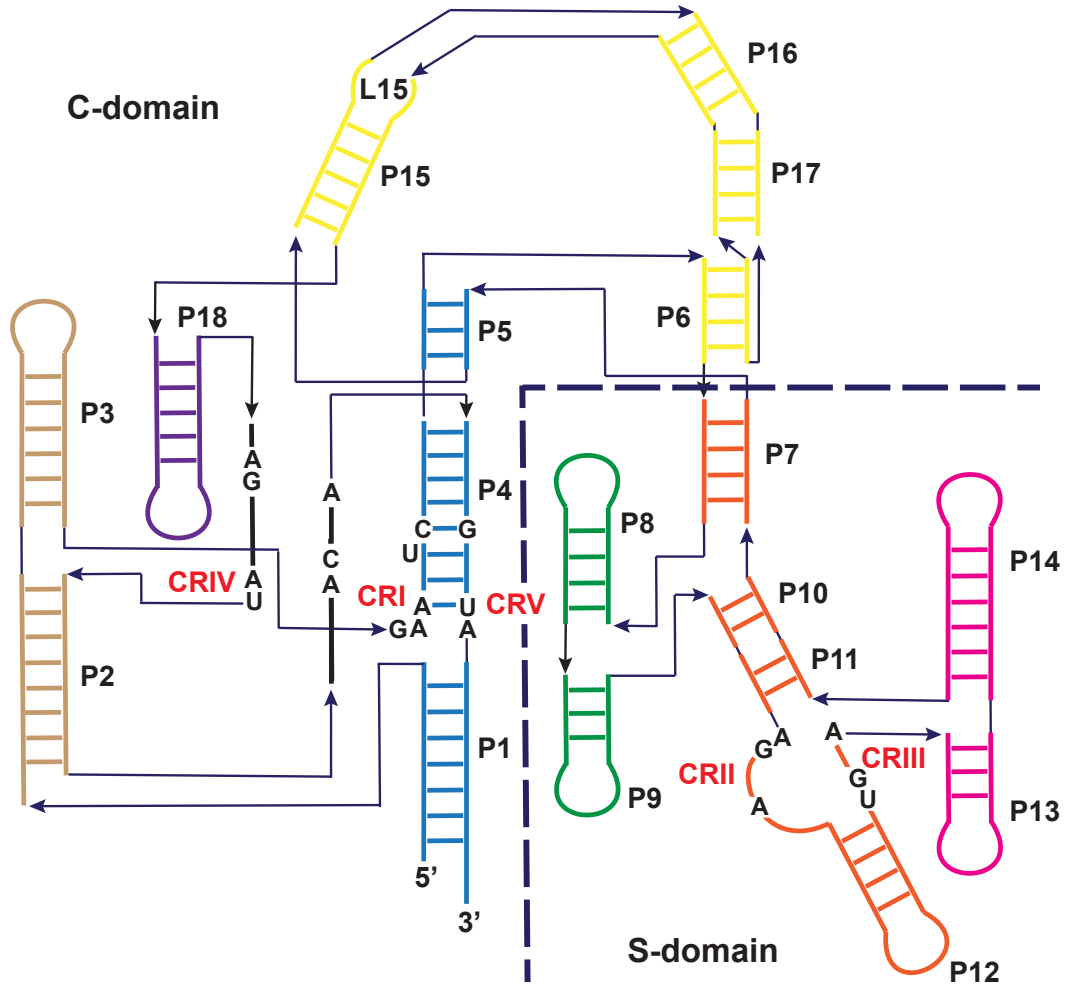

Figure 1-4: Secondary structure of *T. maritima* RNase P RNA [132, 133]. The C-domain of *T. maritime* RNase P RNA includes P1/P4/P5 (in blue), P2/P3 (in brown), P6/P15/P16/P17 (in yellow) and P18 (in purple). The S-domain of the *T. maritima* P RNA consists of P8/P9 (in green), P7/P10/P11/P12 (in orange) and P13/P14 (in pink). Residues that are conserved in bacterial P RNAs are shown in capital letters [31].

In a crystal structure of the *T. maritima* RNase P holoenzyme in complex with a yeast $tRNA^{Phe}$ and soaked with a 5' leader (Figure 1-5) [132], the acceptor stem of tRNA interacts with RNase P. The D- and TψC-loop of tRNA contacts the CR-II and CR-III regions in the S-domain. CR-I, CR-IV and CR-V regions in the C-domain adopt a non-helical module that forms an A-minor interaction with the acceptor-stem of tRNA. The 3'CCA end of tRNA forms a base pair with nucleotides in the L15 region. The 5' leader

also contacts with residues of the protein subunit, which is proposed to enhance substrate and metal ion binding affinity by interacting with the leader to align and position the pre-tRNA in the complex (Figure 1-6) [13, 60, 61, 91, 92].

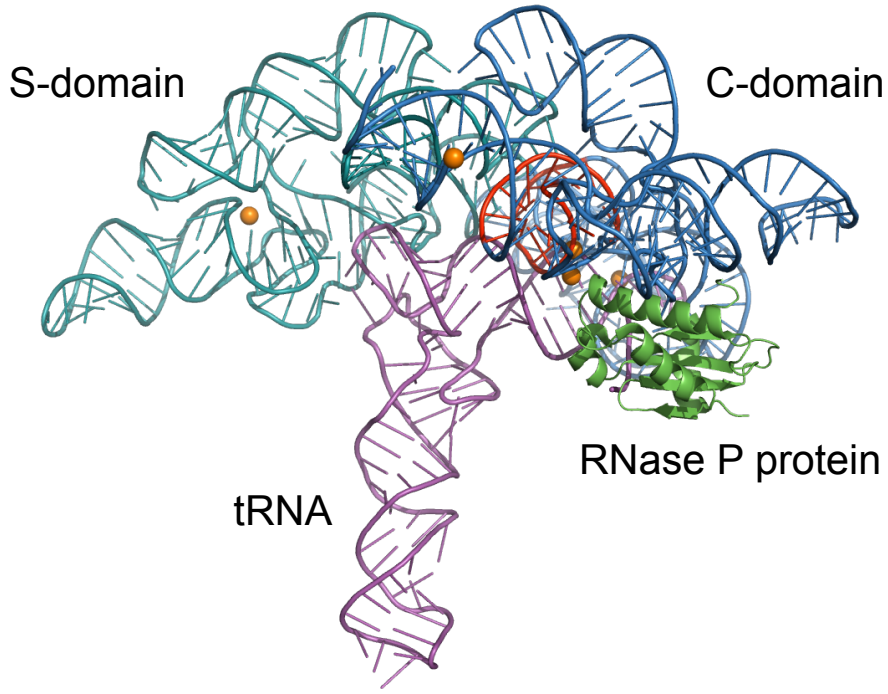

Figure 1-5: Crystal structure of *T. maritima* RNase P [132]. A tertiary complex of *T. maritima* RNase P, tRNA and 5 nt leader (PDB ID: 3Q1R). C-domain is in blue with the P4 helix highlighted in red, S-domain is in cyan, RNase P protein is in green and tRNA and 5 nt leader are in purple. Metal ions are indicated in orange.

The location of the 5'-end of the tRNA is close to the region where P4, P5 and CR-IV intersect, indicating the active site. Soaking of the crystals with Eu^{2+} and Sm^{3+}, led to the identification of two potential metal binding sites in the active site of the *T. maritima* RNase P complex (Figure 1-6) [132]. One site is located between the tRNA 5'-end, the phosphodiester bonds of A50 and G51 (A49 and G50 in *B.subtilis*) and the carbonyl oxygen O4 of universally conserved U52 (U51 in *B.subtilis*). This metal ion is proposed to coordinate a water ligand that functions as the nucleophile in the hydrolytic reaction. The second metal ion is located close to the phosphoryl oxygens of G51, the O3' of the

leader, and the 5'-end of tRNA and is suggested to stabilize the transition state and stabilize the developing charge on the leaving group. However, the resolution of the crystal structure (4.2 Å) is insufficient to identify which ligand contacts a metal ion and distinguish between inner- and outer-sphere metal ion coordination. Higher resolution structures of the RNase P ternary complex with metals that more closely resemble Mg^{2+} in size and coordination preferences are still needed to refine the active site structure and the position of the metal ions bound to RNase P.

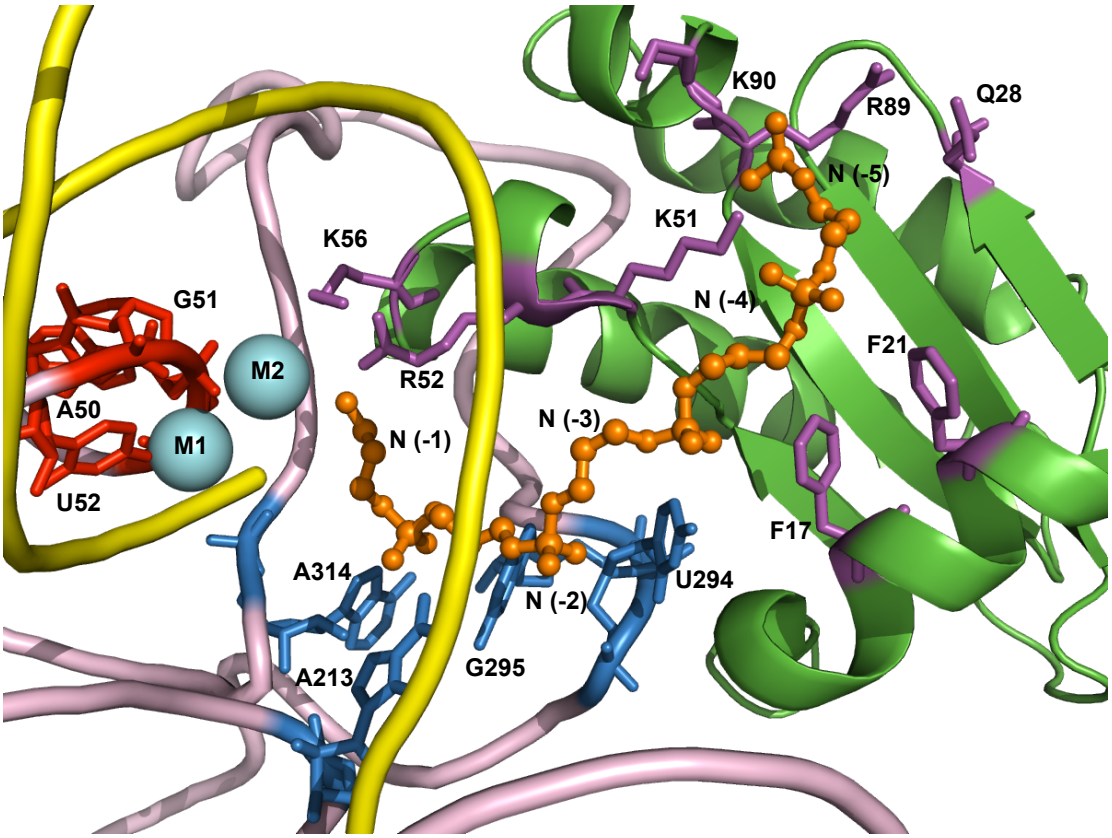

Figure 1-6: Structure of *T. maritima* RNase P active site (PDB ID: 3Q1R) [132]. Two metal ions (M1 and M2, in cyan) are located near the P4 helix (A50, G51 and U52, in red). The 5' leader (in orange) interacts with A213, U294, G295 and A314 (in blue) of the RNase P RNA (in pink) and contacts F17, F21, K51, R52 and K90 and possibly Q28, K56 and R89 of the RNase P protein (in green). tRNA is shown in yellow. Drawn by using Pymol software.

1.3.2 Substrate Recognition by RNase P

RNase P recognizes the L-shape structure of all pre-tRNAs. Both RNase P RNA and RNase P protein contribute to the recognition of pre-tRNA substrates. The precursor tRNA and RNase P RNA complex has been demonstrated to include interactions between the T stem-loop and acceptor stem of the pre-tRNA with the S-domain of RNase P RNA through coaxial stacking and backbone [130, 134, 135]. The crystal structure of the *T. maritima* RNase P ternary complex also shows that the S-domain of RNase P RNA base stacks with the D- and TψC-loop of the tRNA [132], consistent with biochemical data. The *B. subtilis* RNase P holoenzyme binds pre-tRNA 100-fold more tightly than the C-domain- RNase P protein complex [127], suggesting that contacts between the T-stem loop and acceptor stem of pre-tRNA with the S-domain enhance the specificity and affinity of RNase P for pre-tRNA.

In bacteria, the RCCA motif at the 3' end of pre-tRNA forms Watson-Crick base pairs with a conserved GGU-motif in the L15 region of RNase P RNA [136], as observed in the crystal structure of the *T. maritima* RNase P ternary complex [132]. It has been suggested that the function of these base pairs is to anchor the RNase P RNA to the substrate and expose the cleavage site such that phosphodiester bond hydrolysis is accomplished at the correct position [136]. However, not all pre-tRNA transcripts encode the 3' RCCA and the CCA moiety only modestly enhances pre-tRNA affinity to the holoenzyme [137]. The 3' RCCA interaction motif is missing in archaeal type-M P RNA and eukaryal P RNA [23]. Biochemical data also demonstrated that the residue at the N(-1) position of pre-tRNA interacts with a conserved adenine in J5/15 of RNase P RNA [138, 139]. Analysis of pre-tRNA leader sequences in *Bacteria* and *Archaea*

reveals a conserved preference for U at N(-1) [138]. This interaction is proposed to enhance cleavage of pre-tRNA at the correct position.

RNase P protein enhances the substrate affinity and cleavage activity of RNase P. The holoenzyme binds pre-tRNA ~ 500-fold more tightly than tRNA [92], and depending on the leader length of pre-tRNA, the affinity and cleavage rate of pre-tRNA is variable [140, 141]. This preference for pre-tRNA is not observed in RNase P RNA alone [140, 141] suggesting that the RNase P protein enhances the substrate affinity and cleavage efficiency by interacting with the 5' leader of the pre-tRNA [142]. Structure probing, crosslinking and fluorescence resonance energy transfer (FRET) data demonstrate that the 5' leader of pre-tRNA is located near the RNase P RNA - RNase P protein interface, and interacts with the hydrophobic central cleft of the RNase P protein [132, 141-143]. Additional data show that the R60A and R62A mutations in the RNR motif of *B. subtilis* RNase P protein decrease the affinity of the protein subunit for RNA subunit and the RNase P holoenzyme for pre-tRNA, suggesting these two residues stabilize RNase P holoenzyme formation and enhance the substrate affinity [144].

1.3.3 Divalent Metal Ions and RNase P Catalysis

The catalytic activity of RNase P is dependent on divalent metal ions. *In vivo*, the metal requirement is fulfilled by Mg^{2+} [122], while *in vitro*, other divalent metal ions, including Ca^{2+}, Mn^{2+}, Cd^{2+}, Pb^{2+} and Zn^{2+} can activate RNase P catalysis [91, 145-148]. Divalent metal ions can contact RNA via outer-sphere interactions, where the interaction between the metal ion and RNA ligand is water-mediated; or inner-sphere interactions, where the RNA ligand directly coordinates with metal ion without intervening water [15].

A large number of Mg^{2+} ions (>150) associate with RNase P [122, 149, 150], a small number of these Mg^{2+} ions form specific contacts with functional groups in RNase P [91, 122].

1.3.3.1 Function of Divalent Metal Ions in RNase P

Kinetic isotope effect studies on RNase P RNA catalysis have suggested that a metal-bound hydroxide serves as the nucleophile in the reaction [151]. In addition, divalent metal ions also stabilize the folded structure, bound pre-tRNA and the transition state for cleavage [33, 122, 152, 153].

A previous study indicates that a minimal kinetic mechanism for RNase P includes four steps (Figure 1-7) [123]: (1) RNase P binds to pre-tRNA to form an enzyme-substrate (ES) complex; (2) the ES complex undergoes a metal dependent conformational step to form an active conformation (ES*); (3) pre-tRNA is cleaved by RNase P to form mature tRNA and 5'-leader and (4) the products dissociate from RNase P [123, 153]. In this two-step binding mechanism, at least two classes of inner-sphere metal ions are required for RNase P catalytic function [153]. The inner-sphere contacts with metal ions are not crucial for the formation of ES conformer, but a high affinity metal ion is required to stabilize the conformational change essential for catalysis, while a lower-affinity metal ion activates catalytic activity (Figure 1-7) [91]. A two-metal-ion mechanism for activation of RNase P catalysis has been proposed where one metal ion positions and activates a hydroxyl nucleophile, while the second ion stabilizes the transient state and coordinates water to enable proton transfer to the 3' scissile oxygen leaving group (Figure 1-8) [132, 145, 154-156]. The metal ion that

stabilizes the conformational change may also participate in stabilizing the transition state for cleavage or may be a third metal binding site. Single molecule FRET data show that in the presence of cobalt hexamine (Cohex, $Co(NH_3)_6^{3+}$), a $Mg(H_2O)_6^{2+}$ mimic capable of only forming outer-sphere interactions, the majority of the RNase P-pre-tRNA complex is in the ES conformation (80-90%) with ~10% in the ES* conformer. Addition of Ca^{2+} significantly increases the population of ES* relative to ES (Kristin S. Koutmou, Nils G. Walter and Carol A. Fierke, manuscript in preparation), indicating that the metal ions stabilize the active ES* conformation.

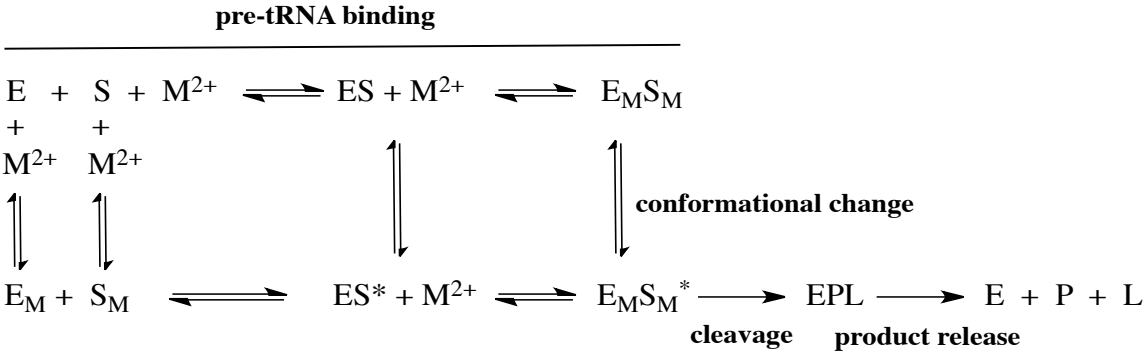

Figure 1-7: Kinetic mechanism of *B. subtilis* RNase P: (E) RNase P holoenzyme; (S) pre-tRNA; (M^{2+}) divalent metal ions; (ES) RNase P•pre-tRNA complex; (ES*) RNase P•pre-tRNA complex after conformational change; (EPL) RNase P•tRNA•5' leader complex; (L) 5' leader; (P) tRNA product [123, 153].

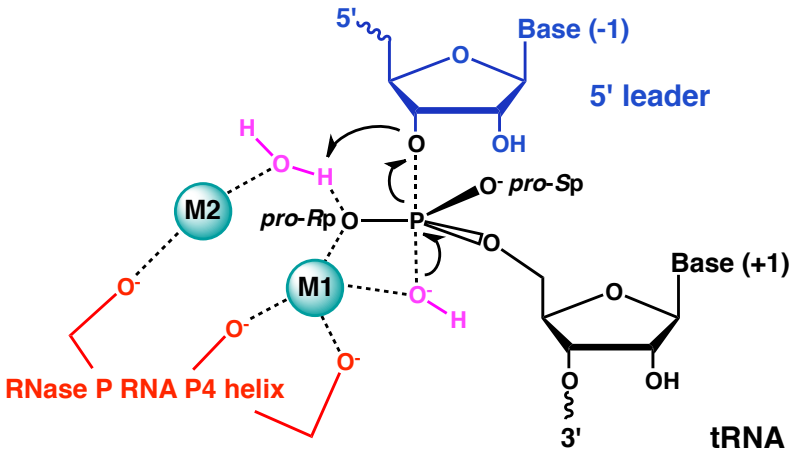

Figure 1-8: Catalytic mechanism of RNase P proposed from the crystal structure of the *T. maritima* RNase P ternary complex [132]. Metal ion M1 coordinates a hydroxide that functions as the nucleophile, creating a new bond and displacing the 3' scissile phosphate oxygen. M2 coordinates water protonates the 3' scissile oxygen leaving group. Both metal ions are proposed to stabilize the developing charge in the transition state.

1.3.3.2 Characterization of Metal Ion Binding Sites in RNase P

Identifying the position of metal ions that site-specifically interact with RNase P RNA is challenging because the majority of divalent metal ions in RNase P RNA bind nonspecifically via electrostatic interactions [15].

The P4 helix is the most highly conserved region in the RNase P RNA [31]. The P4 helix is essential for RNase P activity and has been suggested to contain catalytic and/or co-catalytic metal ion binding sites [157-159]. Atom modifications and functional group substitutions have been used to identify several ligands in the P4 helix important for RNase P catalytic activity. Phosphorothioate modification of non-bridging phosphodiester oxygens at A49 and G50 in the P4 helix of *B. subtilis* RNase P (A67 and G68 in *Escherichia coli*) decreases the cleavage rate constant enormously without (or minimally) affecting the affinity of pre-tRNA [157, 158]. The addition of Mn^{2+} or Cd^{2+} can rescue some of the catalytic defects suggesting that metal ions form an inner-sphere contact with these atoms [35, 157, 158]. 4-thiouridine substitution of the universally

conserved U51 (*B. subtilis* numbering) decreases the cleavage rate and addition of Cd^{2+} can partially rescue this defect, suggesting that the carbonyl oxygen at the O4 position coordinates a metal ion through an inner-sphere interaction (Xin Liu, Yu Chen, and Carol A. Fierke, manuscript in preparation). A 7-deaza-2'-deoxyadenosine substitution of either A65 and A66 in *E. coli* (A47 and A48, *B. subtilis* numbering) RNase P RNA in combination with the *pro-S*p sulfur substitution of A67 (A49, *B. subtilis* numbering) further decreases the cleavage rate suggesting that the base and backbone of A65, A66 and A67 form a metal binding site [152]. Crosslinking studies of *E. coli* RNase P RNA examining the position of the pre-tRNA cleavage site relative to the P4 helix suggest that metal ion binding in the P4 helix leads to indirect stabilization of catalytic metal ions that interact with the scissile phosphodiester bond [159].

Likewise, X-ray crystallography has revealed several potential metal binding sites. Anomalous scattering in diffraction analysis (3.5 Å resolution) of *B. stearothermophilus* RNase P RNA crystals soaked in $Os(NH_3)_6^{3+}$ (which mimics $Mg(H_2O)_6^{2+}$), Pb^{2+}, Sm^{3+}, Gd^{3+} or Yb^{3+} identified a number of possible metal ion binding sites in RNase P with two metal ion binding sites observed near residues A48, A49, G50, G378 and G379 (*B. subtilis* numbering) (Figure 1-9A) [160]. In the crystal structure of *T. maritima* RNase P, metal ion binding sites are proposed from soaking the crystals with Eu^{2+} and Sm^3 [132]. From these data two metal sites are proposed adjacent to the P4 helix at the backbone nonbridging oxygens of the phosphodiester bonds of A50 and G51 (A49 and G50 in *B.subtilis*) and the carbonyl oxygen O4 of U52 (U51 in *B.subtilis*) (Figure 1-9B). These metal sites are consistent with the previous phosphorothioate substitution data indicating metal coordination of the non-bridging phosphoryl oxygens at A49 and G50 in

B. subtilis RNase P (A67 and G68 in *Escherichia coli*) [157, 158], and recent studies of 4-thiouridine substitution of U51 in *B.subtilis* RNase P. However, the low resolution (4.2 Å) of the current ternary complex crystal structure [132] limits the information about the ligands that interact with the metal ions and is not able to distinguish between inner- and outer-sphere metal ion coordination.

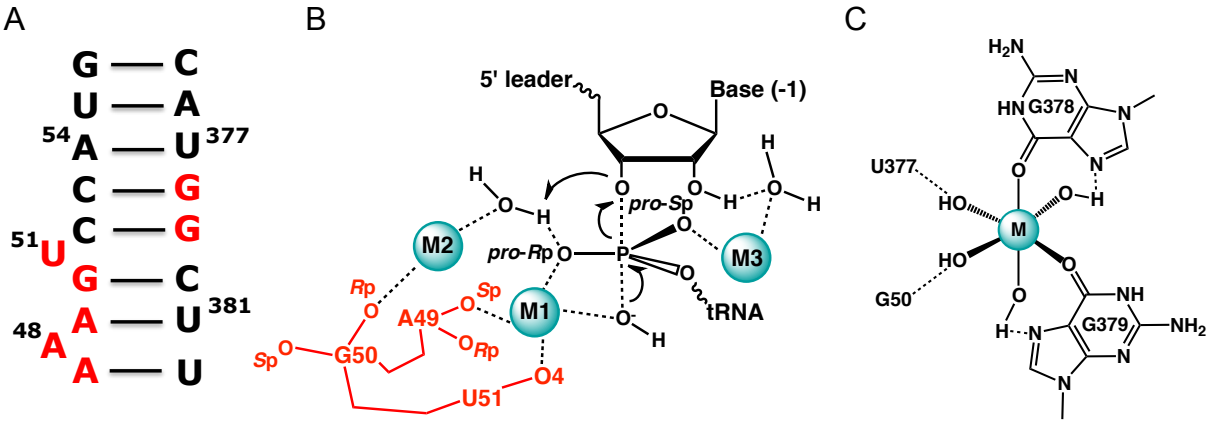

Figure 1-9: Proposed metal ion binding sites in the P4 helix of RNase P RNA identified by structural and biochemical studies. **(A)** Secondary structure of the P4 helix in the *B. subtilis* RNase P RNA. The residues proposed to coordinate with metal ions are highlighted in red. **(B)** Proposed metal ion binding site (*B. subtilis* numbering) according to the crystal structure of *T. maritima* RNase P and biochemical data. [132]. **(C)** Model of metal ion binding sites at G378 and G379 (*B. subtilis* numbering) proposed by NMR and XAS studies of a P4 stem-loop mimic [161].

A nuclear magnetic resonance (NMR) structure of a P4 helix stem-loop mimic revealed association of Mg^{2+} at residues corresponding to G378 and G379 in RNase P (*B. subtilis* numbering) [161-163]. The strategy of combining NMR and X-ray absorption spectroscopy (XAS) for probing RNA-metal binding in solution led to the proposal of an inner-sphere metal binding site at residues G378 and G379 [161], suggesting that the base O6 and N7 of G378/G379 form inner- and outer-sphere interactions with a metal ion, respectively (Figure 1-9C). [161]. However, this model is proposed based on a P4 helix stem-loop model and has not been tested in full-length RNase P by biochemical

experiments.

Additional metal ion binding sites have been identified on the pre-tRNA substrate. Replacement of either the *pro-R_P* or *pro-S_P* non-bridging oxygen with sulfur in the scissile phosphodiester bond of the pre-tRNA substrate decreases the cleavage rate of RNase P RNA by 10^3- to 10^4-fold. The activity of the *pro-R_P* phosphorothioate substituted pre-tRNA can be partially rescued by addition of thiophilic metal ions (Mn^{2+} and Cd^{2+}) suggesting an inner-sphere coordination of a metal ion with this oxygen (Figure 1-9B) [145, 164-167]. In the N(-1) nucleotide of pre-tRNA substrate, 2'-NH_2 and 2'-H substitution for the 2'-OH group decreases both the catalytic rate and the Mg^{2+} affinity for RNase P RNA. Mn^{2+} can rescue cleavage of both the 2'-NH_2- and the 2'-H-modified pre-tRNA suggesting that the 2'-OH of pre-tRNA at the cleavage site interacts with a metal-bound water molecule (Figure 1-9B) [167].

1.3.4 Conformational Change in RNase P Catalysis

Transient kinetic studies of *B. subtilis* RNase P reveal a two-step association mechanism where RNase P and pre-tRNA associate to form a complex (ES) in a near diffusion-limited process followed by an metal ion dependent isomerization in the enzyme-substrate complex (ES*) referred to as the conformational change step (Figure 1-7) [123, 153]. This new RNase P - pre-tRNA conformer (ES*) is stabilized by both a class of high affinity divalent cations capable of inner-sphere coordination [153] and interactions between the pre-tRNA leader and the RNase P protein [140, 144, 153].

1.3.4.1 Structural Changes in the Transition from ES to ES* in RNase P Catalytic Pathway

Structural information about the RNase P conformational change is limited. The currently available crystal structures of RNase P are unlikely in the active conformation as there is no structure that contains pre-tRNA. The solution structure of *B. stearothermophilus* RNase P RNA is not preformed to dock with the substrate suggesting that the conformation of RNase P changes upon binding RNase P protein, metal ions and substrate [32, 125, 168]. The most recent *T. maritima* RNase P holoenzyme crystal structure is a ternary complex containing mature tRNA and the product pre-tRNA 5' leader, but not pre-tRNA substrate [132]. This structure represents the product complex and presumably does not reflect the active ES* conformation. Furthermore, the metal ions in the crystal structure are Eu^{2+} and Sm^{3+}, instead of the catalytic divalent metal ions, such as Mg^{2+}, Mn^{2+} or Ca^{2+} [132], therefore providing additional uncertainty about the binding sites for catalytic/co-catalytic metal ion in the active conformer.

In the active ES* complex of *B. subtilis* RNase P, the central cleft of the RNase P protein binds to the 5' leader of the pre-tRNA substrate between the fourth and seventh nucleotides upstream of the cleavage site, extending the leader and decreasing its structural dynamics to position the cleavage site in the catalytic core [141, 142, 169]. Time-resolved fluorescence resonance energy transfer (trFRET) measurements capture the structural changes that occur between substrate and RNA - protein interface during the conformational change from ES to ES* under equilibrium conditions [153]. In this ES to ES* transition, the 5' leader of pre-tRNA moves 4 to 6 Å closer to the RNA - protein

interface suggesting the conformational change reorganizes the bound substrate in the active site to form a catalytically competent ES* complex.

Furthermore, as measured by fluorescence stopped-flow and trFRET experiments, the conformational change coupled to pre-tRNA binding is also observed for the C-domain alone albeit with a reduced rate (John Hsieh and Carol A. Fierke, unpublished data). Since the P4 helix is located in the C-domain and proposed to be the active site of RNase P catalysis [31, 70, 157-159], the direct involvement of the P4 helix in catalysis could require a conformational change that allows the structure of the P4 to be dynamically satisfied by the enzyme. However, currently there are no available data on the conformational dynamics of the P4 helix or the role of the P4 helix during the transition from ES to ES*. Nevertheless, an NMR study on a mutant P4 helix stem-loop mimic suggests that the highly conserved U7 (U51 in *B. subtilis* RNase P), which coordinates an inner-sphere metal ion [132] (Xin Liu, Yu Chen, and Carol A. Fierke, manuscript in preparation), and helical residue C8 (C52 in *B. subtilis* RNase P) are locally mobile on picosecond-to-nanosecond time scales suggesting the existence of functionally important fast internal motions in the P4 helix [163]. It indicates the flexibility of bulged U7 in the P4 helix stem-loop mimic, potentially in the P4 helix of full-length RNase P RNA as well.

1.3.4.2 Function of the Conformational Change for RNase P Catalysis

The ES to ES* transition is an essential step that occurs prior to the cleavage reaction in the kinetic mechanism of RNase P, and this new RNase P - pre-tRNA conformer (ES*) is stabilized by specific interactions between the pre-tRNA leader and the RNase

P protein in the RNase P - pre-tRNA complex [140, 144, 153]. Due to the limited structural information on the conformational change of RNase P - pre-tRNA complex, it is currently unclear precisely what role the conformational change is playing in the RNase P catalytic pathway.

The movement of the 5' leader of pre-tRNA closer to the RNase P RNA - RNase P protein interface during the ES to ES* transition suggests that the substrate is repositioned in the active site [153]. The conformational change in the RNase P - substrate complex could allow optimal interaction of the two independently folded C-domain and S-domain of RNase P RNA to position functional groups and catalytically important ions in the active site [170]. Additionally, the nucleotide base at the N(-1) position in the 5' leader has been proposed to form hydrogen bonds with a highly conserved adenosine in RNase P RNA to strengthen the fidelity of pre-tRNA cleavage [138]. To form this base pair, a structural rearrangement is required [169, 171]. Other possible functions of the conformation change include: positioning of the active-site residues and magnesium-hydroxide nucleophile to catalyze hydrolysis [172, 173], and facilitating the proposed unwinding of the 5'- and 3-'ends of pre-tRNA [174]. The conformational change might also act as a proofreading step to distinguish cognate from non-cognate substrates given the near-diffusion-controlled association kinetics and high substrate affinity [153]. Additionally, a conformational change could enhance the ability of RNase P to recognize the wide variety of pre-tRNAs and other substrates [36, 153, 175].

1.4 Charactering RNA Structure and Dynamics by Nuclear Magnetic Resonance

RNA performs widespread roles in cells [4-8] due to both the intricate three-dimensional structures [176-178] and the conformational changes induced by environmental factors [179, 180]. The dynamic properties of RNA structures play an important role in these conformational change [181]. Studying the relationship between structure and function and characterizing the RNA dynamics are important for understanding how an RNA molecule executes a particular function in cells. Nuclear magnetic resonance (NMR) is an indispensible tool for the determination of RNA structure and dynamics, as it is the experimental technique that offers resolution of biomolecules in solution at an atomic level [182-187].

1.4.1 Studying RNA Structure by NMR

Every NMR active atom in an RNA molecule has a unique property, the NMR chemical shift, which is the variation of the resonance frequency for the same kind of nucleus due to variations in its electronic environment. Chemical shifts differentiate magnetically nonequivalent nuclei and provide information on the local environment thus allowing for the atomic-resolution study of large biomolecules. The information about RNA that can be derived from NMR includes: base pairing pattern, secondary structure motifs, metal ion and ligand binding, and interaction with other molecules [188].

To obtain structural information about an RNA molecule, the essential first step is assigning the identity of each chemical shift in an NMR spectrum to a given atom. NMR methodologies for resonance assignments of nucleic acida are well established.

Generally, individual nuclei are connected to nearby nuclei via through-space or through-bond correlations. Subsequently, a network of sequential connectivities can be created and then used in the determination of secondary structure and base pairing [188, 189].

Nuclear Overhauser effect spectroscopy (NOESY) is one of the most powerful tools for structural determination of biomolecules in the solution state ([190]. Nuclear overhauser effects (NOEs) occur between protons that are less than 5 Å apart. The transfer of nuclear spin polarization from one nuclear spin population to another via dipolar cross-relaxation results in an NOE cross peak, where the intensity of this cross peak is related to the distance between the two protons. In a nonexchangeable NOESY, an H1’ proton in sugar has an NOE peak to its own H6/8 in nucleobase and to the H6/8 of the 3'-adjacent residue [188] (Figure 1-10). In this way, sequential connectivities can be obtained from the 5' to 3' direction. Furthermore, H2 of adenosine has a cross peak to the neighboring H2, to the H1' on the opposite strand in the 3' direction, and to the H3 imino proton of a base paired uridine [188]. Additional intranucleotide connections, including H5 to H6 of cytosine and uridine, and internucleotide connections, including H4 of cytosine to H1 imino proton of a base paired guanosine are also observed in NOESY [188]. An exchangeable NOESY can be used to not only assign imino resonances, but also to determine the base pair pattern of the RNA, because non-base paired imino proton resonances exchange rapidly with water and are not observed [188].

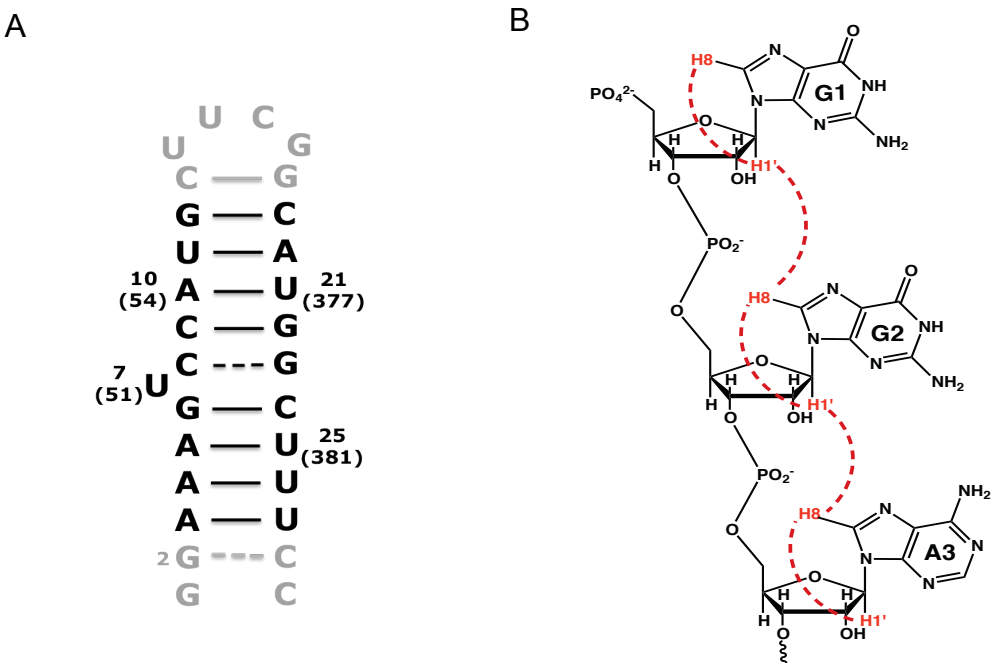

Figure 1-10: A cartoon showing the sequential connectivities in a nonexchangeable NOESY. **(A)** Secondary structure of a P4 helix mimic [161]. **(B)** Intra- and internucleotide connectivities between H8 and H1' of first three residues in the P4 helix mimic.

Proton assignments can be easily translated to 2D ^{13}C-^{1}H and ^{15}N-^{1}H heteronuclear correlation spectra (HSQC or HMQC) to acquire the corresponding carbon and nitrogen chemical shifts. Information from through-bond assignment experiments that utilize scalar couplings, such as the HCN triple resonance experiment used for $^{13}C/^{15}N$ labeled samples [191], can supplement the assignment of carbon and nitrogen. HCN experiment connects C6H6 or C8H8 of the nucleobase to the ribose C1'H1' via their shared N1/9 [188].

1.4.2 Probing RNA Dynamics by NMR

Beside structural information of RNA, NMR can also be used to determine the local and global dynamics of a biomolecule on the picosecond to second timescale [181,

188]. RNA dynamics exhibit a wide range of timescales from picoseconds to minutes [192, 193]. Those related to biological function often occur on the microseconds to milliseconds time scale. The RNA dynamics result in transient, low populated conformer(s), which include rearrangements in the secondary structure base pairing, sugar puckering, ligand binding and RNA architecture [192, 194-197]. Determination of the structure of this low populated conformer is not feasible using traditional structural approaches. One way to detect RNA dynamics at these time scales is to use an experimental approach called NMR rotating frame ($R_{1\rho}$) relaxation dispersion methods. Relaxation dispersion NMR spectroscopy is one technique that can be used to site-specifically quantify motions occurring on microsecond-to-millisecond time scale [184-186, 198-201].

The relaxation dispersion experiment monitors chemical exchange, a phenomenon that refers to the process of a nucleus experiencing two chemically distinct states [186, 202]. When a nuclear spin has two chemically distinct states, a highly populated state A (ground state) and a weakly populated state B (transient state), and these two states are mutually exclusive, the intensity of the observed resonance for each state is proportional to its population (Figure 1-11A). If exchange occurs between two resonances, the low abundance resonance B is broadened (Figure 1-11A) due to the chemical exchange phenomenon and cannot be detected directly. However, relaxation dispersion experiments can measure such chemical exchange to observe resonance B.

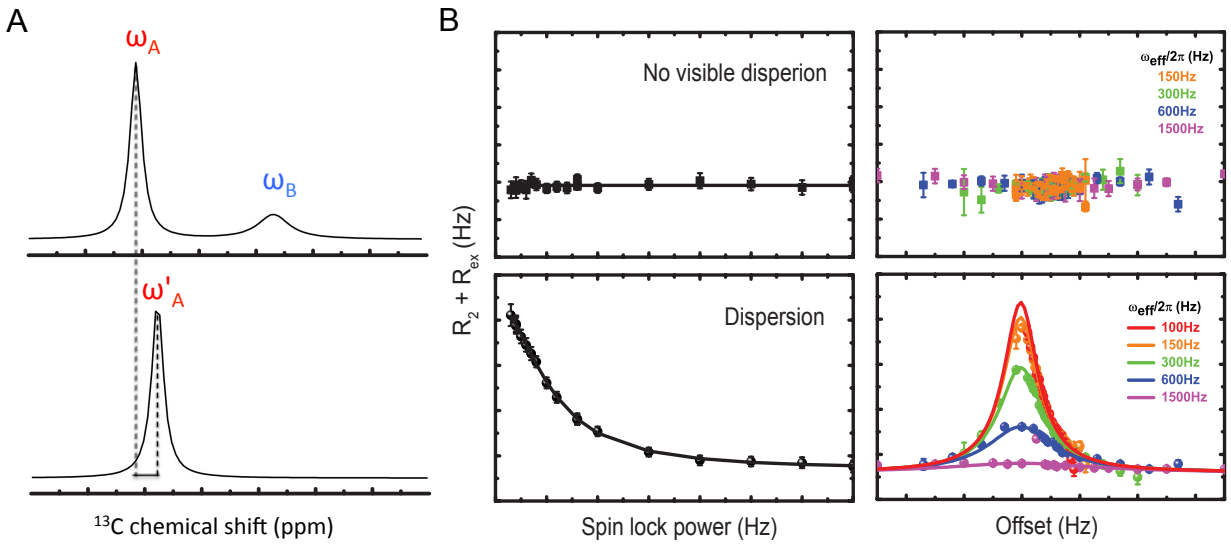

Figure 1-11: Measurement of chemical exchange by $R_{1\rho}$ relaxation dispersion. **(A)** A resonance with two chemically distinct states has no chemical exchange (upper) or exchange between two chemically distinct states A and B (lower). **(B)** Example of on- (left) and off-resonance (right) profiles in which there is no visible dispersion (upper) and in which there is dispersion (lower).

$R_{1\rho}$ relaxation dispersion measures the relaxation rate of the transverse magnetization decay in a combination of R_2 and chemical exchange (R_{ex}) because exchange between two states increases the relaxation rate of transverse magnetization [186, 202, 203]. It probes the intensity of the observed resonance as a function of spin lock power (ω_{SL}) and resonance offset from the spin lock carrier frequency (Ω) (Figure 1-11B) to reveal the rate of chemical exchange. The increased spin lock power suppresses the chemical exchange and consequently decreases the contribution of R_{ex} to transverse magnetization decay, and results in observed intensity of the target peak decaying faster. Resonance offset from the spin lock carrier frequency varies from negative to positive values, the greatest sensitivity of the chemical exchange occurs when Ω equals to Ω_B (resonance offset for state B) due to the maximum of R_{ex}, therefore resulting in the slowest decay of the observed peak intensity. By fitting the two-state exchange to Laguerre approximation [186, 204], the intrinsic longitudinal (R_1) and transverse

relaxation rate constants (R_2), the ground (p_{GS}) and transient state fractional population (p_{TS}) and the chemical shift difference between the ground state and transient state ($\Delta\omega$) can be obtained. Therefore, by determining the chemical shift changes in the weakly populated conformer (transient state) relative to the highly populated conformer (ground state), the insights into the structure of the unobservable conformer can be provided.

1.5 Objectives of this Research

The overall objectives of this research are to further understand the catalytic function of RNase P, including determining the roles of metal ions in catalysis, probing transient state conformation of the P4 helix in RNase P, and characterizing the nature and function of the RNase P conformation change.

Chapter 2 investigates the putative metal ion binding sites proposed by NMR and XAS using a P4 stem-loop mimic model. By using atom modifications and enzyme kinetics, the proposed metal ion binding sites were examined in the full-length *B. subtilis* RNase P RNA and the data suggest an outer-sphere metal ion interacts with the carbonyl oxygen O4 of residue G379. This metal ion participates in both the conformational change and hydrolytic cleavage steps of RNase P catalysis.

In Chapter 3, a P4 helix stem-loop mimic is used to characterize the dynamics of the P4 helix. An alternative conformer of the P4 helix is detected by NMR $R_{1\rho}$ relaxation dispersion experiments. The data suggest that in the ground state to transient state transition, three-adenines at the bottom of helix unwind, G6 transits from *anti* to *syn* and a kink forms at the backbone between A5 and G6, creating an electronegative patch

that enhances metal affinity. Additionally, the bulged U7 rapidly and independently oscillates in and out of the helix.

Following Chapter 3, the structural rearrangement detected in the P4 helix mimic by NMR $R_{1\rho}$ relaxation dispersion is further examined in Chapter 4 in the full-length *B. subtilis* RNase P RNA. The kinetic data show that the conformational change in the P4 helix of RNase P mimics the transient state observed in the stem-loop model. The function of this structure alteration is to position the catalytic metal ion and enhance the metal ion affinity, and is essential for catalysis.

At last, Chapter 5 discusses future directions to further investigate the metal ion binding and conformational dynamics for RNase P catalysis.

1.6 References

1. Caspersson, T. and Schultz, J., *Pentose Nucleotides in the Cytoplasm of Growing Tissues.* Nature, 1939. **143**: p. 602-603.
2. Crick, F.H., *On protein synthesis.* Symp Soc Exp Biol, 1958. **12**: p. 138-63.
3. Sharp, P.A., *The centrality of RNA.* Cell, 2009. **136**(4): p. 577-80.
4. Doudna, J.A., *Structural genomics of RNA.* Nat Struct Biol, 2000. **7 Suppl**: p. 954-6.
5. DeRose, V.J., *Metal ion binding to catalytic RNA molecules.* Curr Opin Struct Biol, 2003. **13**(3): p. 317-24.
6. Steitz, T.A. and Moore, P.B., *RNA, the first macromolecular catalyst: the ribosome is a ribozyme.* Trends Biochem Sci, 2003. **28**(8): p. 411-8.
7. Szymanski, M. and Barciszewski, J., *Regulation by RNA.* Int Rev Cytol, 2003. **231**: p. 197-258.
8. Gebauer, F. and Hentze, M.W., *Molecular mechanisms of translational control.* Nat Rev Mol Cell Biol, 2004. **5**(10): p. 827-35.
9. Mello, C.C. and Conte, D., Jr., *Revealing the world of RNA interference.* Nature, 2004. **431**(7006): p. 338-42.
10. Hannon, G.J. and Rossi, J.J., *Unlocking the potential of the human genome with RNA interference.* Nature, 2004. **431**(7006): p. 371-8.
11. Robertson, M.P. and Joyce, G.F., *The origins of the RNA world.* Cold Spring Harb Perspect Biol, 2012. **4**(5).
12. Kruger, K., et al., *Self-splicing RNA: autoexcision and autocyclization of the ribosomal RNA intervening sequence of Tetrahymena.* Cell, 1982. **31**(1): p. 147-57.
13. Guerrier-Takada, C., et al., *The RNA Moiety of Ribonuclease P is the Catalytic Subunit of the Enzyme.* Cell, 1983. **35**(3 Part 2): p. 849-857.
14. Nissen, P., et al., *The structural basis of ribosome activity in peptide bond synthesis.* Science, 2000. **289**(5481): p. 920-30.
15. Misra, V.K. and Draper, D.E., *On the role of magnesium ions in RNA stability.* Biopolymers, 1998. **48**(2-3): p. 113-35.
16. Pyle, A.M., *Ribozymes: a distinct class of metalloenzymes.* Science, 1993. **261**(5122): p. 709-14.
17. Lilley, D.M., *The origins of RNA catalysis in ribozymes.* Trends Biochem Sci, 2003. **28**(9): p. 495-501.
18. Lilley, D.J., *Analysis of Global Conformational Transitions in Ribozymes*, in *Ribozymes and siRNA Protocols*, Sioud, M., Editor. 2004, Humana Press. p. 77-108.
19. Dunham, C.M., Murray, J.B., and Scott, W.G., *A helical twist-induced conformational switch activates cleavage in the hammerhead ribozyme.* J Mol Biol, 2003. **332**(2): p. 327-36.
20. Hoogstraten, C.G., Wank, J.R., and Pardi, A., *Active site dynamics in the lead-dependent ribozyme.* Biochemistry, 2000. **39**(32): p. 9951-8.
21. Zhuang, X., et al., *Correlating structural dynamics and function in single ribozyme molecules.* Science, 2002. **296**(5572): p. 1473-6.
22. Ke, A., et al., *A conformational switch controls hepatitis delta virus ribozyme catalysis.* Nature, 2004. **429**(6988): p. 201-5.
23. Hartmann, R.K., et al., *The Making of tRNAs and More - RNase P and tRNase Z.* Prog Nucleic Acid Res Mol Biol, 2009. **85**: p. 319-368.
24. Iwata-Reuyl, D., *An embarrassment of riches: the enzymology of RNA modification.* Curr Opin Chem Biol, 2008. **12**(2): p. 126-33.
25. Xiong, Y. and Steitz, T.A., *A story with a good ending: tRNA 3'-end maturation by CCA-adding enzymes.* Curr Opin Struct Biol, 2006. **16**(1): p. 12-7.

26. Phizicky, E.M. and Hopper, A.K., *tRNA biology charges to the front.* Genes & Development, 2010. **24**(17): p. 1832-1860.
27. Randau, L., Schroder, I., and Soll, D., *Life without RNase P.* Nature, 2008. **453**(7191): p. 120-3.
28. Walker, S.C. and Engelke, D.R., *Ribonuclease P: the evolution of an ancient RNA enzyme.* Crit Rev Biochem Mol Biol, 2006. **41**(2): p. 77-102.
29. Apirion, D., *Genetic mapping and some characterization of the rnpA49 mutation of Escherichia coli that affects the RNA-processing enzyme ribonuclease P.* Genetics, 1980. **94**(2): p. 291-9.
30. Eder, P.S., et al., *Bacterial RNase P as a potential target for novel anti-infectives.* Curr Opin Investig Drugs, 2003. **4**(8): p. 937-43.
31. Frank, D.N. and Pace, N.R., *Ribonuclease P: unity and diversity in a tRNA processing ribozyme.* Annu Rev Biochem, 1998. **67**: p. 153-80.
32. Kazantsev, A.V. and Pace, N.R., *Bacterial RNase P: a new view of an ancient enzyme.* Nat Rev Microbiol, 2006. **4**(10): p. 729-40.
33. Smith, J.K., Hsieh, J., and Fierke, C.A., *Importance of RNA-protein interactions in bacterial ribonuclease P structure and catalysis.* Biopolymers, 2007. **87**(5-6): p. 329-38.
34. Kirsebom, L.A., *RNase P RNA mediated cleavage: substrate recognition and catalysis.* Biochimie, 2007. **89**(10): p. 1183-94.
35. Harris, M.E. and Christian, E.L., *Recent insights into the structure and function of the ribonucleoprotein enzyme ribonuclease P.* Current Opinion in Structural Biology, 2003. **13**(3): p. 325-333.
36. Hernandez-Cid, A., et al., *Ribonucleases P/MRP and the expanding ribonucleoprotein world.* IUBMB Life, 2012. **64**(6): p. 521-8.
37. Bothwell, A.L., Garber, R.L., and Altman, S., *Nucleotide sequence and in vitro processing of a precursor molecule to Escherichia coli 4.5 S RNA.* J Biol Chem, 1976. **251**(23): p. 7709-16.
38. Peck-Miller, K.A. and Altman, S., *Kinetics of the processing of the precursor to 4.5 S RNA, a naturally occurring substrate for RNase P from Escherichia coli.* J Mol Biol, 1991. **221**(1): p. 1-5.
39. Komine, Y., et al., *A tRNA-like structure is present in 10Sa RNA, a small stable RNA from Escherichia coli.* Proc Natl Acad Sci U S A, 1994. **91**(20): p. 9223-7.
40. Gimple, O. and Schön, A., *In vitro and in vivo processing of cyanelle tmRNA by RNase P.* Biol Chem, 2001. **382**(10): p. 1421-9.
41. Li, Y. and Altman, S., *A specific endoribonuclease, RNase P, affects gene expression of polycistronic operon mRNAs.* Proc Natl Acad Sci U S A, 2003. **100**(23): p. 13213-8.
42. Alifano, P., et al., *Ribonuclease E provides substrates for ribonuclease P-dependent processing of a polycistronic mRNA.* Genes Dev, 1994. **8**(24): p. 3021-31.
43. Altman, S., et al., *RNase P cleaves transient structures in some riboswitches.* Proc Natl Acad Sci U S A, 2005. **102**(32): p. 11284-9.
44. Li, Y. and Altman, S., *Polarity effects in the lactose operon of Escherichia coli.* J Mol Biol, 2004. **339**(1): p. 31-9.
45. Ko, J.H. and Altman, S., *OLE RNA, an RNA motif that is highly conserved in several extremophilic bacteria, is a substrate for and can be regulated by RNase P RNA.* Proc Natl Acad Sci U S A, 2007. **104**(19): p. 7815-20.
46. Hartmann, R.K., et al., *Precursor of C4 antisense RNA of bacteriophages P1 and P7 is a substrate for RNase P of Escherichia coli.* Proc Natl Acad Sci U S A, 1995. **92**(13): p. 5822-6.
47. Hartmann, E. and Hartmann, R.K., *The enigma of ribonuclease P evolution.* Trends Genet, 2003. **19**(10): p. 561-9.

48. Hall, T.A. and Brown, J.W., *The ribonuclease P family.* Methods Enzymol, 2001. **341**: p. 56-77.
49. Hsieh, J., Andrews, A.J., and Fierke, C.A., *Roles of protein subunits in RNA-protein complexes: lessons from ribonuclease P.* Biopolymers, 2004. **73**(1): p. 79-89.
50. Lai, L.B., et al., *Unexpected diversity of RNase P, an ancient tRNA processing enzyme: challenges and prospects.* FEBS Lett, 2010. **584**(2): p. 287-96.
51. Esakova, O. and Krasilnikov, A.S., *Of proteins and RNA: the RNase P/MRP family.* RNA, 2010. **16**(9): p. 1725-47.
52. Thomas, B.C., et al., *Spinach chloroplast RNase P: a putative protein enzyme.* Nucleic Acids Symp Ser, 1995(33): p. 95-8.
53. Gobert, A., et al., *A single Arabidopsis organellar protein has RNase P activity.* Nature Structural and Molecular Biology, 2010. **17**(6): p. 740-744.
54. Holzmann, J., et al., *RNase P without RNA: Identification and Functional Reconstitution of the Human Mitochondrial tRNA Processing Enzyme.* Cell, 2008. **135**(3): p. 462-474.
55. Trang, P., Kim, K., and Liu, F., *Developing RNase P ribozymes for gene-targeting and antiviral therapy.* Cell Microbiol, 2004. **6**(6): p. 499-508.
56. Willkomm, D.K., et al., *Evaluation of bacterial RNase P RNA as a drug target.* Chembiochem, 2003. **4**(10): p. 1041-8.
57. Gossringer, M., Kretschmer-Kazemi Far, R., and Hartmann, R.K., *Analysis of RNase P protein (rnpA) expression in Bacillus subtilis utilizing strains with suppressible rnpA expression.* J Bacteriol, 2006. **188**(19): p. 6816-23.
58. Waugh, D.S. and Pace, N.R., *Complementation of an RNase P RNA (rnpB) gene deletion in Escherichia coli by homologous genes from distantly related eubacteria.* J Bacteriol, 1990. **172**(11): p. 6316-22.
59. Kobayashi, K., et al., *Essential Bacillus subtilis genes.* Proc Natl Acad Sci U S A, 2003. **100**(8): p. 4678-83.
60. Tsai, H.-Y., et al., *Functional reconstitution and characterization of Pyrococcus furiosus RNase P.* Proc Natl Acad Sci U S A, 2006. **103**(44): p. 16147-16152.
61. Kikovska, E., Svärd, S.G., and Kirsebom, L.A., *Eukaryotic RNase P RNA mediates cleavage in the absence of protein.* Proc Natl Acad Sci U S A, 2007. **104**(7): p. 2062-2067.
62. Reich, C., et al., *Role of the protein moiety of ribonuclease P, a ribonucleoprotein enzyme.* Science, 1988. **239**(4836): p. 178-181.
63. Evans, D., Marquez, S.M., and Pace, N.R., *RNase P: interface of the RNA and protein worlds.* Trends Biochem Sci, 2006. **31**(6): p. 333-41.
64. Gößringer, M., Kretschmer-Kazemi Far, R., and Hartmann, R.K., *Analysis of RNase P Protein (rnpA) Expression in Bacillus subtilis Utilizing Strains with Suppressible rnpA Expression.* Journal of Bacteriology, 2006. **188**(19): p. 6816-6823.
65. Schedl, P. and Primakoff, P., *Mutants of Escherichia coli thermosensitive for the synthesis of transfer RNA.* Proc Natl Acad Sci U S A, 1973. **70**(7): p. 2091-5.
66. Lee, J.Y., et al., *Characterization of RPR1, an essential gene encoding the RNA component of Saccharomyces cerevisiae nuclear RNase P.* Mol Cell Biol, 1991. **11**(2): p. 721-30.
67. Morales, M.J., et al., *A 105-kDa protein is required for yeast mitochondrial RNase P activity.* Proc Natl Acad Sci U S A, 1992. **89**(20): p. 9875-9.
68. Morales, M.J., et al., *Characterization of yeast mitochondrial RNase P: an intact RNA subunit is not essential for activity in vitro.* Nucleic Acids Res, 1989. **17**(17): p. 6865-81.
69. Haas, E.S. and Brown, J.W., *Evolutionary variation in bacterial RNase P RNAs.* Nucleic Acids Res, 1998. **26**(18): p. 4093-9.
70. Chen, J.L. and Pace, N.R., *Identification of the universally conserved core of ribonuclease P RNA.* RNA, 1997. **3**(6): p. 557-60.
71. Ellis, J.C. and Brown, J.W., *The RNase P family.* RNA Biol, 2009. **6**(4): p. 362-9.

72. Brown, J.W., *The Ribonuclease P Database.* Nucleic Acids Res, 1999. **27**(1): p. 314.
73. Brown, J.W., et al., *Phylogenetic analysis and evolution of RNase P RNA in proteobacteria.* J Bacteriol, 1991. **173**(12): p. 3855-63.
74. Marquez, S.M., et al., *Structural implications of novel diversity in eucaryal RNase P RNA.* RNA, 2005. **11**(5): p. 739-51.
75. Brown, J.W., et al., *Comparative analysis of ribonuclease P RNA using gene sequences from natural microbial populations reveals tertiary structural elements.* Proc Natl Acad Sci U S A, 1996. **93**(7): p. 3001-6.
76. Massire, C., Jaeger, L., and Westhof, E., *Phylogenetic evidence for a new tertiary interaction in bacterial RNase P RNAs.* RNA, 1997. **3**(6): p. 553-6.
77. Massire, C., Jaeger, L., and Westhof, E., *Derivation of the three-dimensional architecture of bacterial ribonuclease P RNAs from comparative sequence analysis.* J Mol Biol, 1998. **279**(4): p. 773-93.
78. Pomeranz Krummel, D.A. and Altman, S., *Verification of phylogenetic predictions in vivo and the importance of the tetraloop motif in a catalytic RNA.* Proc Natl Acad Sci U S A, 1999. **96**(20): p. 11200-5.
79. Haas, E.S., et al., *Structure and evolution of ribonuclease P RNA in Gram-positive bacteria.* Nucleic Acids Res, 1996. **24**(23): p. 4775-82.
80. Siegel, R.W., et al., *Mycoplasma fermentans simplifies our view of the catalytic core of ribonuclease P RNA.* RNA, 1996. **2**(5): p. 452-62.
81. Loria, A. and Pan, T., *Domain structure of the ribozyme from eubacterial ribonuclease P.* Rna, 1996. **2**: p. 551-563.
82. Pan, T. and Jakacka, M., *Multiple substrate binding sites in the ribozyme from Bacillus subtilis RNase P.* EMBO J, 1996. **15**(9): p. 2249-55.
83. Harris, J.K., et al., *New insight into RNase P RNA structure from comparative analysis of the archaeal RNA.* RNA, 2001. **7**(2): p. 220-32.
84. Lai, L.B., et al., *Discovery of a minimal form of RNase P in Pyrobaculum.* Proc Natl Acad Sci U S A, 2010. **107**(52): p. 22493-8.
85. Wise, C.A. and Martin, N.C., *Dramatic size variation of yeast mitochondrial RNAs suggests that RNase P RNAs can be quite small.* J Biol Chem, 1991. **266**(29): p. 19154-7.
86. Frank, D.N., et al., *Phylogenetic-comparative analysis of the eukaryal ribonuclease P RNA.* RNA, 2000. **6**(12): p. 1895-904.
87. Pace, N.R. and Brown, J.W., *Evolutionary perspective on the structure and function of ribonuclease P, a ribozyme.* J Bacteriol, 1995. **177**(8): p. 1919-28.
88. Pagan-Ramos, E., Lee, Y., and Engelke, D.R., *Mutational analysis of Saccharomyces cerevisiae nuclear RNase P: randomization of universally conserved positions in the RNA subunit.* RNA, 1996. **2**(5): p. 441-51.
89. Gopalan, V., Vioque, A., and Altman, S., *RNase P: variations and uses.* J Biol Chem, 2002. **277**(9): p. 6759-62.
90. J. Christopher Ellis and Brown, J.W., *The Evolution of RNase P and Its RNA. Ribonuclease P*. Protein Reviews, ed. Liu, F. and Altman, S. Vol. 10. 2010, New York: Springer-Verlag.
91. Kurz, J.C. and Fierke, C.A., *The affinity of magnesium binding sites in the Bacillus subtilis RNase P x pre-tRNA complex is enhanced by the protein subunit.* Biochemistry, 2002. **41**(30): p. 9545-58.
92. Kurz, J.C., Niranjanakumari, S., and Fierke, C.A., *Protein component of Bacillus subtilis RNase P specifically enhances the affinity for precursor-tRNAAsp.* Biochemistry, 1998. **37**(8): p. 2393-400.
93. Kirsebom, L.A. and Vioque, A., *RNase P from bacteria. Substrate recognition and function of the protein subunit.* Mol Biol Rep, 1995. **22**(2-3): p. 99-109.

94. Jovanovic, M., et al., *Elucidation of structure-function relationships in the protein subunit of bacterial RNase P using a genetic complementation approach.* Nucleic Acids Res, 2002. **30**(23): p. 5065-73.
95. Stams, T., et al., *Ribonuclease P protein structure: evolutionary origins in the translational apparatus.* Science, 1998. **280**(5364): p. 752-5.
96. Spitzfaden, C., et al., *The structure of ribonuclease P protein from Staphylococcus aureus reveals a unique binding site for single-stranded RNA.* J Mol Biol, 2000. **295**(1): p. 105-15.
97. Kazantsev, A.V., et al., *High-resolution structure of RNase P protein from Thermotoga maritima.* Proc Natl Acad Sci U S A, 2003. **100**(13): p. 7497-502.
98. Gosringer, M. and Hartmann, R.K., *Function of heterologous and truncated RNase P proteins in Bacillus subtilis.* Mol Microbiol, 2007. **66**(3): p. 801-13.
99. Andrews, A.J., Hall, T.A., and Brown, J.W., *Characterization of RNase P holoenzymes from Methanococcus jannaschii and Methanothermobacter thermoautotrophicus.* Biol Chem, 2001. **382**(8): p. 1171-7.
100. Jarrous, N. and Gopalan, V., *Archaeal/eukaryal RNase P: subunits, functions and RNA diversification.* Nucleic Acids Res, 2010. **38**(22): p. 7885-94.
101. Chamberlain, J.R., et al., *Purification and characterization of the nuclear RNase P holoenzyme complex reveals extensive subunit overlap with RNase MRP.* Genes Dev, 1998. **12**(11): p. 1678-90.
102. Sinapah, S., et al., *Cleavage of model substrates by archaeal RNase P: role of protein cofactors in cleavage-site selection.* Nucleic Acids Res, 2011. **39**(3): p. 1105-16.
103. Xiao, S., Houser-Scott, F., and Engelke, D.R., *Eukaryotic ribonuclease P: Increased complexity to cope with the nuclear pre-tRNA pathway.* Journal of Cellular Physiology, 2001. **187**(1): p. 11-20.
104. Van Eenennaam, H., et al., *Architecture and Function of the Human Endonucleases RNase P and RNase MRP*. IUBMB Life, 2000. **49**(4): p. 265-272.
105. Dang, Y.L. and Martin, N.C., *Yeast mitochondrial RNase P. Sequence of the RPM2 gene and demonstration that its product is a protein subunit of the enzyme.* Journal of Biological Chemistry, 1993. **268**(26): p. 19791-19796.
106. Wang, M.J., Davis, N.W., and Gegenheimer, P., *Novel mechanisms for maturation of chloroplast transfer RNA precursors.* EMBO J, 1988. **7**(6): p. 1567-74.
107. Rossmanith, W. and Karwan, R.M., *Characterization of human mitochondrial RNase P: novel aspects in tRNA processing.* Biochem Biophys Res Commun, 1998. **247**(2): p. 234-41.
108. Vilardo, E., et al., *A subcomplex of human mitochondrial RNase P is a bifunctional methyltransferase-extensive moonlighting in mitochondrial tRNA biogenesis.* Nucleic Acids Research, 2012. **40**(22): p. 11583-11593.
109. Jackman, J.E., et al., *Identification of the yeast gene encoding the tRNA m1G methyltransferase responsible for modification at position 9.* RNA, 2003. **9**(5): p. 574-85.
110. Nagy, E., et al., *Identification of the NAD(+)-binding fold of glyceraldehyde-3-phosphate dehydrogenase as a novel RNA-binding domain.* Biochem Biophys Res Commun, 2000. **275**(2): p. 253-60.
111. Hentze, M.W., *Enzymes as RNA-binding proteins: a role for (di)nucleotide-binding domains?* Trends Biochem Sci, 1994. **19**(3): p. 101-3.
112. Dupureur, C.M., *Roles of metal ions in nucleases.* Curr Opin Chem Biol, 2008. **12**(2): p. 250-5.
113. Ofman, R., et al., *2-Methyl-3-hydroxybutyryl-CoA dehydrogenase deficiency is caused by mutations in the HADH2 gene.* Am J Hum Genet, 2003. **72**(5): p. 1300-7.
114. Howard, M.J., et al., *Mitochondrial ribonuclease P structure provides insight into the evolution of catalytic strategies for precursor-tRNA 5' processing.* Proc Natl Acad Sci U S A, 2012. **109**(40): p. 16149-16154.

115. Gutmann, B., Gobert, A., and Giegé, P., *PRORP proteins support RNase P activity in both organelles and the nucleus in Arabidopsis.* Genes & Development, 2012. **26**(10): p. 1022-1027.
116. Howard, M.J., Klemm, B.P., and Fierke, C.A., *Mechanistic Studies Reveal Similar Catalytic Strategies for Phosphodiester Bond Hydrolysis by Protein-only and RNA-dependent Ribonuclease P.* J Biol Chem, 2015. **290**(21): p. 13454-64.
117. Gobert, A., et al., *Structural insights into protein-only RNase P complexed with tRNA.* Nature Communications, 2013. **4**(1353): p. 1-8.
118. Imai, T., et al., *Pentatricopeptide repeat motifs in the processing enzyme PRORP1 in Arabidopsis thaliana play a crucial role in recognition of nucleotide bases at TψC loop in precursor tRNAs.* Biochemical and Biophysical Research Communications, 2014. **450**(4): p. 1541-1546.
119. Hsieh, J., et al., *Pre-tRNA turnover catalyzed by the yeast nuclear RNase P holoenzyme is limited by product release.* RNA, 2009. **15**(2): p. 224-34.
120. Pavlova, L.V., et al., *tRNA processing by protein-only versus RNA-based RNase P: kinetic analysis reveals mechanistic differences.* Chembiochem, 2012. **13**(15): p. 2270-6.
121. Howard, M.J., et al., *RNase P enzymes: divergent scaffolds for a conserved biological reaction.* RNA Biol, 2013. **10**(6): p. 909-14.
122. Beebe, J.A., Kurz, J.C., and Fierke, C.A., *Magnesium ions are required by Bacillus subtilis ribonuclease P RNA for both binding and cleaving precursor tRNA^{Asp}.* Biochemistry, 1996. **35**(32): p. 10493-505.
123. Hsieh, J. and Fierke, C.A., *Conformational change in the Bacillus subtilis RNase P holoenzyme--pre-tRNA complex enhances substrate affinity and limits cleavage rate.* RNA, 2009. **15**(8): p. 1565-77.
124. Torres-Larios, A., et al., *Crystal structure of the RNA component of bacterial ribonuclease P.* Nature, 2005. **437**(7058): p. 584-7.
125. Kazantsev, A.V., et al., *Crystal structure of a bacterial ribonuclease P RNA.* Proceedings of the National Academy of Sciences of the United States of America, 2005. **102**(38): p. 13392-13397.
126. Green, C.J., Rivera-Leon, R., and Vold, B.S., *The catalytic core of RNase P.* Nucleic Acids Res, 1996. **24**(8): p. 1497-503.
127. Loria, A. and Pan, T., *Modular construction for function of a ribonucleoprotein enzyme: the catalytic domain of Bacillus subtilis RNase P complexed with B.subtilis RNase P protein.* Nucleic acids research, 2001. **29**(9): p. 1892-1897.
128. Wu, S., et al., *Cleavage mediated by the catalytic domain of bacterial RNase P RNA.* J Mol Biol, 2012. **422**(2): p. 204-14.
129. Harris, M.E., et al., *Use of photoaffinity crosslinking and molecular modeling to analyze the global architecture of ribonuclease P RNA.* EMBO J, 1994. **13**(17): p. 3953-63.
130. Pan, T., Loria, A., and Zhong, K., *Probing of tertiary interactions in RNA: 2'-hydroxyl-base contacts between the RNase P RNA and pre-tRNA.* Proc Natl Acad Sci U S A, 1995. **92**(26): p. 12510-4.
131. Westhof, E. and Altman, S., *Three-dimensional working model of M1 RNA, the catalytic RNA subunit of ribonuclease P from Escherichia coli.* Proc Natl Acad Sci U S A, 1994. **91**(11): p. 5133-7.
132. Reiter, N.J., et al., *Structure of a bacterial ribonuclease P holoenzyme in complex with tRNA.* Nature, 2010. **468**(7325): p. 784-9.
133. Lim, W.H., *Importance of Substrate Recognition and Metal Ions in the Ribonuclease P Catalysis*. 2011, University of Michigan, Ann Arbor.
134. Hansen, A., et al., *Exploring the minimal substrate requirements for trans-cleavage by RNase P holoenzymes from Escherichia coli and Bacillus subtilis.* Mol Microbiol, 2001. **41**(1): p. 131-43.

135. Loria, A. and Pan, T., *Recognition of the T stem-loop of a pre-tRNA substrate by the ribozyme from Bacillus subtilis ribonuclease P.* Biochemistry, 1997. **36**(21): p. 6317-25.
136. Kirsebom, L.A. and Svard, S.G., *Base pairing between Escherichia coli RNase P RNA and its substrate.* EMBO J, 1994. **13**(20): p. 4870-6.
137. Oh, B.K. and Pace, N.R., *Interaction of the 3'-end of tRNA with ribonuclease P RNA.* Nucleic Acids Res, 1994. **22**(20): p. 4087-94.
138. Zahler, N.H., Christian, E.L., and Harris, M.E., *Recognition of the 5' leader of pre-tRNA substrates by the active site of ribonuclease P.* RNA, 2003. **9**(6): p. 734-45.
139. Zahler, N.H., et al., *The pre-tRNA nucleotide base and 2'-hydroxyl at N(-1) contribute to fidelity in tRNA processing by RNase P.* J Mol Biol, 2005. **345**(5): p. 969-85.
140. Crary, S.M., Niranjanakumari, S., and Fierke, C.A., *The Protein Component of Bacillus subtilis Ribonuclease P Increases Catalytic Efficiency by Enhancing Interactions with the 5,Äò Leader Sequence of Pre-tRNAAsp.* Biochemistry, 1998. **37**(26): p. 9409-9416.
141. Rueda, D., et al., *The 5' Leader of Precursor tRNA(Asp) Bound to the Bacillus subtilis RNase P Holoenzyme Has an Extended Conformation.* Biochemistry, 2005. **44**(49): p. 16130-9.
142. Niranjanakumari, S., et al., *Protein component of the ribozyme ribonuclease P alters substrate recognition by directly contacting precursor tRNA.* Proc Natl Acad Sci U S A, 1998. **95**(26): p. 15212-7.
143. Christian, E.L., et al., *Analysis of substrate recognition by the ribonucleoprotein endonuclease RNase P.* Methods, 2002. **28**(3): p. 307-22.
144. Koutmou, K.S., Day-Storms, J.J., and Fierke, C.A., *The RNR motif of B. subtilis RNase P protein interacts with both PRNA and pre-tRNA to stabilize an active conformer.* RNA (New York, N.Y.), 2011. **17**(7): p. 1225-1235.
145. Warnecke, J.M., et al., *Ribonuclease P (RNase P) RNA is converted to a Cd2+-ribozyme by a single Rp-phosphorothioate modification in the precursor tRNA at the RNase P cleavage site.* Proceedings of the National Academy of Sciences of the United States of America, 1996. **93**(17): p. 8924-8.
146. Cuzic, S. and Hartmann, R.K., *Studies on Escherichia coli RNase P RNA with Zn2+ as the catalytic cofactor.* Nucleic Acids Res, 2005. **33**(8): p. 2464-74.
147. Brannvall, M. and Kirsebom, L.A., *Manganese ions induce miscleavage in the Escherichia coli RNase P RNA-catalyzed reaction.* J Mol Biol, 1999. **292**(1): p. 53-63.
148. Smith, D., et al., *Influence of metal ions on the ribonuclease P reaction. Distinguishing substrate binding from catalysis.* J Biol Chem, 1992. **267**(4): p. 2429-36.
149. Smith, D. and Pace, N.R., *Multiple magnesium ions in the ribonuclease P reaction mechanism.* Biochemistry, 1993. **32**(20): p. 5273-81.
150. Perreault, J.P. and Altman, S., *Pathway of activation by magnesium ions of substrates for the catalytic subunit of RNase P from Escherichia coli.* J Mol Biol, 1993. **230**(3): p. 750-6.
151. Cassano, A.G., Anderson, V.E., and Harris, M.E., *Analysis of solvent nucleophile isotope effects: evidence for concerted mechanisms and nucleophilic activation by metal coordination in nonenzymatic and ribozyme-catalyzed phosphodiester hydrolysis.* Biochemistry, 2004. **43**(32): p. 10547-59.
152. Christian, E.L., Kaye, N.M., and Harris, M.E., *Evidence for a polynuclear metal ion binding site in the catalytic domain of ribonuclease P RNA.* EMBO J, 2002. **21**(9): p. 2253-62.
153. Hsieh, J., et al., *A divalent cation stabilizes the active conformation of the B. subtilis RNase P x pre-tRNA complex: a role for an inner-sphere metal ion in RNase P.* J Mol Biol, 2010. **400**(1): p. 38-51.
154. Sun, L. and Harris, M.E., *Evidence that binding of C5 protein to P RNA enhances ribozyme catalysis by influencing active site metal ion affinity.* Rna, 2007. **13**: p. 1505-1515.

155. Steitz, T.A. and Steitz, J.A., *A general two-metal-ion mechanism for catalytic RNA.* Proc Natl Acad Sci U S A, 1993. **90**(14): p. 6498-502.
156. Chen, Y., Li, X., and Gegenheimer, P., *Ribonuclease P catalysis requires Mg2+ coordinated to the pro-RP oxygen of the scissile bond.* Biochemistry, 1997. **36**(9): p. 2425-38.
157. Christian, E.L., Kaye, N.M., and Harris, M.E., *Helix P4 is a divalent metal ion binding site in the conserved core of the ribonuclease P ribozyme.* RNA, 2000. **6**(4): p. 511-9.
158. Crary, S.M., Kurz, J.C., and Fierke, C.A., *Specific phosphorothioate substitutions probe the active site of Bacillus subtilis ribonuclease P.* RNA, 2002. **8**(7): p. 933-47.
159. Christian, E.L., et al., *The P4 metal binding site in RNase P RNA affects active site metal affinity through substrate positioning.* RNA, 2006. **12**(8): p. 1463-7.
160. Kazantsev, A.V., Krivenko, A.A., and Pace, N.R., *Mapping metal-binding sites in the catalytic domain of bacterial RNase P RNA.* RNA, 2009. **15**(2): p. 266-276.
161. Koutmou, K.S., et al., *NMR and XAS reveal an inner-sphere metal binding site in the P4 helix of the metallo-ribozyme ribonuclease P.* Proceedings of the National Academy of Sciences, 2010. **107**(6): p. 2479-2484.
162. Schmitz, M. and Tinoco, I., *Solution structure and metal-ion binding of the P4 element from bacterial RNase P RNA.* RNA (New York, N.Y.), 2000. **6**(9): p. 1212-1225.
163. Getz, M.M., et al., *Structural plasticity and Mg2+ binding properties of RNase P P4 from combined analysis of NMR residual dipolar couplings and motionally decoupled spin relaxation.* RNA (New York, N.Y.), 2007. **13**(2): p. 251-66.
164. Li, X. and Gegenheimer, P., *Ribonuclease P Catalysis Requires Mg2+ Coordinated to the pro-RP Oxygen of the Scissile Bond†.* Biochemistry, 1997. **36**(9): p. 2425-2438.
165. Warnecke, J.M., et al., *Role of metal ions in the hydrolysis reaction catalyzed by RNase P RNA from Bacillus subtilis.* J Mol Biol, 1999. **290**(2): p. 433-45.
166. Pfeiffer, T., et al., *Effects of phosphorothioate modifications on precursor tRNA processing by eukaryotic RNase P enzymes.* Journal of Molecular Biology, 2000. **298**(4): p. 559-565.
167. Persson, T., Cuzic, S., and Hartmann, R.K., *Catalysis by RNase P RNA: unique features and unprecedented active site plasticity.* J Biol Chem, 2003. **278**(44): p. 43394-401.
168. Kazantsev, A.V., et al., *Solution structure of RNase P RNA.* RNA, 2011. **17**(6): p. 1159-71.
169. Niranjanakumari, S., et al., *Probing the architecture of the B. subtilis RNase P Holoenzyme active site by crosslinking and affinity cleavage.* RNA, 2007. **13**: p. 512-35.
170. Loria, A. and Pan, T., *Recognition of the 5' leader and the acceptor stem of a pre-tRNA substrate by the ribozyme from Bacillus subtilis RNase P.* Biochemistry, 1998. **37**(28): p. 10126-33.
171. Buck, A.H., et al., *Structural perspective on the activation of RNAse P RNA by protein.* Nat Struct Mol Biol, 2005. **12**(11): p. 958-64.
172. Loria, A. and Pan, T., *The cleavage step of ribonuclease P catalysis is determined by ribozyme-substrate interactions both distal and proximal to the cleavage site.* Biochemistry, 1999. **38**(27): p. 8612-20.
173. Brannvall, M., et al., *Evidence for induced fit in bacterial RNase P RNA-mediated cleavage.* J Mol Biol, 2007. **372**(5): p. 1149-64.
174. Pomeranz Krummel, D.A., et al., *Evidence for helical unwinding of an RNA substrate by the RNA enzyme RNase P: use of an interstrand disulfide crosslink in substrate.* J Mol Biol, 2000. **295**(5): p. 1113-8.
175. Sun, L., et al., *Evidence that substrate-specific effects of C5 protein lead to uniformity in binding and catalysis by RNase P.* The EMBO journal, 2006. **25**(17): p. 3998-4007.
176. Leontis, N.B. and Westhof, E., *Analysis of RNA motifs.* Curr Opin Struct Biol, 2003. **13**(3): p. 300-8.
177. Moore, P.B., *Structural motifs in RNA.* Annu Rev Biochem, 1999. **68**: p. 287-300.
178. Tinoco, I., Jr. and Bustamante, C., *How RNA folds.* J Mol Biol, 1999. **293**(2): p. 271-81.

179. Draper, D.E., *A guide to ions and RNA structure.* RNA, 2004. **10**(3): p. 335-43.
180. Kortmann, J. and Narberhaus, F., *Bacterial RNA thermometers: molecular zippers and switches.* Nat Rev Microbiol, 2012. **10**(4): p. 255-65.
181. Al-Hashimi, H.M., *Dynamics-based amplification of RNA function and its characterization by using NMR spectroscopy.* Chembiochem, 2005. **6**(9): p. 1506-19.
182. Prestegard, J.H., al-Hashimi, H.M., and Tolman, J.R., *NMR structures of biomolecules using field oriented media and residual dipolar couplings.* Q Rev Biophys, 2000. **33**(4): p. 371-424.
183. Tolman, J.R., *Dipolar couplings as a probe of molecular dynamics and structure in solution.* Curr Opin Struct Biol, 2001. **11**(5): p. 532-9.
184. Palmer, A.G., 3rd, *NMR characterization of the dynamics of biomacromolecules.* Chem Rev, 2004. **104**(8): p. 3623-40.
185. Palmer, A.G., 3rd, Kroenke, C.D., and Loria, J.P., *Nuclear magnetic resonance methods for quantifying microsecond-to-millisecond motions in biological macromolecules.* Methods Enzymol, 2001. **339**: p. 204-38.
186. Palmer, A.G., 3rd and Massi, F., *Characterization of the dynamics of biomacromolecules using rotating-frame spin relaxation NMR spectroscopy.* Chem Rev, 2006. **106**(5): p. 1700-19.
187. Mittermaier, A.K. and Kay, L.E., *Observing biological dynamics at atomic resolution using NMR.* Trends Biochem Sci, 2009. **34**(12): p. 601-11.
188. Furtig, B., et al., *NMR spectroscopy of RNA.* Chembiochem, 2003. **4**(10): p. 936-62.
189. Cromsigt, J., et al., *Resonance assignment and structure determination for RNA.* Methods Enzymol, 2001. **338**: p. 371-99.
190. Wüthrich, K., *NMR of proteins and nucleic acids*. The George Fisher Baker non-resident lectureship in chemistry at Cornell University. 1986, New York: Wiley. xv, 292.
191. Sklenar, V., et al., *Two- and three-dimensional HCN experiments for correlating base and sugar resonances in 15N,13C-labeled RNA oligonucleotides.* J Biomol NMR, 1993. **3**(6): p. 721-7.
192. Al-Hashimi, H.M. and Walter, N.G., *RNA dynamics: it is about time.* Curr Opin Struct Biol, 2008. **18**(3): p. 321-9.
193. Bothe, J.R., et al., *Characterizing RNA dynamics at atomic resolution using solution-state NMR spectroscopy.* Nat Meth, 2011. **8**(11): p. 919-931.
194. Lee, J.H. and Pardi, A., *Thermodynamics and kinetics for base-pair opening in the P1 duplex of the Tetrahymena group I ribozyme.* Nucleic Acids Res, 2007. **35**(9): p. 2965-74.
195. Johnson, J.E., Jr. and Hoogstraten, C.G., *Extensive backbone dynamics in the GCAA RNA tetraloop analyzed using 13C NMR spin relaxation and specific isotope labeling.* J Am Chem Soc, 2008. **130**(49): p. 16757-69.
196. Blad, H., et al., *Dynamics and metal ion binding in the U6 RNA intramolecular stem-loop as analyzed by NMR.* J Mol Biol, 2005. **353**(3): p. 540-55.
197. Latham, M.P., Zimmermann, G.R., and Pardi, A., *NMR chemical exchange as a probe for ligand-binding kinetics in a theophylline-binding RNA aptamer.* J Am Chem Soc, 2009. **131**(14): p. 5052-3.
198. Mittermaier, A. and Kay, L.E., *New tools provide new insights in NMR studies of protein dynamics.* Science, 2006. **312**(5771): p. 224-8.
199. Latham, M.P., et al., *NMR methods for studying the structure and dynamics of RNA.* Chembiochem, 2005. **6**(9): p. 1492-505.
200. Shajani, Z. and Varani, G., *NMR studies of dynamics in RNA and DNA by 13C relaxation.* Biopolymers, 2007. **86**(5-6): p. 348-59.
201. Hansen, A.L., et al., *Extending the range of microsecond-to-millisecond chemical exchange detected in labeled and unlabeled nucleic acids by selective carbon R(1rho) NMR spectroscopy.* J Am Chem Soc, 2009. **131**(11): p. 3818-9.

202. Palmer Iii, A.G., *Chemical exchange in biomacromolecules: Past, present, and future.* Journal of Magnetic Resonance, 2014. **241**: p. 3-17.
203. Neudecker, P., Lundström, P., and Kay, L.E., *Relaxation Dispersion NMR Spectroscopy as a Tool for Detailed Studies of Protein Folding.* Biophysical Journal, 2009. **96**(6): p. 2045-2054.
204. Miloushev, V.Z. and Palmer, A.G., 3rd, *R(1rho) relaxation for two-site chemical exchange: general approximations and some exact solutions.* J Magn Reson, 2005. **177**(2): p. 221-7.

CHAPTER 2
PROBING METAL ION BINDING SITES IN THE P4 HELIX OF *BACILLUS SUBTILIS* RNASE P[1]

2.1 Abstract

The endoribonuclease P (RNase P) is responsible for catalyzing the 5'-end maturation of precursor tRNAs (pre-tRNAs). Like many large ribozymes, divalent ions stabilize the folded structure and enhance catalytic function of RNase P. Identifying the ligands in RNA that bind metal ions and discerning the function of RNA-metal ion interactions are important questions in RNA catalysis. P4 helix, the most highly conserved region in RNase P RNA, is essential for RNase P activity and has been suggested to contain catalytic and/or co-catalytic metal ion binding sites. Nuclear magnetic resonance spectroscopy and X-ray absorption spectroscopy of a *Bacillus subtilis* P4 stem-loop mimic suggested an inner-sphere metal interaction with the O6, and an outer-sphere metal interaction with the N7 of the bases corresponding to G378 and G379 in the active site P4 helix of *B. subtilis* RNase P. To evaluate the structure and function of these putative metal ion binding sites, 2-aminopurine nucleoside (2AP), 7-deazaguanosine (N7G), 6-thioguanosine (6SG) and abasic (abG) are specifically substituted for G378 and G379. These substitutions have no or minimal effect on the

[1] Data in Chapter 2 are in preparation for a manuscript entitled "Inner-sphere divalent metal ion coordinates nucleobase in RNA" by Xin Liu*, Yu Chen*, and Carol A. Fierke. (* Co-first authorship)

global structure of RNase P RNA (PRNA). However, they decrease the pre-tRNA binding affinity at low concentrations of metal ion but not at high concentrations. Single-turnover kinetics show that the 2AP substitution at G379 decreases the cleavage rate constant in Mg^{2+} 9-fold, without altering the apparent affinity of metal ion for the Mg^{2+}-dependent activation of cleavage. The removal of the entire base of G379 decreases the rate constants of both the conformational change and cleavage steps that occur during the RNase P catalytic mechanism, as well as the apparent affinity for Mg^{2+}. These data indicate that O6 of G379 is important for both stabilizing pre-tRNA affinity in a metal-dependent fashion and for enhancing catalytic activity. Furthermore, the activity of the G379-6SG modified holoenzyme is not rescued by the addition of Cd^{2+} ions, arguing against an inner-sphere metal interaction. These data suggest that G379 is important for metal-dependent pre-tRNA binding and catalysis by RNase P, likely by interacting with at least one metal ion through an outer-sphere contact and stabilization of an active enzyme-substrate conformation.

2.2 Background

RNA molecules are large polyanions that associate with numerous divalent metal ions that are crucial for the structural integrity and biological activity of RNA. Metal ions not only interact electrostatically with the negatively charged phosphate backbone to stabilize the complex three-dimensional structure of the RNA [1], but can also coordinate functional groups in ribozymes to stabilize substrate binding, transition states and participate in structural changes important for catalysis. Studies have shown that metal ions are important for the specific structure and function of many RNAs, including

the hammerhead ribozyme, hairpin ribozyme, tetrahymena group I intron, group II intron, and ribonuclease P ribozyme [2-6]. Divalent metal ions can form direct contacts with RNA in two ways, via outer-sphere interactions, where the interaction between the metal ion and RNA ligand is water-mediated; or inner-sphere interactions, where the RNA ligand directly coordinates with metal ions and is not mediated by water [1].

Ribonuclease P (RNase P) is a divalent metal ion dependent ribonucleoprotein endonuclease that catalyzes the hydrolysis of a specific phosphodiester bond in precursor tRNAs (pre-tRNAs) to remove the 5' leader sequence [7-9]. In most organisms, RNase P is composed of one conserved catalytic RNA subunit (PRNA) and a varying number of protein subunits (P protein) depending on the organism [10-12]. The RNA subunit of RNase P can mediate pre-tRNA 5'-end cleavage at the correct position in the absence of P protein [13-15]. However *in vivo*, both the RNA and protein subunits are necessary for function [8, 16-18]. The P protein plays a role in enhancing substrate and metal ion binding affinity and substrate selectivity in addition to contributing to cleavage efficiency [19-23]. Because the RNA component of RNase P is essential for activity, RNase P is therefore characterized as a ribozyme.

Like many large ribozymes, divalent ions stabilize the folded structure and contribute to the catalytic function of RNase P by enhancing ligand binding and stabilizing the transition state for cleavage [8, 24-26]. Kinetic isotope effect studies on PRNA catalysis have suggested that a metal-bound hydroxide serves as the nucleophile in the reaction [27]. Catalysis by RNase P is activated by Mg^{2+} ions *in vivo* [24], while *in vitro*, other divalent metal ions, including Ca^{2+}, Mn^{2+}, Cd^{2+}, Pb^{2+} and Zn^{2+} can activate catalysis to various extents [21, 28-31]. A large number of Mg^{2+} ions (>150) associate with RNase P

[24, 32, 33] but only a handful of these Mg^{2+} ions form specific contacts with functional groups in RNase P [21, 24]. Two classes of inner-sphere metal ions are essential for catalytic activity: one stabilizes the active conformation of the RNase P - pre-tRNA complex while the other one facilitates cleavage [26, 27]. The exact divalent metal ion binding sites essential for catalysis and ligand binding and the function of these metal ions have not yet been characterized.

Bacterial PRNA is composed of two independently folding domains, termed the specificity (S), and catalytic (C) domains (Figure 2-1A) [34-36]. The C-domain contains the active site of PRNA and is sufficient to catalyze the cleavage of pre-tRNA *in vitro* [37, 38]. The P4 helix is the most highly conserved region in the C-domain of PRNA, possessing 11 of the 21 universally conserved nucleotides in PRNA (Figure 2-1A) [39]. The crystal structure of *Thermotoga maritima* RNase P revealed that the P4 helix is positioned at the core of the enzyme and is ideally situated to interact with both the P protein and substrate simultaneously [37]. The P4 helix is essential for RNase P activity and has been suggested to contain catalytic and/or co-catalytic metal ion binding sites [40-42].

Some of the ligands involved in metal ion coordination in the P4 helix have been implicated by biochemical studies. Phosphorothioate modification of non-bridging phosphodiester oxygens at A49 and G50 in the P4 helix of *Bacillus subtilis* RNase P (A67 and G68 in *Escherichia coli*) decreases the cleavage rate constant enormously without (or minimally) affecting the affinity of pre-tRNA [40, 41]. The addition of Mn^{2+} can rescue some of the catalytic defects suggesting that metal ions form an inner-sphere contact with the backbone at these sites [40, 41, 43]. Crosslinking studies of *E.*

coli PRNA examining the position of the pre-tRNA cleavage site relative to the P4 helix suggest that metal ion binding in the P4 helix leads to specific but indirect stabilization of catalytic metal ions at the scissile phosphate of pre-tRNA [42]. Replacement of either the *pro-R_P* or *pro-S_P* non-bridging oxygen with sulfur in the scissile phosphodiester bond of the pre-tRNA substrate decreases the cleavage rate of RNase P RNA by 10^3- to 10^4-fold. The activity of the *pro-R_P* phosphorothioate substituted pre-tRNA can be partially rescued by addition of thiophilic metal ions (Mn^{2+} and Cd^{2+}) suggesting an inner-sphere coordination of a metal ion with this oxygen [28, 44-47]. Atom modification studies also suggested that the 2' OH of pre-tRNA at the cleavage site interacts with a metal ion through a bound water molecule [47].

Likewise, X-ray crystallography has revealed several potential metal binding sites. Anomalous scattering in diffraction analysis (3.5 Å resolution) of *Bacillus stearothermophilus* PRNA crystals soaked in $Os(NH_3)_6^{3+}$ (which mimics $Mg(H_2O)_6^{2+}$), Pb^{2+}, Sm^{3+}, Gd^{3+} or Yb^{3+} identified a number of possible metal ion binding sites in RNase P, in particular two metal ion binding sites were observed near residues A48, A49, G50, G378 and G379 (*B. subtilis* numbering) [48]. The crystal structure of *T. maritima* RNase P (4.2 Å resolution) revealed putative metal binding sites in a bulged loop of helix P4 interacting with A49, G50 and U51 (*B. subtilis* numbering) using crystals soaked with Sm^{3+} and Eu^{3+} [37]. In particular, the carbonyl oxygen at O4 position of the conserved and bulged uridine (U51, *B. subtilis* numbering) in helix P4 was proposed to directly coordinate a catalytic metal ion [37]. Although the crystal structures have suggested a number of possible metal ion binding sites in RNase P [37, 48], the

resolution of these data is insufficient to identify which ligand contacts a metal ion and distinguish between inner- and outer-sphere coordination.

The available nuclear magnetic resonance (NMR) structure of a P4 helix stem-loop mimic (Figure 2-1B) revealed association of Mg^{2+} at residues G22 and G23 corresponding to G378 and G379 in RNase P (*B. subtilis* numbering) [49-51]. The strategy of combining NMR and X-ray absorption spectroscopy (XAS) for probing RNA-metal binding in solution identifies and characterizes an inner-sphere metal binding site at residues G378 and G379 in the P4 stem-loop mimic [51], suggesting that the base O6 of G378 and G379 form inner-sphere interactions, while N7 of G378 and G379 form outer-sphere interactions with a metal ion (Figure 2-1C) [51]. However, this model has not been tested by biochemical experiments in full-length PRNA and the function of the metal at this site also needs to be investigated. Therefore, to examine the metal ion binding sites proposed in the P4 helix stem-loop mimic model, I combined atom modifications with mechanistic studies to assess their effect on the structure, metal affinity, thermodynamic and kinetic properties of RNase P.

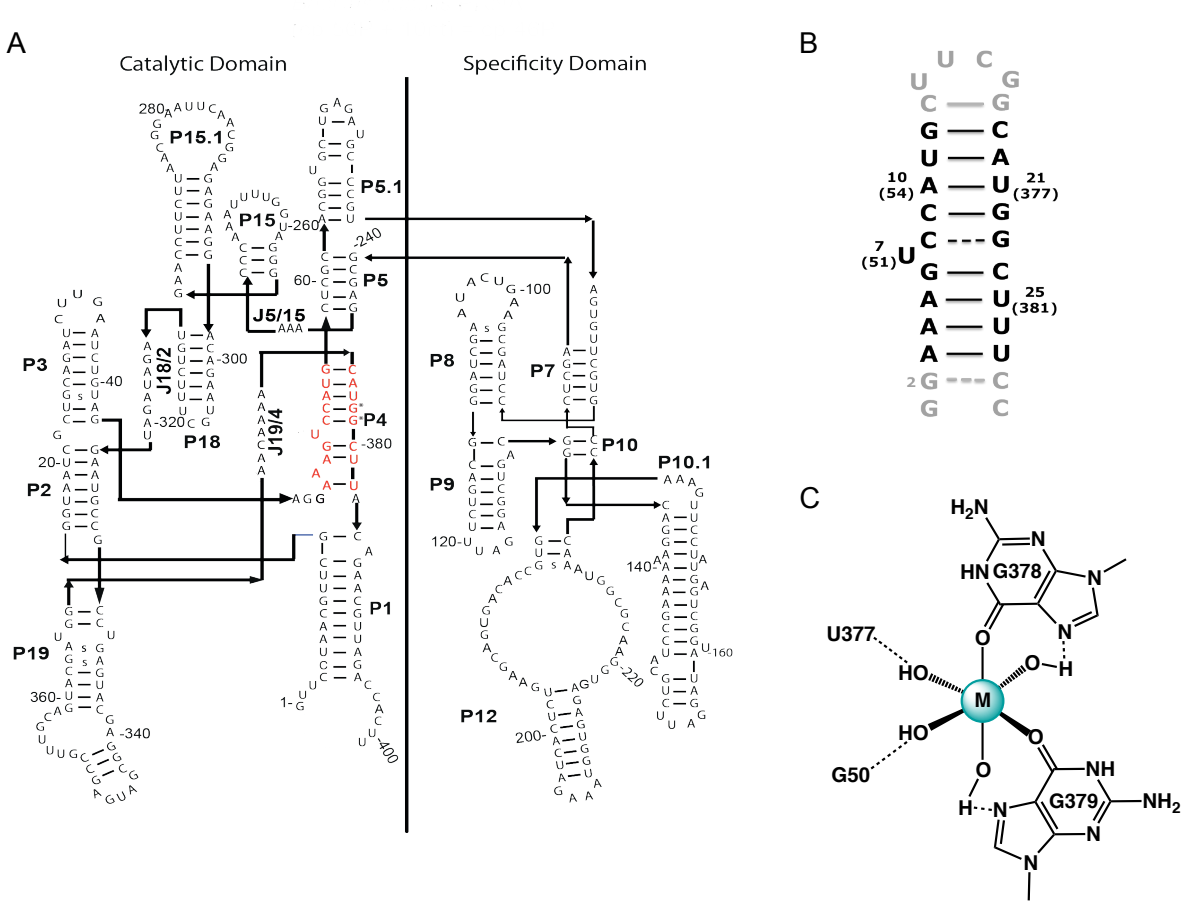

Figure 2-1: Secondary structure of the *B. subtilis* PRNA and proposed metal ion binding sites. **(A)** Secondary structure of the *B. subtilis* PRNA highlighting the P4 helix (red) and G378/G379 (*). The secondary structure was drawn based on the *B. stearothermophilus* PRNA crystal structure [36]. **(B)** Secondary structure of the P4 helix stem-loop mimic construct from *B. subtilis* RNase P RNA used in NMR and XAS [51]. **(C)** Proposed model of G22/G23 (G378/G379 in full-length PRNA) metal ions binding site identified by NMR and XAS [51].

In the model of metal binding sites in the P4 helix of *B. subtilis* RNase P proposed from biophysical studies of a stem-loop mimic, the base O6 and N7 atoms of G378/G379 form inner- and outer-sphere interactions with a metal ion respectively [51]. To examine the importance of inner-sphere metal coordination with the O6 atom, G378 and G379 were substituted by 2-aminopurine nucleoside (2AP) in PRNA. To evaluate the role of outer-sphere metal coordination by the N7 moiety of G379 (Figure 2-2), this base was substituted with 7-deazaguanosine (N7G) [51]. The 6-thioguanosine (6SG)

and abasic (abG) substitutions were also used to further evaluate the function of G379 in catalysis (Figure 2-2).

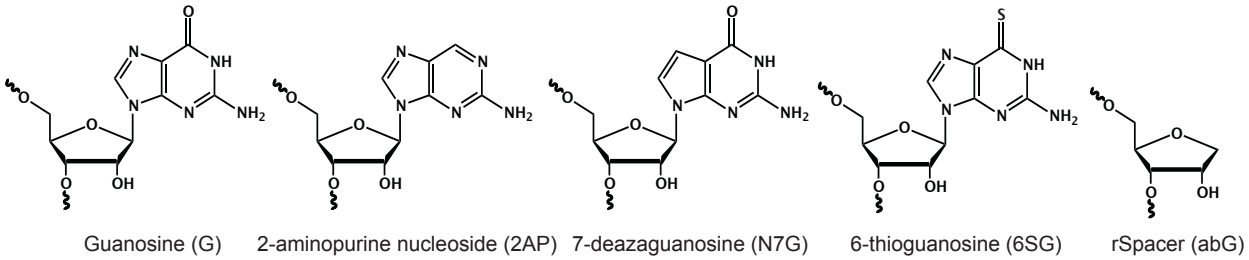

Figure 2-2: Chemical structures of guanosine and substituted bases

Previous study indicates that a minimal kinetic mechanism for RNase P includes four steps (Figure 2-3): (1) RNase P binds to pre-tRNA to form an enzyme-substrate (ES) complex; (2) the ES complex undergoes a metal dependent conformational step to form a reactive species (ES*); (3) pre-tRNA is cleaved by RNase P to form mature tRNA and 5'-leader; and (4) the products dissociate from RNase P [26, 52]. The modifications at G378 and G379 were incorporated into full-length, circularly-permuted PRNA and the functional effects of these modifications on each catalytic step were assessed by thermodynamic and kinetic experiments. These data demonstrate that modifications at G378 have little effect on the function of RNase P. However, modifications at G379 decrease the rate constants for both the conformational change and cleavage steps. These data indicate that O6 of G379 is important for both stabilizing pre-tRNA affinity in a metal-dependent fashion and for enhancing catalytic activity.

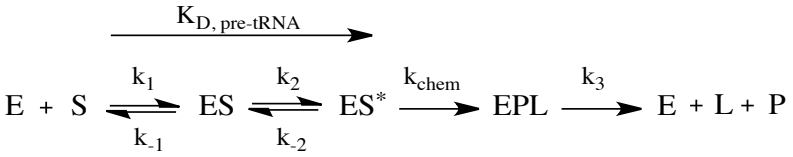

Figure 2-3: Kinetic mechanism of bacterial RNase P: (E) RNase P holoenzyme; (S) pre-tRNA; (ES) RNase P•pre-tRNA complex; (ES*) RNase P•pre-tRNA complex after conformational change; (EPL) RNase P•tRNA•5' leader complex; (L) 5' leader; (P) tRNA product.

2.3 Results

To examine the effect of the atom modifications of G378 and G379 on the divalent metal ion-dependent RNase P activity, the substrate affinity, rate constant of conformational change, single-turnover (STO) cleavage rate constant, metal ion dependence of cleavage and metal ion rescue were measured. .

2.3.1 Preparation of PRNA with Atom Modifications in the P4 Helix

To prepare PRNA with atom modification, a 20-mer RNA oligonucleotide with a sequence identical to half of the P4 helix (G366 to A385) except for the incorporation of the modification was purchased from commercial resources. A circularly permuted PRNA (cpPRNA) construct encoded on a plasmid where the 5' and 3' termini of PRNA are covalently attached with a linker sequence was used as a template for transcription (Figure 2-4A) [53]. cpPRNA, lacking half of the P4 helix (386-365P) was prepared by *in vitro* run-off transcription (Figure 2-4B). Using an optimized ligation method (see Materials and Methods) [41], the RNA oligonucleotide containing the atom modification was ligated to the 386-365P by T4 ligase to reconstitute the full length cpPRNA (Figure 2-4B) [41, 54]. The cpPRNA without modification (366P) was also made as a positive

control (Figure 2-4B) [53]. The efficiency of the RNA ligation was determined by primer extension analysis [55] demonstrating that the ligation efficiency is 60%-90%, depending on the modification (Figure A-1). The modified RNA was refolded and reconstituted with the P protein to form active RNase P holoenzyme.

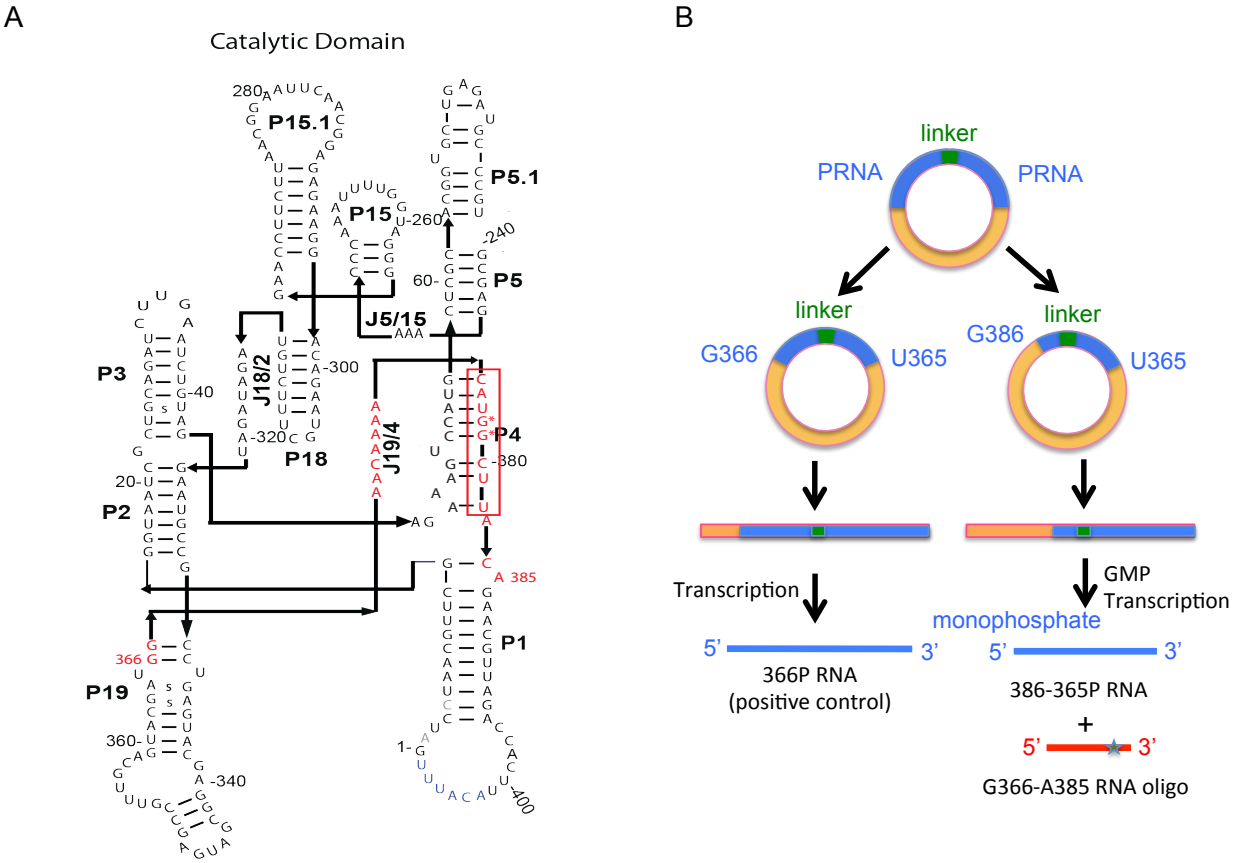

Figure 2-4: Incorporation of modifications into *B. subtilis* PRNA by using circularly permuted PRNA (cpPRNA). **(A)** Secondary structure of the C-domain from circularly permuted *B. subtilis* PRNA (cpPRNA) [53] highlighting one strand of the P4 helix (in box) and 20-mer RNA oligonucleotide for ligation (red). The usual 5' and 3' termini of PRNA are joined by a six-nucleotide loop (blue). The secondary structure was drawn based on the *B. stearothermophilus* PRNA crystal structure [36]. **(B)** Scheme of the preparation of cpPRNA and incorporation of modification into PRNA.

Since the ligation efficiency is not 100%, the ligated PRNA contains varying amounts of the 386-365P. However, no substrate binding or cleavage activity was observed when 386-365P RNA was incubated with pre-tRNA^{Asp} (Figure 2-5) demonstrating that the

presence of 386-365P does not interfere with the analysis of the activity of the ligated 366P constructs. Furthermore, 366P (without modifications) was prepared both by *in vitro* transcription and ligation, and the rate constants of substrate binding, RNase P - pre-tRNA conformational change and pre-tRNA cleavage were measured [52]. These data show that 366P is comparable with the WT RNase P, illustrating that the activity is not altered by circular permutation (see below for details).

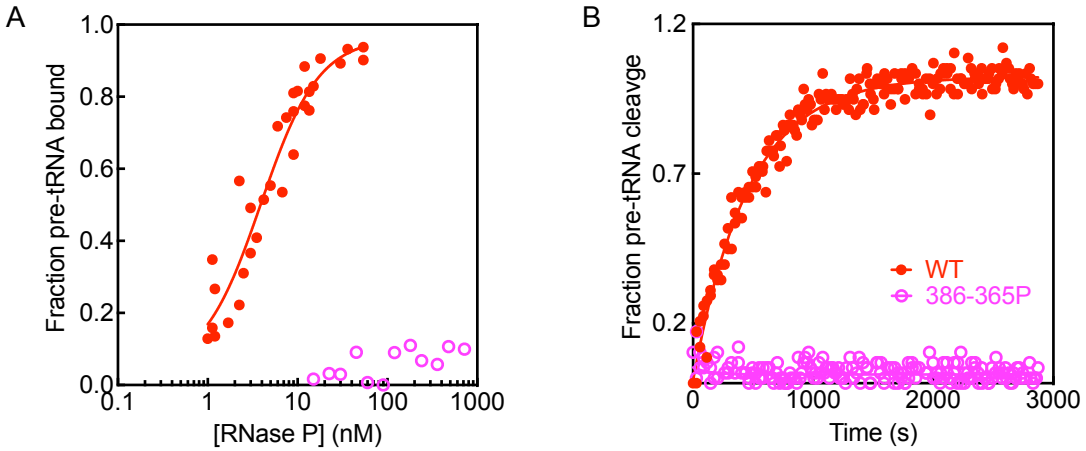

Figure 2-5: 386-365P does not bind to pre-tRNA substrate or catalyze pre-tRNA cleavage. **(A)** Fraction pre-tRNA^{Asp} bound to WT (●) and 386-365P (O) holoenzyme measured by spin column in 50 mM Tris/MES, pH 6.0, 3 mM $CaCl_2$ and 403.5 mM KCl at 37°C. 386-365P concentration is up to 720 nM. **(B)** WT (●) and 386-365P (O) PRNA-catalyzed cleavage of fluorescein-labeled pre-tRNA^{Asp} determined by changes anisotropy under multiple-turnover conditions (10 nM of RNase P and 1 μM of pre-tRNA^{Asp}). The measurements were performed in 50 mM Tris-HCl, pH 8.0, 40 mM $MgCl_2$, 980 mM KCl and 20 mM DTT at 37 °C.

2.3.2 Modifications at G378 and G379 Affect Metal Dependent Pre-tRNA binding affinity

The dissociation constant of RNase P for pre-tRNA is metal dependent [21, 56]. The value of K_D increases as the concentration of divalent metal ion decreases [26, 56]. To evaluate whether the modification on RNase P alters the metal dependent pre-tRNA affinity, the binding affinities of a γ-^{32}P-ATP 5' end labeled pre-tRNA^{Asp} to WT and

modified RNase P holoenzymes were measured under various Ca^{2+} concentrations at pH 6.0. Ca^{2+} was used in place of Mg^{2+} because the pre-tRNA cleavage in Ca^{2+} is slower by 10^4-fold [20, 21].

In the presence of saturating Ca^{2+} (5-8 mM), both WT and modified RNase P have similar $K_{D, app}$ values and bind tightly to pre-$tRNA^{Asp}$ (Table 2-1). These data indicate that the circular permutation and the modification used affect the interaction between RNase P and pre-tRNA at saturating Ca^{2+} modestly (≤2-fold).

The affinity of WT RNase P and 366P for pre-tRNA decreases ~2-fold and ~4-fold, respectively, as the Ca^{2+} concentration decreases from 5 mM to 3 mM (Table 2-1, Figure 2-6). This small difference in binding affinity at lower Ca^{2+} concentrations is likely due to a modest perturbation of the PRNA stability caused by circular permutation. In contrast, the substrate affinity of RNase P with modifications at G378 and G379 decreases significantly as the Ca^{2+} concentration decreases from 8 mM to 3 mM (Table 2-1, Figure 2-6). While substitution on G379 lowers affinity 12-30-fold, the 2AP substitution for G378 decreases binding affinity for pre-tRNA >50-fold (Table 2-1, Figure 2-6). This illustrates that N7 and O6 atoms of G378 and G379 are important for stabilizing pre-tRNA binding affinity in a metal-dependent fashion. However, it is not possible to distinguish whether the low substrate binding affinity is due to the modification affecting a metal-dependent contact with the substrate or lowering the stability of the PRNA folded structure at low concentrations of Ca^{2+}.

Table 2-1: Pre-tRNA^{Asp} substrate binding affinity for WT and modified *B. subtilis* RNase P at low and saturating Mg^{2+}

Holoenzyme	3 mM $CaCl_2$		Saturating $CaCl_2$[b]	
	$K_{D,\,app}$ (nM)[a]	$K_{D,\,app}^{modified}/K_{D,\,app}^{WT}$	$K_{D,\,app}$ (nM)[a]	$K_{D,\,app}^{modified}/K_{D,\,app}^{WT}$
WT	4.1 ± 0.8	1	2.0 ± 0.5	1
366P	10.5 ± 1.6	3	2.8 ± 0.8	1
366P ligation	15.8 ± 4.1	4	ND[c]	ND[c]
G378-2AP	> 200	> 49	4.2 ± 1.3	2
G379-2AP	47.8 ± 4.8	12	3.9 ± 1.0	2
G379-N7G	47.5 ± 9.6	12	1.6 ± 0.6	1

[a] The apparent dissociation constant ($K_{D,\,app}$) was determined under the condition [E] >> [S] ([^{32}P-pre-tRNA^{Asp}] << 1 nM) in 50 mM Tris/MES, pH 6.0, 2-8 mM $CaCl_2$ and 386.5-404.5 mM KCl at 37°C and calculated by a fit of a binding isotherm to the data (Equation 1).
[b] 5 mM $CaCl_2$ for WT and 366P RNase P and 8 mM $CaCl_2$ for RNase P with modification.
[c] ND: Not determined.

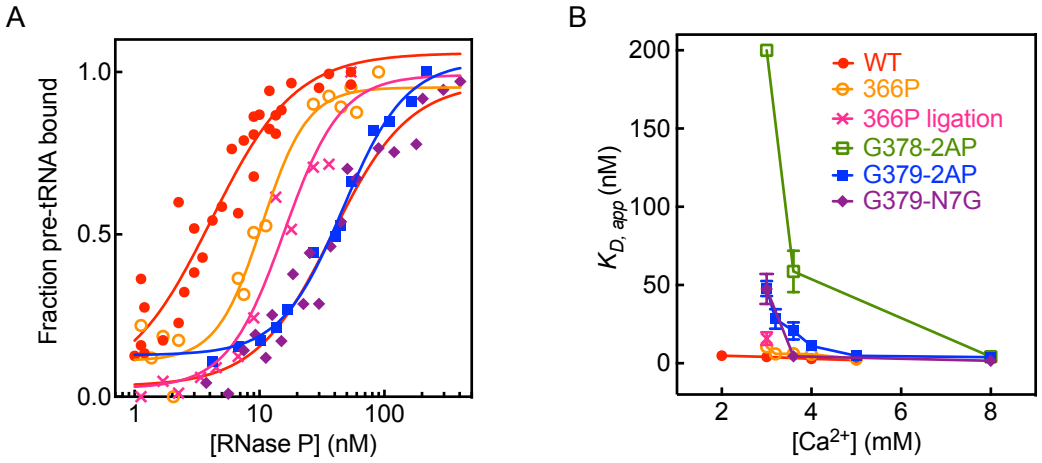

Figure 2-6: Modifications at G378 and G379 affect metal dependent pre-tRNA substrate binding affinity for *B. subtilis* RNase P. **(A)** The apparent dissociation constant ($K_{D,\,app}$) measurement of WT (●), 366P (O), 366P ligation (×), G378-2AP (□), G379-2AP (■) and G379-N7G (◆) RNase P for pre-tRNA^{Asp} substrate in 50 mM Tris/MES, pH 6.0, 3 mM $CaCl_2$ and 403.5 mM KCl at 37°C. The dissociation constants, $K_{D,\,app}$ were determined from a fit of a binding isotherm to these data (solid lines). **(B)** Ca^{2+} dependence of the binding affinity of WT and modified RNase P for pre-tRNA^{Asp} substrate.

2.3.3 Modifications at G378 and G379 Do Not Affect the Global structure of PRNA at High Concentrations of Mg^{2+} ion

To examine whether the weak substrate binding affinity for modified RNase P at low Ca^{2+} is caused by perturbation of the PRNA global structure, the Mg^{2+} dependence of PRNA folding was measured by both ultraviolet absorbance (UV) and circular dichroism (CD) absorbance spectroscopies.

PRNA is largely unfolded in the absence of divalent metal ion. Titration of Mg^{2+} into denatured PRNA induces folding, resulting in a decrease in the UV absorbance at 260 nm due to hypochromism of nucleotide bases as a result of helical stacking [57]. Therefore, UV absorbance spectroscopy can be used to investigate the formation of the secondary structure of PRNA. The magnesium dependence of PRNA secondary structure formation ($K_{1/2}^{Mg^{2+}}$) for WT and modified PRNA folding was determined from the dependence of the A_{260} on the Mg^{2+} concentration (Figure 2-7). As shown in Table 2-2, the $K_{1/2}^{Mg^{2+}}$ values for folding of modified PRNAs are similar to WT PRNA (~1 mM). These results suggest that modifications on G378 and G379 have no effect on stability of the secondary structure of PRNA. The same concentration of modified PRNAs (0.1 μM) was used in the experiments. Since the ligation efficiencies of various ligated PRNAs are different, the concentrations of unligated 386-365P are varied in different samples resulting in the different absorbance values for each sample. However, each sample has similar absorbance change between unfolded and folded state indicating the similar concentrations of modified PRNAs. It is also consistent with PRNA without the P4 helix does not fold into compact structure as WT [41].

To further investigate the effect of modification on the stability of PRNA tertiary structure, CD absorbance spectroscopy was used to examine the Mg^{2+} dependence of folding the modified PRNA. As previously described, there are two Mg^{2+} dependent transitions in *B. subtilis* PRNA folding observable by CD spectroscopy [57]. The first transition is observable at 260 nm and reflects the formation of secondary structure, while the second transition, which is attributed to PRNA tertiary folding, can be monitored by CD changes at 278 nm [57]. The magnesium dependence ($K_{1/2}^{Mg^{2+}}$) of $\Delta\varepsilon_{278}$ was measured; the value for G379-2AP (1.5 mM) is similar to the WT value (0.9 mM) while G378-2AP (3.3 mM) requires more Mg^{2+} to stabilize the tertiary folding (Table 2-2, Figure 2-7). These data suggest that the 2AP substitution at G378 perturbs the stability of the tertiary fold of PRNA and affects its global structure at low concentration of Mg^{2+}. This result is consistent with the increased metal-dependence of pre-tRNA affinity.

Table 2-2: $K_{1/2}^{Mg^{2+}}$ (mM) for stabilization of folded WT and modified *B. subtilis* PRNA

Holoenzyme	WT	366P	366P	G378-2AP	G379-2AP	G379-N7G
UV[a]	0.9 ± 0.2	0.8 ± 0.2	1.0 ± 0.2	0.8 ± 0.1	0.8 ± 0.1	1.0 ± 0.2
CD[b]	0.9 ± 0.1	ND[c]	ND[c]	3.3 ± 0.6	1.5 ± 0.5	ND[c]

[a] 0.1 μM of PRNA was used for the folding experiment that measures formation of secondary structure. The experiments were performed in 50 mM Tris/MES, pH 6.0, 0-8 mM $MgCl_2$ and 200 mM KCl at 37°C. $K_{1/2}^{Mg^{2+}}$ was determined from a fit of a binding isotherm to these data (Equation 3).

[b] 0.1 μM of PRNA was used for the folding experiment measuring the magnesium dependence of the second transition, representing the formation of tertiary structure. The experiments were performed in 20 mM Tris-HCl, pH 8.0 and 0~10 mM $MgCl_2$ at 37°C. $K_{1/2}^{Mg^{2+}}$ was determined from a fit of a binding isotherm to these data (Equation 3).

[c] ND: Not determined.

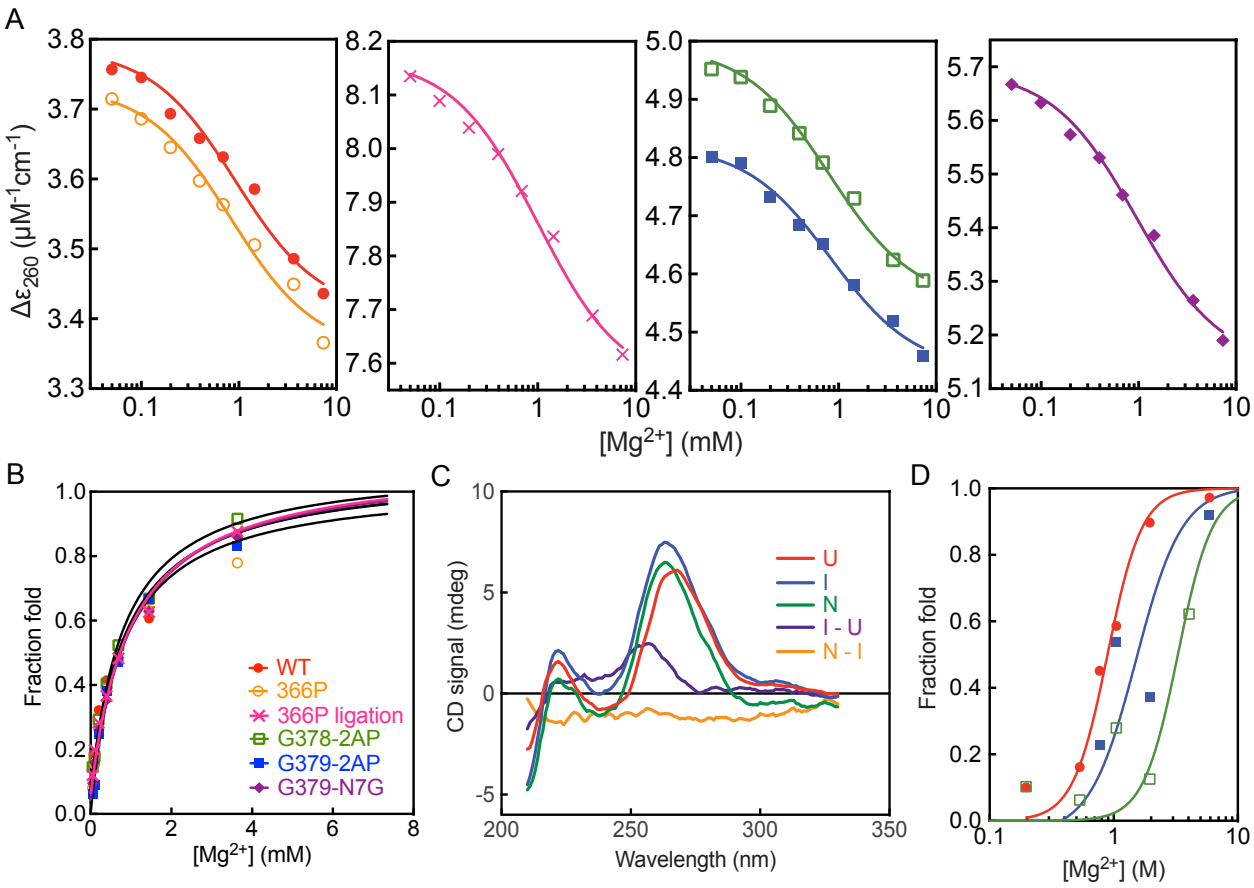

Figure 2-7: Equilibrium folding of WT and modified *B. subtilis* PRNA. **(A)** Mg^{2+} dependence of $\Delta\varepsilon_{260}$ values in 50 mM Tris/MES, pH 6.0 and 200 mM KCl at 37°C with $MgCl_2$ varying from 0 to 8 mM for WT (●), 366P (O), 366P ligation (×), G378-2AP (□), G379-2AP (■) and G379-N7G (◆) PRNA determined from UV absorbance measurement. **(B)** Mg^{2+} dependence of fraction folded from UV absorbance measurement. Solid lines are best fit to the fraction folded from the equilibrium Mg^{2+} titration. $K_{1/2}^{Mg^{2+}}$ values were determined from a fit of a binding isotherm to these data. **(C)** CD absorbance spectra of WT PRNA in unfolded state (U, no $MgCl_2$, red), intermediate state (I, 0.4 mM $MgCl_2$, blue) and native state (N, 10 mM $MgCl_2$, green) and the difference spectra of I-U (purple) and N-I (orange). The experiments were performed in 20 mM Tris, pH 8.0 and 0-10 mM $MgCl_2$ at 37°C. **(D)** Mg^{2+} dependence of fraction folded based on the changes in CD absorbance at 278 nm. Solid lines are the best fit to the fraction folded from the equilibrium Mg^{2+} titration. $K_{1/2}^{Mg^{2+}}$ values were determined from a fit of a binding isotherm to these data.

2.3.4 O6 at G379 Is Important for Pre-tRNA Cleavage Catalyzed by RNase P

To investigate the effects of modifications at G378 and G379 on RNase P catalysis, the single-turnover (STO) rate constants for cleavage at different pH values were

measured. Under STO conditions, the WT RNase P rate constant for catalysis of pre-tRNA cleavage in Mg^{2+} is log-linearly dependent on pH from pH 4.5 to 6 and becomes pH independent at higher pH. Previous data have shown that the rate-limiting step in k_{obs} is the pH dependent hydrolytic step at low pH (≤6), while the pH independent conformational change step becomes rate limiting at high pH (≥8) as indicated by a plateau in the pH profile (k_{max}) [52]. By fitting the data with a single ionization model (Equation 7), the apparent pK_a and k_{max} values can be calculated. This apparent pK_a reflects the change in rate-limiting steps and it is the pH at which the apparent constants for conformational change and cleavage are the same. By measuring the pH dependence of modified RNase P catalyzed cleavage under STO conditions, the effect of modifications at G378 and G379 on both the kinetics of the conformational change step and the hydrolytic cleavage step are evaluated.

A fluorescence polarization assay [58] was used to measure the observed cleavage rate constants (k_{obs}) of 5' fluorescein labeled pre-$tRNA^{Asp}$ (Fl-pre-$tRNA^{Asp}$) cleavage under single-turnover (STO) conditions in saturating divalent metal ion conditions, such as 20 mM Mg^{2+}, where the substrate binding affinity of the modified RNase P is comparable to that of WT. The experiments were performed at saturating concentrations of RNase P, where k_{obs} values are not dependent on the enzyme concentration (varying from 360 nM to 720 nM). These STO cleavage data are well described by a single exponential function (Equation 6).

First, the STO rate constants at different pH values were compared for 366P and 366P ligation to examine the effect of circular permutation on RNase P catalysis. The

k_{obs} values are similar at low pHs (Table 2-3, Figure 2-8A) indicating the circular permutation has no effect on cleavage step for RNase P catalysis.

To test the proposed inner-sphere metal ion interaction with the O6 position of G379, three modifications were analyzed, including deletion of the oxygen (2AP), substitution of oxygen to sulfur (6SG) and removal of the entire base (abG). The pH profile shows that the value of log k_{obs} for cleavage catalyzed by G379-2AP decreases linearly at low pH as observed for WT RNase P (Figure 2-8B). At pH 5.9, the 2AP modification, which replaces the O6 of G379 with a hydrogen, decreases the RNase P STO cleavage rate constant 9-fold (Table 2-3). Since this rate constant is dependent on pH, k_{obs} reflects k_{chem} thereby demonstrating that the 2AP modification decreases the rate constant for hydrolysis of the phosphodiester bond [52, 59]. The STO rate constant at high pH, reflecting the conformational change, is comparable to WT, therefore the apparent pK_a of the STO cleavage catalyzed by G379-2AP shifts to a higher value compared WT RNase P (from 7.0 ± 0.1 to 8.1 ± 0.1) (Table 2-3). Removal of the entire base of G379 has a smaller effect than the AP modification, decreasing the cleavage rate constant by 3-fold at pH 5.9 (Table 2-3, Figure 2-8B). The G379-6SG substitution where O6 is replaced by a sulfur has comparable activity to WT (Table 2-3, Figure 2-8B). Furthermore, in all cases the cleavage of Fl-pre-tRNA^{Asp} by modified RNase P is at the correct site, as indicated by denatured-PAGE analysis (Figure A-2). These data demonstrate that a hydrogen bond acceptor at the O6 position of guanine at position 379 is important for efficient cleavage. Two additional modifications, G379-N7G and G378-2AP, show the same catalytic efficiency at pH 5.9 as WT (Table 2-3, Figure

2-8A). These data demonstrate that O6 of G379, but not N7 of G379 or O6 of G378, is required for stabilizing the hydrolytic step of RNase P catalysis.

Table 2-3: Single-turnover observed rate constants for cleavage of Fl-pre-tRNA^{Asp} catalyzed by *B. subtilis* WT and modified RNase P

Holoenzyme	pH 5.9		High pH		pK_a[b]
	k_{obs} (s^{-1})[a]	$k_{obs}^{WT}/k_{obs}^{modified}$	k_{max} (s^{-1})[b]	$k_{max}^{WT}/k_{max}^{modified}$	
WT	0.16 ± 0.06	1	1.70 ± 0.05	1	7.0 ± 0.1
366P	0.11 ± 0.01	1.5	ND[c]	ND[c]	ND[c]
366P ligation	0.10 ± 0.01	1.6	ND[c]	ND[c]	ND[c]
G378-2AP	0.13 ± 0.01	1.2	1.70 ± 0.12	1	6.8 ± 0.1
G379-2AP	0.018 ± 0.001	8.9	2.09 ± 0.20	0.8	8.1 ± 0.1
G379-6SG	0.11 ± 0.02	1.5	ND[c]	ND[c]	ND[c]
G379-N7G	0.14 ± 0.03	1.1	2.00 ± 0.11	0.9	7.0 ± 0.1
G379-abG	0.049 ± 0.005	3.3	0.45 ± 0.02	3.8	6.8 ± 0.1

[a] STO cleavage was measured in a saturating concentration of RNase P (360-720 nM), 10 nM Fl-pre-tRNA^{Asp} substrate, 50 mM Tris/MES, pH 5.9, 20 mM $MgCl_2$, 200 mM KCl and 20 mM DTT. k_{obs} was calculated by a fit of a single exponential (Equation 6) to the fraction cleavage of Fl-pre-tRNA^{Asp} substrate, which was calculated from the decrease in anisotropy using Equation 5.
[b] The k_{max} and pK_a values were calculated from fitting a single ionization model (Equation 7) to the pH dependence of RNase P STO cleavage rate constants.
[c] ND: Not determined.

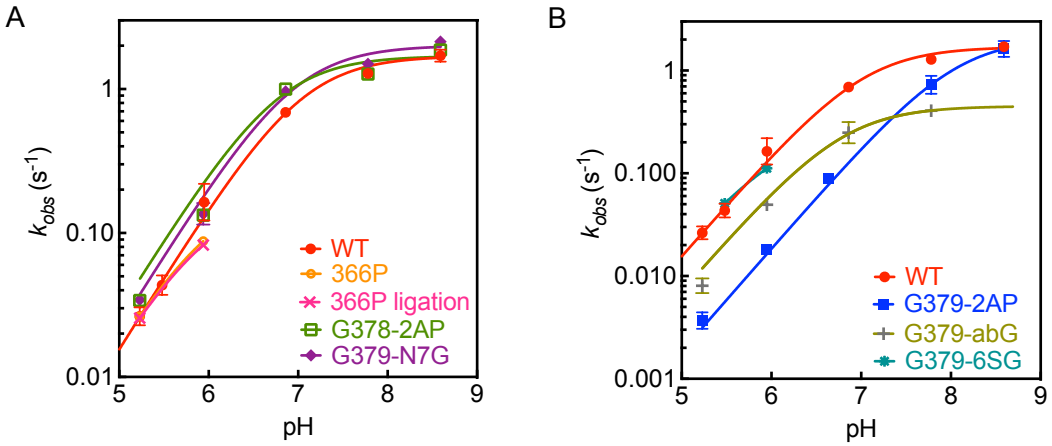

Figure 2-8: Modifications at G379, but not G378, affect catalysis of pre-tRNA cleavage by *B. subtilis* RNase P. The pH dependence of the STO rate constants for **(A)** WT (●), 366P (O), 366P ligation (×), G378-2AP (□) and G379-N7G (◆) RNase P; and **(B)** WT (●), G379-2AP (■), G379-abG (+) and G379-6SG (∗) were measured in 50 mM Tris/MES, pH 5.2-8.6, 20 mM $MgCl_2$ and 20 mM DTT with KCl concentrations (~200 mM) adjusted to maintain constant ionic strength. 360-720 nM of RNase P holoenzyme and 10 nM of Fl-pre-tRNA^{Asp} were used and the reaction was measured by changes in fluorescence polarization. A single ionization equation was fit to these data to calculate the apparent pK_a and k_{max} (solid lines).

2.3.5 The Base of G379 Is Important for the Conformational Change Step of RNase P Catalysis

The plateau in the pH profile reflects the rate constant of the pH independent conformational change [52], referred to as $k_{max.}$ For G379-2AP the pH independent k_{obs} has a similar value with WT at high pH (Table 2-3, Figure 2-8B). This indicates that the rate constant of conformational change is not affected by this modification [52, 59]. However, the abasic modification at G379 decreases both the rate constant for cleavage and the conformational change, k_{max}, by ~4-fold (Table 2-3, Figure 2-8B). Other modifications, including G379-N7G and G378-2AP, have the same k_{max} as WT RNase P. Additionally, since G379-N7G and G378-2AP retain the same activity as WT, this also corroborates the fact that circularly permuted 366P construct does not interfere with RNase P activity. All of these data demonstrate that the G379 base facilitates the conformation change step during RNase P catalysis, although this step is not sensitive to small modifications of either the G378 or G379 base.

To further investigate the role of G379 on the conformational change step, the kinetics for binding Fl-pre-tRNA^{Asp} to G379-2AP and G379-7NG were examined by stopped-flow fluorescence in Ca^{2+} under pseudo-first-order conditions. Under these conditions, biphasic kinetics are observed that reflect both the substrate association and the conformational change steps (Figure 2-9A). The value of $k_{obs,1}$ increases linearly with the concentration of RNase P (Figure 2-9B) while $k_{obs,2}$ shows an apparent hyperbolic dependence (Figure 2-9C). For the kinetic scheme shown in Figure 2-3, the slope of $k_{obs,1}$ reflects the rate constant for substrate association (k_1) (Equation 10) [60, 61]. This G379-2AP or G379-N7G modifications have little effect on this rate constant, as

compared with 366P (Table 2-4). With increasing RNase P concentration, the value of $k_{obs,2}$ reaches a plateau, which reflects the sum of the rate constants for the conformational change step (k_2 + k_{-2}) (Figure 2-3, Equation 11, [60, 61]). Values measured for k_2 + k_{-2} for G379-2AP and G379-7NG modified RNase P are comparable to 366P RNase P (Table 2-4). This is consistent with the same value of k_{max} for cleavage obtained from the pH profile (Table 2-3), corroborating the conclusion that G379-2AP or G379-N7G has no effect on the conformational change step of RNase P - pre-tRNA. The similar biphasic stopped-flow experiment can also be used to examine the effect of G379-abG in conformational change. Taken together, these data indicate that only the G379-abG modification decreased the rate constant of conformational change while other atom modifications have no effect, suggesting that the entire base of G379 is required for enhancing the conformational change step of RNase P catalysis.

Table 2-4: Biphasic kinetics parameters of Fl-pre-tRNA^{Asp} catalyzed by WT and modified *B. subtilis* RNase P[a]

	WT[b]	366P	G379-2AP	G379-7NG
k_1 ($\mu M^{-1}s^{-1}$)[c]	4.0 ± 0.1	11.6 ± 0.2	7.1 ± 0.2	10.2 ± 0.5
$k_2 + k_{-2}$ (s^{-1})[d]	0.43 ±0.02	0.42 ± 0.06	0.31 ± 0.09	0.42 ± 0.11

[a] The reaction was performed in 50 mM Tris/MES, pH 6.0, 10 mM $CaCl_2$, 200 mM KCl and 20 mM DTT at 25°C under pseudo-first-order conditions. 10 nM of Fl-pre-tRNA^{Asp} was used for each reaction and the concentration of RNase P varied from 50 nM to 400 nM.
[b] The values were taken from referece [52]. The difference between the rate constants for 366P and WT RNase P is probably due to the calculation of RNase P concentration.
[c] k_1 is the value of substrate association and was calculated from the slope of Equation 10.
[d] k_2 was calculated from the plateau ($k^{max}_{obs,2}$) of Equation 11. At high concentration of RNase P, $k^{max}_{obs,2} = k_2 + k_{-2}$.

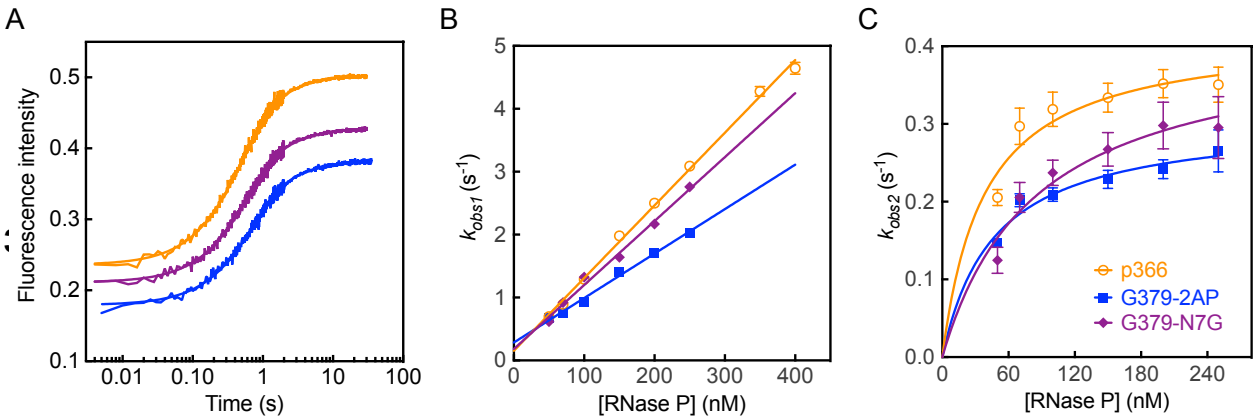

Figure 2-9: Biphasic stopped-flow kinetics of Fl-pre-tRNA^{Asp} binding to *B. subtilis* RNase P under pseudo-first-order conditions. 10 nM of Fl-pre-tRNA^{Asp} was used for each reaction and the concentration of RNase P varied from 50 nM to 400 nM. The reaction was performed in 50 mM Tris/MES, pH 6.0, 10 mM $CaCl_2$, 200 mM KCl and 20 mM DTT at 25°C. **(A)** Representative biphasic stopped-flow trace for 150 nM 366P (**O**, orange), G379-2AP (■, blue) and G379-N7G (◆, purple) RNase P. A two exponential equation was fit to these data to calculate $k_{obs,1}$ and $k_{obs,2}$. **(B)** Dependence of $k_{obs,1}$ on the concentration of RNase P; **(C)** Dependence of $k_{obs,2}$ on the concentration of RNase P.

To further examine the effect of modifications on G378 and G379 for RNase P catalysis, stopped-flow experiments were performed in the presence of Mg^{2+} instead of Ca^{2+}. In this case, the fluorescence trace has three phases, monitoring all of the steps in the kinetic pathway, including pre-tRNA binding, conformational change, cleavage and product release. The additional third phase ($k_{obs,3}$) reflects substrate cleavage and/or product release step [52].For 360 nM WT RNase P the apparent rate constants for the three phases are calculated from the stopped flow trace as: 3.5 s^{-1}, 1.1 s^{-1} and 0.011 s^{-1} (Figure 2-10, Table 2-5). These data are consistent with other measurements of these rate constants. The calculated value for k_1 of 9.7 $\mu M^{-1}s^{-1}$ is comparable to the value in Ca^{2+} (Table 2-4) while the value of k_2 + k_{-2} of 1.1 s^{-1} is slightly faster than the Ca^{2+} value, consistent with previous measurements [52]. Finally, the value of k_3 is comparable to the previous stopped-flow data at pH 5.5 [52]. As shown in Figure 2-10,

G379-2AP results in an 8-fold decrease in $k_{obs,3}$ compared with 366P while the rate constants for substrate binding and conformational change are comparable to the values for 366P (Table 2-5). These data are consistent with the pH dependence of RNase P STO cleavage which indicate a ~ 9-fold decrease in cleavage at pH 5.9 (Table 2-3). Similarly, both the pH profile and stopped-flow kinetics show that G379-N7G and G378-2AP modifications have no effect on RNase P catalysis (Figure 2-8A, Figure 2-9C and Figure 2-10).

Table 2-5: Three-phase kinetics parameters of Fl-pre-tRNA^{Asp} catalyzed by WT and modified *B. subtilis* RNase P[a]

(s^{-1})	WT	366P	366P ligation	G379-2AP	G378-2AP
$k_{obs,1}$	3.5 ± 0.9	3.7 ± 0.8	5.6 ± 2.6	2.8 ± 1.1	6 ± 22
$k_{obs,2}$	1.1 ± 0.3	1.1 ± 0.2	1.2 ± 0.1	0.8 ± 0.2	1.1 ± 0.1
$k_{obs,3}$ ($\times 10^{-2}$)	1.07 ± 0.04	1.65 ± 0.06	1.38 ± 0.05	0.22 ± 0.03	1.67 ± 0.12

[a] The reaction was performed in 50 mM Tris/MES, pH 5.5, 20 mM $MgCl_2$, 200 mM KCl and 20 mM DTT at 25°C with 360 nM of RNase P and 10 nM of Fl-pre-tRNA^{Asp}.

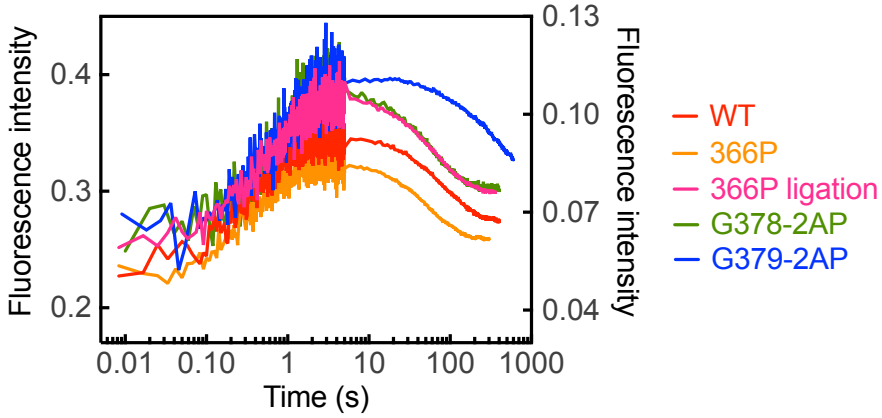

Figure 2-10: Stopped-flow fluorescence trace after mixing 10 nM of Fl-pre-tRNA^{Asp} with 360 nM of WT (red), 366P (orange), 366P ligation (pink), G378-2AP (green) and G379-2AP (blue) *B. subtilis* RNase P reveals three phases. A triple exponential was fit to the data to calculate values for $k_{obs,1}$, $k_{obs,2}$ and $k_{obs,3}$.

2.3.6 G379 Modifications Affect Pre-tRNA Cleavage Catalyzed by PRNA Without Altering the Cooperativity of the Apparent Affinity of Mg^{2+} to PRNA

To examine whether the modifications affect the metal dependence of PRNA, the Mg^{2+} dependence of the STO cleavage rate constant catalyzed by PRNA alone was measured at pH 5.9 where the cleavage step is rate-limiting (Figure 2-11). k_{max}^{PRNA} for the cleavage catalyzed by G379-2AP and G379-abG PRNA is about 9- and 5-fold slower than WT PRNA, respectively (Figure 2-11, Table 2-6). This is consistent with the pH profile data of RNase P holoenzyme (Figure 2-8B). However, the apparent affinity of Mg^{2+} for cleavage, $K_{1/2,app}^{Mg^{2+}}$, of G379-2AP and G378-AP as well as the Hill coefficients are comparable to the WT values, suggesting little interaction with a catalytic metal ion (Table 2-6, Figure 2-11). However, the G379-abG modification increases the value of $K_{1/2,app}^{Mg^{2+}}$ modestly (3-fold). This demonstrates that O6 or the base of G379 is important for enhancing catalytic activity without significantly altering the apparent affinity for Mg^{2+} dependent activation of cleavage.

Table 2-6: Mg^{2+} dependence of WT and modified *B. subtilis* PRNA catalyzed STO cleavage[a]

Holoenzyme	k_{max}^{PRNA} (s^{-1})[b] (×10^{-2})	$K_{1/2,app}^{Mg^{2+}}$ (mM)[b]	n_H[b]	$k_{max}^{PRNA,\ WT}/k_{max}^{PRNA,\ modified}$
WT	2.5 ± 0.1	13.0 ± 0.5	4.0 ± 0.5	1
366P	2.5 ± 0.1	12.0 ± 0.4	4.0 ± 0.2	1
G378-2AP	2.2 ± 0.2	14.1 ± 1.5	4.1 ± 1.4	1.1
G379-2AP	0.28 ± 0.02	10.3 ± 0.7	4.6 ± 1.3	8.9
G379-abG	0.48 ± 0.07	36.1 ± 5.0	3.2 ± 1.4	5.2

[a] The reaction was performed with 360 nM PRNA and 10 nM Fl-pre-$tRNA^{Asp}$ at 37°C in 50 mM Tris/MES, pH 5.9, 20 mM DTT with 4 - 700 mM $MgCl_2$, and varying KCl concentrations from 118 to 10 mM. At higher Mg^{2+} concentration KCl was maintained at 10 mM. k_{obs} was calculated by a fit of single exponential (Equation 6) to the fraction cleavage of Fl-pre-$tRNA^{Asp}$ substrate, which was calculated from the decrease in anisotropy using Equation 5.

[b] Equation 8 was fit to the Mg^{2+} dependence of k_{obs} to calculate k_{max}^{PRNA}, $K_{1/2,app}^{Mg^{2+}}$ and n_H of PRNA-catalyzed cleavage.

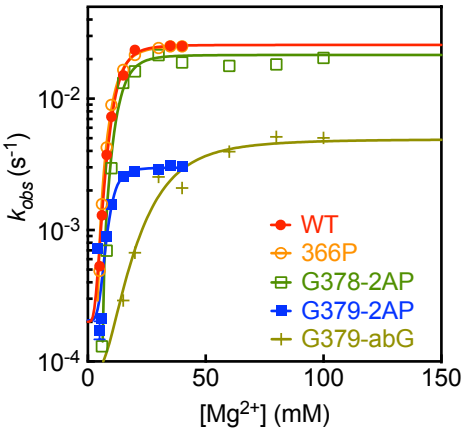

Figure 2-11: Mg^{2+} dependence of WT (●), 366P (O), G378-2AP (□), G379-2AP (■) and G379-abG (+) *B. subtilis* PRNA STO cleavage for Fl-pre-$tRNA^{Asp}$. The reaction was measured with 360 nM PRNA and 10 nM Fl-pre-$tRNA^{Asp}$ at 37°C in 50 mM Tris/MES, pH 5.9, 20 mM DTT with 4-700 mM $MgCl_2$, and varying KCl concentrations from 118 to 10 mM. At higher Mg^{2+} concentration KCl was maintained at 10 mM. A single exponential was fit to the data to calculate the STO cleavage rate constants (k_{obs}). Equation 8 was fit to the Mg^{2+} dependence of k_{obs} (solid lines).

2.3.7 Cd^{2+} Ion Does Not Rescue G379-6SG Holoenzyme Activity

Even though G379-2AP and G379-abG decrease cleavage activity of both *B. subtilis* RNase P holoenzyme and PRNA (Figure 2-8B, Figure 2-11), the effects are much

smaller than previously observed deleterious effects on catalysis caused by disrupting an inner-sphere Mg^{2+} binding site [25, 40, 41, 62]. To further rule out the possibility that the O6 atom directly coordinates Mg^{2+} ion, the activity of G379-6SG RNase P was measured in the presence of a thiophilic ion, Cd^{2+} ion to evaluate whether this enhanced the catalytic activity. However, increasing concentrations of Cd^{2+} in the presence of 20 mM Mg^{2+} decrease the STO rate constant for both the 366P and G379-6SG holoenzymes (Figure 2-12A) and both show similar observed rate constants and inhibition by Cd^{2+} (Figure 2-12B). The relative rescue effect (k_{rel} = $(k_{Cd}/k_{Mg})^{6SG}/(k_{Cd}/k_{Mg})^{366P}$ = 1) of G379-6SU clearly shows that Cd^{2+} does not enhance the G379-6SG activity (Figure 2-12C), providing no evidence for inner-sphere coordination of the O6 site of G379. Therefore, O6 of G379 enhances catalysis by RNase P but does not coordinate an inner-sphere Mg^{2+} ion.

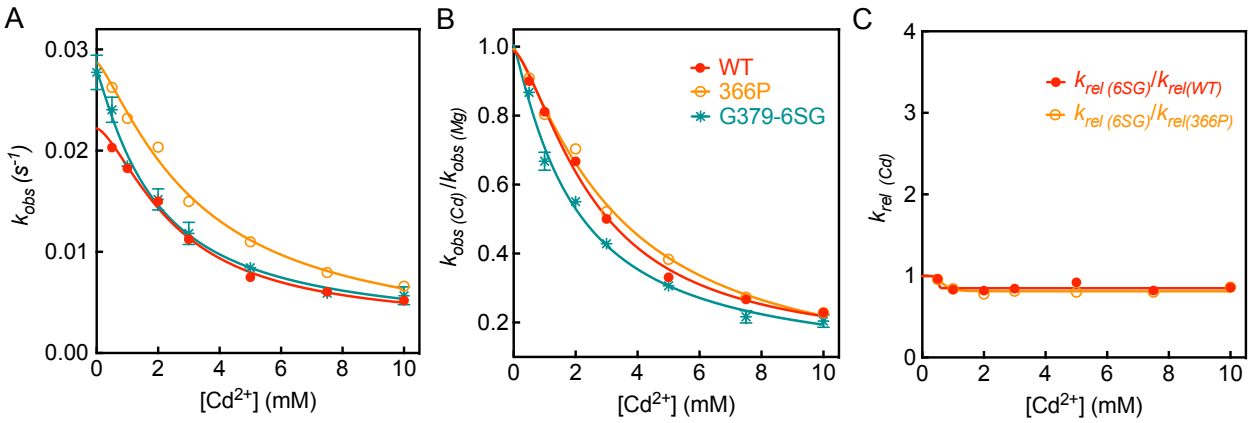

Figure 2-12: Cd^{2+} dependence of STO cleavage catalyzed by WT and modified *B. subtilis* RNase P in the presence of 20 mM of Mg^{2+}. **(A)** STO rate constant (k_{obs}) for cleavage of 10 nM Fl-pre-$tRNA^{Asp}$ catalyzed by 360 nM WT (●), 366P (**O**) and G379-6SG (∗) RNase P in 50 mM Tris/MES, pH 5.2, 200 mM KCl and 20 mM $MgCl_2$ with varying concentrations of $CdCl_2$ (0-10 mM). **(B)** Relative inhibition of RNase P by Cd where k_{rel} = k_{Cd}/k_{Mg}. **(C)** Activity of G379-6SG variant in comparison to WT where k_{rel} = $(k_{Cd}/k_{Mg})^{6SG}/(k_{Cd}/k_{Mg})^{WT}$ or k_{rel} = $(k_{Cd}/k_{Mg})^{6SG}/(k_{Cd}/k_{Mg})^{366P}$.

2.4 Discussion

Helix P4 contains 6 of the 13 universally conserved nucleotides in PRNA [39] and is proposed to be part of the active site of RNase P. A study on a P4 helix stem-loop mimic construct by NMR and XAS revealed association of Mg^{2+} at residues corresponding to G378 and G379 in RNase P [51]. This study led to a proposal suggesting that the base O6 and N7 of G378/G379 form inner- and outer-sphere interactions with a metal ion, respectively. To test this hypothesis, I examined the biochemical role of G378 and G379 in *B. subtilis* RNase P by combining atom modifications and enzyme kinetic. The results show that the modifications on both G378 and G379 alter the metal-dependent pre-tRNA affinity, due to either stabilization of the RNA structure or interactions between RNase P and pre-tRNA. Removal of the O6 carbonyl oxygen of G379 decreases RNase P catalyzed cleavage rate constant at low pH without affecting Mg^{2+} cooperativity of PRNA folding, but has no effect on the cleavage activity of RNase P at high pH where a conformational change is rate-limiting. Deletion of the entire base of G379 decreases the cleavage rate constant at both low and high pH and affects the Mg^{2+} cooperativity. Furthermore, the G379-6SG modification does not reduce the cleavage rate constant and a thiophilic metal ion, Cd^{2+}, does not enhance the cleavage catalyzed by this enzyme. These data argue against an inner-sphere coordination of the O6 on G379 to a catalytic metal ion, but suggest that hydrogen bond acceptor at this position on G379 might interact with a metal ion. There is no evidence to support the metal coordination at O6 of G378 or N7 of G379.

2.4.1 G378 and G379 Are Important for Metal Ion Dependent Substrate Binding

To incorporate the atom modifications into RNase P, a circularly permuted PRNA was used in this study. A previous study showed that circular permutation at the 5' side of the P4 helix has minimal effect on the substrate affinity at saturating divalent metal ion concentrations [41]. In this study, I introduced the circular permutation on the 3' side of the P4 helix and also observed comparable affinity of the pre-tRNA^{Asp} substrate with WT RNase P at saturating Ca^{2+} (Table 2-1, Figure 2-6). However, at sub-saturating Ca^{2+} (3 mM), the circularly permuted construct (366P) destabilizes the substrate affinity by 0.6 kcal/mol[2]. The replacement of O6 with a hydrogen or carbon substitution at N7 in G379 decreases substrate affinity by an additional 0.9 kcal/mol in comparison to WT holoenzyme. Moreover, the removal of O6 at G378 decreases the stability of substrate binding by an additional 1.8 kcal/mol. It suggests the structure of the bases at G378 and G379 are important for substrate binding.

There are two possible explanations for how these modifications affect substrate affinity under low divalent metal conditions. Modifications could destabilize the folded structure of RNase P that is required to bind pre-tRNA since folding is stabilized by divalent cations. Alternatively, base modifications could cause perturbations in one or more specific metal ion coordination sites that stabilize substrate binding. The Mg^{2+} dependence of PRNA folding observed by UV and CD suggests that the stability of the secondary and tertiary structures of PRNA is not affected by those modifications, with the exception that the 2AP substitution at G378 requires more Mg^{2+} to stabilize the tertiary fold compared to WT (Table 2-2, Figure 2-7). These data also suggest that the

[2] Calculated by $\Delta\Delta G = -RT\ln (K_{D,\,app}^{modified}/K_{D,\,app}^{WT})$

global structures of these modified PRNAs are undisturbed. Nonetheless, the substrate binding affinity defect caused by these perturbations can be rescued by saturating concentrations of divalent metal ion, demonstrating that pre-tRNA substrate affinity to RNase P is coupled to metal ion binding and suggesting that the bases of G378 and G379 enhance a bound metal ion that is associated with substrate affinity.

2.4.2 G379 Coordinates a Co-catalytic Metal Ion through Outer-sphere Coordination

Previous phosphorothioate substitutions in RNase P that disrupt inner-sphere metal ion contacts with the non-bridging oxygen atoms in the backbone phosphodiester bonds of A49 and G50 (*B. subtilis* numbering) [25, 40, 41] lead to large decreases in catalytic activity (300- to 10^4-fold). Therefore, removing the proposed inner-sphere metal ion ligand, O6 of G378 and G379 [51], was expected to cause a significant decrease in the cleavage rate constant. However, the 2-aminopurine nucleoside substitution of G378 (G378-2AP) has no effect on STO cleavage rate constants at both high pH and low pH (Table 2-3, Figure 2-8A). This argues that O6 of G378 does not directly contact a catalytic metal ion. For G379, a 9-fold decrease pH in the value of the STO rate constant at low pH is observed for the G379-2AP substitution (Table 2-3, Figure 2-8B), but this effect is much smaller than the 300- to 10^4-fold decrease previously observed for the disruption of an inner-sphere metal ion coordination [25, 40, 41]. Furthermore, the G379-6SG modification (substitution of the O6 with sulfur) has similar activity as the WT enzyme and the addition of Cd^{2+} did not increase the pre-tRNA cleavage activity (Table 2-3, Figure 2-8B, Figure 2-12). The O6 atom of G379 may interact with a metal

ion, but this interaction is either not an inner-sphere contact or the metal ion is not essential to stabilize the transition state for catalysis. Furthermore, carbon substitution for the nitrogen-7 at G379 (G379-N7G) is used to examine the proposed outer-sphere metal ion coordination on N7 [51]. This modified RNase P has the same activity as WT at both low and high pH (Table 2-3, Figure 2-8A), demonstrating that N7 of G379 does not interact with a catalytic metal ion.

The Mg^{2+} dependence of pre-tRNA cleavage catalyzed by PRNA alone shows that the G378-2AP enzyme has similar k_{obs} value to WT PRNA with no effect on the apparent Mg^{2+} affinity and Hill coefficient (Table 2-6). This result confirms that O6 of G378 does not coordinate a catalytic metal ion. The G379-2AP modification has no effect on the value of $K_{1/2,app}^{Mg^{2+}}$ and Hill coefficient compared with WT PRNA, even though it decreases cleavage rate constant (Table 2-6). Therefore the O6 of G379 enhances catalytic activity without significantly altering the $K_{1/2}$ for Mg^{2+}-dependent activation of cleavage. However, the G379-abG modification increases the value of $K_{1/2,app}^{Mg^{2+}}$ by ~3-fold and decreases Hill coefficient by <1 compared with WT PRNA. It could suggest the alteration or loss of an active site metal ion caused by G379-abG. This result suggests that G379 coordinates a metal ion by an outer-sphere interaction through water.

Outer-sphere metal ions have previously been suggested to enhance RNase P reactivity [21, 29]. The data presented above suggest that the carbonyl oxygen of G379 likely positions one co-catalytic metal ion through a water-mediated outer-sphere interaction. It is possible that the O6 oxygen in G379 is a hydrogen bond acceptor for a metal-coordinated water molecule to optimally position a co-catalytic metal ion activity (Figure 2-13A). Therefore, the substitution of O6 with a hydrogen on G379 (Figure

2-13B) or the deletion of the entire base (abG) (Figure 2-13D) sterically disturbs the metal ion binding site or affects the hydrogen-bonding interactions that alter the position or affinity of the metal ion. Since G379-abG has a smaller effect than G379-2AP on the cleavage rate constant, removal of the base could generate space for additional water molecules at the active site that allow the co-catalytic metal ion to be positioned more optimally than in G379-2AP RNase P. Nevertheless, the G379-6SG variant has similar activity as WT, suggesting that G379 also interacts with a water-mediated metal ion via the sulfur atom (Figure 2-13C).

Therefore, there is no evidence that suggests that O6 of G378 or N7 of G379 form contact with a catalytic metal ion. Furthermore, the data suggest that the O6 of G379 forms an outer sphere contact with a metal ion. The proposed model of the metal ion binding site on G378 and G379 was based on the available NMR structure of the P4 helix stem-loop mimic [49, 50] and the combination of solution NMR and XAS methods that probe RNA-metal binding to the P4 helix stem-loop mimic [51]. It is important to note that these studies are based on the P4 helix stem-loop mimic, which has small differences in the interhelical angle compared to the P4 helix in PRNA, as shown in the available crystal structure [50]. Tertiary contacts between the upper stem of P4 and L8 in PRNA likely contribute to the native structure of the P4 helix, which are not present in the isolated P4 stem-loop mimic construct. Thus, the results obtained from P4 helix stem-loop mimic may not reflect the situation in full-length PRNA completely. Furthermore, different ways to interpret the data from Extended X-ray absorption fine structure (EXAFS) spectroscopy that led to the model of putative metal ion binding sites

in the P4 stem-loop mimic [51] could be another reason for the inconsistency between the model and biochemical data.

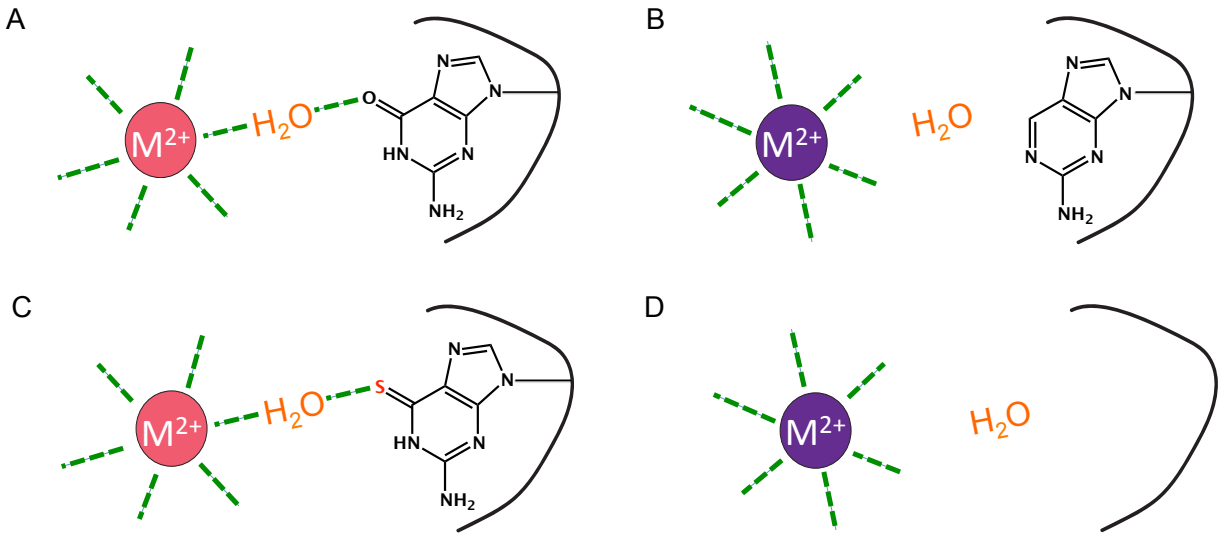

Figure 2-13: Model of effects of G379 modifications on co-catalytic metal ion coordination. **(A)** O6 of G379 interacts with a Mg^{2+} ion through a water-mediated outer-sphere contact; **(B)** G379-2AP disrupts the Mg^{2+} binding site by the removal of O6; **(C)** G379-6SG can also interact with an outer-sphere Mg^{2+} ion using the sulfur atom instead of oxygen; **(D)** Lack of base disrupts the specific interaction with Mg^{2+}.

2.4.3 The Base of G379 Participates in the Conformational Change of RNase P Catalysis

A previous study indicated that during the RNase P catalytic cycle, after RNase P binds to pre-tRNA to form an enzyme-substrate complex, the ES complex undergoes a metal dependent conformational change to form an active conformer (ES*) prior to the chemical cleavage step (Figure 2-3) [52]. At high pH (pH > 8), the rate limiting step for RNase P cleavage is a conformational change and k_{max} reflects the rate constant of this step [52]. The removal of the guanine base to form an abasic site (G379-abG) reduces this conformational change rate constant about 4-fold and decreases the rate constant for cleavage without affecting the apparent kinetic pK_a. Similar abasic modifications

have previously been shown to dramatically reduce activity (up to 10^6-fold) of a hammerhead ribozyme by reducing the stability of the folded RNA [63]. Since G379 forms a canonical Watson-Crick base pair with C52 on the opposite strand in P4 in PRNA, deleting the base disrupts hydrogen bonding and base stacking which can be important for sterics or for coordinating with a co-catalytic metal ion in the conformational change step. In some cases, the reduced activity as a result of abasic modifications in the hammerhead ribozyme could be partially rescued (20- to 300-fold activation) by addition of exogenous bases that restore hydrogen bonding and base stacking interaction [63]. To test the importance of hydrogen bonding or base stacking interactions in G379 for RNase P catalysis, the addition of guanine to the pre-tRNA cleavage by RNase P could be used.

In the RNase P kinetic pathway, the ES* conformer is stabilized by a high affinity inner-sphere divalent metal ion, as indicated by the stabilization of this complex with Ca^{2+} or Mg^{2+} but not $Co(NH_3)_6^{3+}$ [26]. The STO cleavage by G379-6SG PRNA is not activated by substitution of Cd^{2+} for Mg^{2+} arguing against a specific inner-sphere metal coordination by O6 at G379. However, it is possible there is a metal ion associated with this conformational change through a possible outer-sphere interaction with G379. Studies on the P4 helix conformational change will be discussed in further detail in Chapter 3.

2.5 Conclusion

A combination of atom modifications and enzyme kinetics demonstrate that the carbonyl oxygen at O6 of G379 in RNase PRNA is important for a hydrogen bond donor

and likely forms an outer-sphere contact with a metal ion important for substrate binding and catalysis. The function of this moiety is likely to position the metal ion at a favorable site and enhance metal affinity for catalysis. Notably, the guanosine base of this nucleotide is essential for both catalysis and stabilization of an active conformer of RNase P. The decrease in rate constant of conformational change caused by removal of the G379 base could be due to the disruption of hydrogen bonding with C52 or base stacking which is potentially involved in conformational change sterically or loss of a co-catalytic metal ion. There is no evidence to support N7 of G379 or O6 of G378 interacting with a metal ion important for RNase P catalysis.

Identification of the RNA moieties involved in metal ion binding and discerning the function of these interactions is an important question in the RNA catalysis field. This study identified an outer-sphere metal ion binding site in the P4 helix of RNase P. This metal ion is involved in stabilizing substrate affinity, enhancing catalysis of pre-tRNA cleavage as well as participating in a conformational change in the RNase P kinetic pathway.

2.6 Materials and Methods

2.6.1 Materials and Reagents

All nucleotide triphosphates and other chemicals were purchased from Sigma at the highest purity (RNase and DNase free grade) unless otherwise specified. Sodium dodecyl sulfate (SDS) was purchased from Fisher Scientific. Inorganic pyrophosphatase was purchased from Roche Applied Science. Ultra-pure urea was from MP Biomedicals. 5-Iodoacetamido-fluorescein (5-IAF) was obtained from Invitrogen (now Life

Technologies) and dissolved in anhydrous DMSO (Sigma). Guanosine 5'-monothiophosphate (GMPS) was synthesized from 2', 3' isopropylidene-guanosine and thiophosphoryl chloride as described [64]. His_6-T7 RNA polymerase was purified using Ni-NTA chromatography, as described previously [65]. Buffer solutions were prepared using Milli-Q (Millipore Corporation) treated deionized water and sterilized either by autoclaving (inorganic buffers such as $MgCl_2$, $CaCl_2$ and KCl) or filtration (EDTA stock solution and solutions containing MES) using Stericup filter units (Millipore Corporation). Tris/MES stock solutions at various pH values were made at room temperature and the pH was re-measured at 37˚C. All DNA oligonucleotides were purchased from Integrated DNA Technologies (IDT). Ribo-oligonucleotides containing atom modifications were purchased from different vendors and 2'-deprotected before use. The ribo-oligonucleotides containing 2-aminopurine nucleoside (2AP), 7-deazaguanosine (N7G) and 6-thiogunaosine (6SG) were purchased from Dharmacon (now Thermo Scientific). The ribo-oligonucleotide with rSpacer (abasic) modification was synthesized by the Keck Oligo Synthesis Resource (Yale School of Medicine).

2.6.2 Preparation of P Protein, Substrate and WT PRNA

B. subtilis RNase P protein was recombinantly expressed in BL21(DE3)pLysS cells with plasmid encoding the P protein (pPWT1) and purified as previously described [66, 67]. The *B. subtilis* Fl-pre-$tRNA^{Asp}$ substrate containing a 5-nucleotide leader sequence was prepared as described previously [26, 68] by 5′ monothiophosphate guanosine (5' GMPS) primed *in vitro* run-off transcription (4 mM ATP, GMPS, CTP, UTP, and 0.8 mM GTP in 50 mM Tris-HCl pH 8.0, 20 mM $MgCl_2$, 1 mM spermidine and 5 mM DTT for 6-

12 hrs at 37˚C) using T7 RNA polymerase from a DNA template (plasmid: pDW152) linearized using *Bst*NI restriction enzyme (New England Biolabs, NEB). The transcribed 5'-GMPS-pre-tRNA was buffer exchanged and concentrated into a degassed labeling buffer (10 mM Tris-HCl, pH 7.2 and 1 mM EDTA) for labeling by incubation with 5-IAF (molar ratio of RNA: dye = 1:40) at 37 °C overnight. The ^{32}P 5' end labeled pre-tRNA substrate was prepared by incubating regularly transcribed pre-tRNA with calf intestinal alkaline phosphatase (NEB) followed by 5′ end-labeling using T4 polynucleotide kinase (NEB) and γ-^{32}P-ATP according to manufacturing instructions and purified by denaturing PAGE followed by phenol/chloroform extraction and ethanol precipitation [20]. The WT PRNA was transcribed *in vitro* by T7 polymerase using DNA template (plasmid: pDW25) linearized by *Dra*I restriction enzymes (NEB). All RNAs were purified by electrophoresis on a 6% (PRNA) or 10-12% (pre-tRNA) denaturing PAGE containing 7M urea, followed by buffer-exchange and concentration using Amicon Ultra (10K MWCO) and ethanol precipitation for storage at -80 ˚C.

2.6.3 Preparation of Circularly Permuted 366P and 386-365P RNA

Plasmid containing DNA template for transcribing circularly permuted 386-365P (p386P) was cloned from p2PRNA plasmid containing tandem repeats of RNase P RNA [53] as described before [41]. The plasmid p2PRNA was used as the template for PCR (Primers: 5'-TAA TAC GAC TCA CTA TAG AAC GTT AGA CCA CTT ACA TTT G-3'; 5'-ATG GAG ATA TCG TAC TGC AAA CGG CTC-3') to create a DNA fragment beginning with a T7 RNA promoter followed by PRNA nucleotide G386 and ending with nucleotide U365 then followed by the sequence recognized by the restriction enzyme *EcoR*V. This

DNA fragment was then subcloned into plasmid pUC18 at the blunt site created by digestion with *Sma*I (New England Biolabs) to create plasmid p386P. In the plasmids, the native 3' and 5' termini of the PRNA molecule are joined by the sequence 3'- ACA UUU-5' [41]. The circularly permuted 366P plasmid (p366P) was prepared in the same way to create a DNA fragment beginning with a T7 RNA promoter followed by PRNA nucleotide G366 and ending with nucleotide U365 then followed by the sequence recognized by the restriction enzyme *EcoR*V. Following linearization of the DNA template by the *EcoR*V restriction enzyme (NEB), the circularly permuted PRNAs were transcribed *in vitro* with a 5′ guanosine monophosphate primed (5’-GMP) RNA, as previously reported [41].

2.6.4 Preparation of Modified PRNA by Ligation

For the G378/G379 modifications, the 20-mer ribo-oligonucleotide containing the same sequence as the 3’ end strand of the P4 helix (5’-GGA ACA AAA CAU G*^{378}G*^{379}C UUA CA-3’) with guanosine modifications (indicated by the asterisk sign and numbering) was ligated to the 5’-GMP transcribed 386-365P in the presence of a DNA splint that is complementary to all 20-nt of the RNA oligo and the first 56 nt of 386-365P (5’-CAA GAT CTG CAG CGA TTA CCC GAA CGT TAA GAA CAA ATG TAA GTG GTC TAA CGT TCT GTA AGC CAT GTT TTG TTC C-3’).

For ligation reactions, 4 μM 5’-GMP PRNA, 28 μM 20-mer ribo-oligonucleotide and 28 μM DNA splint were annealed in 66 mM Tris-HCl (pH 7.6), 6.6 mM $MgCl_2$ and 10 mM DTT by denaturing at 75°C for 3 min and cooling down at room temperature for 15 min. After addition of a final concentration of 200 μM ATP, 4 μM T4 DNA ligase and 0.2

unit/μl of Sperase·In^{TM} RNase inhibitor (Ambion, now Life Technology), the reaction was incubated at 30˚C for 3.5 h or overnight [69-71].

The ligation efficiency was determined by primer extension analysis (Figure A-1) using a 6FAM labeled primer that anneals to nucleotide 28 to 1 of the ligated PRNA (5'-6FAM-CTG CAG CGA TTA CCC GAA CGT TAA GAA C-3'). The 6FAM-primer (9 pmol) was annealed to PRNA (27 pmol) in 50 mM Tris-HCl, pH 8.3, 75 mM NaCl and 10 mM DTT by denaturing for 3 min at 95˚C followed by 15 min incubation at 37˚C. A subsequent extension step took place at 42˚C for 30 min by the addition of 10 mM $MgCl_2$, 0.8 mM dNTPs, and 2.5 unit/μl reverse transcriptase (Promega). Reactions were visualized by a 6% denaturing PAGE, scanned using a Typhoon Phosphorimager (detection limit was determined to be 5 fmol of fluorescein) and quantified by ImageJ software.

2.6.5 Determination of Pre-tRNA Dissociation Constant by Spin Column

The affinity of ^{32}P 5' end labeled pre-tRNA^{Asp} with a 5-nt leader to RNase P holoenzyme was measured as described previously [59]. The recombinant P protein was dialyzed against binding buffers containing 50 mM Tris/MES, pH 6.0, 2-8 mM $CaCl_2$ and 386.5-404.5 mM KCl at 4˚C. PRNA was folded by denaturation in water at 95˚C for 3 min followed by 15 min incubation at 37˚C before addition of the desired binding buffers. The PRNA was then buffer exchanged with the same binding buffer using at least three iterations of Amicon centrifugation filters (MWCO 10K, Millipore). RNase P holoenzyme was reconstituted by mixing PRNA and P protein at a 1:1 ratio. RNase P holoenzyme (0-400 nM) was incubated with ^{32}P 5' end labeled pre-tRNA^{Asp} (<< 1 nM) for 5 min at 37˚C. The holoenzyme-substrate mixture was loaded onto a pre-packed G-

75 Sephadex (GE health) spin column (Corning Life Sciences). The column was pre-centrifuged for 15 seconds before the experiment. The unbound substrate was separated from the mixture by centrifugation for 15 seconds at 6000 rpm. The amount of bound and unbound substrate was measured by scintillation counting. A single binding isotherm (Equation 1)

$$\text{Fraction bound} = \frac{[\text{ES}] + [\text{ES}^*]}{[\text{S}_{\text{total}}]} = \frac{[\text{E}_{\text{total}}]}{K_{\text{D,app}} + [\text{E}_{\text{total}}]} \qquad \textbf{Equation 1}$$

was fit to the data to obtain the dissociation constant, $K_{\text{D, app}}$.

2.6.6 PRNA Folding Measured by Ultraviolet Absorbance (UV) and Circular Dichrosm (CD) Spectroscopy

The UV folding experiments were performed with a Cary 100 Bio UV-Visible spectrometer equipped with a temperature controller and thermostated cell holder. 0.1 μM PRNA was heat denatured at 95°C for 3 min in water, then incubated at 37°C for 15 min. Then 50 mM Tris/MES, pH 6.0, 0-8 mM $MgCl_2$, 200 mM KCl was added and the mixture was incubated at 37°C for 30 min. The samples were then placed in a quartz semi-micro cuvette capped with a Telflon stopper and the data were collected at 260 nm at 37°C. The buffer only was the background control. $\Delta\varepsilon_{260}$ was calculated by:

$$\Delta\varepsilon_{260} = \frac{\text{A}_{260}^{\text{PRNA}} - \text{A}_{260}^{\text{buffer}}}{[\text{PRNA}] \times \text{L}} \qquad \textbf{Equation 2}$$

where A is the UV absorbance at 260 nm and L is the cell path length (1 cm). $K_{1/2}^{Mg^{2+}}$ was determined from a fit of a binding isotherm to these data.

$$\text{Fraction bound} = 1 - \frac{\Delta\varepsilon_{260} - \Delta\varepsilon_{260,\infty}}{\Delta\varepsilon_{260,0} - \Delta\varepsilon_{260,\infty}} = \frac{[\mathrm{Mg}^{2+}]}{K_{1/2}^{\mathrm{Mg}^{2+}} + [\mathrm{Mg}^{2+}]} \qquad \textbf{Equation 3}$$

The $\Delta\varepsilon_{260,0}$ and $\Delta\varepsilon_{260,\infty}$ are the values of the unfolded and fully folded PRNA, respectively.

For the CD experiments, the PRNA samples were prepared in the same way as described for the UV experiments in 20 mM Tris-HCl, pH 8.0 and 0-10 mM $MgCl_2$. CD spectra were recorded using an AVIV spectropolarimeter and the data were obtained every 1 nm at a scan rate 20 nm/min. The data were analyzed using Equation 4 to obtain the Δε of A_{278}.

$$\Delta\varepsilon_{278} = \frac{\theta_{278}^{\mathrm{PRNA}} - \theta_{278}^{\mathrm{buffer}}}{32980 \times [\mathrm{PRNA}] \times \mathrm{L} \times \mathrm{N}} \qquad \textbf{Equation 4}$$

where θ is the raw CD amplitude in mdeg, L is the cell path length (1 cm), and N is the number of nucleotides in PRNA which is 401 for WT and 407 for circularly permuted PRNA. Then $K_{1/2}^{Mg^{2+}}$ was determined by Equation 3.

All concentrations of PRNA and Mg^{2+} were corrected for the dilution introduced by addition of Mg^{2+} stock solutions.

2.6.7 Single-turnover Kinetic Experiments

Single-turnover (STO) experiments were performed at saturating concentrations of divalent metal ions (50 mM Tris/MES pH 5-9, 20 mM $MgCl_2$, 200 mM KCl and 20 mM DTT.) and saturating concentrations of both RNase P holoenzyme (360-720 nM) and Fl-pre-$tRNA^{Asp}$ substrate (10 nM). For metal rescue experiments, the STO reactions were

supplemented with 0.5 to 10 mM $CdCl_2$ in 50 mM Tris/MES, pH 5.2, 20 mM $MgCl_2$ and 200 mM KCl at 37˚C. For the Mg^{2+} dependence of STO cleavage catalyzed by PRNA alone, the concentration of $MgCl_2$ was 4-700 mM with varying KCl concentrations from 118 to 10 mM. The STO cleavage of Fl-pre-$tRNA^{Asp}$ was carried out either in a black 96-well microplate (Corning Incorporation, #3686) by monitoring the anisotropy change of fluorescein (filters with λ_{ex} = 485 ± 20 nm and λ_{em} = 535 ± 25 nm) using a TECAN plate-reader (Infinite F500, G factor = 0.93) [58] (for k_{obs} < 0.1 s^{-1}) or by quenching the reaction at short time points (for k_{obs} > 0.1 s^{-1}) using a mechanical rapid quench apparatus (Model RQF-3, Kintek Corporation) [52] and then analyzing the products by denaturing PAGE.

For the RNase P holoenzyme catalyzed STO reactions measured by FA assay [58], the total fluorescence intensity decreased from the initial substrate-RNase P complex (F^0) to cleaved product (F^∞), and the extent of this decrease varies with pH. Therefore, an enhancement factor g, defined as described previously [72], was used to correct for the total fluorescence change when converting the anisotropy time course to a fraction cleaved (Y) trace using Equation 5:

$$Y = 1 - \frac{r - r_\infty}{r_0 - r_\infty + (g-1)(r_0 - r)} \qquad \textbf{Equation 5}$$

The enhancement factor is defined by $g = F^0/F^\infty$. The r_0 and r_∞ are the anisotropy values of the RNase P holoenzyme-bound substrate and cleaved product, respectively, measured for each experiment.

The STO cleavage rate constant (k_{obs}) was then calculated by fitting a single exponential model (Equation 6) to the fraction cleavage as a function of time.

$$Y = Y_{\infty}(1 - e^{-k_{obs}t}) \quad \textbf{Equation 6}$$

The pK_a values and pH-independent rate constants for reactions catalyzed by RNase P holoenzyme were calculated by fitting a single ionization model (Equation 7) to the pH profile:

$$\mathrm{pH} = \frac{k_{max}}{1 + 10^{(\mathrm{p}K_a - \mathrm{pH})}} \quad \textbf{Equation 7}$$

Equation 8 was fit to the Mg^{2+} dependence of the PRNA catalyzed STO cleavage data to calculate the apparent Mg^{2+} affinity ($K_{1/2,app}^{Mg^{2+}}$) and Hill coefficient (n_H):

$$k_{obs} = \frac{k_{max}^{PRNA}\,[Mg^{2+}]^{n_H}}{\left(K_{1/2,app}^{Mg^{2+}}\right)^{n_H} + [Mg^{2+}]^{n_H}} \quad \textbf{Equation 8}$$

2.6.8 Fluorescence Stopped-flow Kinetics Experiments

Stopped-flow experiments were performed using a KinTek model SF-2001 stopped-flow equipped with a 75W Xenon arc lamp in two-syringe mode. Fluorescein was excited at 488 nm and its emission was monitored at wavelengths > 510 nm using a cut-on filter (Corion). For the two phase kinetics, 10 nM of Fl-pre-$tRNA^{Asp}$ was used for each reaction and the concentration of RNase P varied from 50 nM to 400 nM. The reaction was performed in 50 mM Tris/MES, pH 6.0, 10 mM $CaCl_2$, 200 mM KCl and 20 mM DTT at 25°C. For three phase kinetics, the reaction was initiated by mixing 10 nM Fl-pre-$tRNA^{Asp}$ with 360 nM RNase P holoenzyme under same conditions except 20 mM $MgCl_2$ is substituted for $CaCl_2$. The sum of exponentials (Equation 9) was fit to the transient kinetic time courses, F(t), of three to eight independent determinations to

obtain the fluorescence amplitude (A) and the observed rate constant, k_{obs}, for each exponential phase where F(0) is the initial fluorescence intensity, and t, time:

$$\mathrm{F(t)} = \sum \mathrm{A_n}(\mathrm{e}^{-k_{\mathrm{obs,N}}\mathrm{t}}) + \mathrm{F}(0) \qquad \textbf{Equation 9}$$

For biphasic kinetics, the slope of Equation 10 reflects the apparent bimolecular association rate constant (k_1) for RNase P and pre-tRNA. At saturating RNase P concentration, the plateau value of Equation 11 approximates the sum of the rate constants for the conformational change step (k_2 + k_{-2}).

$$k_{obs,1} \approx k_1[\mathrm{RNase\ P}] + k_{-1} + k_2 + k_{-2} \qquad \textbf{Equation 10}$$

$$k_{obs,2} \approx \frac{k_1[\mathrm{RNase\ P}](k_2 + k_{-2}) + k_{-1}k_{-2}}{k_1[\mathrm{RNase\ P}] + k_{-1} + k_2 + k_{-2}} \qquad \textbf{Equation 11}$$

2.7 References

1. Misra, V.K. and Draper, D.E., *On the role of magnesium ions in RNA stability.* Biopolymers, 1998. **48**(2-3): p. 113-35.
2. DeRose, V.J., *Metal ion binding to catalytic RNA molecules.* Curr Opin Struct Biol, 2003. **13**(3): p. 317-24.
3. Hougland, J.L., et al., *Functional identification of catalytic metal ion binding sites within RNA.* PLoS Biol, 2005. **3**(9): p. e277.
4. Forconi, M., et al., *Functional identification of ligands for a catalytic metal ion in group I introns.* Biochemistry, 2008. **47**(26): p. 6883-94.
5. Pyle, A.M., *Ribozymes: a distinct class of metalloenzymes.* Science, 1993. **261**(5122): p. 709-14.
6. Cate, J.H., et al., *Crystal structure of a group I ribozyme domain: principles of RNA packing.* Science, 1996. **273**(5282): p. 1678-85.
7. Kazantsev, A.V. and Pace, N.R., *Bacterial RNase P: a new view of an ancient enzyme.* Nat Rev Microbiol, 2006. **4**(10): p. 729-40.
8. Smith, J.K., Hsieh, J., and Fierke, C.A., *Importance of RNA-protein interactions in bacterial ribonuclease P structure and catalysis.* Biopolymers, 2007. **87**(5-6): p. 329-38.
9. Kirsebom, L.A., *RNase P RNA mediated cleavage: substrate recognition and catalysis.* Biochimie, 2007. **89**(10): p. 1183-94.
10. Walker, S.C. and Engelke, D.R., *Ribonuclease P: the evolution of an ancient RNA enzyme.* Crit Rev Biochem Mol Biol, 2006. **41**(2): p. 77-102.
11. Hartmann, E. and Hartmann, R.K., *The enigma of ribonuclease P evolution.* Trends Genet, 2003. **19**(10): p. 561-9.
12. Hall, T.A. and Brown, J.W., *The ribonuclease P family.* Methods Enzymol, 2001. **341**: p. 56-77.
13. Guerrier-Takada, C., et al., *The RNA Moiety of Ribonuclease P is the Catalytic Subunit of the Enzyme.* Cell, 1983. **35**(3 Part 2): p. 849-857.
14. Tsai, H.-Y., et al., *Functional reconstitution and characterization of Pyrococcus furiosus RNase P.* Proc Natl Acad Sci U S A, 2006. **103**(44): p. 16147-16152.
15. Kikovska, E., Svärd, S.G., and Kirsebom, L.A., *Eukaryotic RNase P RNA mediates cleavage in the absence of protein.* Proc Natl Acad Sci U S A, 2007. **104**(7): p. 2062-2067.
16. Reich, C., et al., *Role of the protein moiety of ribonuclease P, a ribonucleoprotein enzyme.* Science, 1988. **239**(4836): p. 178-181.
17. Evans, D., Marquez, S.M., and Pace, N.R., *RNase P: interface of the RNA and protein worlds.* Trends Biochem Sci, 2006. **31**(6): p. 333-41.
18. Gößringer, M., Kretschmer-Kazemi Far, R., and Hartmann, R.K., *Analysis of RNase P Protein (rnpA) Expression in Bacillus subtilis Utilizing Strains with Suppressible rnpA Expression.* Journal of Bacteriology, 2006. **188**(19): p. 6816-6823.
19. Crary, S.M., Niranjanakumari, S., and Fierke, C.A., *The Protein Component of Bacillus subtilis Ribonuclease P Increases Catalytic Efficiency by Enhancing Interactions with the 5,Äò Leader Sequence of Pre-tRNAAsp.* Biochemistry, 1998. **37**(26): p. 9409-9416.
20. Kurz, J.C., Niranjanakumari, S., and Fierke, C.A., *Protein component of Bacillus subtilis RNase P specifically enhances the affinity for precursor-tRNAAsp.* Biochemistry, 1998. **37**(8): p. 2393-400.
21. Kurz, J.C. and Fierke, C.A., *The affinity of magnesium binding sites in the Bacillus subtilis RNase P x pre-tRNA complex is enhanced by the protein subunit.* Biochemistry, 2002. **41**(30): p. 9545-58.
22. Sun, L., et al., *Evidence that substrate-specific effects of C5 protein lead to uniformity in binding and catalysis by RNase P.* The EMBO journal, 2006. **25**(17): p. 3998-4007.

23. Sun, L. and Harris, M.E., *Evidence that binding of C5 protein to P RNA enhances ribozyme catalysis by influencing active site metal ion affinity.* Rna, 2007. **13**: p. 1505-1515.
24. Beebe, J.A., Kurz, J.C., and Fierke, C.A., *Magnesium ions are required by Bacillus subtilis ribonuclease P RNA for both binding and cleaving precursor tRNA^{Asp}.* Biochemistry, 1996. **35**(32): p. 10493-505.
25. Christian, E.L., Kaye, N.M., and Harris, M.E., *Evidence for a polynuclear metal ion binding site in the catalytic domain of ribonuclease P RNA.* EMBO J, 2002. **21**(9): p. 2253-62.
26. Hsieh, J., et al., *A divalent cation stabilizes the active conformation of the B. subtilis RNase P x pre-tRNA complex: a role for an inner-sphere metal ion in RNase P.* J Mol Biol, 2010. **400**(1): p. 38-51.
27. Cassano, A.G., Anderson, V.E., and Harris, M.E., *Analysis of solvent nucleophile isotope effects: evidence for concerted mechanisms and nucleophilic activation by metal coordination in nonenzymatic and ribozyme-catalyzed phosphodiester hydrolysis.* Biochemistry, 2004. **43**(32): p. 10547-59.
28. Warnecke, J.M., et al., *Ribonuclease P (RNase P) RNA is converted to a Cd2+-ribozyme by a single Rp-phosphorothioate modification in the precursor tRNA at the RNase P cleavage site.* Proceedings of the National Academy of Sciences of the United States of America, 1996. **93**(17): p. 8924-8.
29. Cuzic, S. and Hartmann, R.K., *Studies on Escherichia coli RNase P RNA with Zn2+ as the catalytic cofactor.* Nucleic Acids Res, 2005. **33**(8): p. 2464-74.
30. Brannvall, M. and Kirsebom, L.A., *Manganese ions induce miscleavage in the Escherichia coli RNase P RNA-catalyzed reaction.* J Mol Biol, 1999. **292**(1): p. 53-63.
31. Smith, D., et al., *Influence of metal ions on the ribonuclease P reaction. Distinguishing substrate binding from catalysis.* J Biol Chem, 1992. **267**(4): p. 2429-36.
32. Smith, D. and Pace, N.R., *Multiple magnesium ions in the ribonuclease P reaction mechanism.* Biochemistry, 1993. **32**(20): p. 5273-81.
33. Perreault, J.P. and Altman, S., *Pathway of activation by magnesium ions of substrates for the catalytic subunit of RNase P from Escherichia coli.* J Mol Biol, 1993. **230**(3): p. 750-6.
34. Pan, T., *Higher order folding and domain analysis of the ribozyme from Bacillus subtilis ribonuclease P.* Biochemistry, 1995. **34**(3): p. 902-909.
35. Loria, A. and Pan, T., *Domain structure of the ribozyme from eubacterial ribonuclease P.* Rna, 1996. **2**: p. 551-563.
36. Kazantsev, A.V., et al., *Crystal structure of a bacterial ribonuclease P RNA.* Proceedings of the National Academy of Sciences of the United States of America, 2005. **102**(38): p. 13392-13397.
37. Reiter, N.J., et al., *Structure of a bacterial ribonuclease P holoenzyme in complex with tRNA.* Nature, 2010. **468**(7325): p. 784-9.
38. Loria, A. and Pan, T., *Modular construction for function of a ribonucleoprotein enzyme: the catalytic domain of Bacillus subtilis RNase P complexed with B.subtilis RNase P protein.* Nucleic acids research, 2001. **29**(9): p. 1892-1897.
39. Frank, D.N. and Pace, N.R., *RIBONUCLEASE P: Unity and Diversity in a tRNA Processing Ribozyme.* Annual Review of Biochemistry, 1998. **67**(1): p. 153-180.
40. Christian, E.L., Kaye, N.M., and Harris, M.E., *Helix P4 is a divalent metal ion binding site in the conserved core of the ribonuclease P ribozyme.* RNA, 2000. **6**(4): p. 511-9.
41. Crary, S.M., Kurz, J.C., and Fierke, C.A., *Specific phosphorothioate substitutions probe the active site of Bacillus subtilis ribonuclease P.* RNA, 2002. **8**(7): p. 933-47.
42. Christian, E.L., et al., *The P4 metal binding site in RNase P RNA affects active site metal affinity through substrate positioning.* RNA, 2006. **12**(8): p. 1463-7.

43. Harris, M.E. and Christian, E.L., *Recent insights into the structure and function of the ribonucleoprotein enzyme ribonuclease P.* Current Opinion in Structural Biology, 2003. **13**(3): p. 325-333.
44. Li, X. and Gegenheimer, P., *Ribonuclease P Catalysis Requires Mg2+ Coordinated to the pro-RP Oxygen of the Scissile Bond†.* Biochemistry, 1997. **36**(9): p. 2425-2438.
45. Warnecke, J.M., et al., *Role of metal ions in the hydrolysis reaction catalyzed by RNase P RNA from Bacillus subtilis.* J Mol Biol, 1999. **290**(2): p. 433-45.
46. Pfeiffer, T., et al., *Effects of phosphorothioate modifications on precursor tRNA processing by eukaryotic RNase P enzymes.* Journal of Molecular Biology, 2000. **298**(4): p. 559-565.
47. Persson, T., Cuzic, S., and Hartmann, R.K., *Catalysis by RNase P RNA: unique features and unprecedented active site plasticity.* J Biol Chem, 2003. **278**(44): p. 43394-401.
48. Kazantsev, A.V., Krivenko, A.A., and Pace, N.R., *Mapping metal-binding sites in the catalytic domain of bacterial RNase P RNA.* RNA, 2009. **15**(2): p. 266-276.
49. Schmitz, M. and Tinoco, I., *Solution structure and metal-ion binding of the P4 element from bacterial RNase P RNA.* RNA (New York, N.Y.), 2000. **6**(9): p. 1212-1225.
50. Getz, M.M., et al., *Structural plasticity and Mg2+ binding properties of RNase P P4 from combined analysis of NMR residual dipolar couplings and motionally decoupled spin relaxation.* RNA (New York, N.Y.), 2007. **13**(2): p. 251-66.
51. Koutmou, K.S., et al., *NMR and XAS reveal an inner-sphere metal binding site in the P4 helix of the metallo-ribozyme ribonuclease P.* Proceedings of the National Academy of Sciences, 2010. **107**(6): p. 2479-2484.
52. Hsieh, J. and Fierke, C.A., *Conformational change in the Bacillus subtilis RNase P holoenzyme--pre-tRNA complex enhances substrate affinity and limits cleavage rate.* RNA, 2009. **15**(8): p. 1565-77.
53. Nolan, J.M., et al., *Circularly Permuted tRNAs as Specific Photoaffinity Circularly Probes of Ribonuclease P RNA Structure.* Advancement Of Science, 1993. **261**(5122): p. 762-765.
54. Moore, M. and Sharp, P., *Site-specific modification of pre-mRNA: the 2'-hydroxyl groups at the splice sites.* Science, 1992. **256**(5059): p. 992-997.
55. Perrotta, a.T. and Been, M.D., *A toggle duplex in hepatitis delta virus self-cleaving RNA that stabilizes an inactive and a salt-dependent pro-active ribozyme conformation.* Journal of Molecular Biology, 1998. **279**(2): p. 361-73.
56. Koutmou, K.S., et al., *Protein-Precursor tRNA Contact Leads to Sequence-Specific Recognition of 5' Leaders by Bacterial Ribonuclease P.* J Mol Biol, 2010. **396**(1): p. 195-208.
57. Pan, T. and Sosnick, T.R., *Intermediates and kinetic traps in the folding of a large ribozyme revealed by circular dichroism and UV absorbance spectroscopies and catalytic activity.* Nat Struct Biol, 1997. **4**(11): p. 931-8.
58. Liu, X., Chen, Y., and Fierke, C.A., *A real-time fluorescence polarization activity assay to screen for inhibitors of bacterial ribonuclease P.* Nucleic Acids Res, 2014. **42**(20): p. e159.
59. Koutmou, K.S., Day-Storms, J.J., and Fierke, C.A., *The RNR motif of B. subtilis RNase P protein interacts with both PRNA and pre-tRNA to stabilize an active conformer.* RNA (New York, N.Y.), 2011. **17**(7): p. 1225-1235.
60. Gutfreund, H., *Kinetics for the Life Sciences: Receptors, Transmitters and Catalysts*. 1995: Cambridge University Press.
61. Johnson, K.A., *Transient-State Kinetic Analysis of Enzyme Reaction Pathways*, in *The Enzymes*, David, S.S., Editor. 1992, Academic Press. p. 1-61.
62. Pecoraro, V.L., Hermes, J.D., and Cleland, W.W., *Stability constants of Mg2+ and Cd2+ complexes of adenine nucleotides and thionucleotides and rate constants for formation and dissociation of MgATP and MgADP.* Biochemistry, 1984. **23**(22): p. 5262-71.

63. Peracchi, A., et al., *Rescue of abasic hammerhead ribozymes by exogenous addition of specific bases.* Proc Natl Acad Sci U S A, 1996. **93**(21): p. 11522-7.
64. Behrman, E.J., *An improved synthesis of guanosine 5'-monothiophosphate.* Journal of Chemical Research (Synopses), 2000. **2000**(9): p. 446-447.
65. He, B., et al., *Rapid mutagenesis and purification of phage RNA polymerases.* Protein Expr Purif, 1997. **9**(1): p. 142-51.
66. Niranjanakumari, S., et al., *Protein component of the ribozyme ribonuclease P alters substrate recognition by directly contacting precursor tRNA.* Proc Natl Acad Sci U S A, 1998. **95**(26): p. 15212-7.
67. Niranjanakumari, S., Kurz, J.C., and Fierke, C.A., *Expression, purification and characterization of the recombinant ribonuclease P protein component from Bacillus subtilis.* Nucleic Acids Res, 1998. **26**(13): p. 3090-6.
68. Rueda, D., et al., *The 5' Leader of Precursor tRNA(Asp) Bound to the Bacillus subtilis RNase P Holoenzyme Has an Extended Conformation.* Biochemistry, 2005. **44**(49): p. 16130-9.
69. Moore, M.J. and Query, C.C., *Joining of RNAs by splinted ligation.* Methods Enzymol, 2000. **317**: p. 109-23.
70. Kurschat, W.C., et al., *Optimizing splinted ligation of highly structured small RNAs.* RNA, 2005. **11**(12): p. 1909-14.
71. Ke, A. and Doudna, J.A., *Crystallization of RNA and RNA-protein complexes.* Methods, 2004. **34**(3): p. 408-14.
72. Mocz, G., et al., *Probing the nucleotide binding sites of axonemal dynein with the fluorescent nucleotide analogue 2'(3')-O-(-N-Methylanthraniloyl)-adenosine 5'-triphosphate.* Biochemistry, 1998. **37**(27): p. 9862-9.

CHAPTER 3
VISUALIZING THE TRANSIENT STATE OF THE P4 HELIX FROM *BACILLUS SUBTILIS* RNASE P[1]

3.1 Abstract

Ribonuclease P (RNase P) is an endonuclease that catalyzes the 5' end maturation of precursor-tRNA (pre-tRNA). In the kinetic pathway of bacterial RNase P, a conformational change occurs in the RNase P - pre-tRNA complex. P4 helix, the most highly conserved region in RNase P RNA, is essential for RNase P activity. Direct involvement of the P4 in conformational change step could be important for RNase P catalysis. To investigate this conformational change, I measured the dynamics of a stem-loop RNA that serves as a model for the *Bacillus subtilis* RNase P helix P4 (P4 helix mimic). Using ^{13}C and ^{15}N $R_{1\rho}$ relaxation dispersion NMR experiments, I probed the existence of alternate conformers in the P4 helix mimic. The significant $R_{1\rho}$ relaxation dispersion, indicative of chemical exchange, was observed in and around the bulged U7 (mimicking U51) and three adenines (A-tract) regions. A two-state off-resonance analysis of the data reveals a shared transient state (TS) for the helix and an independent TS on U7. By using mutagenesis, chemical modification, drug and metal ion titration, thermodynamics study and a computational MCSYM-LARMORD approach,

[1] Data in Chapter 3 and Chapter 4 are in preparation for a manuscript entitled "RNA dynamics reveals the conformational change of catalytic RNA" by Yu Chen, Aaron T. Frank, Huiqing Zhou, Katja Petzold, Xin Liu, Ryszard Kierzek, Charles L. Brooks III, Hashim M. Al-Hashim and Carol A. Fierke.

the structure of the TS was examined and a 3D model of the TS was propsed. In this model, A-tract region unwinds and G6 changes from *anti* conformation to *syn*. This leads to kink formation of the backbone between A5 and G6 that creates a favorable binding pocket for metal ion coordination. The other process is involved in U7 flipping in and out of the helix independently with a relatively faster motion compared with the shared TS. This TS is only detectable in the presence of high concentration of Mg^{2+} suggesting it is either metal ion dependent or Mg^{2+} slows the exchange rate consent to the time scale of experiment detection. This study demonstrates a transient conformer of the P4 helix mimic, which includes two processes, and for the first time identifies a transient *syn* base in an RNA helix. The TS of the P4 helix mimic visualized here provides structural insights for metal ion binding sites and conformational change step during RNase P catalysis.

3.2 Background

RNAs perform widespread roles in cells, such as RNA splicing and modification, transcriptional and translational gene expression regulation and carrying out catalysis reaction [1-5]. Even though RNA can form into intricate three-dimensional structures [6-8], most of the functional complexity is not only due to the stationary structures but also derived from conformational changes, which are always induced by environmental factors, including such as changes of temperature, binding cofactors and recognition of protein or nucleic acid [9, 10]. The dynamical properties of RNA structures play an important role in such adaptive conformational change [11].

To understand how an RNA molecule executes a particular function in cells, it requires studying the structural conformation related to the function and characterize RNA dynamics. Nuclear magnetic resonance (NMR) is an indispensible tool for the determination of RNA structure and dynamics, as it is the only experimental technique that offers resolution of biomolecules in solution at atom level [12-17]. Nearly half of all 3D RNA structures have been solved by NMR spectroscopy [18]. The information of RNA molecule can be derived from NMR including base pairing pattern, secondary structure motifs, metal ion and ligand binding, interaction with other molecules and local and global dynamics [18]. The dynamics of RNA results in a transient, low populated conformer, which includes the secondary structure rearrangement in base pairing, sugar puckering, metal ion and small molecule binding and RNA architecture altering [19-22]. These dynamic processes usually occur on microsecond-to-second time scales [23]. The characterization of low abundance and structures with short lifetimes is difficult using traditional approaches. One way to detect RNA dynamics at this time scales is to use an experiment approach called NMR rotating frame ($R_{1\rho}$) relaxation dispersion methods. Relaxation dispersion NMR spectroscopy is one technique that can be used to site-specifically quantify chemical exchange occurring on microsecond-to-millisecond time scales [14-16, 24-27]. In addition to providing information about the population and lifetime of the transient, low populated conformer (transient state), this approach provides the NMR chemical shift of the transient state which can in turn be used to obtain insights into its biological function [14-16, 25, 26].

RNase P is a ribonucleoprotein enzyme that catalyzes the hydrolysis of a specific phosphodiester bond in all precursor tRNAs (pre-tRNAs), generating mature tRNAs with

a phosphate at the 5'-end [28-30]. In most organisms, RNase P is composed of one conserved catalytic RNA subunit (PRNA) and a varying number of protein subunits (P protein) depending on the organism [31-33]. The RNA subunit of RNase P is essential for activity. It can mediate pre-tRNA 5'-end cleavage at the correct position in the absence of P protein *in vitro* [34-36]. Therefore, RNase P is characterized as a ribozyme.

The kinetics studies of RNase P suggest a two-step binding mechanism where RNase P and pre-tRNA associate to form a complex in a near diffusion-limited process followed by an metal ion dependent isomerization in the enzyme-substrate complex referred to as the conformational change step [37, 38]. Conformational change enhances the affinity of substrate and likely includes formation of specific interactions between the pre-tRNA leader and the P protein in the RNase P - pre-tRNA complex [38-40]. This conformational change is proposed to strengthen the efficiency and fidelity of pre-tRNA cleavage by reorganizing the active site of RNase P complex [38, 39].

The P4 helix is the most highly conserved region in PRNA [41]. The crystal structure of *Thermotoga maritima* RNase P in complex with mature tRNA and 5'leader revealed that the P4 helix is positioned at the core of the enzyme and is ideally situated to interact with both the P protein and substrate simultaneously [42]. The P4 helix is essential for RNase P activity and has been demonstrated to contain catalytic and/or cocatalytic metal ion binding sites [43-45]. For example, the non-bridging phosphoryl oxygens at A49 and G50 in the P4 helix of *Bacillus subtilis* RNase P (A67 and G68 in *Escherichia coli*) form inner-sphere coordination with catalytic metal ions [43, 44, 46]. The carbonyl oxygen-4 (O4) of the conserved uridine (U51, *B. subtilis* numbering) in the

helix P4 directly coordinates the catalytic metal ion in the crystal structure [42] (Xin Liu, Yu Chen, and Carol A. Fierke, manuscript in preparation). As measured by fluorescence stopped-flow and time-resolved fluorescence resonance energy transfer (trFRET) experiments, the conformational change is observed for the catalytic domain (C-domain) (John Hsieh and Carol A. Fierke, unpublished data). Since P4 is located in C-domain and proposed to be the active site of RNase P catalysis, following substrate recognition, the direct involvement of the P4 in catalysis could require a conformational change that allow the structural requirements to be dynamically satisfied by the enzyme.

The current available structures of RNase P are unlikely in the active conformation. The solution structure of *Bacillus stearothermophilus* PRNA shows an unfulfilled contacts with substrate and the crystal structure of PRNA is inconsistent with *in vitro* studies, suggesting the conformation of RNase P may change upon P protein, metal ions and substrate binding [28, 47, 48]. The most recent *T. maritima* RNase P holozenzyme crystal structure is a tertiary complex with matured tRNA and cleavage product pre-tRNA 5' leader, but not substrate, pre-tRNA [42]. It represents the complex after RNase P catalysis and presumably does not reflect the active conformation. Furthermore, the metal ion binding sites identified in the crystal structure are characterized by soaking in Eu^{2+} and Sm^{3+}, instead of the catalytic divalent metal ions, such as Mg^{2+}, Mn^{2+} or Ca^{2+} [42]. Therefore, it raises the uncertainty about the binding sites for catalytic/co-catalytic metal ion in active conformation. Nevertheless, an NMR study on a mutant P4 helix stem-loop mimic suggests the highly conserved U7 (U51 in *B. subtilis* RNase P), which coordinates an inner-sphere metal ion, and helical residue

C8 are locally mobile on picosecond-to-nanosecond time scales indicating the existence of functionally important fast internal motions in the P4 helix [49].

Therefore, due to the limitation and uncertainty of current crystal structures and lack of information regarding the flexibility of the P4 helix in RNase P and its role in conformational change, it is important to ask the question whether P4 helix is involved in the conformational change of RNase P - pre-tRNA complex. If so, discerning this structural change and identifying its function related to RNase P catalysis are also remaining problems to solve.

In order to determine whether P4 helix participates the conformational change in RNase P catalysis, I studied the structural dynamics of a stem-loop RNA that serves as a model for the *B. subtilis* RNase P helix P4 (P4 helix mimic) and probed the existence of the alternative conformer of the P4 helix mimic. Here, I applied $R_{1\rho}$ ^{13}C and ^{15}N relaxation dispersion to identify the low populated, transient state of the P4 helix mimic and characterize the structure by a combination of mutagenesis, chemical modification, drug and metal ion titration, and thermodynamics analysis. A 3D structure model of the transient state is built by using MCSYM-LARMORD approach [50] and this transient conformer is proposed to facilitate metal ion binding. The dynamics of the P4 helix mimic visualized here provides structural insights for metal ion binding sites and conformational change step during RNase P catalysis.

3.3 Results

To probe the existence of the transient state of the P4 helix mimic, the secondary structure was characterized by ^{1}H-^{1}H NOESY, 2D ^{13}C-^{1}H and ^{15}N-^{1}H HSQC and $R_{1\rho}$ ^{13}C

and ^{15}N relaxation dispersion was applied to C2, C6/C8 and N1/N3 to detect the transient state at different temperatures and pHs. The further structural insight of the ground state and the transient state were investigated by using mutagenesis, atom modification, drug titration and metal titration. By using MCSYM-LARMORD approach [50], a 3D model of both ground state and the transient state was built.

3.3.1 Secondary Structure of the P4 Helix Mimic

In the previous published *B. subtilis* P4 helix stem-loop mimic, there are three A-U base pairs at the bottom of the P4 [49, 51]. According to the secondary structure of *B. subtilis* PRNA, there is an extra uridine in this P4 construct [52]. Therefore, by deleting one uridine I designed a new P4 helix mimic, which better resembles the P4 helix compared with the previous P4 mimic (Mutant P4) (Figure 2-1 in Chapter 2, Figure 3-1).

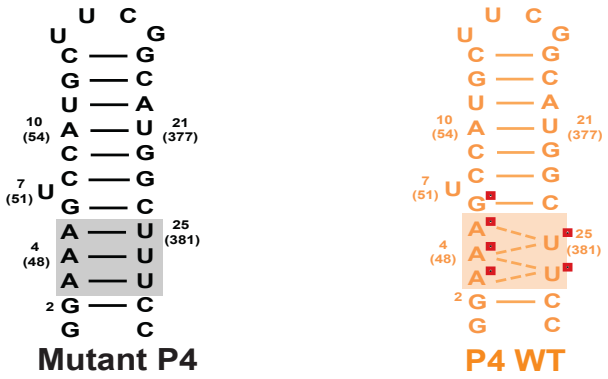

Figure 3-1: Comparison of the secondary structures between previous reported P4 helix mimic (mutant P4) [49] and the construct used in this study (WT P4). The sequence difference of two constructs is indicated in box. Residues with chemical shifts that are significantly different from the mutant P4 construct are highlighted by squares. The numbering of the P4 helix in *B. subtilis* full-length PRNA is given in parentheses.

The ^{1}H, ^{13}C, and ^{15}N resonances were assigned using standard NMR experiments employing uniformly $^{13}C/^{15}N$ labeled P4 helix mimic [53]. The NOE walk between

exchangeable protons was traced from G6 to G18 without interruption to assign all detected imino resonances of guanosines and uridines (Figure 3-2A). The imino resonance of G1 was not detected and G2 slightly exchange broadened due to end-fraying effects. The imino resonances of U25 and U26 were significantly broadened and not observed. The NOE walk between non-exchangeable protons was also uninterrupted from G1 to C28, indicating a continuous helical conformation, while the NOE walk was interrupted at the G6–U7 is consistent with bulged uridine (Figure 3-2B). 2D HCN experiments were also used to assign base and sugar resonances (Figure 3-2C). The proton assignments were then correlated with the carbon and nitrogen spins using 2D HSQC experiments (Figure 3-2C, D, E, F).

Comparison of chemical shifts of 2D ^{13}C-^{1}H HSQC between P4 WT and mutant P4 shows very good agreement for the U7 bulge (mimicking of U51) and helix above U7. The bulged U7 is confirmed by the significant downfield-shift of the U7C6 (Figure 3-2C) and higher peak intensity (Figure B-1) indicative of fast internal motions as observe before [49]. It is also consistent with both solution and crystal structures showing the universally conserved uridine (U51) is bulged out in RNase P [42, 47, 48]. The expected differences were observed near the site of the deleted uridine (Figure 3-2C). For the guanosine (G6) below the bulged U7, chemical shift perturbation on both sugar C1' (upfield-shifted) and nucleobase C8 (downfield-shifted) were observed for the new construct, but G6 and C24 still stay base paired same as in the mutant P4 (Figure 3-2C) [49]. Unlike other guanosines in the helix, the sugar C1' chemical shift of G6 is consistent with C2'-endo sugar pucker rather than C3'-endo sugar pucker (Figure 3-2C). Furthermore, deletion of one uridine at the bottom of the helix destabilizes the Watson-

Crick A-U base pairs observed before in mutant P4 [49]. There were only very weak imino protons observed for U25 and U26 on 2D ^{15}N-^{1}H HSQC, and no imino resonances observed on exchangeable NOESY (Figure 3-2F) suggesting unstable hydrogen bonds forming between these three adenosines and two uridines. C8 of the three adenosines also showed upfield-shifted compared with mutant P4, but they still stay in helical formation since they have similar chemical shift compared with A10 and A20 which form stable helix (Figure 3-2C). This is different from the P4 as seen in crystal structure, instead of the three adenosines all staying helical, a bulged adenosine (A4 in the P4 helix mimic, A48 in *B. subtilis* PRNA) was observed in crystal structure [42, 48]. This could be attributed to the tertiary interaction in the PRNA stabilizing the bulge conformation of A48 but not in the isolated P4 helix stem-loop mimic. However in the solution structure probing using 2'-hydroxyl acylation analyzed by primer extension (SHAPE) indicates that the A48 is solvent exposed in *Agrobacterium tumefaciens*, but not in *B. stearothermophilus* or *Escherichia coli* [47]. It raises the uncertainty of the adenosine conformation.

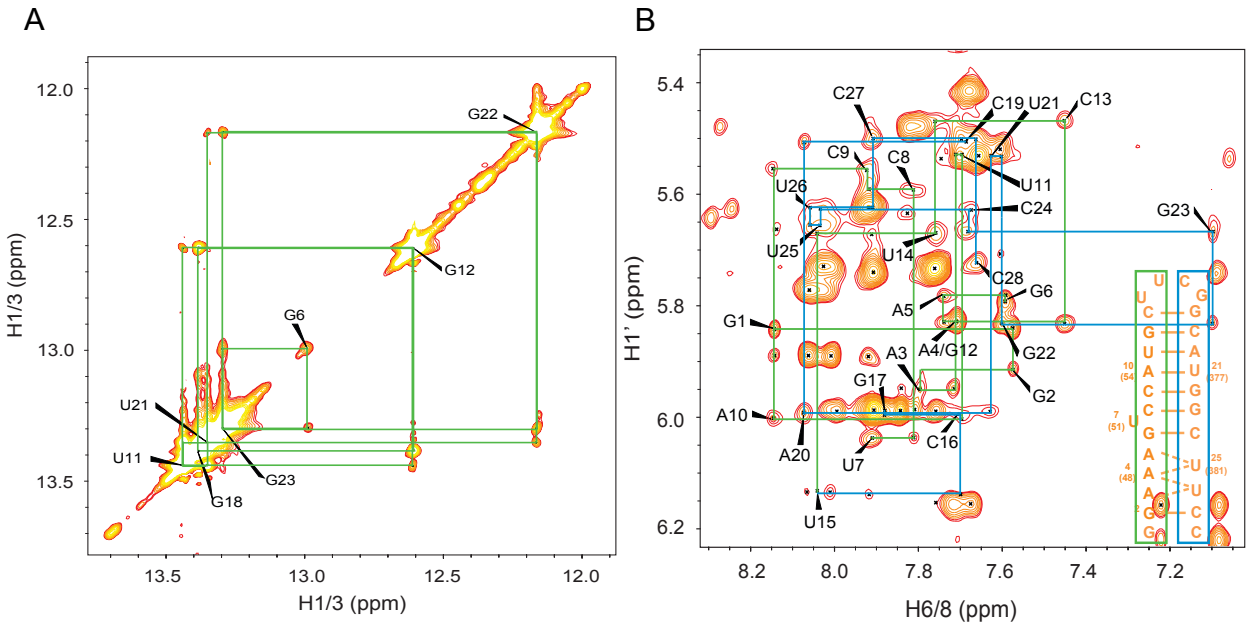

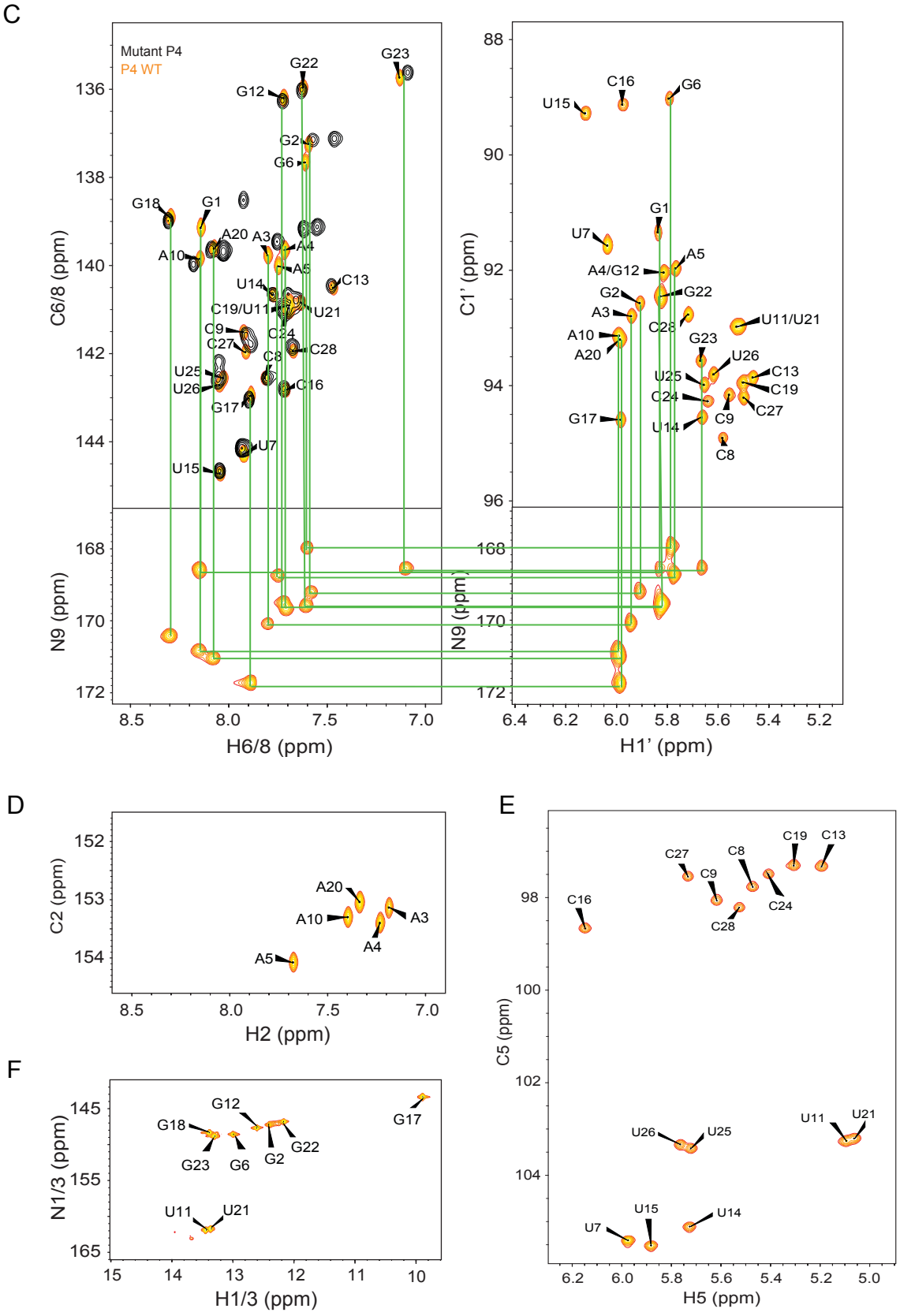
C
Mutant P4
P4 WT
C6/8 (ppm)
N9 (ppm)
H6/8 (ppm)
C1' (ppm)
H1' (ppm)
D
C2 (ppm)
H2 (ppm)
E
C5 (ppm)
H5 (ppm)
F
N1/3 (ppm)
H1/3 (ppm)

Figure 3-2: Resonance assignments of the P4 helix mimic from *B. subtilis* PRNA. The data were collected in the buffer condition of 15 mM NaH_2PO_4, 25 mM NaCl and 0.1 mM EDTA under pH 6.8 at 25°C with 2.3 mM of the P4 WT. **(A**) Exchangeable ^{1}H-^{1}H NOESY correlation of the P4 WT showing imino walk from residue G6 to G18. **(B)** Non-exchangeable ^{1}H-^{1}H NOESY correlation of the P4 WT showing nucleobase H6/8 to sugar H1' NOE walk. The connectivity from residue G1 to U15 is shown in green and U15 to C28 is in blue. **(C)** P4 WT 2D ^{13}C-^{1}H HSQC spectra showing nucleobase C6/8-H6/8 and sugar C1'-H1' correlation; ^{15}N-^{1}H HCN spectra showing their corresponding intra-residue N9 peaks of all the guanosines and adenosines. The comparison of mutant P4 (black) and WT P4 (orange) is shown by overlay of their 2D ^{13}C-^{1}H aromatic HSQC resonances. **(D)** P4 WT 2D ^{13}C-^{1}H HSQC spectra showing C2 and H2 correlation. **(E)** P4 WT 2D ^{13}C-^{1}H HSQC spectra showing C5 and H5 correlation. **(F)** P4 WT 2D ^{15}N-^{1}H imino HSQC spectra showing nitrogen/proton (N1/3-H1/3) correlation.

3.3.2 Relaxation Dispersion Reveals a Shared Transient, Low Populated State of the P4 Helix Mimic

I used ^{13}C and ^{15}N $R_{1\rho}$ relaxation dispersion NMR experiments to probe for the existence of the transient, low populated state in the P4 helix mimic. While the upper helix of the P4 (above C8-G23 base pair) stays stable between the ground, high populated state (GS) and the transient, low populated state (TS) (Figure B-2), I observed significant $R_{1\rho}$ relaxation dispersion, indicative of chemical exchange, on sugar (C1') and nucleobase carbon sites (C2, C6 and C8) in and around the conserved bulged U7 and three adenosines (A-tract) regions (Figure 3-3B, Figure B-2).

A two-state off-resonance analysis (Equation 12) was applied to each nucleus individually to obtain the populations and lifetimes of the GS and the TS, as well as chemical shift changes between two states. The similarity on the populations and lifetimes were observed among the nuclei in and around the conserved bulged U7 and three adenosines (A-tract) regions revealing a shared TS with altered chemical shifts at the lower helix (below and include C8-G23 base pair) (Table B-5). The data was then fit globally with shared TS population (p_{TS}) and exchange rate constant (k_{ex}) (Equation 12)

among all the residues but allowed to float, while all other parameters were allowed to vary individually (Table 3-1). The best-fit model was determined using F-statistics at the 95% confidence level. The results of global fitting and F-test statistics are consistent with a single TS existing in the P4 helix mimic (Table 3-1). The TS has a population of ~0.6% and the lifetime of ~465 μs at 25°C (Figure 3-3A) (Table 3-1).

A

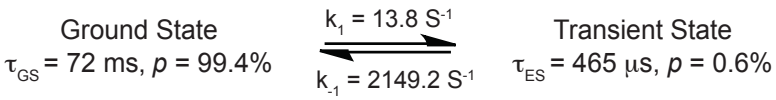

B

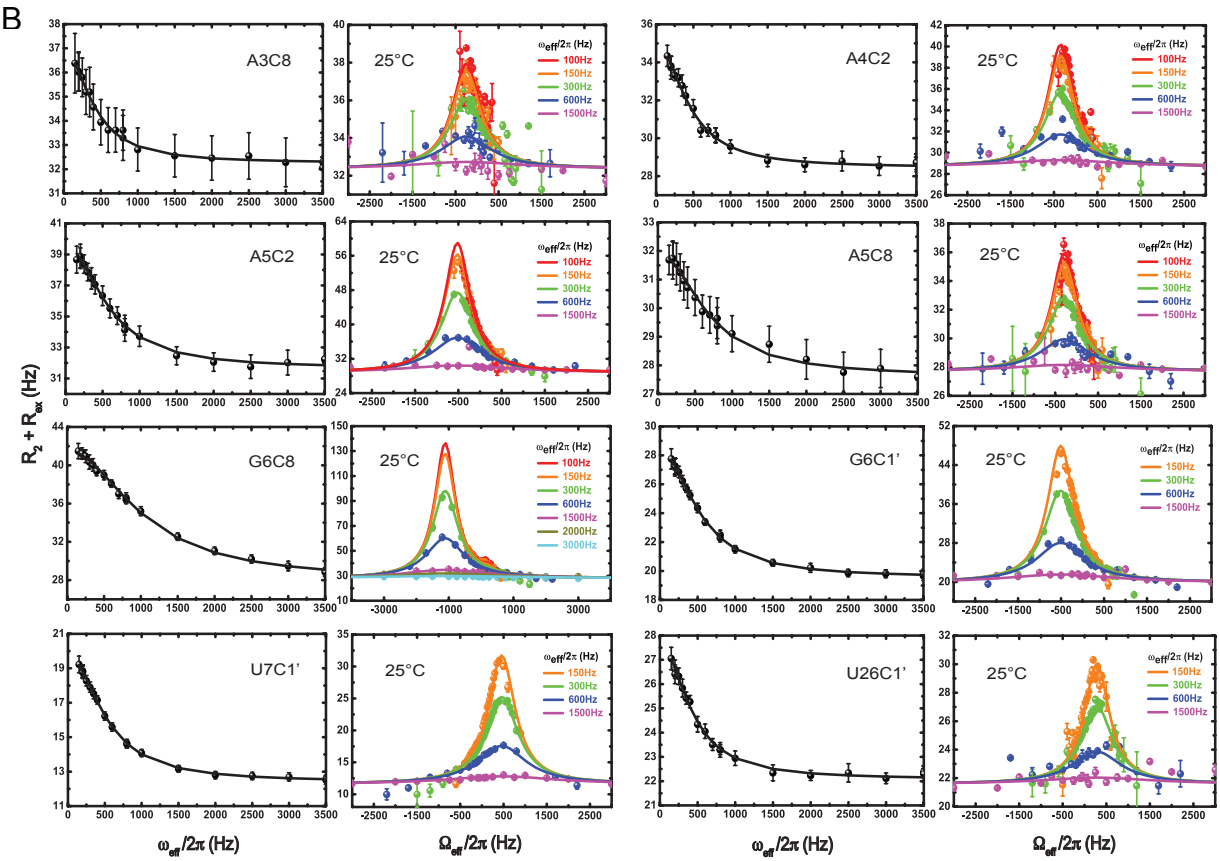

C

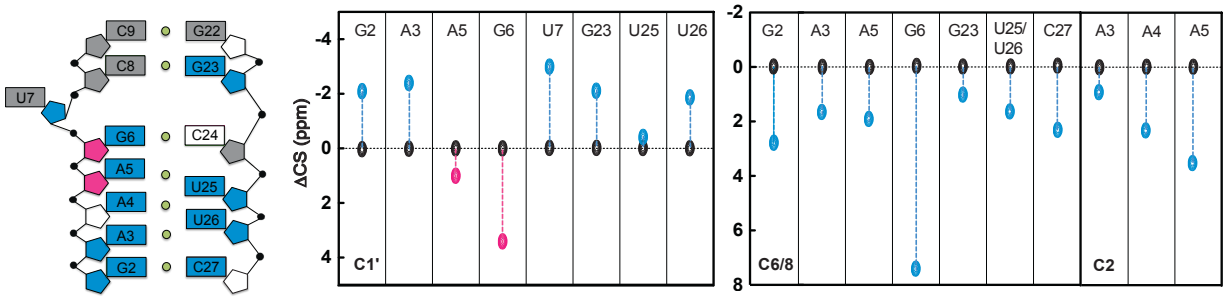

Figure 3-3: Observation of the shared transient state in and around U7 and A-tract of the P4 helix mimic from *B. subtilis* PRNA at the condition of 15 mM NaH_2PO_4, 25 mM NaCl and 0.1 mM EDTA under pH 6.8 at 25°C with 2.3 mM of the P4 WT. **(A)** A scheme of transition between between GS and TS with exchange rate constants and populations. The parameters were obtained by global fits of off-resonance $R_{1\rho}$ relaxation dispersion. **(B**) Reprehensive of on- and off-resonance of $R_{1\rho}$ relaxation dispersion profiles and best fits (solid lines) to a two-state exchange model. All data are included in **Figure B-2**. (**C)** Comparison of the chemical shifts between the GS (black) and the TS (pink, increased stacking or toward to C3'-endo sugar pucker direction; blue, decreased stacking or *syn* glycosidic angle, or toward to non-C3'-endo sugar pucker direction). The corresponding residues are shown in the secondary structure of P4 WT on the left. Sites with little to no exchange are grey and the residues not measured are in blank.

By examining the sugar and base chemical shift change between the GS and the TS ($\Delta\omega = \Omega_{TS} - \Omega_{GS}$), which reports the information regarding sugar pucker, base stacking, and *syn* versus *anti* conformation of glycosidic bond angles, the insights into the TS structure can be obtained. The downfield-shifted bases C6/8 below the bulged uridine in TS (Figure 3-3C) suggest deviations from an A-form helical conformation as compared to the GS. Notably, the large 7.4 ppm downfield chemical shift was observed on G6C8 in TS (Figure 3-3C) strongly suggests a *syn* base. The downfield-shifted G6C1' (Figure 3-3C) could be caused by base flipping to *syn* conformation or it indicates the G6 changes to C3'-endo sugar pucker in TS from an unusual C2'-endo in GS. A downfield-shifted A5C1' in the TS (Figure 3-3C) suggests a more helical conformation on the sugar, while the upfield-shifted sugar C1' for other residues in the lower helix (Figure 3-3C) suggests a less helical conformation, consistent with the downfield-shifted bases

C6/8. There is no significant ^{15}N relaxation dispersion observed on any N1 of guanosine or N3 of uridine (Figure B-2). The reason for no significant relaxation dispersion detected on imino N1H1 of G6 is probably due to the small chemical shift change for the TS on N1H1.

3.3.3 A-tract Stabilizes the Transient State of the P4 Helix Mimic

To further investigate the transient state of the P4 helix, I created a mutant P4 by removing one of the three adenosines at the lower helix (DelA4) (Figure 3-4). The structure of WT P4 and DelA4 mutant show great agreement at the upper helix and bulged U7 while the perturbation was observed at G6 and A-tract region. The NOE walk between exchangeable protons was traced from G2 to G18 without interruption (Figure 3-4A). The detection of NOE walk at U25 and U26 is consistent with strong imino proton peaks of 2D ^{15}N-^{1}H HSQC observed for U25 and U26 (Figure 3-4C) suggesting the stable base pairs formation between A3-U26 and A5-U25, which is different from P4 WT (Figure 3-2B). The NOE walk between non-exchangeable protons was also uninterrupted from G1 to C28 except for G6–U7 and U7-C8 due to the bulged uridine (Figure 3-4B). It indicates the formation of continuous helical. Furthermore, comparing with WT, the upfield-shift of C8 and downfield-shift of C1' of residues at G6 and A-tract (Figure 3-4C) in DelA4 suggest a more helical conformation.

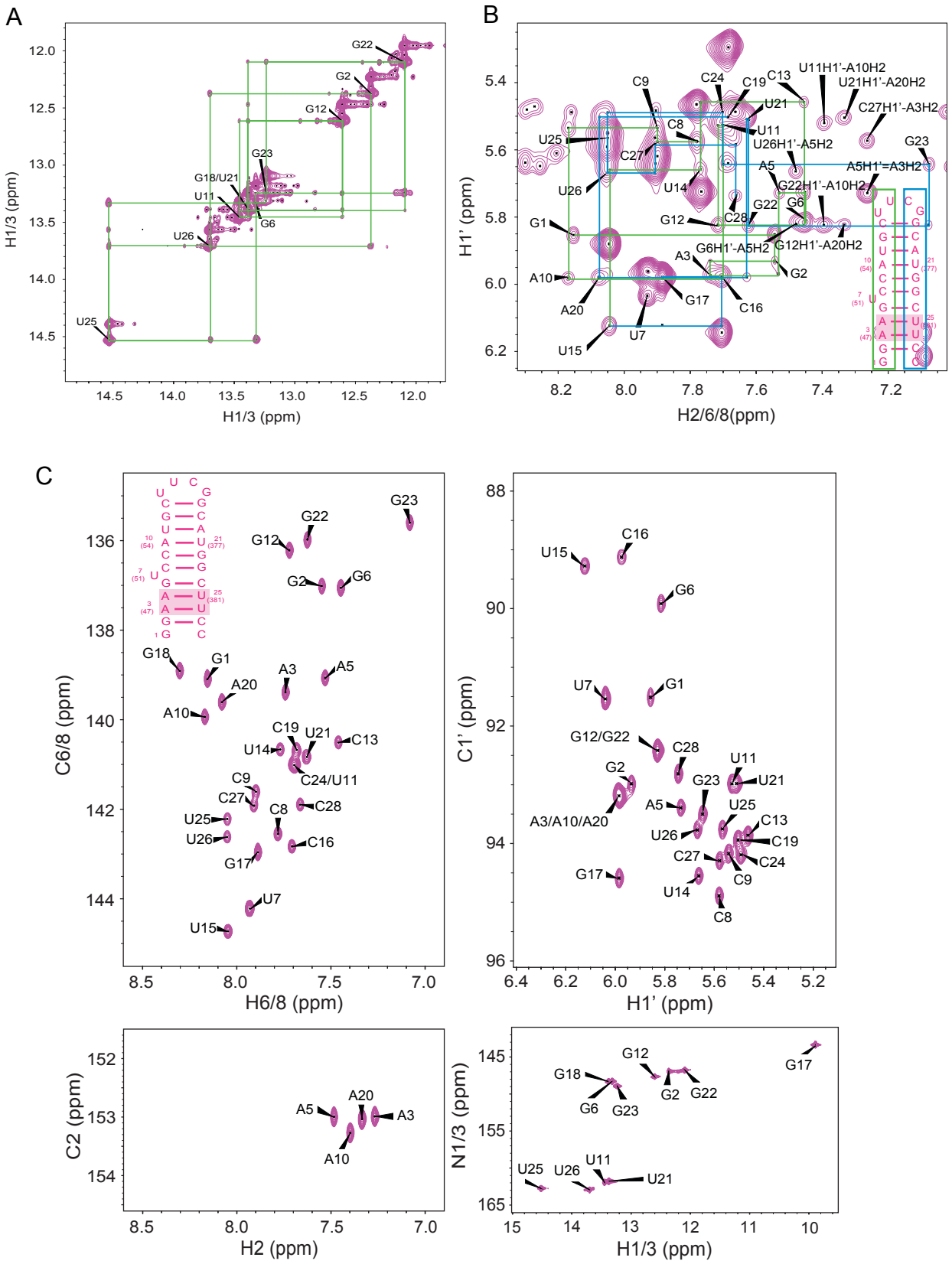
A
H1/3 (ppm)
H1/3 (ppm)
G22
G2
G12
G23
G18/U21
U11
G6
U26
U25
B
H1' (ppm)
H2/6/8(ppm)
C9
C24
C19
C13
U11H1'-A10H2
U21H1'-A20H2
C27H1'-A3H2
U21
C8
U11
U26H1'-A5H2
G23
U25
C27
A5
A5H1'=A3H2
U26
U14
G22H1'-A10H2
G1
G22
G6
G12
C28
G6H1'-A5H2
G12H1'-A20H2
A3
G2
A10
G17
C16
A20
U7
U15
C
C6/8 (ppm)
H6/8 (ppm)
G23
G22
G12
G2
G6
G18
G1
A3
A5
A20
A10
C19
U21
C13
U14
C24/U11
C9
C27
C8
C28
U25
U26
C16
G17
U7
U15
C1' (ppm)
H1' (ppm)
C16
U15
G6
U7
G1
G12/G22
C28
U11
G2
G23
U21
A5
U25
A3/A10/A20
C13
U26
C19
C27
C24
G17
C9
U14
C8
C2 (ppm)
H2 (ppm)
A20
A5
A3
A10
N1/3 (ppm)
H1/3 (ppm)
G12
G17
G18
G2
G22
G6
G23
U25
U26
U11
U21

Figure 3-4: Resonance assignments of DelA4 P4 mutant from *B. subtilis* PRNA. The data were collected in the buffer condition of 15 mM NaH_2PO_4, 25 mM NaCl and 0.1 mM EDTA under pH 6.8 at 25°C with 2.5 mM of DelA4 mutant. **(A)** Exchangeable ^{1}H-^{1}H NOESY correlation of the DelA4 showing imino walk from residue G2 to G18. **(B)** Non-exchangeable ^{1}H-^{1}H NOESY correlation of the DelA4 showing nucleobase H2/6/8 to sugar H1' NOE walk. The connectivity from residue G1 to U15 is shown in green and U15 to C28 is in blue. **(C)** DelA4 2D ^{13}C-^{1}H HSQC spectra showing nucleobase C2/6/8-H2/6/8 and sugar C1'-H1' correlation; ^{15}N-^{1}H imino HSQC spectra showing nitrogen/proton (N1/3-H1/3) correlation. The secondary structure of DelA4 is shown as inset and the sequence different from WT is indicated in box.

To examine the effect of A-tract on the transient state of P4, the $R_{1\rho}$ relaxation dispersion experiments were also performed on DelA4. Surprisingly, by deleting one adenosine, the relaxation dispersion observed on WT were either totally eliminated or significantly diminished (Figure 3-5, Figure B-3). Only small relaxation dispersion was observed on G6C1' and U7C1' (Figure 3-5). Removal of the adenosine influencing all the dispersion observed in and around conserved bulged U7 and A-tract regions further suggests a shared transient state for the P4 helix mimic that requires all three adenosines.

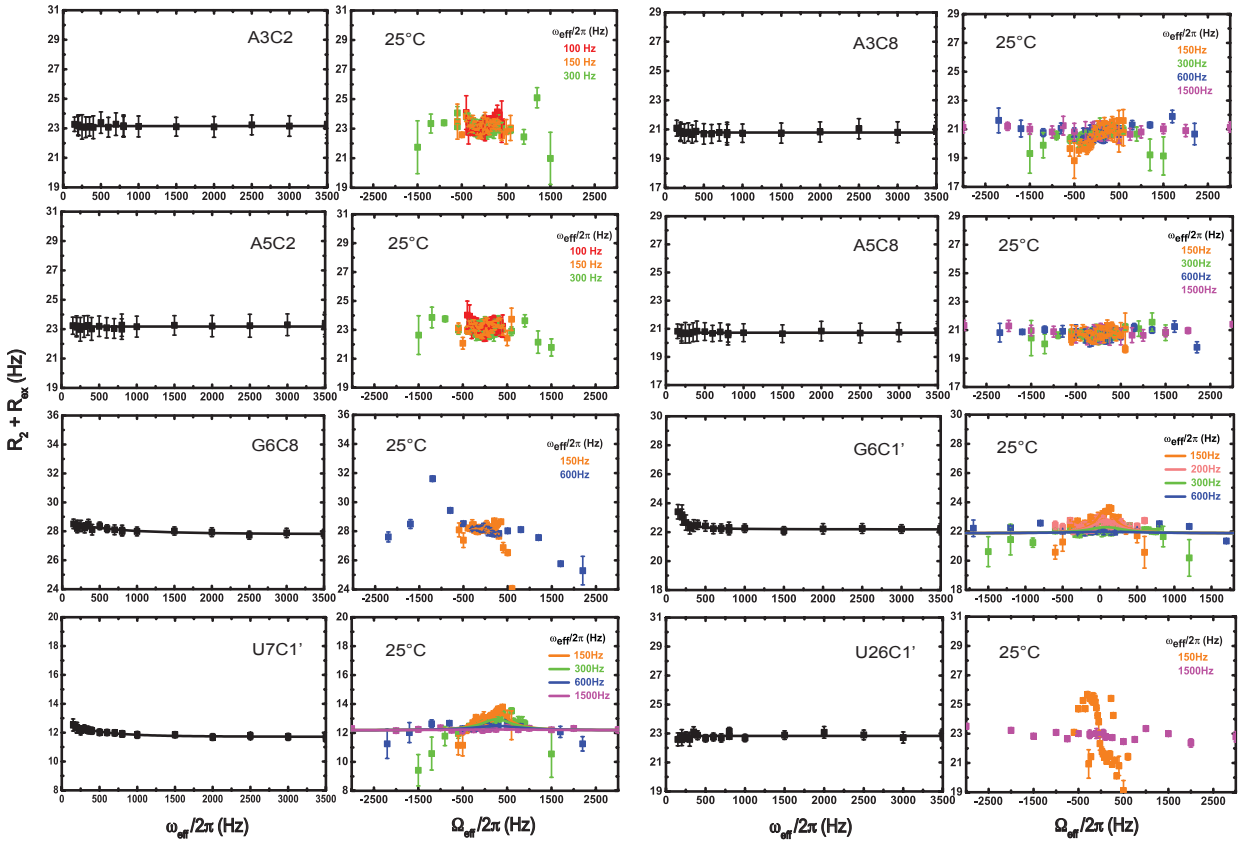

Figure 3-5: DelA4 mutant eliminates relaxation dispersion observed for the P4 WT in and around U7 and A-tract regions. The figures show reprehensive of on- and off-resonance of DelA4 $R_{1\rho}$ relaxation dispersion profiles and best fits (solid lines) to a two-state exchange model. The data were collected at the condition of 15 mM NaH_2PO_4, 25 mM NaCl and 0.1 mM EDTA under pH 6.8 at 25°C with 2.5 mM of DelA4 mutant. All data are included in **Figure B-3**.

3.3.4 Probing the Structure of Transient State of the P4 Helix Mimic

In order to obtain more insights into the structure of transient state of the P4 helix mimic, the different approaches were used to stabilizing the TS, including mutagenesis, small molecule titration and performing temperature and pH dependence of $R_{1\rho}$ relaxation dispersion experiments. By comparing the experimental chemical shift with the proposed chemical shift of potential TS, the structural information of the TS can be obtained.

3.3.4.1 The transient state of the P4 helix mimic is not caused by helix melting

Since the chemical shift change obtained from relaxation dispersion experiments suggests deviations from A-form helical conformation for residues in the lower helix of P4 in the TS, I tested whether the TS represents a duplex melted state (Figure 3-6). I measured $R_{1\rho}$ relaxation dispersion as a function of temperature at 15°C, 25°C and 37°C (Figure 3-7, Figure B-2). Increasing the temperature increased the population of the TS (p_{TS}) and the exchange rate constant (k_{ex}) (Table 3-1). Under these three temperatures, each residue had similar chemical shift changes between the GS and the TS (Table 3-1) suggesting a similar TS structure at the different temperature.

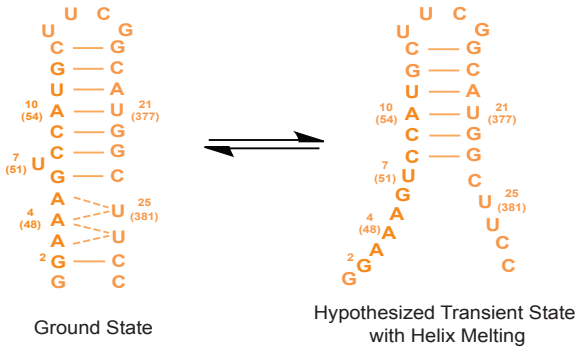

Figure 3-6: Hypothesized transient state of the P4 helix mimic caused by helix melting at bulge

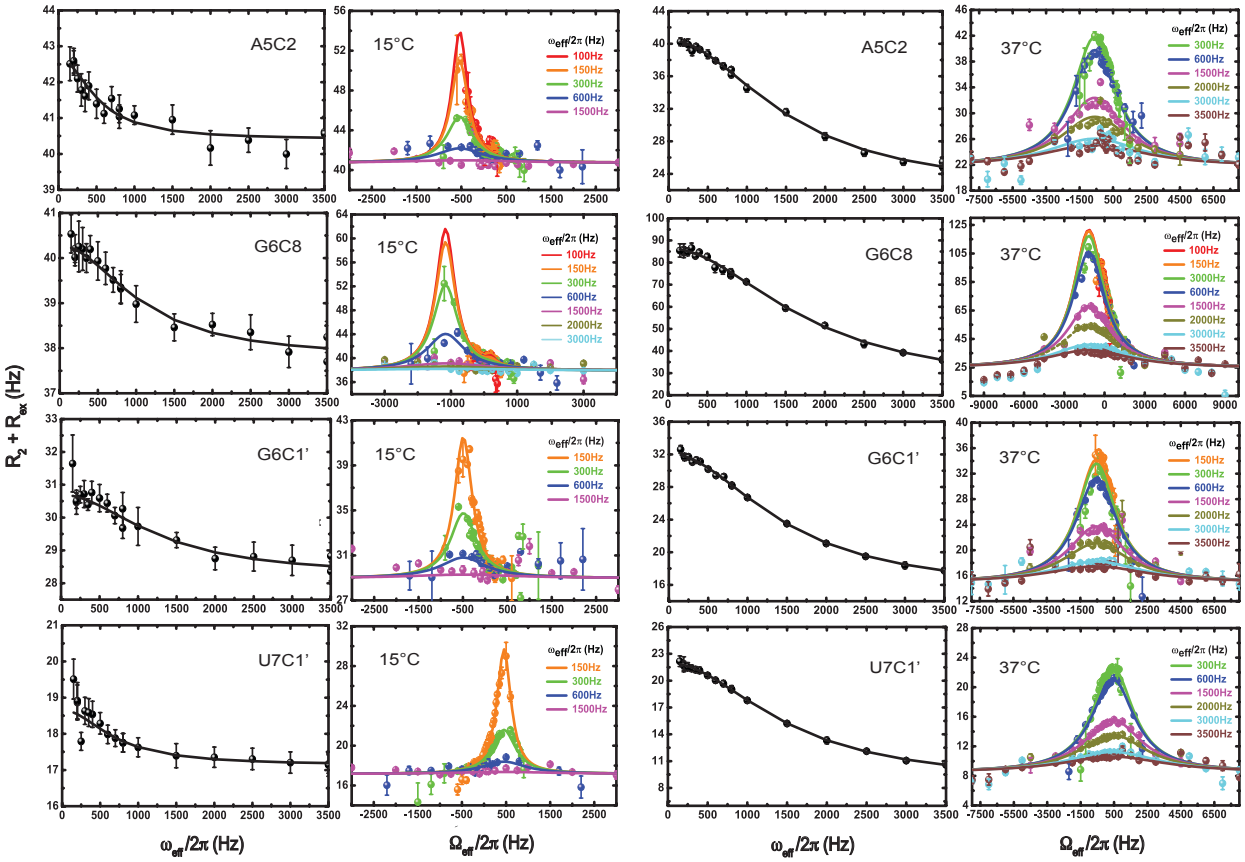

Figure 3-7: Temperature dependence of on- and off-resonance of $R_{1\rho}$ relaxation dispersion profiles for selected residues of the P4 WT and best fits (solid lines) to a two-state exchange model. The data were collected at the condition of 15 mM NaH_2PO_4, 25 mM NaCl and 0.1 mM EDTA under pH 6.8 at 15°C and 37°C with 2.3 mM of the P4 WT. All data are included in **Figure B-2**.

Table 3-1: Global fits of off-resonance $R_{1\rho}$ relaxation dispersion of the P4 helix mimic at 15°C, 25°C and 37°C[a]

T (°C)	Residue	R_1 (Hz)[b]	R_2 (Hz)[b]	p_B (%)[b]	k_{ex} (s^{-1})[b]	Δω (ppm)[b]
15	**A3C1'**	1.43 ± 0.06	34.7 ± 0.09	0.24 ± 0.01	937 ± 73 k_{GS-TS}: 2.2 ± 0.3 k_{TS-GS}: 935 ± 112	-0.9 ± 0.15
	A4C2	1.63 ± 0.07	39.5 ± 0.11			2.2 ± 0.17
	A5C1'	1.48 ± 0.06	32.0 ± 0.10			1.6 ± 0.13
	A5C2	1.51 + 0.07	40.6 ± 0.10			3.5 ± 0.23
	A5C8	1.66 ± 0.07	41.6 ± 0.11			1.9 ± 0.16
	G6C1'	1.61 ± 0.06	29.2 ± 0.09			3.4 ± 0.18
	G6C8	1.51 ± 0.05	38.1 ± 0.07			7.3 ± 0.24
	U7C1'	2.06 ± 0.03	17.1 ± 0.06			-3.1 ± 0.11
	U26C1'	1.38 ± 0.06	29.9 ± 0.09			-1.2 ± 0.11

	G2C1'	1.60 ± 0.10	29.0 ± 0.18			-1.6 ± 0.07
	G2C8	1.98 ± 0.03	30.7 ± 0.08			2.2 ± 0.03
	A3C1'	1.74 ± 0.03	22.7 ± 0.06			-0.9 ± 0.04
	A3C2	2.23 ± 0.03	44.0 ± 0.09			1.2 ± 0.03
	A3C8	1.90 ± 0.03	32.5 ± 0.08			1.5 ± 0.03
	A4C2	1.96 ± 0.02	28.6 ± 0.06			2.1 ± 0.02
	A5C1'	1.83 ± 0.02	21.4 ± 0.08			0.8 ± 0.05
	A5C2	1.99 + 0.03	28.9 ± 0.09		2163 ± 21	3.6 ± 0.04
	A5C8	2.08 ± 0.03	27.7 ± 0.07		k_{GS-TS}:	1.8 ± 0.03
25	**G6C1'**	1.93 ± 0.03	20.0 ± 0.07	0.64 ± 0.01	13.8 ± 0.3	3.6 ± 0.04
	G6C8	1.81 ± 0.04	28.0 ± 0.08		k_{TS-GS}: 2149 ± 54	7.1 ± 0.07
	U7C1'	2.16 ± 0.03	11.6 ± 0.06			-3.0 ± 0.03
	G23C1'	1.44 ± 0.04	22.7 ± 0.09			-0.9 ± 0.04
	G23C8	1.99 ± 0.02	28.7 ± 0.06			0.7 ± 0.03
	U25C1'	1.54 ± 0.05	22.0 ± 0.12			-0.9 ± 0.05
	U25U26C6[c]	2.55 ± 0.04	33.3 ± 0.10			1.4 ± 0.04
	U26C1'	1.82 ± 0.03	21.5 ± 0.07			-1.9 ± 0.02
	C28C6	2.56 ± 0.09	34.2 ± 0.14			1.5 ± 0.07
	G2C8	2.21 ± 0.16	20.7 ± 0.27			2.7 ± 0.09
	A3C1'	1.87 ± 0.09	16.3 ± 0.44			-0.8 ± 0.18
	A3C8	2.36 ± 0.08	21.4 ± 0.14			1.3 ± 0.06
	A3A4C2[c]	2.16 ± 0.10	24.1 ± 0.15			1.6 ± 0.06
	A5C1'	1.91 ± 0.09	15.0 ± 0.41		8502 ± 190	0.8 ± 0.19
	A5C2	1.97 + 0.17	22.7 ± 0.27		k_{GS-TS}:	3.4 ± 0.09
37	**A5C8**	2.55 ± 0.11	20.4 ± 0.17	1.66 ± 0.01	141 ± 4	1.8 ± 0.06
	G6C1'	2.11 ± 0.09	14.9 ± 0.22		k_{TS-GS}: 8361 ± 237	3.3 ± 0.09
	G6C8	2.29 ± 0.41	21.8 ± 0.85			7.9 ± 0.25
	U7C1'	2.26 ± 0.06	8.74 ± 0.15			-2.9 ± 0.07
	U25U26C6[c]	2.95 ± 0.17	25.8 ± 0.58			0.6 ± 0.37
	U26C1'	2.07 ± 0.19	16.4 ± 0.29			-1.9 ± 0.10

[a] The experiments were performed in 15 mM NaH_2PO_4, 25 mM NaCl and 0.1 mM EDTA at pH 6.8 with 2.3 mM of the P4 WT.
[b] The data were fit to a two-state Laguerre equation (Equation 12) to obtain the values of all the parameters.
[c] The resonance was overlapped in the 2D ^{13}C-^{1}H HSQC for those residues.

Then I used transition-state theory and Van't Hoff analysis to obtain the thermodynamics parameters of the two-state equilibrium based on the global fitting of the relaxation dispersion (Table 3-2, Equation 13). Van't Hoff plots show a linear dependence characteristic of the two-state process (Figure 3-8A). The analysis yields the free energy of ~ 24 kcal/mol and enthalpy of ~ 35 kcal/mol for forward transition (GS to TS) and the free energy of ~ 21 kcal/mol and enthalpy of ~ 17 kcal/mol for backward transition (TS to GS). By using the combination of transition-state theory and Van't Hoff analysis, the temperature where the population of the GS and the TS are both 50% is also calculated and this NMR midpoint temperature is 94.5 ± 22.2°C (Equation 14).

To determine if the TS is due to melting, the UV (ultraviolet absorbance) melting experiments were conducted and the melting temperature of the P4 helix mimic was compared with the NMR midpoint temperature. Two melting temperature were observed, ~57.5°C and ~75.5°C, the lower melting temperature is probably due to the melting of the lower helix and the higher one is for the entire helix melting. Both of the melting temperatures are lower than the NMR midpoint temperature (Figure 3-8B). The inconsistence between the midpoint temperature obtained from relaxation dispersion and UV melting temperature suggests the TS of the P4 helix mimic is unlikely caused by melting.

Table 3-2: Thermodynamics parameters for the transition between GS and TS of the P4 helix mimic[a]

Residue	ΔG^{T}_{GS-TS}[b]	ΔG^{T}_{TS-GS}[b]	ΔH^{T}_{GS-TS}[b]	ΔH^{T}_{TS-GS}[b]
Global fitting	24.01 ± 0.04	21.02 ± 0.06	33.05 ± 1.40	17.15 ± 1.89
A5C2	24.05 ± 0.01	20.95 ± 0.10	33.50 ± 0.02	16.61 ± 3.42
A5C8	23.92 ± 0.14	20.98 ± 0.08	32.51 ± 4.83	15.82 ± 2.58
G6C1'	23.97 ± 0.04	20.97 ± 0.10	29.69 ± 1.38	15.40 ± 3.18
G6C8	24.06 ± 0.04	20.84 ± 0.16	32.69 ± 13.3	10.68 ± 5.17

U7C1'	23.99 ± 0.06	21.05 ± 0.03	33.76 ± 1.97	19.39 ± 1.08
U26C1'	23.70 ± 0.30	20.97 ± 0.12	25.24 ± 9.83	18.68 ± 4.06

[a] The experiments were performed in 15 mM NaH_2PO_4, 25 mM NaCl and 0.1 mM EDTA under pH 6.8 at 15°C, 25°C and 37°C with 2.3 mM of the P4 WT.
[b] The data were fit by Van't Hoff analysis (Equation 13) using the global fits and best fits of experimentally derived rate constants (k_{GS-TS} and k_{TS-GS}) for a two-state chemical exchange model.

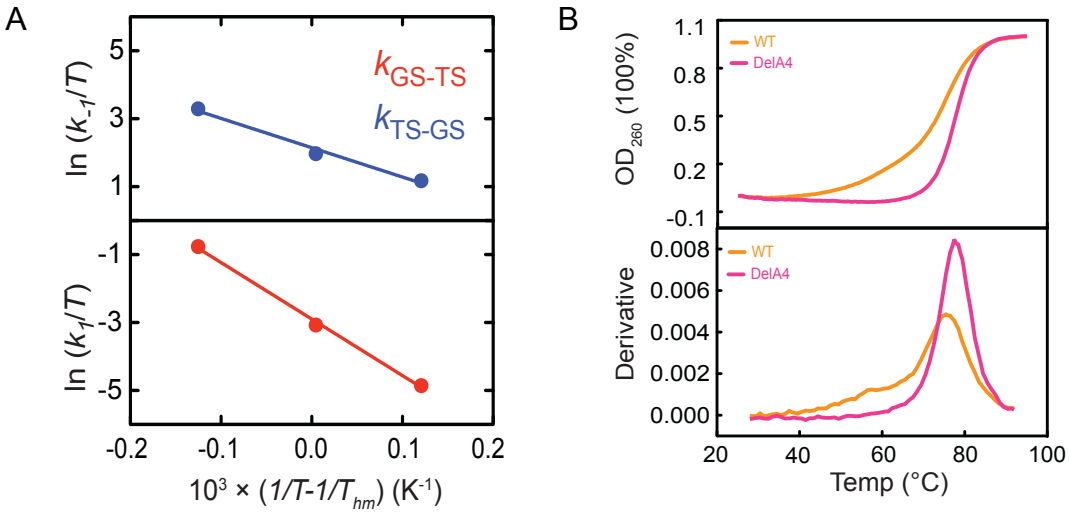

Figure 3-8: Thermodynamics analysis for the transition between the GS and the TS of the P4 helix mimic. **(A)** Van't Hoff plots showing temperature dependence of the forward (k_{GS-TS}) and reverse (k_{TS-GS}) rate constants for the two-state exchange in the P4 helix mimic. The experiments were performed in 15 mM NaH_2PO_4, 25 mM NaCl and 0.1 mM EDTA under pH 6.8 at 15°C, 25°C and 37°C with 2.3 mM of the P4 WT. **(B)** The UV thermal melting curves and derivatives to measure the melting temperatures of P4 WT (orange) and DelA4 mutant (pink). The experiments were performed with 1.5 μM of sample in 15 mM NaCac and 25 mM NaCl at pH 6.8.

Furthermore, the melting temperature for DelA4 obtained from UV melting is ~77.5°C which is two degrees higher than WT (Figure 3-8B). It indicates DelA4 has a more stable helical conformation compared with P4 WT. If the TS of the P4 helix mimic is caused by helix melting, the higher temperature could induce relaxation dispersion for DelA4. Therefore, the same $R_{1\rho}$ relaxation dispersion experiments as a function of temperature were also conducted for DelA4 mutant. There was no chemical exchange

observed at either lower or higher temperature (Figure 3-9, Figure B-3) suggesting DelA4 destabilizing the TS of the P4 helix mimic is not due to the increased melting temperature. Those results are consistent with the TS of the P4 helix mimic is not caused by helix melting.

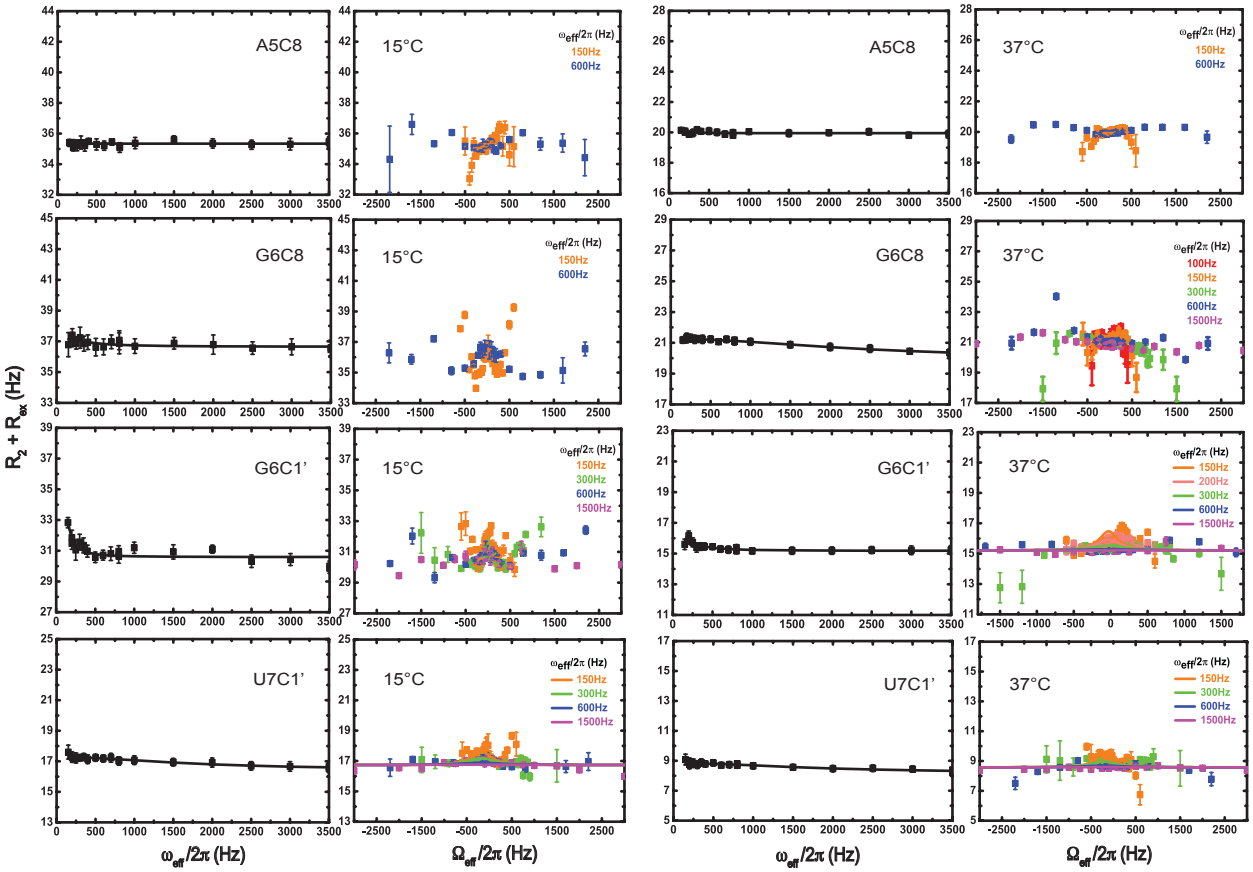

Figure 3-9: Temperature dependence of on- and off-resonance of $R_{1\rho}$ relaxation dispersion profiles for selected residues of DelA4 and best fits (solid lines) to a two-state exchange model. The data were collected at the condition of 15 mM NaH_2PO_4, 25 mM NaCl and 0.1 mM EDTA under pH 6.8 at 15°C and 37°C with 2.5 mM of DelA4 mutant. All data are included in **Figure B-3**.

To further investigate the possibility of helix melting, a $^{13}C/^{15}N$ uniformly labeled single-strand RNA oligonucleotides containing nucleotides from G2 to U11 of the P4 helix was made and the ^{1}H, ^{13}C, and ^{15}N resonances were assigned using standard

NMR experiments (Figure 3-10). As expected, no imino protons were observed indicating no secondary structure formation for the single-strand RNA. By comparing the nucleobase and sugar chemical shifts with the TS of P4 WT, as seen in Figure 3-10D, the single-stand RNA has similar chemical shift with the TS at C2/6/8 and C1' for G2, A3 and A4, but not for the A5, G6 and U7. It demonstrates the possibility of the P4 helix melting to single strand from G2 to A4 in the TS. However, there is more complicated structure change, rather than helix melting, occurring at A5, G6 and U7, for example, the base of G6 flips from *anti* to *syn*.

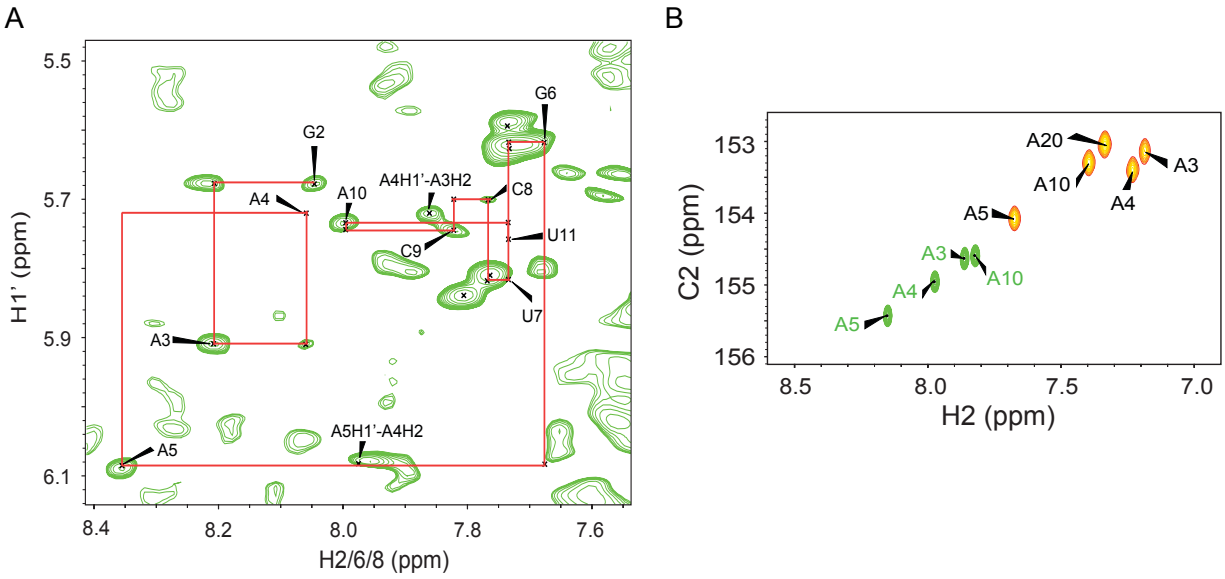

C

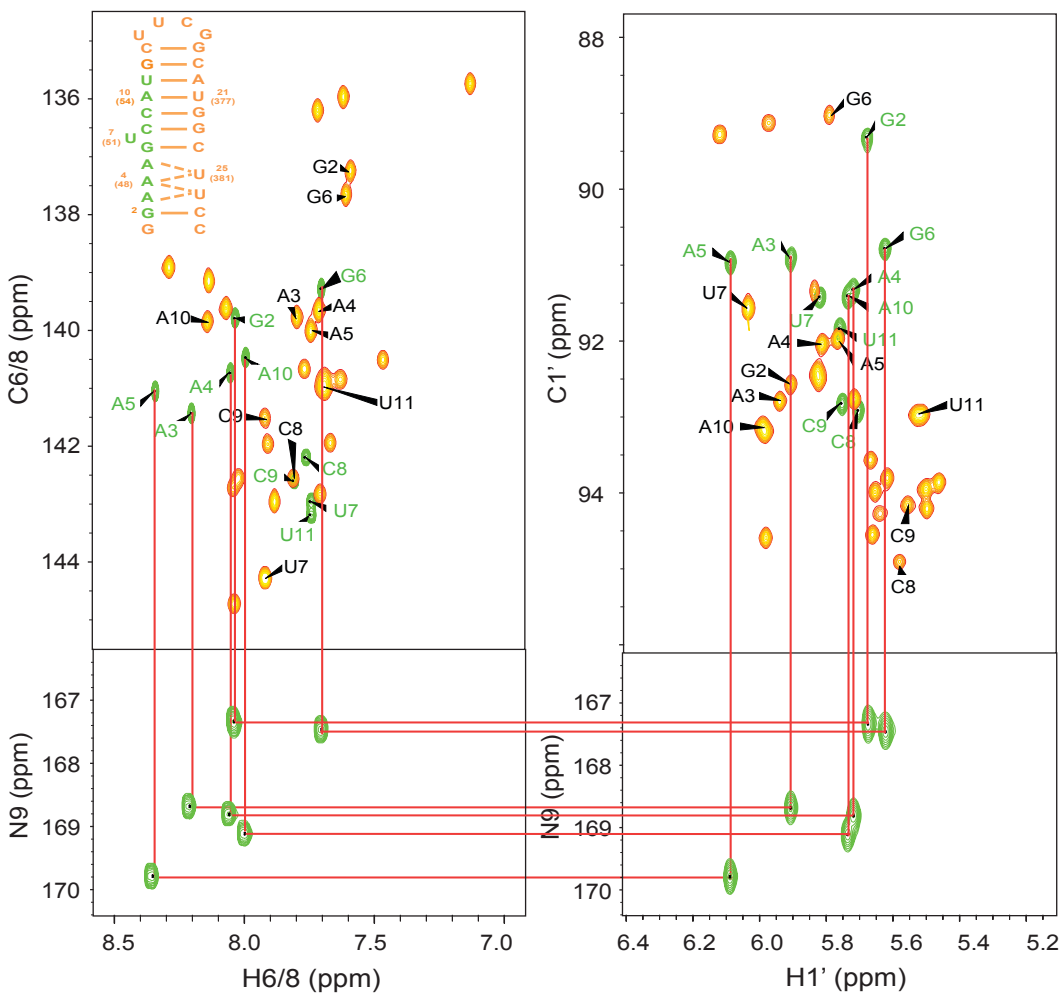
C6/8 (ppm)
N9 (ppm)
H6/8 (ppm)
C1' (ppm)
N9 (ppm)
H1' (ppm)
G2
G6
A3
A4
A5
A10
U11
U7
C8
C9

D

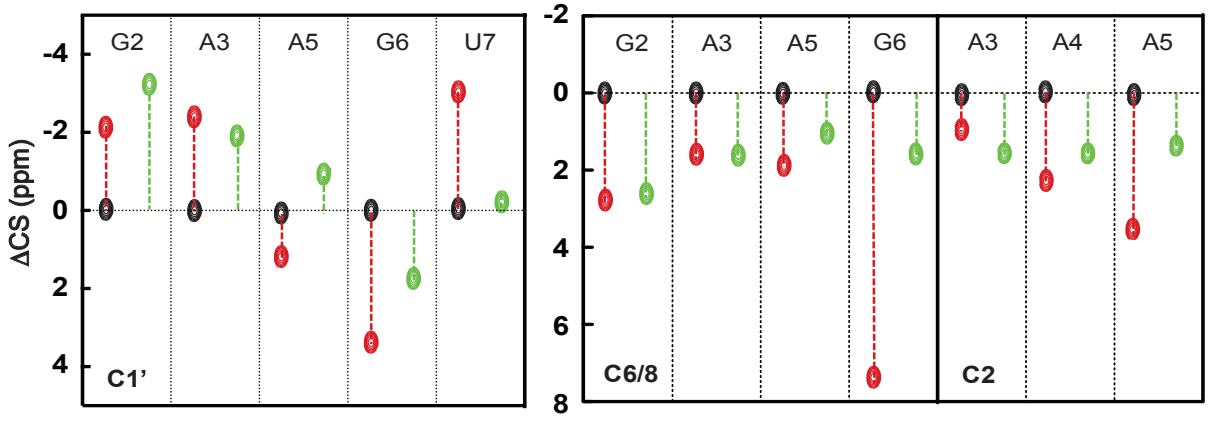
ΔCS (ppm)
G2
A3
A5
G6
U7
C1'
C6/8
A3
A4
A5
C2

Figure 3-10: Resonance assignments and chemical shifts of single-strand RNA containing G2 to U11 of the P4 helix mimic from *B. subtilis* PRNA. The data were collected in the buffer condition of 15 mM NaH_2PO_4, 25 mM NaCl and 0.1 mM EDTA under pH 6.8 at 25°C with 1 mM of single-strand RNA. **(A)** Non-exchangeable ^{1}H-^{1}H NOESY correlation of the single-strand RNA showing nucleobase H2/6/8 to sugar H1' NOE walk. **(B)** 2D ^{13}C-^{1}H HSQC spectra showing C2 and H2 correlation of P4 WT (orange) and single-strand RNA (green) **(C)** 2D ^{13}C-^{1}H HSQC spectra showing nucleobase C6/8-H6/8 and sugar C1'-H1' correlation for P4 WT (orange) and single-strand RNA (green); ^{15}N-^{1}H HCN spectra showing the corresponding intra-residue N9 peaks of all the guanosines and adenosines of single-strand RNA. The secondary structure of the P4 helix mimic is shown as inset and the single-strand RNA sequence is indicated in green. **(D)** Comparison of the chemical shifts between single-strand RNA (green) and the GS (black) and the TS (red) of the P4 WT.

3.3.4.2 Paromomycin stabilized the ground state instead of the transient state of the P4 helix mimic

Previous data shows that the internal loop in the ribosomal A-site, which has essential roles in decoding messenger RNA, involves flipping out two tandem internal-loop adenosines to interact with the codon–anticodon mini-helix formed between the cognate aminoacyl tRNA and mRNA [54, 55]. And this conformation can be stabilized by titrating paromomycin and built a drug-bound A-site [56]. Therefore, to test the hypothesis of three adenosines tract flipping out in the TS of the P4 helix mimic (Figure 3-11), I titrated paromomycin into WT P4 and compared the chemical shift with both the GS and the TS. As showed in Figure 3-12A, the perturbation of chemical shift was observed for the P4 helix mimic in the presence of paromomycin indicating paromomycin binds to the helix. At the saturating paromomycin, the chemical shift of the drug-bound state is comparable to the GS, but not the TS Figure 3-12B. It indicates that paromomycin stabilizes the GS of the P4 helix mimic and is not able to trap the TS. Therefore, there is no evidence to suggest the adenosines tract flipping out in the TS. Moreover, paromomycin destabilizing the TS is consistent with inhibiting *B. subtilis* RNase P

catalysis for pre-tRNA^{Asp} cleavage with an IC_{50} more than 1mM (Xin Liu and Carol A. Fierke, unpublished data). It's likely due to paromomycin binding to P4 helix of RNase P and hindering the occurrence of the conformation change.

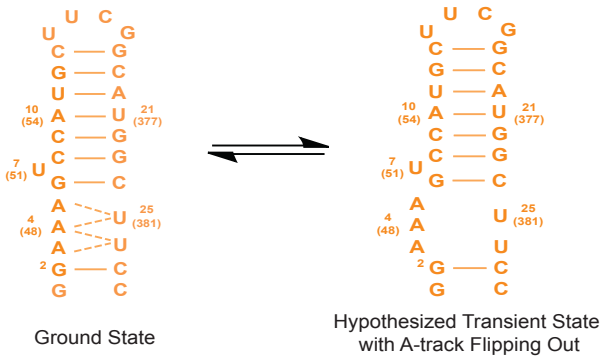

Figure 3-11: Hypothesized transient state of the P4 helix mimic involving in A-tract flipping out.

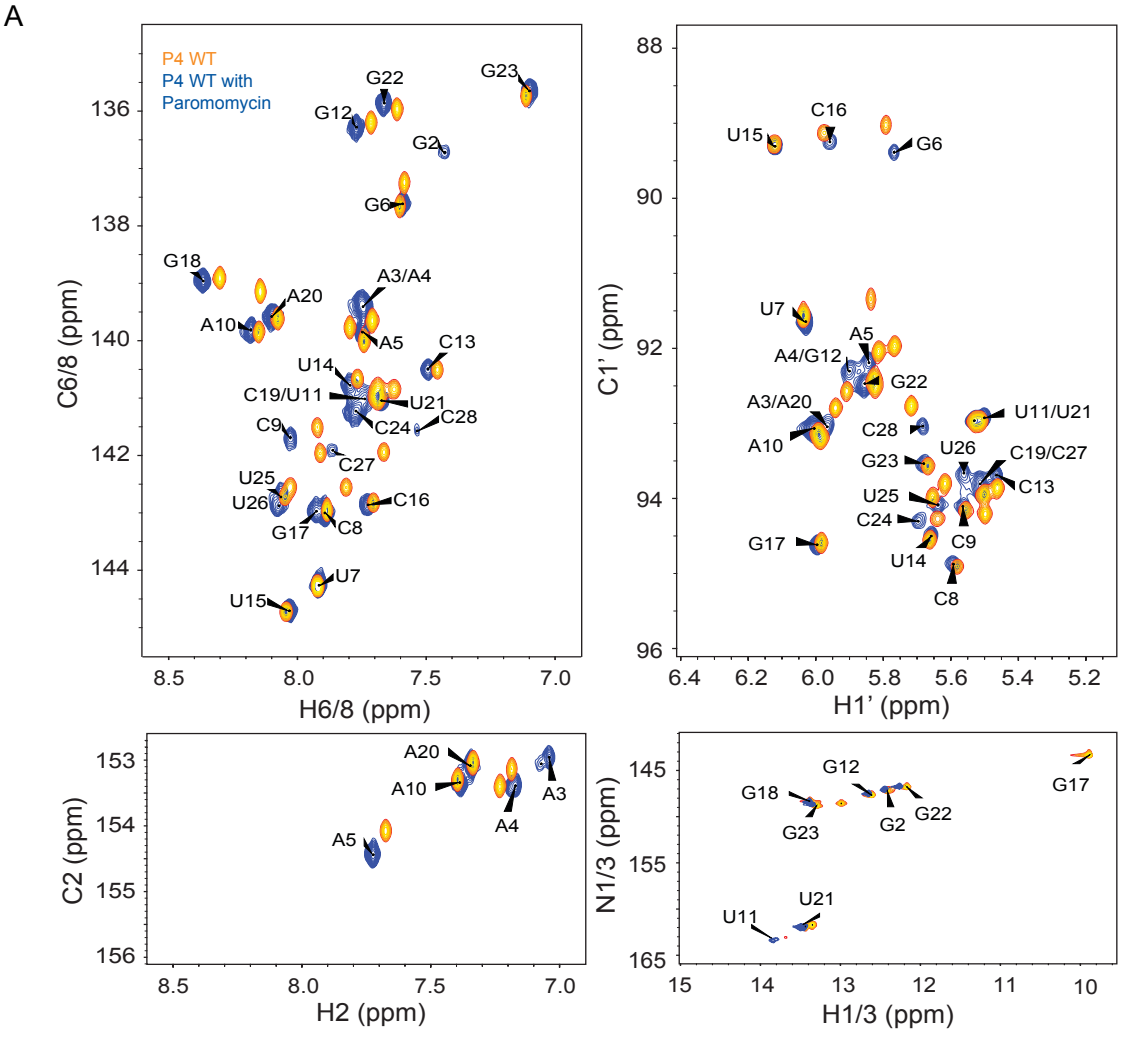

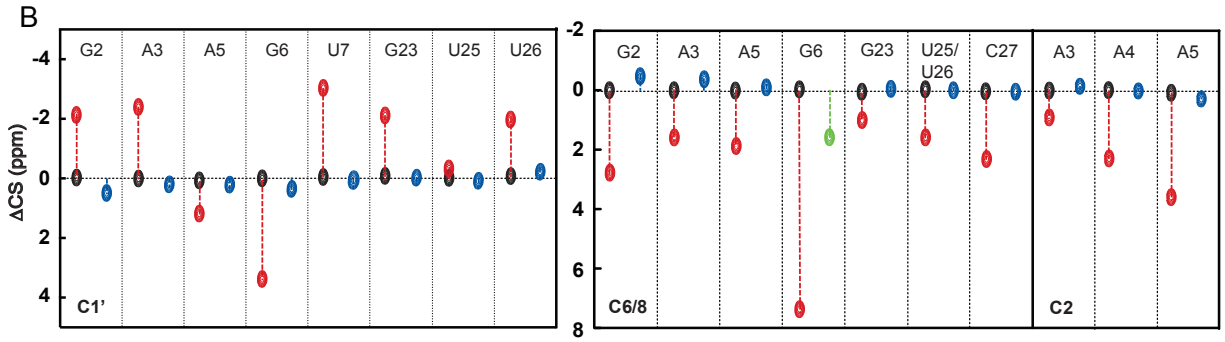

Figure 3-12: Chemical shifts of P4 WT titrated with saturating paromomycin. Paromomycin was gradually titrated into 150 μM of the P4 WT sample until no additional peak perturbation observed by additional paromomycin. The final concentration of paromomycin is 1.2 mM. The data were collected in the buffer condition of 15 mM NaH_2PO_4, 25 mM NaCl and 0.1 mM EDTA under pH 6.8 at 25°C. **(A)** 2D ^{13}C-^{1}H HSQC spectra showing nucleobase C2/6/8-H2/6/8 and sugar C1'-H1' correlation for P4 WT without (orange) and with (blue) saturating paromomycin; ^{15}N-^{1}H imino HSQC spectra showing nitrogen/proton (N1/3-H1/3) correlation. **(B)** Comparison of the chemical shifts between the P4 WT titrated with saturating paromomycin (blue) and the GS (black) and the TS (red) of the P4 WT.

3.3.4.3 Trapping the transient state of the P4 helix mimic by 8-bromoguanosine substitution at G6

The 7.4 ppm downfield chemical shift of G6C8 detected by relaxation dispersion suggests a *syn* base for G6 in the TS. To further investigate the structural feature of the TS, by collaborating with Huiqing Zhou in Al-Hashim's lab and Kierzek's lab, we used atom modification to trap the *syn* conformation of G6 in order to stabilize the TS of the P4 helix mimic. This allowed us to directly compare the carbon chemical shift signatures of the trapped state with those measured for the TS using relaxation dispersion. A guanosine analogue, 8-bromoguanosine (8BrG), was incorporated into the P4 helix mimic to substitute G6. 8BrG is a conformationally restricted nucleoside that preferentially adopts the *syn* glycosidic torsion angle, because the steric bulk of bromine precludes its residence over the ribose ring (Figure 2-2) [57-59]. It has been used to

successfully trap *syn* conformation of guanosine in both biochemical and NMR studies [60, 61].

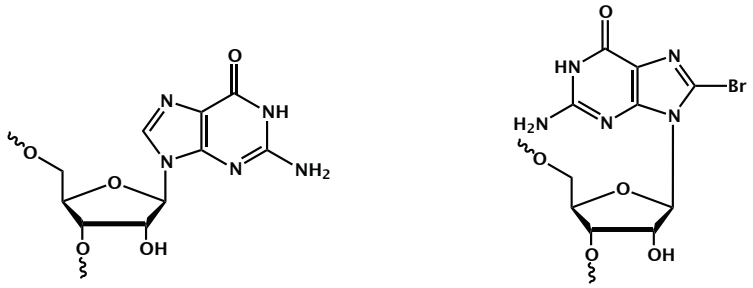

Guanosine (G), *anti*

8-bromoguanosine (8BrG), *syn*

Figure 3-13: Chemical structures of the guanosine with *anti* conformation and 8-bromoguanosine with restricting *syn* conformation, wherein the nucleobase is positioned over the ribose sugar.

The 1D spectra show the G6-8BrG modified P4 helix is in high purity without contaminations (Figure B-4). The ^{1}H and ^{13}C resonances of G6-8BrG were assigned using standard NMR experiments by using the unlabeled sample. The upper helix (above C8-G23 base pair) stay undisturbed compared with P4 WT (Figure 3-14C), consistent with no relaxation dispersion detected in this region for P4 WT. Same with P4 WT, only partial exchangeable NOE walk was observed (from G23 to G18) and no imino resonance was detected from G1 to U26. Additionally, different from the P4 WT, by substituting G6 with 8BrG, imino resonance of G6 disappeared and no NOE walk observed between G6 and G23 as well. It suggests 8BrG substitution disrupts or destabilizes the Watson-Crick base pair between G6 and C24 (Figure 3-14A), consistent with G6 changes to *syn* conformation in the TS. In the non-exchangeable NOESY spectra, beside the disruptions caused by the bulged out U7, the NOE walk between A5H1' and G6H8 was also interrupted and no H8-H1' inner-residue interaction observed for 8BrG (Figure 3-14B). This suggests the bromo modification is successfully

incorporated into C8 position and substitutes the proton. It is consistent with the disappearance of 8BrG C8-H8 resonance in 2D aromatic ^{13}C-^{1}H spectra (Figure 3-14C). The disappearance of H1' in NOESY and the weak C1'-H1' resonance also indicate the highly dynamic of the 8BrG.

To examine whether G6-8BrG stabilizes the TS, the sugar C1' chemical shifts of the residues around G6 (A5, G6 and U7) were compared with the GS and the TS of the P4 helix mimic. As shown in sugar C1'-H1' 2D HSQC, there were significant downfield-shifted C1' observed for A5 and G6 while up-shifted C1' for U7 (Figure 3-14C). And these chemical shift changes are comparable with the one detected by relaxation dispersion for the TS of the P4 helix mimic (Figure 3-14D). The value differences of ΔCS between G6-8BrG and the TS could be explained by the highly dynamic 8BrG stabilizes a conformation between the GS and the TS. Those results demonstrate that the *syn* conformation of G6 disrupts the Watson-Crick base pair between G6 and C24, and meantime stabilizes the sugar conformation of A5, G6 and U7 in the TS of P4 helix mimic.

The C6 of U7 base in G6-8BrG has same chemical shift compared with the GS of P4 WT, consistent with no relaxation dispersion observed on C6. C8 resonances of A3 and A5 in G6-8BrG are slightly upfield-shifted, which is different from observed downfield-shifted in the TS of the P4 helix mimic. It is probably because 8BrG substitution at G6 affecting backbone conformation due to the locked *syn* [62], thereby is able to trap the residues nearby at the TS, but cannot force the bases of A-tract into the TS that is partially caused by A-tract region melting.

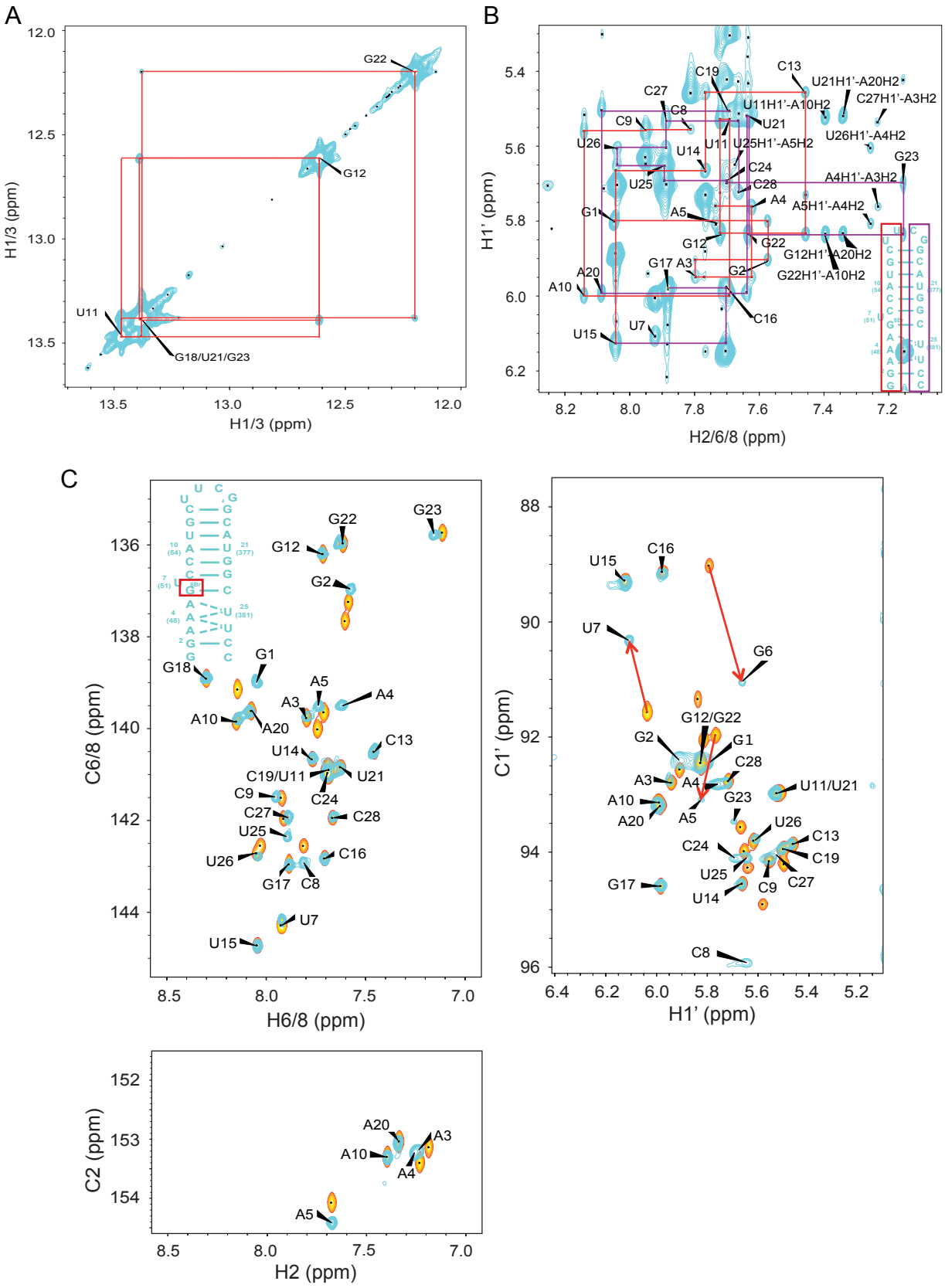
A
H1/3 (ppm)
H1/3 (ppm)
G22
G12
U11
G18/U21/G23
B
H1' (ppm)
H2/6/8 (ppm)
C
C6/8 (ppm)
H6/8 (ppm)
C1' (ppm)
H1' (ppm)
C2 (ppm)
H2 (ppm)

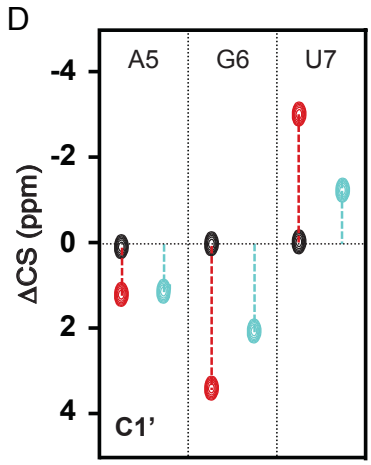

Figure 3-14: Resonance assignments of G6-8BrG P4 helix mimic construct from *B. subtilis* PRNA. The data were collected in the buffer condition of 15 mM NaH_2PO_4, 25 mM NaCl and 0.1 mM EDTA under pH 6.8 at 25°C with 1 mM of unlabeled G6-8BrG. **(A)** Exchangeable ^{1}H-^{1}H NOESY correlation of G6-8BrG showing imino walk from residue G23 to G18. **(B)** Non-exchangeable ^{1}H-^{1}H NOESY correlation of the G-8BrG showing nucleobase H2/6/8 to sugar H1' NOE walk. The connectivity from residue G1 to U15 is shown in red and U15 to C28 is in purple. **(C)** 2D ^{13}C-^{1}H natural abundance HSQC/HMQC spectra showing nucleobase C2/6/8-H2/6/8 and sugar C1'-H1' correlation for P4 WT (orange) and G6-8BrG (cyan). The guanosine substituted with 8BrG is indicated in the secondary structure of the P4 helix mimic as inset. The chemical shift perturbation of A5, G6 and U7C1' are indicated in red arrows. **(D)** Comparison of the chemical shifts between the G6-8BrG (cyan) and the GS (black) and the TS (red) of the P4 WT.

3.3.4.4 Investigation of the possible Hoogsteen base pair in the transient state of the P4 helix mimic

As mentioned before, the *syn* base of G6 in the TS detected by relaxation dispersion disrupts the Watson-Crick base pair with C24 on the other side of the helix (Figure 3-14A). It can potentially form a Hoogsteen base pair with C24 (Figure 3-15). Since G-C Hoogsteen base pair involves a protonated cytosine N3 (Figure 3-15), the formation of Hoogsteen base pair is more pronounced at lower pH conditions that favor the protonation of cytosine N3 [63, 64].

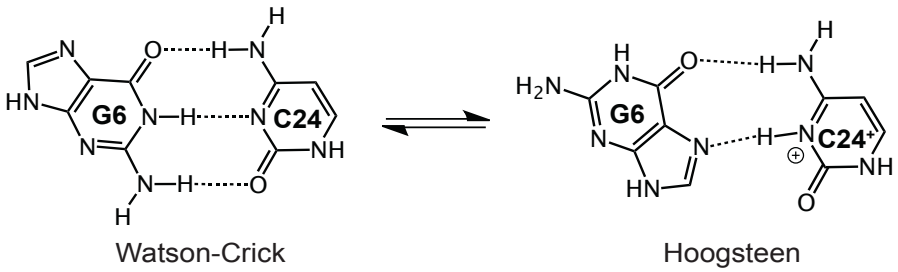

Figure 3-15: Chemical structures for Watson-Crick G6-C24 and hypothesized Hoogsteen G6-C24^{+} base pairs. G6 adopts *anti* conformation in Watson-Crick and *syn* in Hoogsteen base pairs. N3 of C24 is protonated in Hoogsteen base pair with G6.

To examine if the transient Hoogsteen base pair is formed in the TS, I measured the $R_{1\rho}$ relaxation dispersion on the dependence of pH (Figure 3-16A). At different pHs, the P4 helix mimic has the same structure of the TS because the similar chemical shift changes were observed under pH 5.4, 6.8 and 7.6 by relaxation dispersion (Figure 3-16B). However, reducing the pH resulted in slightly increase of the TS population to ~ 0.8% (Table 3-3), which is lower (~ 0.6%) at near neutral pH (pH 6.8 and 7.6, Table 3-2, Table 3-3). This population difference between different pHs is smaller than the transient Hoosgsteen base pair observed before in DNA [63].

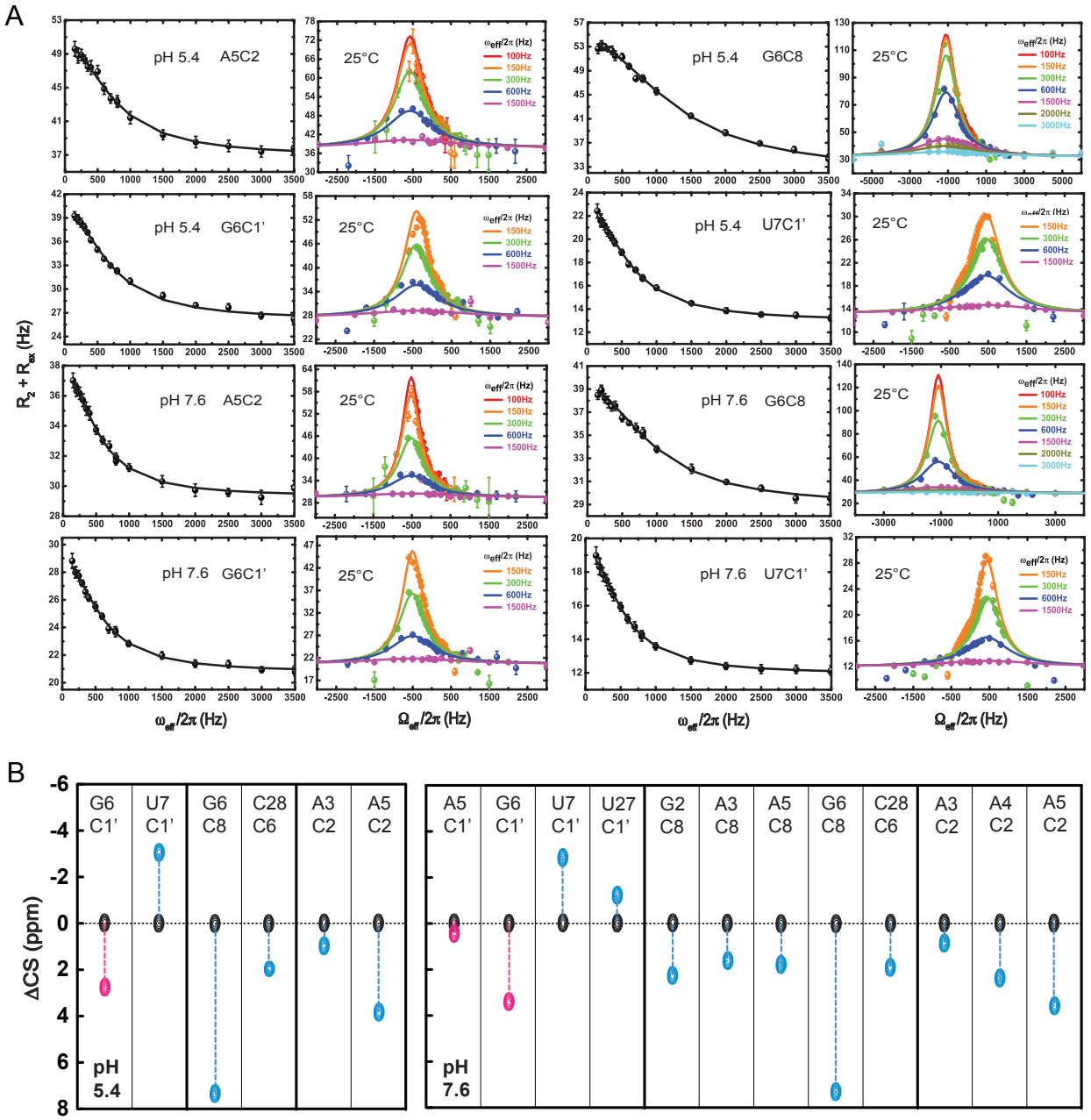

Figure 3-16: pH dependence of $R_{1\rho}$ relaxation dispersion for the P4 helix mimic from *B. subtilis* PRNA. The data were collected in 15 mM NaH_2PO_4, 25 mM NaCl and 0.1 mM EDTA at 25°C under pH 5.4 and pH 7.8 with 2.3 mM of the P4 WT. **(A)** Reprehensive of on- and off-resonance of $R_{1\rho}$ relaxation dispersion profiles and best fits (solid lines) to a two-state exchange model. All data are included in **Figure B-2**. **(B)** Comparison of the chemical shifts between the GS (black) and the TS (pink, increased stacking or toward to C3'-endo sugar pucker direction; blue, decreased stacking or *syn* glycosidic angle, or toward to non-C3'-endo sugar pucker direction) at pH 5.4 and pH 7.6.

Table 3-3: Global fits of off-resonance $R_{1\rho}$ relaxation dispersion of the P4 helix mimic at pH 5.4 and pH 7.6[a]

pH	Residue	R_1 (Hz)[b]	R_2 (Hz)[b]	p_B (%)[b]	k_{ex} (s^{-1})[b]	Δω (ppm)[b]
5.4	**A3C2**	1.97 ± 0.08	34.0 ± 0.19	0.84 ± 0.01	2821 ± 45 k_{GS-TS}: 23.7 ± 0.7 k_{TS-GS}: 2797 ± 78	1.8 ± 0.05
	A5C2	1.74 + 0.10	37.2 ± 0.25			3.4 ± 0.08
	G6C1'	1.83 ± 0.05	26.7 ± 0.15			3.3 ± 0.05
	G6C8	1.52 ± 0.06	33.4 ± 0.15			7.1 ± 0.07
	U7C1'	2.25 ± 0.03	13.0 ± 0.09			-2.6 ± 0.03
	C27C6	2.18 ± 0.13	33.7 ± 0.24			1.3 ± 0.08
7.6	**G2C8**	1.91 ± 0.04	28.7 ± 0.10	0.55 ± 0.01	1969 ± 26 k_{GS-TS}: 10.8 ± 0.3 k_{TS-GS}: 1958 ± 61	2.4 ± 0.05
	A3C2	1.91 ± 0.06	32.8 ± 0.10			1.0 ± 0.05
	A3C8	1.89 ± 0.04	28.9 ± 0.10			1.5 ± 0.04
	A4C2	1.77 ± 0.05	29.6 ± 0.10			2.2 ± 0.04
	A5C1'	1.69 ± 0.03	21.6 ± 0.07			0.7 ± 0.05
	A5C2	1.59 + 0.05	29.0 ± 0.11			3.5 ± 0.06
	A5C8	1.99 ± 0.04	28.5 ± 0.08			1.8 ± 0.04
	G6C1'	1.86 ± 0.03	20.6 ± 0.07			3.5 ± 0.04
	G6C8	1.93 ± 0.04	28.4 ± 0.08			7.2 ± 0.06
	U7C1'	2.11 ± 0.02	12.1 ± 0.05			-2.8 ± 0.03
	U26C1'	1.62 ± 0.04	22.2 ± 0.07			-1.8 ± 0.03
	C27C6	2.02 ± 0.09	33.8 ± 0.18			1.7 ± 0.09

[a] The experiments were performed in 15 mM NaH_2PO_4, 25 mM NaCl and 0.1 mM EDTA at 25°C with 2.3 mM of the P4 WT.
[b] The data were fit to a two-state Laguerre equation (Equation 12) to obtain the values of all the parameters.

Furthermore, in G6-8BrG ^{1}H-^{1}H NOESY correlation, no chemical shift perturbation was observed for H5 or H6 of C24 (Figure 3-14B). Therefore, there is no evidence for the protonation on the N3 of C24, which is required to form G6-C24$^+$ Hoogsteen base pair. Additionally, I also used N1-methylated guanosine (1mG) substitution on G6 to trap the TS (Figure B-5) [63]. 1mG is a structural analog to N1-methylated adenosine (1mA), which has been used to disrupt Watson-Crick base pair and stabilize Hoogsteen base pair in DNA [63, 65, 66]. Due to the impurity in the sample, only limited information

can be obtained. It is challenging to determine the sugar chemical shift of G6, U7, C24 and A-tract (Figure B-5) in ^{13}C-^{1}H 2D correlation therefore it creates uncertainty of whether the TS is trapped by G6-1mG or not. The upper helix (above C8-G23 base pair) of G6-1mG stay undisturbed compared with P4 WT (Figure B-5), consistent with no relaxation dispersion detected in this region for P4 WT, while the upfield-shifted U7C6 (Figure B-5) is inconsistent with no relaxation dispersion observed on U7C6 in P4 WT. It could be explained by the bulky methyl group affecting the base conformation of U7. Even though the possible downfield-shifted G6C8 and the disappearance of imino proton of G6 likely indicate the *syn* conformation of G6 is successfully trapped and there are perturbation observed for C24 on H4, H5 and H6 (Figure B-5), the weak H1'-H8 NOE peaks for both of G6 and C24 (Figure B-5) illustrate highly dynamic residues, likely not forming a stable base pair.

Taken together, P4 helix mimic showed weak pH dependence of chemical exchange and all the atom modification used did not successfully trap Hoogsteen base pair between G6 and C24 suggesting no evidence for the transient Hoogsteen base pair in the TS of the P4 helix mimic.

3.3.5 The individual transient state of bulged U7 observed in the presence of Mg^{2+}

I have already investigated the TS of the P4 helix mimic in the absence of divalent metal ions. Since RNase P is a divalent cations dependent enzyme and *in vivo* this metal ion is fulfilled by Mg^{2+} [29, 38, 67-74], it is necessary to examine the TS in the presence of Mg^{2+}. I titrated $MgCl_2$ into the P4 WT gradually until reached saturation where no further perturbation of the chemical shift occurred.

In the presence of near-physiological concentration of Mg^{2+} (5 mM), 2D $^{13}C^{-1}H$ and $^{13}N^{-1}H$ HSQC show great agreement on nucleobase and sugar chemical shift suggesting the GS of the P4 helix mimic is not perturbed by addition of low concentration of Mg^{2+} (Figure 3-17A). The TS also adopts the same structure as in the absence of Mg^{2+} since the similar chemical shift change detected by relaxation dispersion was observed (Table 3-4, Figure 3-18A, C). As shown before, Mg^{2+} decreased the k_{ex} and population of the TS [75].

When reached to the saturating Mg^{2+} (44 mM), peak perturbation was observed for both nucleobase and sugar. Notably, the sugar C1' of A5, G6 and U7 shift towards the direction of the TS detected by relaxation dispersion (Figure 3-17B), even though the values of these chemical shift changes are relatively small. Other residues showing relatively large peak perturbation including A3, A4, G22 and G23. It indicates the interaction with Mg^{2+}, consistent with the metal ion binding site in the P4 helix suggested before [49, 51, 68] (Xin Liu, Yu Chen and Carol A. Fierke, manuscript in preparation). In the presence of 44 mM Mg^{2+}, the peaks showing relaxation dispersion in the absence of Mg^{2+} have significant line broadening and relaxation dispersion was very difficult to detect. However, U7C1' still retained relaxation dispersion (Figure 3-18B) with greater k_{ex}, higher population and different chemical shift change comparing with the P4 helix mimic in the absence of Mg^{2+} (Table 3-5). Surprisingly, there was significant relaxation dispersion observed on U7C6 that is not found without Mg^{2+} (Figure 3-18B). It has comparable k_{ex} and population with U7C1' and both of the chemical shift change (Table 3-5) indicates more stacking structural change in the TS. This process was only detected in the presence of Mg^{2+} but not without Mg^{2+} (Figure

B-2) demonstrating bulged U7 has its own process separated from the global structure change observed in the absence of Mg^{2+}. Or the chemical exchange on U7C6 was too small to detect in the absence of Mg^{2+}, and the chemical shift is enhanced by the presence of Mg^{2+}. The Similar relaxation dispersion also found on the neighboring residues G6 and C8 (Figure B-2).

To further examine this individual process on U7, under the same condition, I measured relaxation dispersion on DelA4 mutant, which eliminates the relaxation dispersion of the P4 WT and destabilizes the TS (Figure 3-5, Figure B-3). With saturating Mg^{2+}, U7 of DelA4 showed the comparable chemical shift changes in the TS with similar k_{ex} and population comparing with WT P4 helix mimic (Table 3-5, Figure 3-18B, D), as well as G6 and C8 (Figure B-3). This further demonstrates bulged U7 has its individual process towards the TS, which is independent of the global structural change.

A

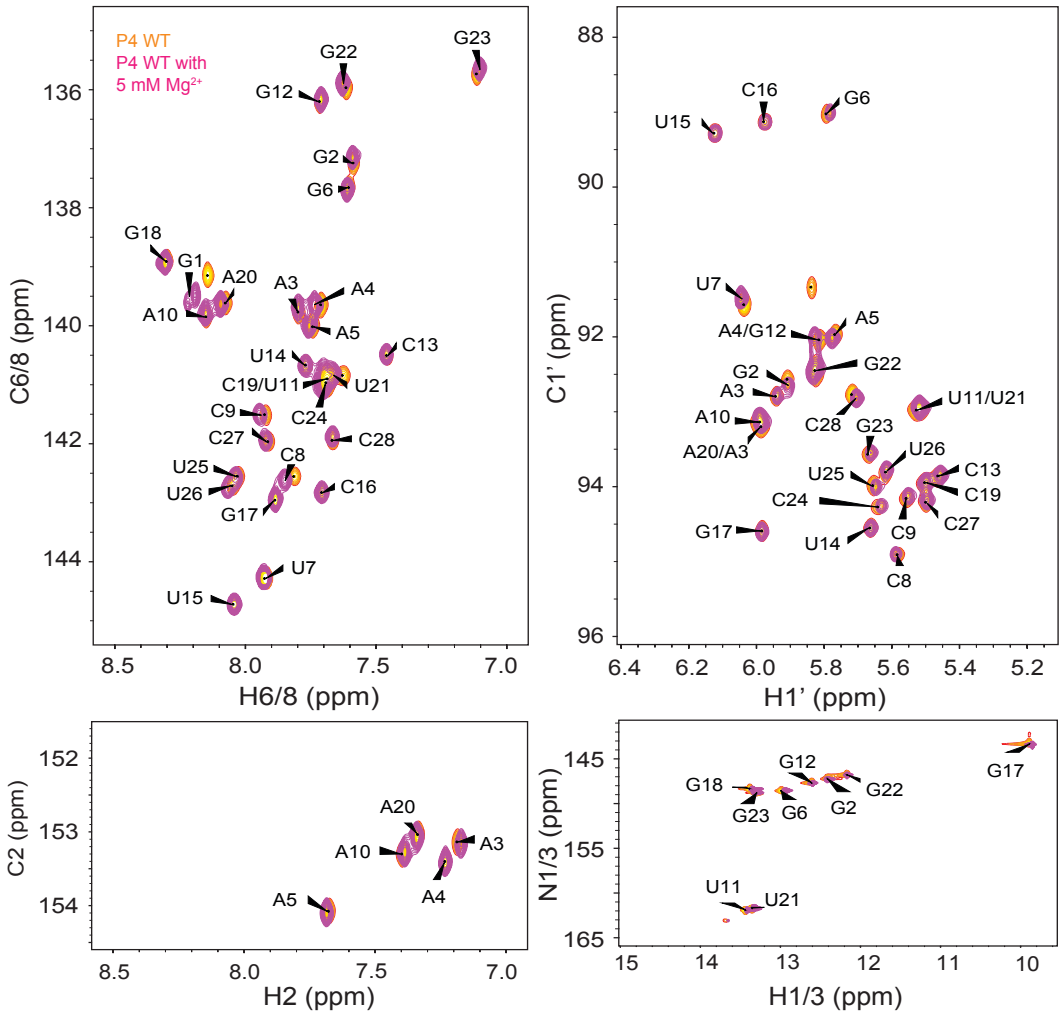
P4 WT
P4 WT with
5 mM Mg2+
C6/8 (ppm)
H6/8 (ppm)
C1' (ppm)
H1' (ppm)
C2 (ppm)
H2 (ppm)
N1/3 (ppm)
H1/3 (ppm)

B

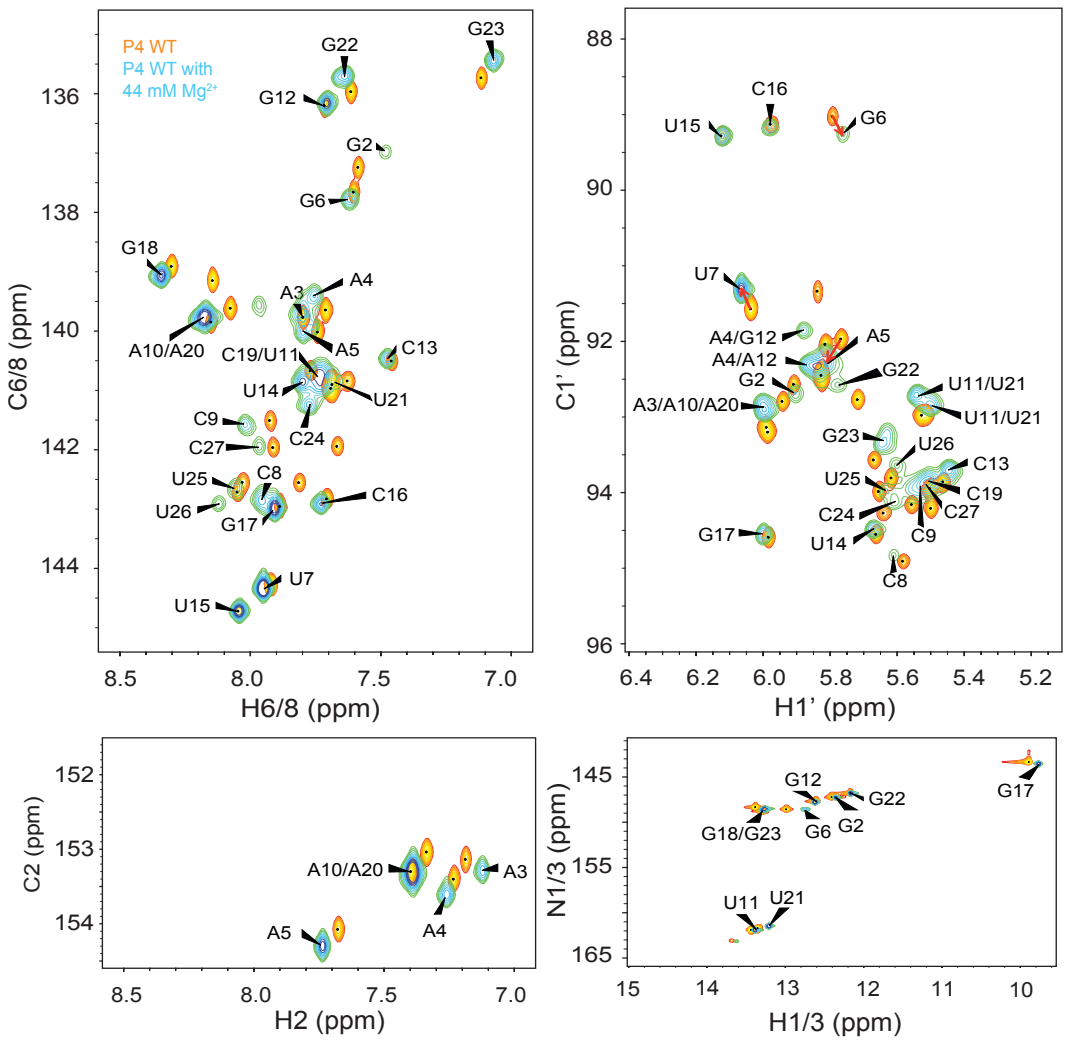

Figure 3-17: Chemical shifts of P4 WT titrated $MgCl_2$. $MgCl_2$ was gradually titrated into 2.3 mM of the P4 WT sample until no further peak perturbation observed by additional $MgCl_2$ to get 44 mM $MgCl_2$ is the saturating concentration. The data shown were collected by dialyzing sample into 15 mM NaH_2PO_4, 25 mM NaCl, 0.1 mM EDTA and 5 mM or 44 mM $MgCl_2$ under pH 6.8 at 25°C. **(A)** 2D ^{13}C-^{1}H HSQC spectra showing nucleobase C2/6/8-H2/6/8 and sugar C1'-H1' correlation for P4 WT without (orange) and with (pink) 5 mM $MgCl_2$; ^{15}N-^{1}H imino HSQC spectra showing nitrogen/proton (N1/3-H1/3) correlation. **(B)** 2D ^{13}C-^{1}H HSQC spectra showing nucleobase C2/6/8-H2/6/8 and sugar C1'-H1' correlation for P4 WT without (orange) and with (blue) 44 mM $MgCl_2$; ^{15}N-^{1}H imino HSQC spectra showing nitrogen/proton (N1/3-H1/3) correlation. The chemical shift perturbation of A5, G6 and U7C1' are indicated in red arrows.

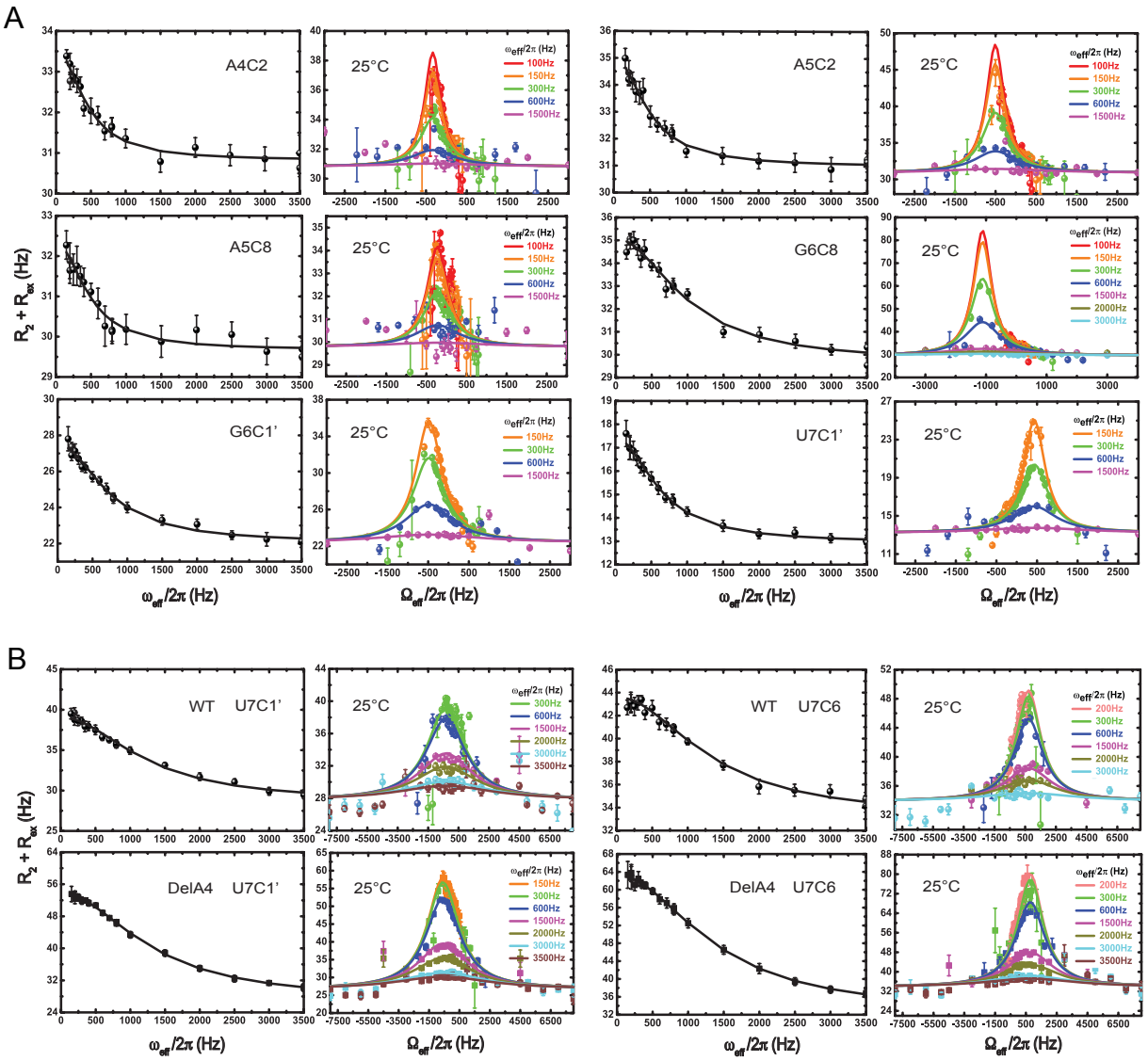
A
A4C2
A5C2
A5C8
G6C8
G6C1'
U7C1'
25°C
100Hz
150Hz
300Hz
600Hz
1500Hz
2000Hz
3000Hz
R2 + Rex (Hz)
ωeff/2π (Hz)
Ωeff/2π (Hz)
B
WT U7C1'
WT U7C6
DelA4 U7C1'
DelA4 U7C6
200Hz
3500Hz
C
A3 C1'
G6 C1'
U7 C1'
A5 C8
G6 C8
A4 C2
A5 C2
ΔCS (ppm)
D
C1'
C6
WT
DelA4

Figure 3-18: $R_{1\rho}$ relaxation dispersion for the P4 WT (2.3 mM) and DelA4 mutant (2.5 mM) from *B. subtilis* PRNA in the presence of Mg^{2+}. The sample were dialyzed into 15 mM NaH_2PO_4, 25 mM NaCl, 0.1 mM EDTA and 5 mM or 44mM $MgCl_2$ under pH 6.8 at 25°C. **(A**) Reprehensive of P4 WT on- and off-resonance of $R_{1\rho}$ relaxation dispersion profiles and best fits (solid lines) to a two-state exchange model in the presence of 5 mM $MgCl_2$. All data are included in **Figure B-2**. **(B**) On- and off-resonance of P4 WT and DelA4 mutant U7C1' and U7C6 $R_{1\rho}$ relaxation dispersion profiles and best fits (solid lines) to a two-state exchange model in the presence of 44 mM $MgCl_2$. All data are included in **Figure B-3**. **(C)** Comparison of the chemical shifts between the GS (black) and the TS (pink, increased stacking or toward to C3'-endo sugar pucker direction; blue, decreased stacking or *syn* glycosidic angle, or toward to non-C3'-endo sugar pucker direction) of P4 WT in the presence of 5 mM $MgCl_2$. **(D)** Comparison of U7C1' and U7C6 chemical shifts between the GS (black) and the TS (pink, increased stacking or toward to C3'-endo sugar pucker direction) of P4 WT and DelA4 mutant in the presence of 44 mM $MgCl_2$.

Table 3-4: Global fits of off-resonance $R_{1\rho}$ relaxation dispersion of the P4 helix mimic in the presence of 5 mM Mg^{2+} [a]

Residue	R_1 (Hz)[b]	R_2 (Hz)[b]	p_B (%)[b]	k_{ex} (s^{-1})[b]	Δω (ppm)[b]
A3C1'	1.61 ± 0.04	25.2 ± 0.07			-1.1 ± 0.06
A4C2	1.99 ± 0.04	30.6 ± 0.08		1739 ± 48	2.0 ± 0.06
A5C2	1.87 + 0.05	30.7 ± 0.11		k_{GS-TS}:	3.1 ± 0.11
A5C8	2.08 ± 0.05	29.9 ± 0.09	0.33 ± 0.01	5.7 ± 0.3	1.7 ± 0.07
G6C1'	1.97 ± 0.04	22.9 ± 0.08		k_{TS-GS}:	3.6 ± 0.09
G6C8	1.87 ± 0.04	29.5 ± 0.07		1733 ± 100	7.0 ± 0.12
U7C1'	2.17 ± 0.03	13.3 ± 0.06			-3.0 ± 0.07

[a] The experiments were performed in 15 mM NaH_2PO_4, 25 mM NaCl, 5 mM of $MgCl_2$ and 0.1 mM EDTA under pH 6.8 at 25°C with 2.3 mM of the P4 WT.
[b] The data were fit to a two-state Laguerre equation (Equation 12) to obtain the values of all the parameters.

Table 3-5: $R_{1\rho}$ relaxation dispersion off-resonance analysis for U7C1' and U7C6 of P4 WT and DelA4 mutant in the presence of 44 mM Mg^{2+} [a]

Construct	Residue	R_1 (Hz)[b]	R_2 (Hz)[b]	p_B (%)[b]	k_{ex} (s^{-1})[b]	Δω (ppm)[b]
WT	**U7C1'**	1.84 ± 0.06	28.1 ± 0.22	1.85 ± 0.35	8205 ± 366	2.5 ± 0.25
	U7C6	2.09 ± 0.06	33.9 ± 0.17	0.46 ± 0.03	5948 ± 274	-4.8 ± 0.21
DelA4	**U7C1'**	1.53 ± 0.14	26.7 ± 0.64	1.82 ± 0.25	7744 ± 446	3.9 ± 0.33
	U7C6	1.25 ± 0.10	33.8 ± 0.26	1.17 ± 0.03	6052 ± 153	-5.3 ± 0.11

[a] The experiments were performed in 15 mM NaH_2PO_4, 25 mM NaCl, 44 mM of $MgCl_2$ and 0.1 mM EDTA under pH 6.8 at 25°C with 2.3 mM of the P4 WT and 2.5 mM of DelA4 mutant.
[b] The data were fit to a two-state Laguerre equation (Equation 12) to obtain the values of all the parameters.

3.3.6 Building a 3D model of the TS of the P4 helix mimic

In order to interpret the chemical shift change in the TS compared with GS and better visualized the TS structure, I collaborated with Dr. Aaron Frank in the Brooks lab and built 3D models for both the GS and the TS by using the chemical shift data without Mg^{2+}. The 3D structures of the P4 helix mimic were built by MCSYM-LARMORD approach [50], which allows predicting RNA 3D structures based on non-exchangeable ^{1}H and protonated ^{13}C and ^{15}N RNA chemical shifts.

As shown in Figure 3-19, in the GS, the upper helix forms a stable helix, G6 base pairs with C24, U7 is bulged out and three adenosines stay in helical conformation, which is consistent with the structure suggested by ^{1}H-^{1}H NOESY, ^{13}C-^{1}H and ^{15}N-^{1}H HSQC. However, A3-U26 and A4-U25 forms base pairs in the GS model. It is inconsistent with no imino resonances observed for U25 and U27 in ^{1}H-^{1}H NOESY. It is probably due to current MCSYM-LARMORD approach on structure prediction having less accuracy using iminio chemical shift comparing with using carbon chemical shift [50].

In the model of the TS, the helix at A-tract region unwinds and G6 adopts a *syn* conformation. It is consistent with the chemical shift detected by relaxation dispersion, the single-strand RNA comparison and G6-8BrG trapping the TS. The prediction also suggests G6 changes from C2'-endo to C3'-endo-like sugar pucker (Table B-8). Strikingly, there is kink formed at the backbone between A5 and G6, which is not observed in the GS. This kink formation could explain the downfield-shifted C1' of A5 and G6, and upfield-shift on U7 and A-tract. Moreover, the base of U7 move inward the P4 helix compared with the position in the GS. This structural change on U7 was not

detected by relaxation dispersion in the absence of Mg^{2+}, but it is consistent with the one observed by relaxation dispersion in the presence of saturating Mg^{2+}.

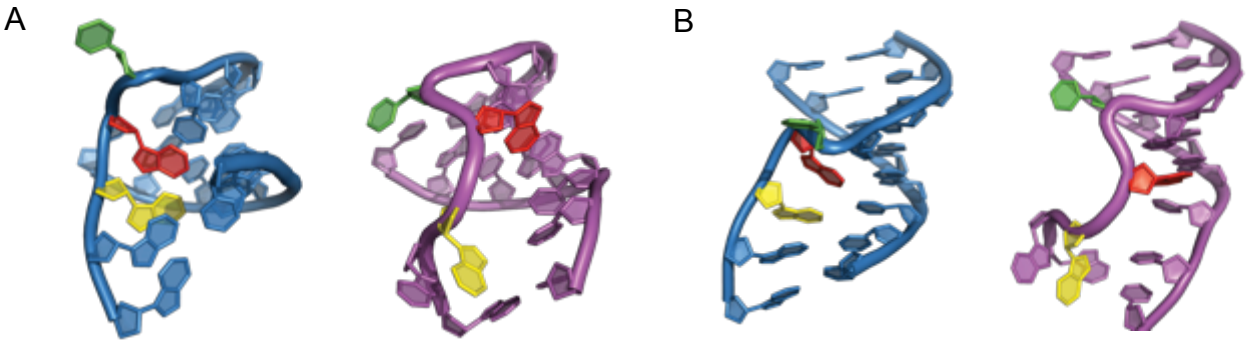

Figure 3-19: Two different views showing 3D models of the GS (blue) and TS (purple) of the P4 helix mimic form *B. subtilis* PRNA predicted by MCSYM-LARMORD method. **(A)** G6 adopts *anti* conformation in the GS (blue) and *syn* conformation in the TS (purple). The nucleosides of A5, G6 and U7 are indicated in different color: A5 is in yellow, G6 is in red and U7 is in green. **(B)** The model of the GS (blue) of the P4 helix mimic shows the structure containing bulged U7, and A-tract in flexible helical conformation. The model of the TS shows the kink formation on the backbone between A5 and G6. The sugar and base of A5, G6 and U7 are color coded as indicated in (A).

To further probe which residues are responsible for selecting the model with a kink formation between A5 and G6, a set of selections were carried out with various combinations of chemical shifts data in which chemical shifts for A5, G6 and U7 are excluded data set. Kink between A5 and G6 is obliterated if all the chemical shift data for residues A5, G6 and U7, G6 and U7, or A5 and G6 are excluded, respectively (Figure 3-20A). In contrast, when only A5 chemical shift data were excluded the same kinked model is selected (Figure 3-20B), suggesting that the selection of the kinked TS model is driven by the G6 and U7 chemical shift dispersion data. To further pinpoint the chemicals shifts that favor selection of the kinked TS model, selections were carried out when excluding A5 and utilizing only sugar chemical shifts, or base chemical shifts of G6 an U7, respectively. For sugar only selection, a model more closely resembling the

GS structure was observed (Figure 3-20A), whereas for base only selection, a model with kink was selected but the kink observed bended to a different direction (Figure 3-20B). These results indicate that the kinked model selection was driven by the G6 nucleobase chemical dispersion data since no relaxation dispersion observed on U7 base. It suggests the base conformation of G6 changing from *anti* to *syn* is important to stabilized the TS. And it is consistent with G6-8BrG modified P4 helix, which forces G6 to *syn* conformation, adopts the similar structure as the TS at A5, G6 and U7 (Figure 3-14D). However, the kink direction in the TS is also restrained by the sugar conformation of G6 and U7. Together, the predicted model of the TS illustrates a kink formation between A5 and G6 and this kink formation is driven by the *syn* conformation of G6 and restrained by the sugar of G6 and U7.

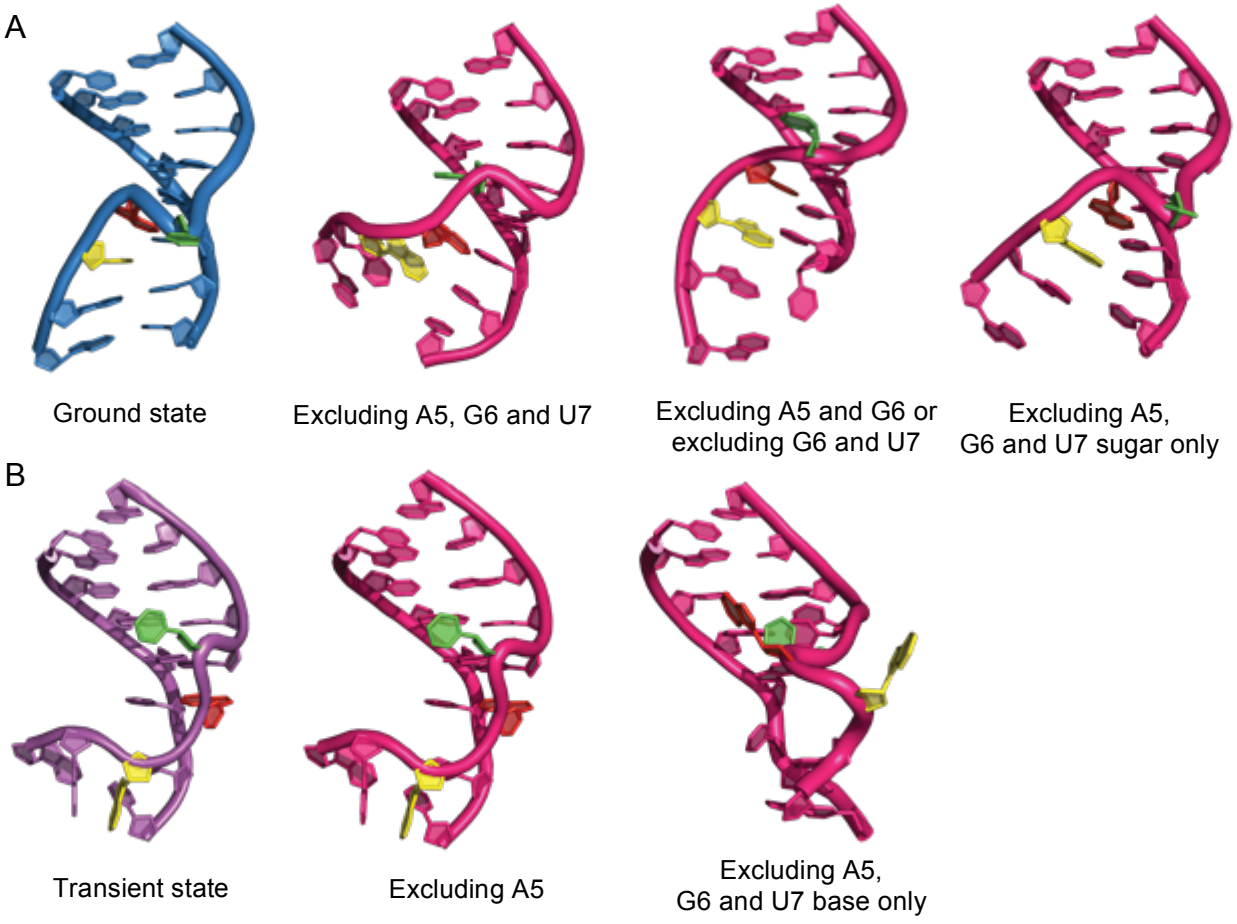

Figure 3-20: Determining the chemical shift data responsible for selecting the TS model with the kink formation between A5 and G6. **(A)** The selections that result in the model resembling the GS (blue) or eliminating the kink between A5 and G6 in the P4 helix mimic. The nucleosides of A5, G6 and U7 are indicated in different color: A5 is in yellow, G6 is in red and U7 is in green. **(B)** The selections that result in the model resembling the TS (purple) or retaining the kink between A5 and G6 in the P4 helix mimic. The sugar and base of A5, G6 and U7 are color coded as indicated in (A).

3.4 Discussion

The kinetic study of RNase P catalysis shows that a metal ion dependent conformational change step in the enzyme-substrate complex occurs following RNase P and pre-tRNA association [37, 38]. P4 helix is positioned at the core of the enzyme and essential for RNase P activity [42-45]. A reasonable hypothesis is that alterations in the structure of this helix are involved in the conformational change to arrange the active site structure optimally for enzyme catalysis. By using $R_{1\rho}$ ^{13}C and ^{15}N relaxation dispersion experiments, I characterized the TS of a P4 helix stem-loop mimic of *B. subtilis* RNase P. The data indicate a TS that includes changes in and around U7 and the A-tract regions, Additionally, U7 also has an individual process independent of the shared TS. The structure of the TS was probed by mutagenesis and atom modification in the stem-loop mimic. A 3D model was built from these data by using a MCSYM-LARMORD approach [50] suggesting the formation of a *syn* base at G6 and a kink in the backbone of A5, G6 and U7. This model is consistent with the result that G6-8BrG in the P4 helix mimic has a comparable chemical shift to the TS at A5, G6 and U7. Additionally, the DelA4 mutant eliminates the relaxation dispersion observed on the WT P4 mimic suggesting that the three adenosines are important for stabilizing the TS of the P4 helix mimic.

3.4.1 The Shared Transient State of the P4 Helix Mimic

3.4.1.1 The structure of the shared transient state

By using $R_{1\rho}$ relaxation dispersion NMR experiments, a shared TS was detected in and around the bulged U7 and A-tract regions of the P4 helix mimic while no chemical exchange was observed in the upper helix (above C8-G23 base pair) (Figure 3-3B, Figure B-2). Based on the chemical shift changes between the GS and the TS detected from $R_{1\rho}$ relaxation dispersion, a secondary structure of the TS was proposed (Figure 3-21). As shown in Figure 3-3, the chemical shifts of the sugar of U7 in the TS shift in the direction expected for a non-C3'-endo sugar pucker. Additionally, the chemical shift alterations indicate that G6 transits from *anti* to *syn* conformation, and the sugar shifts from an unusual C2'-endo to the C3'-endo direction. The 8BrG modification at G6 stabilizes the TS structure and interrupts the imino walk at G6 since no imino proton was observed for G6 (Figure 3-14A). These data are consistent with disruption of the Watson-Crick base pair between G6 and C24 in the TS. The chemical shifts for the sugar of A5 also shift in the C3'-endo direction in the TS. In contrast, other chemical shifts of residues around the A-tract move in the direction expected for a non-C3'-endo sugar pucker and adopt a conformation with less base stacking in the TS.

To interpret the structural change reflected by the chemical shift alterations and to obtain the insight into the TS structure, mutagenesis, chemical modification and drug titration of the stem-loop mimic were used. The NMR data observed upon titration with paromomycin suggests that the A-tract does not flip out of the helix in the TS (Figure 3-12). Furthermore, the discrepancy between the UV thermal melting temperature and the midpoint temperature calculated from relaxation dispersion (Figure 3-8B) indicates

that the TS of the P4 helix mimic is not simply caused by helix melting. However, the chemical shift comparison between single-strand RNA containing residues G2 to U11 from the P4 helix and the TS of the P4 helix mimic shows similar values at G2, A3 and A4 (Figure 3-10D). These data illustrate that the bottom part of the P4 helix mimic is likely partially or completed melted in the TS. However, other structural changes occur at nucleotides A5, G6 and U7 in addition to melting at bottom helix, which causes the NMR midpoint temperature to be higher than the UV thermal melting temperature.

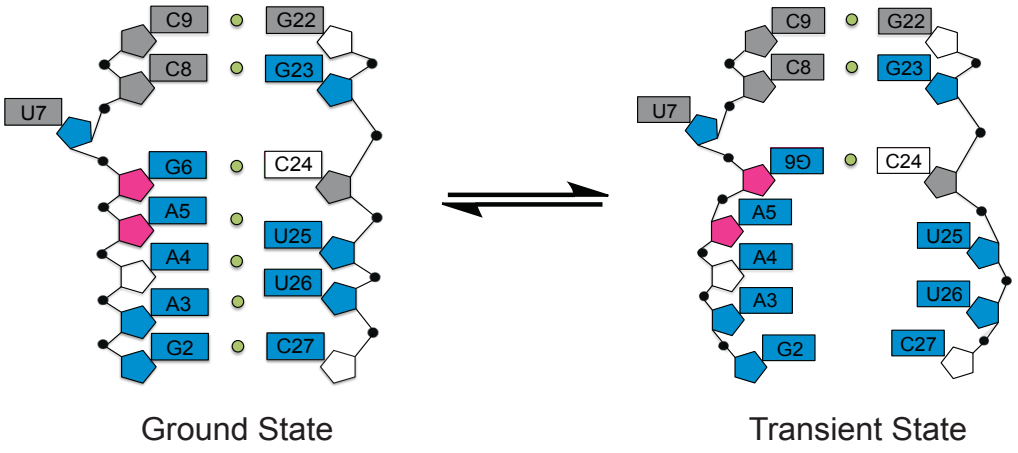

Figure 3-21: Secondary structures of the GS and the TS of the P4 helix mimic from *B. subtilis* PRNA. Chemical shifts alterations indicative of: increased stacking or movement in the direction expected for a C3'-endo sugar pucker are shown in pink; decreased stacking or *syn* glycosidic angle, or movement in the direction expected for a non-C3'-endo sugar pucker direction are shown in blue. Residues with little to no chemical exchange are grey and the residues not measured by $R_{1\rho}$ relaxation dispersion are white. The green dots indicate hydrogen bond and the upside down G6 base is indicative of the formation of a *syn* glycosidic angle.

According to the predicted model, the most significant structural changes between the GS and the TS of the P4 helix mimic occur in the region of A5 and G6, including a kink at the backbone between these nucleotides (Figure 3-19B). This kink can be attributed to changes to the sugar pucker at A5 and G6, as indicated by the downfield-shifted C1', In contrast, the sugar C1' resonance is shifted upfield for both U7 above and A-tract

below A5 and G6 (Figure 3-3C). These alterations in the sugar pucker are predicted to lead to a more helical conformation to the backbone of A5 and G6.

Furthermore, as mentioned before, the enormous 7.4 ppm downfield-shift of C8 at G6 (Figure 3-3C) strongly suggests that this base is in a *syn* conformation, as shown in the 3D model (Figure 3-19A). This conclusion is confirmed by the observation that substitution of G6 with 8BrG, which precludes the *anti* conformation and forces the base to the *syn* orientation [57-61], stabilizes the TS structure. In the G6-8BrG modified P4 helix mimic, the sugar C1' chemical shift of A5, G6 and U7 move in the same direction as the TS in comparison to the WT resonances (Figure 3-14C, D). This result suggesting that similar kink in the backbone is observed for both this modified helix and the TS. Even though the data indicate that G6 flips from *anti* to *syn* in the TS, no significant relaxation dispersion was detected for the G6 imino N1H1 (Figure B-2), likely due to the small chemical shift change for N1H1 in the TS.

The coupling between the G6 *syn* conformation and the formation of the kink in the backbone is demonstrated by alterations in the 3D model that are obtained using different subsets of chemical shift data obtained from relaxation dispersion. Exclusion of the chemical shift data of A5 leads to the same TS model with a backbone kink (Figure 3-20B). However, further excluding the base chemical shifts of G6 and U7 eliminates the kink between A5 and G6 (Figure 3-20A). Since there is no relaxation dispersion observed for the base of U7 (Figure B-2), the chemical shift exchange data on G6C8 is responsible for the kinked formation model in the 3D structure. In contrast, including the chemical shift data for the base of G6 and U7 but excluding the sugar data, leads to an alteration in the direction of a kink between A5 and G6 in the model (Figure 3-20B)

indicating that the kink conformation in the TS is also restrained by the sugar conformations of G6 and U7. In summary, these data suggest that in the TS, the A-tract region unwinds, G6 transits from *anti* to *syn* and a kink forms in the backbone between A5 and G6. This kink formation is coupled to formation of the *syn* base of G6 and restrained by the sugar conformation of G6 and U7.

3.4.1.2 The *syn* G6 stabilized kink forms a pocket favorable for metal ion binding

The occurrence of *syn* geometries in RNA depends in a complex manner, including in the environment of abundant with unstable structure or structurally stressful [62, 76-78]. In helical regions, a *syn* conformation for bases is strongly disfavored owing to disruption of the helix [61]. However, this conformer can be populated either by stabilization through hydrogen bonding and/or base stacking or by steric repulsion of the *anti* conformer [62]. Therefore, the *syn* nucleobase conformation is typically observed in tertiary structures, such as kinks and turns, stacking interactions and tertiary base pairs [62, 76-83]. While only a few X-ray structures have documented the existence of bases with a *syn* conformation in RNA, there are biochemical and NMR studies that have demonstrated the prevalence of the *syn* nucleobase conformer in RNA [60, 61, 81, 84-86]. Some of *the* syn conformers are located in the active site of RNA and are functionally significant, including involvement in tertiary structure packing, participation in ligand binding (metal ion, small molecule) and/or orientation of atoms for catalysis [60, 62, 78, 86-90].

Additionally, NMR data demonstrate that base pairs in a canonical DNA double helix undergo transient flipping to a Hoogsteen geometry in which the purine adopts the *syn*

conformation [63, 64]. This observation indicates the possibility that transient *syn* conformers might exist in RNA as well. A previous study reported evidence for a transient *syn* base at the apical loop of HIV TAR that forms a *trans*-wobble GU base pair [91]. However, no transient *syn* base has yet been observed within a helix.

In this study, a transient *syn* nucleobase was observed on G6 of the P4 helix mimic, where a bulged U7 is above and a backbone kink is underneath (Figure 3-19). This structural environment is similar to the *syn* base observed at P4-P6 in group I intron by crystal structure [84]. Purines with *syn* conformation have been proposed to lead to a kink in the backbone [62, 83]. The *syn* G6 in the P4 helix mimic is coupled to formation of the kink in the backbone and these structural changes may create a favorable metal ion binding pocket. The electrostatic potential calculation shows increased formation of negative charge on the kinked backbone between A5 and G6 in the TS (Figure 3-22), which is favorable for metal ion binding. Therefore, we propose that the kink between A5 and G6 stabilized by *syn* G6 creates a cleft to bind metal ion. Consistent with this proposal, saturating Mg^{2+} causes the sugar chemical shift of A5, G6 and U7 to move in the same direction as the shifts in the TS (Figure 3-17B), suggesting that Mg^{2+} binding stabilizes a structure with similarity to the TS. A similar kink coupled to a *syn* base has been observed in the lead-enzyme where a *syn* guanosine at the core of the active site restrains the backbone structure and facilitates binding of lead to a backbone oxygen [60, 79].

In full-length *B. subtilis* PRNA, the non-bridging oxygens at the backbone of A40 and G50 (A5 and G6 in the P4 helix mimic) bind one or more metal ions important for RNase P catalysis [43, 44]. Disruption of this metal ion site decreases the rate constant

of RNase P-catalyzed cleavage of pre-tRNA by 300- to 10^4-fold [43, 44]. Remarkably, the structural models of the P4 mimic propose that the conformational changes in the TS enhance a metal binding site in the backbone between A5 and G6, at the exact metal binding site in PRNA. This correlation leads to the speculation that the metal-dependent conformational change that occurs after substrate binding in RNase P may have structural similarities to the TS in the stem-loop mimic.

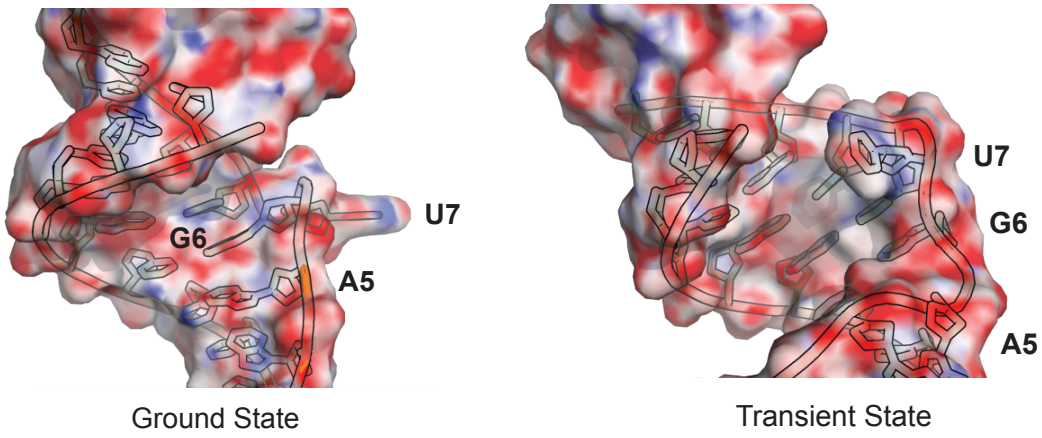

Figure 3-22: Surface electrostatic potential for the GS (left) and the TS (right) of the P4 helix mimic from *B. subtilis* PRNA. Negative charges on the backbone of the kink between A5 and G6 create a binding pocket for metal ion.

3.4.1.3 Examining the possible formation of a Hoogsteen base pair between G6 and C24

The transient *syn* G6 observed in the P4 helix mimic could form a Hoogsteen base pair with C24 on the other side of the helix. Transient Hoogsteen base pairs have been reported before in DNA duplex for both A-T and G-C^+ base pairs [63, 64]. Formation of a Hoogsteen GC base pair requires protonation of cytosine N3 (Figure 3-15). The protonation of this position in the TS could be detected by relaxation dispersion on C6 of the cytosine, downfield-shifted C6 chemical shift, and pH dependent relaxation

dispersion measured at carbon sites [63]. In the P4 helix mimic, a small pH dependence on the relaxation dispersion was observed, however, the pH-dependent change in population is smaller than previously observed for the transient Hoogsteen base pair in DNA (Table 3-3) [63, 64]. Unfortunately, it was not possible to further examine this possibility by evaluating chemical exchange of the C6 resonance at position 24 since this resonance overlaps with other peaks in the ^{13}C-^{1}H correlation (Figure 3-2).

In the previous study, the transient Hoogsteen base pair was trapped using chemical modifications, such as N1-methylated adenosine (1mA) or N1-methylated guanosine (1mG) [63]. In the G10-1mG modified DNA duplex, the protonated cytosine (C15) in the Hoogstein base pair perturbs neighboring protons, lead to a downfield-shifted C15H4 and perturbation of the chemical shift of H1' [63]. However, in the P4 helix mimic substitution of 8BrG for G6, which stabilizes the TS structure, had no effect on the proton chemical shift (H4, H5, H6 and H1') of cytosine (C24) on the other side of the helix at neutral pH (Figure 3-14). This suggests that C24 is likely not protonated as required for Hoogsteen base pair formation. In the future, lowering the pH to 5.4 or 5.2 to enhance protonation of cytosine, could test the possibility that a Hoogsteen base pair at this position is stabilized by acidic conditions. The G6-1mG modification was also examined to explore formation of a Hoogsteen base pair. In this case, peak perturbations were observed for H4, H5 and H6 of C24 (Figure B-5C, D, E), which could be explained by either protonation or enhanced dynamics. However, the weak C6H6 resonance and the disappearance of the H1'-H6 and C1'H1' resonances of C24 argue against formation of stable Hoogsteen base pair (Figure B-5C). Furthermore, the 1mG substitution for the Hoogsteen base paired G10 in DNA duplex has a strong H1'-H8

NOE cross peak and downfield-shift C8 indicative of *syn* [63, 75], while the 1mG substitution for G6 in the P4 helix has a similar downfield-shifted C8 but shows a significantly weaker H1'-H8 NOE peak (Figure B-5C) suggesting that the 1mG nucleobase is dynamic. These results suggest that G6 and C24 do not form a stable base pair in the TS. Taken together, the data indicate that the *syn* G6 is unlikely forming a Hoogsteen base pair with C24 in the TS.

Overall, the shared TS of the P4 helix mimic includes helical unwinding of the A-tract region, transiting G6 from *anti* to *syn* and formation of a kink in the backbone between A5 and G6. The evidence suggests that *syn* G6 is coupled to the formation of a kink in the backbone and these structural changes create cleft with an enhanced electrostatic environment for binding a metal ion. This transition between the GS and the TS could be related to the conformational change in RNase P•pre-tRNA complex, which enhances substrate and metal ion binding affinity and facilitates the catalysis [38, 39]. The correlation between the TS of the P4 helix mimic and the conformational change during RNase P catalysis will be further discussed in Chapter 4.

3.4.2 The Flexible Helical Formation of the P4 Helix Mimic is Important for the Transition between the GS and the TS

The ^{15}N-^{1}H imino HSQC and NOE imino walk of the WT P4 stem-loop mimic show weak or unstable base pairs between three adenosines (A3, A4 and A5) and two uridines (U25 and U26) on the other side of the helix (Figure 3-2A, F). But the data indicate that none of these residues loop out and they all stay in a helical conformation (Figure 3-2C). This indicates a flexible and highly dynamic helical conformation at A-

tract region. Compared with WT, deletion of one adenosine of the A-tract (DelA4) results in a stable helix containing strong Watson-Crick base pairs between A3-U26 and A5-U25 in the P4 helix mimic (Figure 3-4A, C) suggesting the formation of a more stable helix structure than P4 WT. Consistent with this, UV thermal melting data demonstrate that DelA4 has a higher melting temperature than P4 WT (Figure 3-8B). Furthermore, the DelA4 mutant eliminates the relaxation dispersion detected on P4 WT (Figure 3-5) and significantly destabilizes the TS. These results demonstrate that a flexible helix at A-tract region is important for the formation of the TS. The reasonable explanation for this is that melting of A-tract region occurs in the TS and a weakly base-paired region requires less energy to unwind compared with breaking two stable Watson-Crick base pairs in DelA4. Therefore, the TS is more accessible. Additionally, the function of that A-tract unwinding is probably to facilitate the kink formation by allowing adjustments in the backbone conformation of A5 and G6 when G6 flips from *anti* to *syn*. These rearrangements are likely hindered by the strong and stable base pairs formed in DelA4 that stabilize a canonical helical conformation.

3.4.3 Base Flipping of the Bulged U7 Contributes the TS

In addition to the shared TS structure discussed above, a second transition is observed on the bulged U7 and neighboring G6 and C8 at saturating Mg^{2+}. This process is only observed in the presence of high concentration of Mg^{2+} (Figure 3-18B) where the shared TS is not detectable due to peak line broadening caused by Mg^{2+}. This process has a faster exchange rate constant, greater population and different chemical shift change than the shared TS (Figure 3-18C, Table 3-5). This result

indicates that this transition is independent and separate from the previously described TS. Consistent with this conclusion, the bulged U7 transition process is observed in the DelA4 mutant (Figure 3-18B), where the shared TS is significantly diminished (Figure 3-5). This result is also consistent with the observed flexibility of U7 and C8 in a mutant P4 mimic containing 3 A-U base pairs in the A-tract region (Figure 3-1) [49].

In the GS of the WT P4 mimic, U7 adopts a bulged out formation. The chemical shift change between the ground state and the second TS indicates that U7 is either more stacked or has a more helical conformation. This result could be explained by flipping the uridine into the helix in the TS, painting a picture of U7 flipping in and out of the P4 helix mimic between the GS and the TS with a faster motion compared to the shared GS to TS transition. The relaxation dispersion observed on G6 and C8 at high Mg^{2+} probably reflects movement of the bulged U7.

Crystal structures of RNase P suggest that the conserved uridine (U7 in P4 helix mimic, U51 in RNase P, *B. subtilis* numbering) adopts two different conformations (Figure 3-23A). An apo-PRNA only structure (*B. stearothermophilus*) shows the uridine looped out of the helix [48, 92]. In contrast, the crystal structure of *T. maritima* RNase P ternary complex shows the conserved uridine in an inward conformation. The differences between the secondary structures of the A-type (*T. maritima*) and B-type P RNA (*B. stearothermophilus)* could be a possible explanation for this difference. However, solution structure probing indicates that the conserved bulged uridine is largely solvent exposed in both A-type and B-type P RNAs [47]. This result is consistent with the “flipped out” conformation observed in the apo-PRNA only crystal structures [48, 92].

In the current study, two conformations of U7 are observed. The GS structure is consistent with the apo-PRNA only crystal structures (Figure 3-23B) where the bulged U is flipped out of the helix and the TS is similar to the structure of this base in the RNase P ternary complex (Figure 3-23C) at U7. These crystal structures could reflect two different conformers, in and out of the P4 helix, of the conserved uridine under different conditions. In the presence of divalent metal ion and substrate, the conserved uridine in RNase P is stabilized in flipped into the helix, probably to position a catalytic/co-catalytic metal ion or stabilize an active conformer of the enzyme-substrate complex, while it tends to stay looped out in the absence of metal ion and substrate. This explanation is supported by identification of an inner-sphere metal ion binding site on the O4 of U51 base in *B. subtilis* RNae P [42] (Xin Liu, Yu Chen, and Carol A. Fierke, manuscript in preparation). Furthermore, it is also consistent with the detection of the TS on U7 only in the presence of a high concentration of Mg^{2+} either because this process is metal ion dependent or the presence of Mg^{2+} slows down this fast process into the time scale where the TS is detectable by $R_{1\rho}$ relaxation dispersion (see discussion below). This latter possibility is supported by previous studies showing that U7 and C8 in a mutant P4 are locally mobile at the picosecond-to-nanosecond timescale in the absence of Mg^{2+} [49]. This is much faster than relaxation dispersion detection timescales, which explains why the separated TS is not observable in the absence of Mg^{2+} [15, 27]. Bulged nucleotides are common motifs in folded RNA molecules and have been shown to associate with ligand binding and conformational transitions [21, 93-95]. Therefore, it is possible that the movement of the bulged uridine stabilizes a metal ion or assists in the formation of the active ES* complex in the RNase P catalytic cycle. Taken together,

that data suggest that U7 adopts a bulged out conformation in the GS and flips into the helix in the TS. This process has a faster motion and is independent of the shared transition from the GS to the TS of the P4 helix mimic.

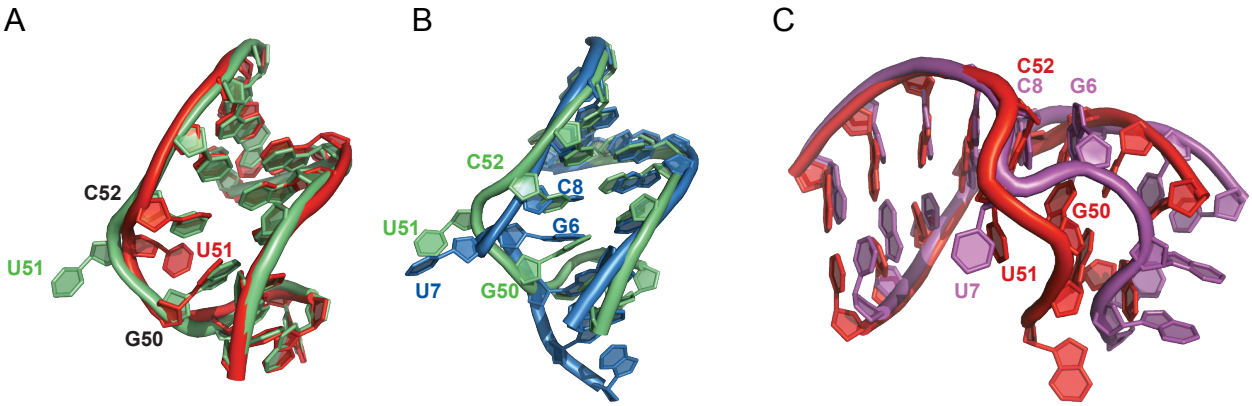

Figure 3-23: U7 in the P4 helix mimic (U51 in RNase P, *B. subtilis* numbering) adopts two different conformations between the GS and the TS. (A) The universally conserved uridine in P4 helix is in different conformations between apo-PRNA only and RNase P ternary complex. An overlay of the P4 helix region in crystal structures of the *B. stearothermophilus* PRNA (PDB ID: 2A64, green) [48] showing conserved uridine is bulged out, and the *T. maritima* RNase P ternary complex (PDB ID: 3Q1R, red) [42] showing conserved uridine is in an inward position. The RMSD is 0.84 by superimposing the helix using PyMOL software. (B) U7 in P4 helix is bulged out of the helix in the GS. An overlay of the model of the GS of the P4 helix mimic using MCSYM-LARMORD approach (blue), and the P4 helix region in crystal structures of the *B. stearothermophilus* PRNA (PDB ID: 2A64, green) [48]. The RMSD is 1.38 by superimposing the helix using PyMOL software. (C) U7 in P4 helix flips inward the helix in the TS. An overlay of the model of the TS of the P4 helix mimic using MCSYM-LARMORD approach (purple), and the P4 helix region in crystal structures of the *T. maritima* RNase P ternary complex (PDB ID: 3Q1R, red) [42]. The RMSD is 1.12 by superimposing the helix using PyMOL software.

3.4.4 Mg^{2+} Decreases the Population and Exchange Rate Constant of the TS

In the presence of low concentration of Mg^{2+}, the relaxation dispersion of the P4 helix mimic shows similar chemical exchange as without Mg^{2+}, but with a smaller population of the TS and a slower exchange rate constant (Figure 3-18A, C, Table 3-4). RNA is a highly negatively charged polyelectrolyte and the charge neutralization is presumably achieved through the interaction with positively charged mono- and divalent cations [9, 96]. Divalent metal ions play an important role in thermal stabilization of RNA structure

by interacting with various sites in RNA, including phosphoryl backbone oxygen, carbonyl oxygen of guanine (O6) and uracil (O4), and N7 of guanine [96]. Electrostatic interactions with cations allow the neighboring phosphate and opposite sugar-phosphate in RNA to minimize the charge repulsion as they approach each other [9, 96]. Crystallographic data and NMR studies have shown that divalent metal ions can bind deep in the major groove or in the outer mouth of the narrow major groove in RNA and A-form DNA [97]. The reduced population and rate constant for the formation of the TS could be a consequence of Mg^{2+} binding nonspecifically to the major groove [49, 97]. Such binding can induce groove compression and could thereby obstruct the A-tract region unwinding and the *anti* to *syn* rotation of guanosine base. A similar effect was previously observed for a decrease in the population and exchange rate constant of the transient Hoogsteen G-C^+ base pair in a DNA duplex in the presence of Mg^{2+} [75].

3.5 Conclusion

The dynamics of the P4 helix mimic from *B. subtilis* RNase P was studied by ^{13}C and ^{15}N $R_{1\rho}$ relaxation dispersion NMR experiments and two transient states were detected. One is shared process for the P4 helix mimic and a 3D structure model of the TS was predicted using MCSYM-LARMORD approach. This TS includes A-tract region unwinding, transition of G6 from *anti* to *syn* and a kink formation on the backbone between A5 and G6. The flexible helical conformation of the A-tract stabilizes the shared TS. The kink formation is coupled to G6 flipping from *anti* to *syn* and leads to the formation of a pocket with increased negative charge that could be a favorable binding site for metal ion. The second process is an independent motion of the bulged U7

flipping in and out of the helix that is observable at high Mg^{2+}.

The dynamical properties of RNA structures play an important role in conformational changes. This study identifies a transient conformer of the P4 helix mimic and it is the first time that a transient *syn* base has been detected in an RNA double helix. The function of this transient *syn* guanosine is to kink the backbone and create a cleft for metal ion binding. The TS of the P4 helix mimic visualized here can potentially supply structural information for metal ion binding sites and conformational change step during RNase P catalysis.

3.6 Materials and Methods

3.6.1 Materials and Reagents

The chemicals, enzyme and buffers used here same as in Chapter 2 were prepared as described unless otherwise specified. Sodium cacodylate were purchased from Sigma at the highest purity (BioXtra, ≥98%). NMR buffer and buffer for UV thermal melting experiments were prepared by Milli-Q (Millipore Corporation) treated deionized water and sterilized by autoclave. Deuterium oxide for H_2O+D_2O NMR experiments was purchased from Fisher Scientific (99.8%, ACROS Organics^{TM}) and for D_2O only experiments was from ISOTEC, Inc., Cambridge Isotope Labs (99.99%). Uniformly $^{13}C/^{15}N$-labeled nucleotide triphosphates were purchased from ISOTEC, Inc., Cambridge Isotope Labs. Synthetic DNA templates for *in vitro* RNA transcription were purchased from Integrated DNA Technologies, Inc. The ribooligonucleotides with N1-methylated guanosine was purchase from GE Dharmacon and the ribooligonucleotides

containing 8-bromoguanosine was synthesized by Kierzek's lab in Polish Academy of Science.

3.6.2 Sample Preparation and Purification for NMR

3.6.2.1 $^{13}C/^{15}N$-labeled WT and mutants of P4 helix stem-loop mimic samples

P4 samples were prepared as previous described by *in viro* transcription using T7 RNA polymerase [49, 51, 98], uniformly $^{13}C/^{15}N$-labeled nucleotide triphosphates and synthetic DNA templates containing the T7 promoter and sequence of interest. Then all RNA transcripts were purified by 22% (w/v) denatured PAGE, passively eluted, concentrated in Amicon Ultra-15 Centrifugal Filter Unit (3,000 MWCO, Millipore Corp.) and precipitated with ethanol. The RNA pellets were dissolved in water, annealed by heating to 95°C for 5 min and cooling on ice, then buffer exchanged into NMR buffer (15 mM NaH_2PO_4, 25 mM NaCl and 0.1 mM EDTA at pH 5.4, 6.8 or 7.6) with or without 5 mM or 44 mM $MgCl_2$ using an Amicon Ultra-4 Centrifugal Filter Unit (3,000 MWCO, Millipore Corp.). 10% of 99.9% D_2O was added into the sample before the experiment. The final concentration of the RNA sample is 2.3 - 2.5 mM. For NMR experiments in ~100% D_2O, the sample in the NMR buffer was lyophilized for 24 h first, followed by adding 99.99% D_2O (Cambridge Isotope Labs) and lyophilized again for 24 h. The lyophilized pellet was finally dissolved in the same volume of D_2O as the NMR buffer.

3.6.2.2 $^{13}C/^{15}N$-labeled single-strand RNA sample

The single-strand RNA was prepared differently. A plasmid of *B. subtilis* pre-$tRNA^{Asp}$ where the leader sequence contains the ribooligonucleotide of interest (5'-GAA AGU

CCA U-3') is designed by using pre-tRNA^{Asp}-5 as a template for PCR (Primers: 5'- TAA TAC GAC TCA CTA TAG AAA GTC CAT GGT CCG GTA GTT CAG-3'; 5'-CTA GAG GAT CCT GGC GGT CCG GAC GGG ACT CG-3') to create a DNA fragment beginning with a T7 RNA promoter followed by pre-tRNA^{Asp} with interested leader sequence then followed by the sequence recognized by the restriction enzyme *BstN1* (New England Biolabs). This DNA fragment was then subcloned into plasmid pUC18 at the blunt site created by digestion with *Sma*I (NEB) to create plasmid pre-tRNA^{Asp}-10. After *in vitro* transcription as previous described [38, 99] by using uniformly $^{13}C/^{15}N$-labeled nucleotide triphosphates, *B. subtilis* RNase P, prepared as described before [100, 101], was used to cleave the leader from the precursor-tRNA^{Asp}-10, producing an oligonucleotide with a defined 3' hydroxyl end that contains $^{13}C/^{15}N$ labels. The cleavage reaction was performed under multiple-turnover condition (750 nM of RNase P and 225 μM of precursor-tRNA^{Asp}-10) in 50 mM Tris-MES, pH 8.0, 20 mM $MgCl_2$ and 200 mM KCl at 37°C. Then the single-strand RNA was PAGE purified, ethanol precipitated and buffer exchanged into NMR buffer, pH 6.8 then add 10% of D_2O as described above. The final concentration of single-strand RNA is 1 mM.

3.6.2.3 Unlabelled-modified RNA samples

G6-N1mG and G6-8BrG modified P4 helix mimic at natural isotopic abundance were either purchased or synthesized, then purified by HPLC. The sample was buffer exchanged into NMR buffer, pH 5.4 or 6.8, then 10% of D_2O was added before the data collection. The final concentration of modified P4 helix mimic is 1 mM.

3.6.2.4 Resonance Assignment

The experiments were acquired on an Agilent 600-MHz spectrometer, an Agilent 800-MHz spectrometer or a Bruker Avance 600-MHz NMR spectrometer equipped with a triple-resonance cryogenic probe. Resonance assignment for exchangeable and non-exchangeable ^{1}H was performed using the 2D ^{1}H-^{1}H WATERGATE Nuclear Overhauser effect spectroscopy (NOESY) experiment as described previously [102], and their covalently bonded aromatic ^{13}C-^{1}H, aliphatic ^{13}C-^{1}H and imino ^{15}N-^{1}H were assigned using heteronuclear single/multiple quantum coherence correlation experiments (HSQC or HMQC). For the labeled RNA constructs conventional HSQC experiments were acquired for all spins [102], while for unlabeled RNA constructs conventional HSQC was used for the aliphatic C1′ aromatic C5 spins [102] and band-selective optimized flip angle short-transient (SOFAST) HMQC were employed for the imino and aromatic spins [103, 104]. All data were processed by using the software NMRpipe [105] and analyzed by SPARKY (T. D. Goddard and D. G. Kneller, SPARKY 3, University of California, San Francisco).

3.6.3 Carbon and Nitrogen $R_{1\rho}$ Relaxation Dispersion

All NMR relaxation dispersion experiments were performed on a Bruker Avance 600-MHz NMR spectrometer equipped with a triple-resonance cryogenic probe. Experiments were performed at 15°C, 25 °C or 37 °C using uniformly ^{13}C/^{15}N-labeled P4 helix mimic samples. Rotating frame carbon and nitrogen $R_{1\rho}$ relaxation dispersion data were measured using a 1D acquisition scheme that extends the sensitivity to chemical exchange into millisecond timescales relative to conventional 2D relaxation dispersion

methods [27, 106-108]. On- and off-resonance relaxation dispersion data were recorded at various offset frequencies and spinlock powers listed in Appendix B. Data were processed using NMRpipe [105] and the $R_{1\rho}$ values were computed by fitting the resonance intensities with monoexponential decays using Mathematica 6.0 script (Wolfram Research, Inc.) [109]. Errors in $R_{1\rho}$ were determined using the standard Monte Carlo simulations with 500 iterations. Measured on- and off-resonance relaxation dispersion data were fitted to the two-state Laguerre equation [16] [110] using Origin 8.5.1 (OriginLab).

Two-state Laguerre equation:

$$R_{1\rho} = R_1 cos^2\theta + R_2 sin^2\theta + \frac{sin^2\theta p_{GS} p_{TS} \Delta\omega^2 k_{ex}}{\frac{\omega_{GS}^2 \omega_{TS}^2}{\omega_{eff}^2} + k_{ex}^2 - sin^2\theta p_{GS} p_{TS} \Delta\omega^2 \left(1 + \frac{2k_{ex}^2 (p_{GS}\omega_{GS}^2 + p_{TS}\omega_{TS}^2)}{\omega_{GS}^2 \omega_{TS}^2 + \omega_{eff}^2 k_{ex}^2}\right)}$$

Equation 12

R_1 and R_2 are the intrinsic longitudinal and transverse relaxation rates, respectively (assumed to be identical for GS and TS). $k_{ex} = k_{GS\text{-}TS} + k_{TS\text{-}GS}$ is the exchange rate constant for a two-state equilibrium, where $k_{GS\text{-}TS} = p_{TS}k_{ex}$ and $k_{TS\text{-}GS} = p_{GS}k_{ex}$ are the forward (GS to TS) and reverse (TS to GS) rate constants, respectively. p_{GS} and p_{TS} are the ground and excited state fractional population respectively ($p_{GS} + p_{TS} = 1$). The chemical shift difference between the ground state and transient state is given by $\Delta\omega = \Omega_{TS} - \Omega_{GS}$. The average effective spinlock field in the rotating frame is given by $\omega_{eff}^2 = \Omega^2 + \omega_{SL}^2$, $\omega_{GS}^2 = (\Omega_{GS}\text{-}\omega_{rf})^2 + \omega_{SL}^2$ and $\omega_{TS}^2 = (\Omega_{TS}\text{-}\omega_{rf})^2 + \omega_{SL}^2$, where ω_{SL} is the spinlock power, $\Omega = \Omega_{obs} - \omega_{rf}$ is the offset of the spinlock carrier frequency (ω_{rf}) from

the averaged resonance frequency (Ω_{obs}), $\Omega_{obs} = \Omega_{GS} p_{GS} + \Omega_{TS} p_{TS}$. The tilt angel in the rotating frame is given by θ = arctan (ω_{SL}/Ω).

3.6.4 Experiments in the presence of Mg^{2+}

125 mM or 1 M of $MgCl_2$ was gradually titrated into 2.3 mM of the P4 WT sample until no further peak perturbation observed by additional $MgCl_2$ to get 44 mM $MgCl_2$ is the saturating concentration. The P4 WT or DelA4 sample was then dialyzed into 15 mM NaH_2PO_4, 25 mM NaCl, 0.1 mM EDTA and 5 mM or 44 mM $MgCl_2$ under pH 6.8 at 25°C. 2D aromatic ^{13}C-^{1}H, aliphatic ^{13}C-^{1}H and imino ^{15}N-^{1}H was acquired again and relaxation dispersion was measured.

3.6.5 Thermodynamics Analysis

The observed temperature dependent analysis of forward and reverse rate constants in the WT P4 helix mimic was fit by equation:

$$ln\left(\frac{k_i(T)}{T}\right) = ln\left(\frac{k_B \kappa}{h}\right) - \frac{\Delta G_i^T}{RT_{hm}} - \frac{\Delta H_i^T}{R}\left(\frac{1}{T} - \frac{1}{T_{hm}}\right) \qquad \textbf{Equation 13}$$

where k_i (i = GS-TS, TS-GS) is the forward and reverse rate constant of the two-state equilibrium, ΔG_i^T and ΔH_i^T are the free energy and enthalpy of activation, respectively, R is the universal gas constant, T is the temperature in Kelvin and T_{hm} is the harmonic mean of the experimental temperatures calculated as $T_{hm} = n/\sum_{i=1}^{n}(1/T_i)$. k_B is Boltzmann's constant, h is Planck's constant, κ is the transmission coefficient (assumed to be 1) in the pre-exponential factor of Eyring's theory. ΔG_i^T and ΔH_i^T was calculated from the intercept and slop of the Van't Hoff plots. To calculate NMR midpoint

temperature, the populations of both GS and TS were set to 50% and the forward and reverse rate constants were equal. By using equation:

$$\frac{\Delta G^{T}_{GS-TS}}{RT_{hm}} + \frac{\Delta H^{T}_{GS-TS}}{R}\left(\frac{1}{T} - \frac{1}{T_{hm}}\right) = \frac{\Delta G^{T}_{TS-GS}}{RT_{hm}} + \frac{\Delta H^{T}_{TS-GS}}{R}\left(\frac{1}{T} - \frac{1}{T_{hm}}\right) \quad \textbf{Equation 14}$$

the NMR midpoint temperature was calculated.

3.6.6 UV Thermal Melting Experiments

The UV thermal melting experiments were performed with a Cary 100 Bio UV-Visible spectrometer equipped with a temperature controller and thermostated cell holder. 1 ml sample containing 1.5 μM P4 helix mimic was annealed by heating to 95°C for 5 min and cooling on ice, then prepared in 15 mM NaCac, 25 mM NaCl, pH 6.8 buffer and placed in quartz semi-micro cuvette capped with Telflon stopper. The sample was incubated at 25 °C for 10 min and the data were collected at 260 nm from 25 °C to 95 °C with a temperature ramp 0.5 °C/min increment. The buffer only was the background control. The experiments were repeated three times individually and the data were analyzed by Cary 100 Bio to caculate T_m.

3.6.7 MCSYM-LARMOR 3D RNA Structure Modeling

Representative models of the P4 helix mimic were generated using MC-Fold and MC-Sym webserver pipeline ([111]). Specifically, MC-Sym was used to generate 3D models for 20 lowest energy secondary structures predicted using MC-Fold. All MC-Sym modeling utilized the default webserver settings. In total, 15,994 models were returned by the webserver. Each model was then energy minimized to remove steric clashes.

Non-exchangeable ^{13}C (C1', C5, C6 and C8) and ^{15}N imino (N1 and N3) chemical shifts were used to identify models that were in best agreement between experimentally and predicted chemical shifts for the GS and the TS of the P4 helix mimic, respectively. From each energy-minimized MC-Sym generated model, ^{13}C and ^{15}N imino chemical shifts were back-predicted for residues 2-11 and 19-27 (Figure 3-1) using LARMORD chemical shift predictor [50]. The models with the lowest total error between measured and predicted chemical shifts were then selected as the representative models of the P4 GS and TS, respectively. Here the total error (χ^2) is given by

$$\chi^2 = \frac{1}{N_{CS}} \sum_{i=1}^{N_{CS}} w_i (\delta_i^{\text{meas}} - \delta_i^{\text{pred}})^2 \qquad \textbf{Equation 15}$$

where the weighting factors (w_i) were used to account for the differential accuracy of the predictors is given by

$$w_i = \frac{R_i}{\text{MAE}_i} \qquad \textbf{Equation 16}$$

where R_i and MAE_i are the estimated Pearson correlation coefficient and mean absolute error, respectively, between measured and LARMORD^D predicted chemical shifts for the nucleus type associated with *i*.

3.6.8 Electrostatic Potential Calculations.

The electrostatic properties of the models consistent with the GS and the TS chemical shifts were compared by visualizing their electrostatic potentials. For each representative model, the electrostatic potential were calculated by solving the Poisson-Boltzmann equation (PBEQ) using the CHARMM-GUI PBQE solver [112-114]. The

surface electrostatic potentials were then visualized with the potentials levels ranging between -20.0 kcal/(mol·*e*) and +20.0 kcal/(mol·*e*).

3.7 References

1. Doudna, J.A., *Structural genomics of RNA.* Nat Struct Biol, 2000. **7 Suppl**: p. 954-6.
2. DeRose, V.J., *Metal ion binding to catalytic RNA molecules.* Curr Opin Struct Biol, 2003. **13**(3): p. 317-24.
3. Steitz, T.A. and Moore, P.B., *RNA, the first macromolecular catalyst: the ribosome is a ribozyme.* Trends Biochem Sci, 2003. **28**(8): p. 411-8.
4. Szymanski, M. and Barciszewski, J., *Regulation by RNA.* Int Rev Cytol, 2003. **231**: p. 197-258.
5. Gebauer, F. and Hentze, M.W., *Molecular mechanisms of translational control.* Nat Rev Mol Cell Biol, 2004. **5**(10): p. 827-35.
6. Leontis, N.B. and Westhof, E., *Analysis of RNA motifs.* Curr Opin Struct Biol, 2003. **13**(3): p. 300-8.
7. Moore, P.B., *Structural motifs in RNA.* Annu Rev Biochem, 1999. **68**: p. 287-300.
8. Tinoco, I., Jr. and Bustamante, C., *How RNA folds.* J Mol Biol, 1999. **293**(2): p. 271-81.
9. Draper, D.E., *A guide to ions and RNA structure.* RNA, 2004. **10**(3): p. 335-43.
10. Kortmann, J. and Narberhaus, F., *Bacterial RNA thermometers: molecular zippers and switches.* Nat Rev Microbiol, 2012. **10**(4): p. 255-65.
11. Al-Hashimi, H.M., *Dynamics-based amplification of RNA function and its characterization by using NMR spectroscopy.* Chembiochem, 2005. **6**(9): p. 1506-19.
12. Prestegard, J.H., al-Hashimi, H.M., and Tolman, J.R., *NMR structures of biomolecules using field oriented media and residual dipolar couplings.* Q Rev Biophys, 2000. **33**(4): p. 371-424.
13. Tolman, J.R., *Dipolar couplings as a probe of molecular dynamics and structure in solution.* Curr Opin Struct Biol, 2001. **11**(5): p. 532-9.
14. Palmer, A.G., 3rd, *NMR characterization of the dynamics of biomacromolecules.* Chem Rev, 2004. **104**(8): p. 3623-40.
15. Palmer, A.G., 3rd, Kroenke, C.D., and Loria, J.P., *Nuclear magnetic resonance methods for quantifying microsecond-to-millisecond motions in biological macromolecules.* Methods Enzymol, 2001. **339**: p. 204-38.
16. Palmer, A.G., 3rd and Massi, F., *Characterization of the dynamics of biomacromolecules using rotating-frame spin relaxation NMR spectroscopy.* Chem Rev, 2006. **106**(5): p. 1700-19.
17. Mittermaier, A.K. and Kay, L.E., *Observing biological dynamics at atomic resolution using NMR.* Trends Biochem Sci, 2009. **34**(12): p. 601-11.
18. Furtig, B., et al., *NMR spectroscopy of RNA.* Chembiochem, 2003. **4**(10): p. 936-62.
19. Lee, J.H. and Pardi, A., *Thermodynamics and kinetics for base-pair opening in the P1 duplex of the Tetrahymena group I ribozyme.* Nucleic Acids Res, 2007. **35**(9): p. 2965-74.
20. Johnson, J.E., Jr. and Hoogstraten, C.G., *Extensive backbone dynamics in the GCAA RNA tetraloop analyzed using 13C NMR spin relaxation and specific isotope labeling.* J Am Chem Soc, 2008. **130**(49): p. 16757-69.
21. Blad, H., et al., *Dynamics and metal ion binding in the U6 RNA intramolecular stem-loop as analyzed by NMR.* J Mol Biol, 2005. **353**(3): p. 540-55.
22. Latham, M.P., Zimmermann, G.R., and Pardi, A., *NMR chemical exchange as a probe for ligand-binding kinetics in a theophylline-binding RNA aptamer.* J Am Chem Soc, 2009. **131**(14): p. 5052-3.
23. Al-Hashimi, H.M. and Walter, N.G., *RNA dynamics: it is about time.* Curr Opin Struct Biol, 2008. **18**(3): p. 321-9.
24. Mittermaier, A. and Kay, L.E., *New tools provide new insights in NMR studies of protein dynamics.* Science, 2006. **312**(5771): p. 224-8.

25. Latham, M.P., et al., *NMR methods for studying the structure and dynamics of RNA.* Chembiochem, 2005. **6**(9): p. 1492-505.
26. Shajani, Z. and Varani, G., *NMR studies of dynamics in RNA and DNA by 13C relaxation.* Biopolymers, 2007. **86**(5-6): p. 348-59.
27. Hansen, A.L., et al., *Extending the range of microsecond-to-millisecond chemical exchange detected in labeled and unlabeled nucleic acids by selective carbon R(1rho) NMR spectroscopy.* J Am Chem Soc, 2009. **131**(11): p. 3818-9.
28. Kazantsev, A.V. and Pace, N.R., *Bacterial RNase P: a new view of an ancient enzyme.* Nat Rev Microbiol, 2006. **4**(10): p. 729-40.
29. Smith, J.K., Hsieh, J., and Fierke, C.A., *Importance of RNA-protein interactions in bacterial ribonuclease P structure and catalysis.* Biopolymers, 2007. **87**(5-6): p. 329-38.
30. Kirsebom, L.A., *RNase P RNA mediated cleavage: substrate recognition and catalysis.* Biochimie, 2007. **89**(10): p. 1183-94.
31. Walker, S.C. and Engelke, D.R., *Ribonuclease P: the evolution of an ancient RNA enzyme.* Crit Rev Biochem Mol Biol, 2006. **41**(2): p. 77-102.
32. Hartmann, E. and Hartmann, R.K., *The enigma of ribonuclease P evolution.* Trends Genet, 2003. **19**(10): p. 561-9.
33. Hall, T.A. and Brown, J.W., *The ribonuclease P family.* Methods Enzymol, 2001. **341**: p. 56-77.
34. Guerrier-Takada, C., et al., *The RNA Moiety of Ribonuclease P is the Catalytic Subunit of the Enzyme.* Cell, 1983. **35**(3 Part 2): p. 849-857.
35. Tsai, H.-Y., et al., *Functional reconstitution and characterization of Pyrococcus furiosus RNase P.* Proc Natl Acad Sci U S A, 2006. **103**(44): p. 16147-16152.
36. Kikovska, E., Svärd, S.G., and Kirsebom, L.A., *Eukaryotic RNase P RNA mediates cleavage in the absence of protein.* Proc Natl Acad Sci U S A, 2007. **104**(7): p. 2062-2067.
37. Hsieh, J. and Fierke, C.A., *Conformational change in the Bacillus subtilis RNase P holoenzyme--pre-tRNA complex enhances substrate affinity and limits cleavage rate.* RNA, 2009. **15**(8): p. 1565-77.
38. Hsieh, J., et al., *A divalent cation stabilizes the active conformation of the B. subtilis RNase P x pre-tRNA complex: a role for an inner-sphere metal ion in RNase P.* J Mol Biol, 2010. **400**(1): p. 38-51.
39. Koutmou, K.S., Day-Storms, J.J., and Fierke, C.A., *The RNR motif of B. subtilis RNase P protein interacts with both PRNA and pre-tRNA to stabilize an active conformer.* RNA (New York, N.Y.), 2011. **17**(7): p. 1225-1235.
40. Crary, S.M., Niranjanakumari, S., and Fierke, C.A., *The Protein Component of Bacillus subtilis Ribonuclease P Increases Catalytic Efficiency by Enhancing Interactions with the 5,Äò Leader Sequence of Pre-tRNAAsp.* Biochemistry, 1998. **37**(26): p. 9409-9416.
41. Frank, D.N. and Pace, N.R., *RIBONUCLEASE P: Unity and Diversity in a tRNA Processing Ribozyme.* Annual Review of Biochemistry, 1998. **67**(1): p. 153-180.
42. Reiter, N.J., et al., *Structure of a bacterial ribonuclease P holoenzyme in complex with tRNA.* Nature, 2010. **468**(7325): p. 784-9.
43. Christian, E.L., Kaye, N.M., and Harris, M.E., *Helix P4 is a divalent metal ion binding site in the conserved core of the ribonuclease P ribozyme.* RNA, 2000. **6**(4): p. 511-9.
44. Crary, S.M., Kurz, J.C., and Fierke, C.A., *Specific phosphorothioate substitutions probe the active site of Bacillus subtilis ribonuclease P.* RNA, 2002. **8**(7): p. 933-47.
45. Christian, E.L., et al., *The P4 metal binding site in RNase P RNA affects active site metal affinity through substrate positioning.* RNA, 2006. **12**(8): p. 1463-7.
46. Harris, M.E. and Christian, E.L., *Recent insights into the structure and function of the ribonucleoprotein enzyme ribonuclease P.* Current Opinion in Structural Biology, 2003. **13**(3): p. 325-333.
47. Kazantsev, A.V., et al., *Solution structure of RNase P RNA.* RNA, 2011. **17**(6): p. 1159-71.

48. Kazantsev, A.V., et al., *Crystal structure of a bacterial ribonuclease P RNA.* Proceedings of the National Academy of Sciences of the United States of America, 2005. **102**(38): p. 13392-13397.
49. Getz, M.M., et al., *Structural plasticity and Mg2+ binding properties of RNase P P4 from combined analysis of NMR residual dipolar couplings and motionally decoupled spin relaxation.* RNA (New York, N.Y.), 2007. **13**(2): p. 251-66.
50. Frank, A.T., Law, S.M., and Brooks, C.L., *A Simple and Fast Approach for Predicting 1H and 13C Chemical Shifts: Toward Chemical Shift-Guided Simulations of RNA.* The Journal of Physical Chemistry B, 2014. **118**(42): p. 12168-12175.
51. Koutmou, K.S., et al., *NMR and XAS reveal an inner-sphere metal binding site in the P4 helix of the metallo-ribozyme ribonuclease P.* Proceedings of the National Academy of Sciences, 2010. **107**(6): p. 2479-2484.
52. Liu, F. and Altman, S., *Ribonuclease P*. Protein reviews. 2010, New York: Springer. xvi, 283 p.
53. Batey, R.T., et al., *Preparation of isotopically labeled ribonucleotides for multidimensional NMR spectroscopy of RNA.* Nucleic Acids Res, 1992. **20**(17): p. 4515-23.
54. Yoshizawa, S., Fourmy, D., and Puglisi, J.D., *Recognition of the codon-anticodon helix by ribosomal RNA.* Science, 1999. **285**(5434): p. 1722-5.
55. Schmeing, T.M. and Ramakrishnan, V., *What recent ribosome structures have revealed about the mechanism of translation.* Nature, 2009. **461**(7268): p. 1234-42.
56. Fourmy, D., et al., *Structure of the A site of Escherichia coli 16S ribosomal RNA complexed with an aminoglycoside antibiotic.* Science, 1996. **274**(5291): p. 1367-71.
57. Tavale, S.S. and Sobell, H.M., *Crystal and molecular structure of 8-bromoguanosine and 8-bromoadenosine, two purine nucleosides in the syn conformation.* Journal of Molecular Biology, 1970. **48**(1): p. 109-123.
58. Michelson, A.M., Monny, C., and Kapuler, A.M., *Poly 8-bromoguanylic acid.* Biochim Biophys Acta, 1970. **217**(1): p. 7-17.
59. Ikehara, M., Uesugi, S., and Yoshida, K., *Studies on the conformation of purine nucleosides and their 5'-phosphates.* Biochemistry, 1972. **11**(5): p. 830-6.
60. Yajima, R., et al., *A conformationally restricted guanosine analog reveals the catalytic relevance of three structures of an RNA enzyme.* Chem Biol, 2007. **14**(1): p. 23-30.
61. Proctor, D.J., et al., *Restricting the conformational heterogeneity of RNA by specific incorporation of 8-bromoguanosine.* J Am Chem Soc, 2003. **125**(9): p. 2390-1.
62. Sokoloski, J.E., et al., *Prevalence of syn nucleobases in the active sites of functional RNAs.* RNA, 2011. **17**(10): p. 1775-87.
63. Nikolova, E.N., et al., *Transient Hoogsteen base pairs in canonical duplex DNA.* Nature, 2011. **470**(7335): p. 498-502.
64. Alvey, H.S., et al., *Widespread transient Hoogsteen base pairs in canonical duplex DNA with variable energetics.* Nat Commun, 2014. **5**: p. 4786.
65. Yang, H., et al., *Effect of 1-methyladenine on double-helical DNA structures.* FEBS Lett, 2008. **582**(11): p. 1629-33.
66. Lu, L., et al., *Structure determination of DNA methylation lesions N1-meA and N3-meC in duplex DNA using a cross-linked protein-DNA system.* Nucleic Acids Res, 2010. **38**(13): p. 4415-25.
67. Beebe, J.A., Kurz, J.C., and Fierke, C.A., *Magnesium ions are required by Bacillus subtilis ribonuclease P RNA for both binding and cleaving precursor tRNA^{Asp}.* Biochemistry, 1996. **35**(32): p. 10493-505.
68. Christian, E.L., Kaye, N.M., and Harris, M.E., *Evidence for a polynuclear metal ion binding site in the catalytic domain of ribonuclease P RNA.* EMBO J, 2002. **21**(9): p. 2253-62.
69. Cassano, A.G., Anderson, V.E., and Harris, M.E., *Analysis of solvent nucleophile isotope effects: evidence for concerted mechanisms and nucleophilic activation by metal*

coordination in nonenzymatic and ribozyme-catalyzed phosphodiester hydrolysis. Biochemistry, 2004. **43**(32): p. 10547-59.
70. Warnecke, J.M., et al., *Ribonuclease P (RNase P) RNA is converted to a Cd2+-ribozyme by a single Rp-phosphorothioate modification in the precursor tRNA at the RNase P cleavage site.* Proceedings of the National Academy of Sciences of the United States of America, 1996. **93**(17): p. 8924-8.
71. Cuzic, S. and Hartmann, R.K., *Studies on Escherichia coli RNase P RNA with Zn2+ as the catalytic cofactor.* Nucleic Acids Res, 2005. **33**(8): p. 2464-74.
72. Brannvall, M. and Kirsebom, L.A., *Manganese ions induce miscleavage in the Escherichia coli RNase P RNA-catalyzed reaction.* J Mol Biol, 1999. **292**(1): p. 53-63.
73. Smith, D., et al., *Influence of metal ions on the ribonuclease P reaction. Distinguishing substrate binding from catalysis.* J Biol Chem, 1992. **267**(4): p. 2429-36.
74. Kurz, J.C. and Fierke, C.A., *The affinity of magnesium binding sites in the Bacillus subtilis RNase P x pre-tRNA complex is enhanced by the protein subunit.* Biochemistry, 2002. **41**(30): p. 9545-58.
75. Nikolova, E.N., *The Double Helix in Motion: New Insights into Sequence-specific, Functional DNA Dynamics Using NMR Spectroscopy*. 2011, University of Michigan, Ann Arbor.
76. Baugh, C., Grate, D., and Wilson, C., *2.8 A crystal structure of the malachite green aptamer.* J Mol Biol, 2000. **301**(1): p. 117-28.
77. Yang, Y., et al., *Structural basis of ligand discrimination by two related RNA aptamers resolved by NMR spectroscopy.* Science, 1996. **272**(5266): p. 1343-7.
78. MacElrevey, C., et al., *Structural effects of nucleobase variations at key active site residue Ade38 in the hairpin ribozyme.* RNA, 2008. **14**(8): p. 1600-16.
79. Lemieux, S., et al., *Modeling active RNA structures using the intersection of conformational space: application to the lead-activated ribozyme.* RNA, 1998. **4**(7): p. 739-49.
80. Martick, M. and Scott, W.G., *Tertiary contacts distant from the active site prime a ribozyme for catalysis.* Cell, 2006. **126**(2): p. 309-20.
81. Toor, N., et al., *Crystal structure of a self-spliced group II intron.* Science, 2008. **320**(5872): p. 77-82.
82. Shi, H. and Moore, P.B., *The crystal structure of yeast phenylalanine tRNA at 1.93 A resolution: a classic structure revisited.* RNA, 2000. **6**(8): p. 1091-105.
83. Zhou, H., et al., *New insights into Hoogsteen base pairs in DNA duplexes from a structure-based survey.* Nucleic Acids Research, 2015. **43**(7): p. 3420-3433.
84. Battle, D.J. and Doudna, J.A., *Specificity of RNA-RNA helix recognition.* Proc Natl Acad Sci U S A, 2002. **99**(18): p. 11676-81.
85. Cheong, C., Varani, G., and Tinoco, I., Jr., *Solution structure of an unusually stable RNA hairpin, 5'GGAC(UUCG)GUCC.* Nature, 1990. **346**(6285): p. 680-2.
86. Veeraraghavan, N., et al., *Metal binding motif in the active site of the HDV ribozyme binds divalent and monovalent ions.* Biochemistry, 2011. **50**(13): p. 2672-82.
87. Bevilacqua, P.C., *Mechanistic considerations for general acid-base catalysis by RNA: revisiting the mechanism of the hairpin ribozyme.* Biochemistry, 2003. **42**(8): p. 2259-65.
88. Klein, D.J. and Ferre-D'Amare, A.R., *Structural basis of glmS ribozyme activation by glucosamine-6-phosphate.* Science, 2006. **313**(5794): p. 1752-6.
89. Batey, R.T., Gilbert, S.D., and Montange, R.K., *Structure of a natural guanine-responsive riboswitch complexed with the metabolite hypoxanthine.* Nature, 2004. **432**(7015): p. 411-5.
90. Wilson, T.J. and Lilley, D.M., *Do the hairpin and VS ribozymes share a common catalytic mechanism based on general acid-base catalysis? A critical assessment of available experimental data.* RNA, 2011. **17**(2): p. 213-21.

91. Dethoff, E.A., et al., *Visualizing transient low-populated structures of RNA.* Nature, 2012. **491**(7426): p. 724-8.
92. Torres-Larios, A., et al., *Crystal structure of the RNA component of bacterial ribonuclease P.* Nature, 2005. **437**(7058): p. 584-7.
93. Wu, H.N. and Uhlenbeck, O.C., *Role of a bulged A residue in a specific RNA-protein interaction.* Biochemistry, 1987. **26**(25): p. 8221-7.
94. Ippolito, J.A. and Steitz, T.A., *A 1.3-A resolution crystal structure of the HIV-1 trans-activation response region RNA stem reveals a metal ion-dependent bulge conformation.* Proc Natl Acad Sci U S A, 1998. **95**(17): p. 9819-24.
95. Reiter, N.J., et al., *Dynamics in the U6 RNA intramolecular stem-loop: a base flipping conformational change.* Biochemistry, 2004. **43**(43): p. 13739-47.
96. Misra, V.K. and Draper, D.E., *On the role of magnesium ions in RNA stability.* Biopolymers, 1998. **48**(2-3): p. 113-35.
97. Robinson, H., et al., *Hexahydrated magnesium ions bind in the deep major groove and at the outer mouth of A-form nucleic acid duplexes.* Nucleic Acids Res, 2000. **28**(8): p. 1760-6.
98. Milligan, J.F., et al., *Oligoribonucleotide Synthesis Using T7 Rna-Polymerase and Synthetic DNA Templates.* Nucleic Acids Research, 1987. **15**(21): p. 8783-8798.
99. Rueda, D., et al., *The 5' Leader of Precursor tRNA(Asp) Bound to the Bacillus subtilis RNase P Holoenzyme Has an Extended Conformation.* Biochemistry, 2005. **44**(49): p. 16130-9.
100. Niranjanakumari, S., et al., *Protein component of the ribozyme ribonuclease P alters substrate recognition by directly contacting precursor tRNA.* Proc Natl Acad Sci U S A, 1998. **95**(26): p. 15212-7.
101. Niranjanakumari, S., Kurz, J.C., and Fierke, C.A., *Expression, purification and characterization of the recombinant ribonuclease P protein component from Bacillus subtilis.* Nucleic Acids Res, 1998. **26**(13): p. 3090-6.
102. Cavanagh, J., et al., *Protein NMR spectroscopy: principles and practice*. 1995: Academic Press.
103. Farjon, J., et al., *Longitudinal-relaxation-enhanced NMR experiments for the study of nucleic acids in solution.* J Am Chem Soc, 2009. **131**(24): p. 8571-7.
104. Sathyamoorthy, B., et al., *Development and application of aromatic [(13)C, (1)H] SOFAST-HMQC NMR experiment for nucleic acids.* J Biomol NMR, 2014. **60**(2-3): p. 77-83.
105. Delaglio, F., et al., *NMRPipe: a multidimensional spectral processing system based on UNIX pipes.* J Biomol NMR, 1995. **6**(3): p. 277-93.
106. Massi, F., et al., *NMR R1 rho rotating-frame relaxation with weak radio frequency fields.* J Am Chem Soc, 2004. **126**(7): p. 2247-56.
107. Korzhnev, D.M., Orekhov, V.Y., and Kay, L.E., *Off-resonance R(1rho) NMR studies of exchange dynamics in proteins with low spin-lock fields: an application to a Fyn SH3 domain.* J Am Chem Soc, 2005. **127**(2): p. 713-21.
108. Nikolova, E.N., Gottardo, F.L., and Al-Hashimi, H.M., *Probing transient Hoogsteen hydrogen bonds in canonical duplex DNA using NMR relaxation dispersion and single-atom substitution.* J Am Chem Soc, 2012. **134**(8): p. 3667-70.
109. Spyracopoulos, L., *A suite of Mathematica notebooks for the analysis of protein main chain 15N NMR relaxation data.* J Biomol NMR, 2006. **36**(4): p. 215-24.
110. Miloushev, V.Z. and Palmer, A.G., 3rd, *R(1rho) relaxation for two-site chemical exchange: general approximations and some exact solutions.* J Magn Reson, 2005. **177**(2): p. 221-7.
111. Parisien, M. and Major, F., *The MC-Fold and MC-Sym pipeline infers RNA structure from sequence data.* Nature, 2008. **452**(7183): p. 51-5.
112. Jo, S., et al., *CHARMM-GUI: a web-based graphical user interface for CHARMM.* J Comput Chem, 2008. **29**(11): p. 1859-65.

113. Jo, S., et al., *PBEQ-Solver for online visualization of electrostatic potential of biomolecules.* Nucleic Acids Res, 2008. **36**(Web Server issue): p. W270-5.
114. Im, W., Beglov, D., and Roux, B., *Continuum solvation model: Computation of electrostatic forces from numerical solutions to the Poisson-Boltzmann equation.* Computer Physics Communications, 1998. **111**(1–3): p. 59-75.

CHAPTER 4
CHARACTERIZING THE ROLE OF P4 HELIX IN *BACILLUS SUBTILIS* RNASE P CATALYSIS[1]

4.1 Abstract

Ribonuclease P (RNase P) is responsible for catalyzing the hydrolysis of a phosphodiester bond in precursor tRNA (pre-tRNA) to yield mature tRNA. During RNase P catalysis, a conformational change step following pre-tRNA association with RNase P and preceding cleavage enhances the affinity of RNase P for pre-tRNA and metal ions and strengthens the efficiency of pre-tRNA cleavage. Nuclear magnetic resonance (NMR) data demonstrate the existence of a transient state (TS) for P4 helix in a stem-loop mimic. To investigate if this proposed TS is related to the conformational change of the RNase P - pre-tRNA complex and to investigate the role of the P4 in the conformational change, I incorporated site-specific mutant and atom modifications into the P4 helix of the PRNA and examined their effects on RNase P activity. Kinetics data of these variants show strong correlations with the NMR results demonstrating that the TS observed in the stem-loop model mimics the conformational change in RNase P. The data show that the A-tract and universally conserved bulged uridine stabilize the conformational change of the P4 helix, in which G50 adopts a *syn* conformation and the

[1] Data in Chapter 3 and Chapter 4 are in preparation for a manuscript entitled “RNA dynamics reveals the conformational change of catalytic RNA” by Yu Chen, Aaron T. Frank, Huiqing Zhou, Katja Petzold, Xin Liu, Ryszard Kierzek, Charles L. Brooks III, Hashim M. Al-Hashim and Carol A. Fierke.

backbone of A49 and G50 forms a kink, creating an electronegative patch that could bind metal ions. Importantly, RNase P with 8-bromoguanosine substituted for G50 has WT-like activity indicating that RNase P can tolerate a locked *syn* conformation. The findings suggest that the P4 helix undergoes a structural change during the conformational change of RNase P - pre-tRNA complex. This structure alteration is essential for RNase P catalysis by playing an important role in enhancing metal ion affinity.

4.2 Background

RNA has various functions in cells besides serving as a template for protein production, such as RNA modification, transcription and translation regulation, gene silencing and catalysis [1-4]. RNA can carry out a diverse range of functions with only four types of bases because of the ability to undergo a vast number of conformational states. For example, riboswitches are *cis*-acting mRNA elements that can sense changes in the cellular environment to change gene expression through complex structural rearrangements [5, 6]. Another example is protein p65 binds to *Tetrahymena* telomerase and induces a conformational change to facilitate the binding of telomerase reverse transcriptase [7].

Another type of functional RNA that commonly undergoes conformational changes to conduct biological functions is a ribozyme. Just like protein enzymes, ribozymes exploit structural rearrangements to guide the catalytic process [8-12]. RNase P is a metal-dependent endoribonuclease that catalyzes the 5’ end leader removal from precursor tRNA (pre-tRNA) [13-15]. Classically, RNase P consists of a catalytic RNA subunit

(PRNA) and associated proteins (P protein) [16-18]. Transient kinetics studies of *Bacillus subtilis* RNase P reveal a two-step substrate association mechanism. Pre-tRNA binds to RNase P with a bimolecular rate constant that is near the diffusion limit [19]. Following formation of this initial enzyme–substrate (ES) complex, a unimolecular conformational change that enhances the affinity of RNase P for pre-tRNA occurs [19]. This new RNase P - pre-tRNA conformer (ES*) is stabilized by enhancement of specific interactions that occur between the pre-tRNA leader and the P protein in the RNase P - pre-tRNA complex [20-22].

Previous studies on the RNase P conformational change have demonstrated that inner-sphere contacts with metal ions are not crucial for the formation of ES conformer [23]. However, the ES* conformer is stabilized by a high affinity divalent cation capable of inner-sphere coordination [21]. Additionally, a second, lower-affinity divalent metal ion activates cleavage catalyzed by RNase P [21]. Additional data show that in the absence of divalent metal ions, the ES* conformer exists in equilibrium with ES although at a low population. Addition of Ca^{2+} significantly increases the population of ES* (Kristin S. Koutmou, Nils G. Walter and Carol A. Fierke, manuscript in preparation).

However, structural information of the RNase P conformational change is limited and the role the conformational change playing in the RNase P catalytic pathway is unclear. Time-resolved fluorescence resonance energy transfer (trFRET) measurements indicate that the 5’ leader of pre-tRNA moves 4 to 6 Å closer to the PRNA - P protein interface during the ES to ES* transition. This suggests that the conformational change might act as proofreading step to strengthen the efficiency and fidelity of pre-tRNA cleavage [21].

The crystal structure of *Thermotoga maritima* RNase P in complex with mature tRNA and 5'leader revealed that the P4 helix is positioned at the core of the enzyme and is proposed to be the active site of the ezynme and contain catalytic and/or cocatalytic metal ion binding sites [24-27]. However, it is unlikely that this structure reflects the active conformation since it is a tertiary complex with mature tRNA and pre-tRNA 5' leader representing the product complex. The metal ion binding sites identified in this structure are also uncertain because they are characterized by soaking in Eu^{2+} and Sm^{3+}, instead of the catalytic divalent metal ions, such as Mg^{2+}, Mn^{2+} or Ca^{2+}. NMR studies have probed the existence of an alternative conformer of the P4 helix in a stem-loop mimic model. The data suggest a low populated, transient state (TS) exists in the P4 helix mimic (Figure 4-1), where three adenosines (A-tract) region unwinds, G6 transits from *anti* to *syn,* and a kink forms on the backbone between A5 and G6. Meanwhile, the bulged U7 independently flips in and out of the helix with a faster motion.

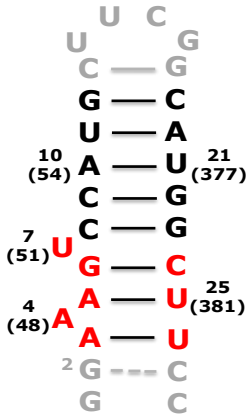

Figure 4-1: Secondary structure of the P4 helix (black) and P4 helix stem-loop mimic (black and grey). The secondary structure of the P4 helix was drawn based on the *Bacillus stearothermophilus* PRNA crystal structure [28]. Residues modified in this study are highlighted in red. The numbering of the P4 helix in *B. subtilis* full-length PRNA is given in parentheses.

To examine whether the TS of the P4 helix mimic observed by NMR is related to the conformational change step that occurs during the RNase P catalysis cycle, I

incorporated mutations and atom modifications (Figure 4-2) in and around the conserved U51, G50 and A-tract regions of the P4 helix (Figure 4-1) in the full-length PRNA and examined the effect on RNase P catalysis using enzyme kinetics. The findings suggest that during the conformational change in RNase P, the P4 helix undergoes a structural rearrangement, which mimics the TS observed from the P4 helix stem-loop model. The function of this structural change is to re-position the residues in the active site thereby forming an electrostatic site favorable for metal ion binding and enhancing the metal ion binding affinity for RNase P catalysis.

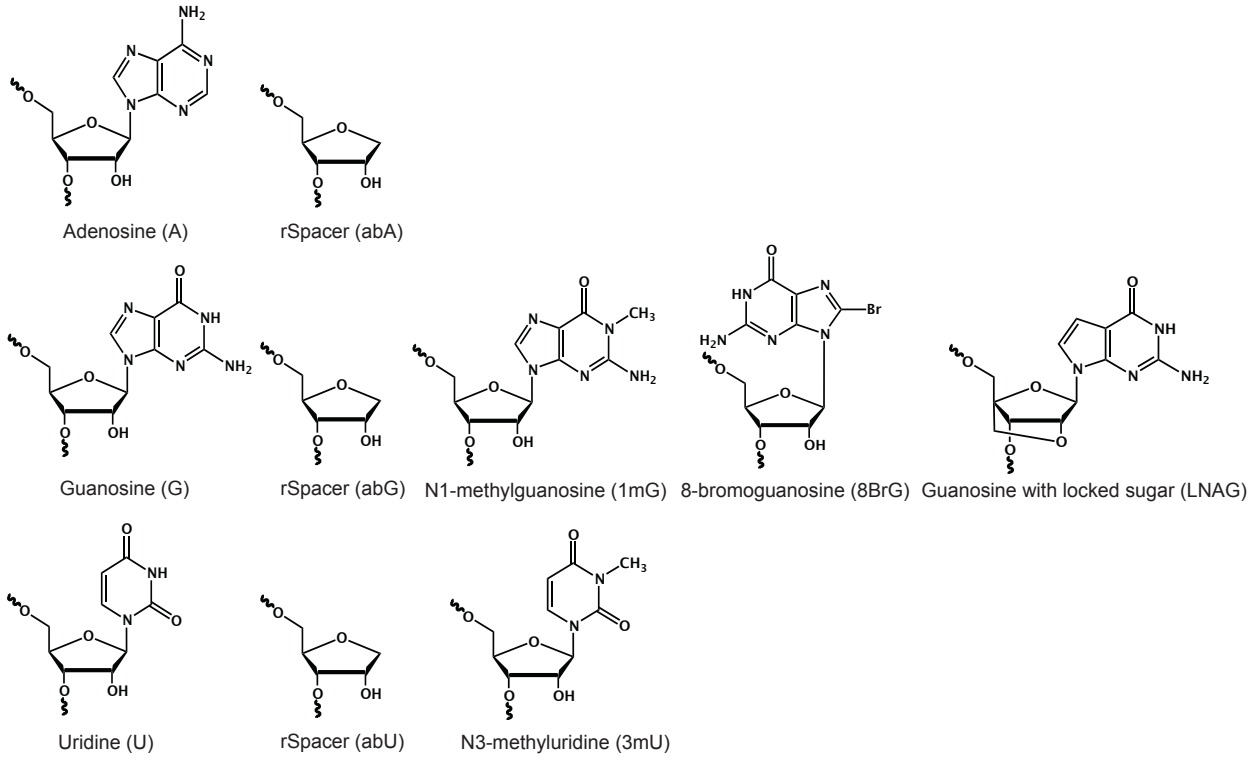

Figure 4-2: Chemical structures of adenosine, guanosine, uridine and substitutions

4.3 Results

As described in Chapter 2, the rate-limiting step for single-turnover (STO) cleavage of pre-tRNA catalyzed by RNase P in Mg^{2+} is the chemistry step, hydrolysis of the phosphodiester bond, at low pH (≤6), while the conformational change step becomes rate limiting at high pH (≥8) [19]. Therefore, the apparent pK_a, obtained by fitting the data with a single ionization model, reflects the pH at which the change in rate-limiting step occurs. Here, I use the pH dependence of activity to evaluate if the mutants or modifications incorporated to the P4 helix alter the kinetics of either the conformational change step or pre-tRNA hydrolysis. A fluorescence polarization assay [29] was used to measure the observed STO cleavage rate constants (k_{obs}). The experiments were performed in saturating divalent metal ion conditions and saturating concentration of RNase P, where the k_{obs} values are not dependent on the Mg^{2+} (varying from 20 mM to 50 mM) or enzyme concentration (varying from 360 nM to 4 μM).

4.3.1 Preparation of PRNA with Atom Modifications in the P4 Helix

To incorporate the atom modifications into PRNA, a circularly permuted PRNA lacking half of the P4 helix was prepared, as described in Chapter 2. The RNA oligonucleotide with a sequence identical to the half of the P4 helix containing modifications was ligated to the circularly permuted PRNA to generate the full-length PRNA. In addition to 366P used in Chapter 2 to study the residue at the 3' side of the P4 helix, 46P was used to investigate the effect of the modifications on the 5' side of the P4 helix [26, 30]. A 10-mer (or 18-mer) ribooligonucleotide containing the same sequence as the 5' side strand of the P4 helix was ligated to the 5'-GMP transcribed 56P (or 64P) RNA to reconstitute

46P. This 46P construct has been used in previous studies and it has STO activity comparable to WT PRNA [26, 30]. The truncated 56P (64P) RNA is inactive and does not interfere with RNase P activity or substrate binding [26, 30].

4.3.2 Modification on A-tract Affects Pre-tRNA Cleavage Catalyzed by RNase P

The NMR data suggest that the A-tract region unwinds in the TS of the P4 helix mimic, and that this flexibility is important to stabilize the TS. To test if this is also true for the conformational change step in the full-length PRNA, I first introduced mutants and atom modifications into the A-tract to examine the role of the three adenosines (A47, A48 and A49) on RNase P catalysis under STO conditions.

To mimic the DelA4 (A48 in *B. subtilis* PRNA) construct used in the P4 helix mimic (Chapter 3), I deleted one of three adenosines in PRNA, called DelA48. As shown in Figure 4-3A, DelA48 significantly decreases the STO rate constants of RNase P catalysis at both low and high pH. At pH 5.2, the k_{obs} value decreases 30-fold, and the plateau of the pH profile, k_{max}, decreases 100-fold (Table 4-1). This result suggests that the deletion of A48 affects both hydrolysis and conformational change steps during RNase P catalysis. The 100-fold effect indicates that the existence of three adenosines is essential for the facile conformational change of the RNase P - pre-tRNA complex.

To further investigate the role of A-tract in the conformational change, I introduced the abasic modification into each of the three adenosines. Removing the base of each adenosine decreases the rate constant for the conformational change by 18-47-fold with little effect on the hydrolytic rate constant (1.7-3.7-fold). Therefore, the apparent pK_a is lowered by 1.4-1.6 pH units (Figure 4-3B, Table 4-1). Substitution of both A47 and A49

with abasic (A47/A49-abG) modifications has a large deleterious effect, comparable to DelA48 (Figure 4-3), decreasing the rate constants for cleavage by ~42-fold and conformational change by ~190-fold (Table 4-1). These data demonstrate the importance of the A-tract bases for enhancing the kinetics of the conformational change step. All of the data suggest that the A-tract plays an important role for stabilizing the transitive state for the conformational change of RNase P - pre-tRNA complex.

Table 4-1: Single-turnover rate constants for cleavage of Fl-pre-tRNA^{Asp} catalyzed by *B. subtilis* WT and A-tract modified RNase P

Holoenzyme	pH 5.2		High pH		pK_a[b]
	k_{obs} (s^{-1}) ($\times 10^{-2}$)[a]	$k_{obs}^{WT}/k_{obs}^{modified}$	k_{max} (s^{-1})[b]	$k_{max}^{WT}/k_{max}^{modified}$	
WT	2.6 ± 0.4	1	1.7 ± 0.1	1	7.0 ± 0.1
DelA48	0.087 ± 0.006	30	0.017 ± 0.001	100	6.6 ± 0.1
A47-abA	0.71 ± 0.11	3.7	0.036 ± 0.006	47	5.8 ± 0.3
A48-abA	2.0 ± 0.5	1.3	0.097 ± 0.011	18	5.8 ± 0.1
A49-abA	1.5 ± 0.3	1.7	0.056 ± 0.005	30	5.6 ± 0.2
A47/A49-abA	0.062 ± 0.017	42	0.009 ± 0.001	189	6.3 ± 0.1

[a] STO cleavage was measured in a saturating concentration of RNase P (360 nM - 2.5 μM), 10 nM Fl-pre-tRNA^{Asp} substrate, 50 mM Tris/MES, pH 5.2, 20 mM $MgCl_2$, 200 mM KCl and 20 mM DTT at 37°C. k_{obs} was calculated by a fit of single exponential (Equation 6) to the fraction cleavage of Fl-pre-tRNA^{Asp} substrate, which was calculated from the decrease in anisotropy using Equation 5 as described in Chapter 2.
[b] The k_{max} and pK_a were calculated from fitting a single ionization model (Equation 7) to the pH dependence of RNase P STO cleavage, as described in Chapter 2.

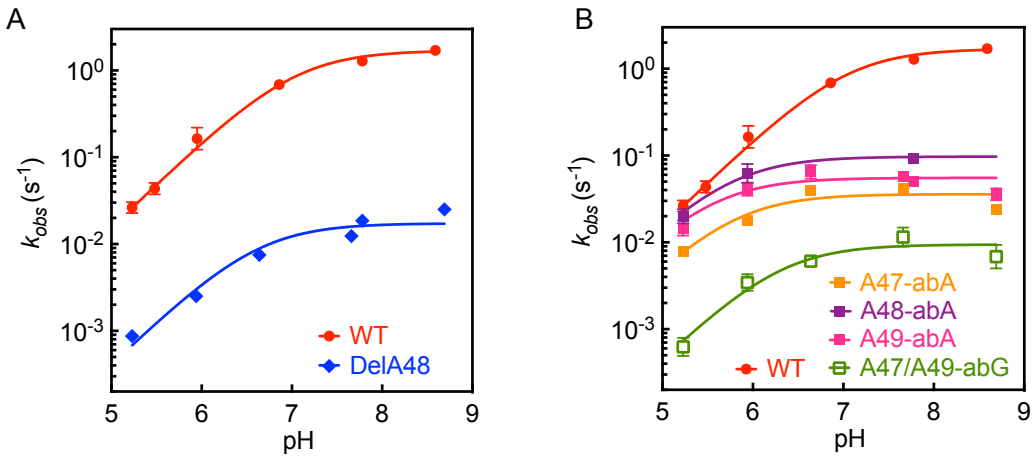

Figure 4-3: Modification at A-tract decreases pre-tRNA cleavage catalyzed by *B. subtilis* RNase P. The pH dependence of STO observed rate constants for **(A)** WT (●, red) and DelA48 (◆, blue); and **(B)** WT (●, red), A47-abA (■, orange), A48-abA (■, purple), A49-abA (■, pink) and A47/A49-abA (□) measured at 37°C in 50 mM Tris/MES, pH 5.2-8.6, 20 mM $MgCl_2$ and 20 mM DTT with KCl concentrations (~200 mM) adjusted to maintain constant ionic strength. 360 nM - 2.5 μM of RNase P holoenzyme and 10 nM of Fl-pre-tRNA^{Asp} were used and the reaction was measured by fluorescence polarization. A single ionization equation was fit to these data to calculate the apparent pK_a and k_{max} (solid lines).

4.3.3 The Structure of G50 Is important for RNase P catalysis

According to the NMR results and 3D model prediction, in the transition from the GS to the TS in the P4 stem-loop model, the glycosidic bond of G6 flips from *anti* to *syn*, and the sugar conformation of G6 (G50 in *B. subtilis* PRNA) likely changes from a C2'-endo to C3'-endo-like sugar pucker. To investigate the effect of the G50 conformation on RNase P catalysis, I substituted G50 with several analogs, abasic (abG), N1-methylguanosine (1mG), 8-bromoguanosine (8BrG) and guanosine with sugar locked at C3'-endo (LNAG) and measured STO cleavage rate constants catalyzed by these modified RNase Ps.

To investigate the importance of the base on G50, I removed the base of G50 and created an abasic site (G50-abG). G50-abG modification significantly decreases both

the cleavage and conformational steps (Figure 4-4A). The value of k_{obs} at low pH is decreased 50-fold and k_{max} at high pH is decreased 28-fold (Table 4-2). These later indicate that the base of G50 is important for RNase P catalysis. To test whether G50 and C380 form an alternative base pair, such as a Hoogsteen base pair rather than Watson-Crick base pair, during the conformational change, a methyl group was added to N1 position (G50-1mG). 1mG has been previously used to disrupt Watson-Crick base pairs and stabilize Hoogsteen base pairs in DNA [31]. In RNase P, addition of a methyl group at the N1 position (G50-1mG) decreases the rate constant for the conformational change by 33-fold (Table 4-2), which is comparable to the G50-abG rate constant, but it has no effect on the cleavage step (Figure 4-4A, Table 4-2). This leads to a significant lowering of the apparent pK_a such that the G50-1mG STO rate constants are pH independent between pH 5.5 to pH 7.8 (Figure 4-4A). These data lead to the conclusion that G50-1mG alters the conformational change step without affecting the hydrolytic cleavage step.

To mimic the *syn* conformation of G6 observed in the TS of P4 helix mimic, the 8BrG modification, which successfully trapped the TS of the P4 helix mimic, was substituted for G50 in full-length PRNA. 8BrG preferentially adopts a *syn* conformation because the steric bulk of bromine disfavors its residence over the ribose sugar [32-34]. G50-8BrG has little effect on k_{obs} values at both low and high pH, and no perturbation of the pK_a is observed (Figure 4-4A, Table 4-2). This effect is much smaller compared to G50-abG or G50-1mG. The same circumstance is also applied to LNAG, which locks sugar pucker of G50 at C3'-endo, the conformation consistent with the NMR relaxation dispersion data and predicted model. G50-LNAG also shows small effect on RNase P activity

(Figure 4-4B, Table 4-2). These data suggest that RNase P tolerates a locked *syn* glycosidic bond and C3'-endo sugar pucker in the active site. Overall, these results demonstrate that the base and structure of G50 is critical for both the cleavage and conformational change steps in the RNase P catalytic cycle.

Table 4-2: Single-turnover rate constants for cleavage of Fl-pre-tRNA^{Asp} catalyzed by *B. subtilis* WT and G50 modified RNase P

Holoenzyme	pH 5.5		High pH		pK_a[b]
	k_{obs} (s^{-1}) ($\times 10^{-2}$)[a]	$k_{obs}^{WT}/k_{obs}^{modified}$	k_{max} (s^{-1})[b]	$k_{max}^{WT}/k_{max}^{modified}$	
WT	4.3 ± 0.7	1	1.7 ± 0.1	1	7.0 ± 0.1
G50-abG	0.086 ± 0.003	50	0.061 ± 0.006	28	7.4 ± 0.1
G50-1mG	3.8 ± 0.1	1.1	0.052 ± 0.004	33	4.9 ± 0.2
G50-8BrG	2.0 ± 0.1	2.2	0.49 ± 0.05	3.5	6.9 ± 0.1
G50-LNAG	0.97 ± 0.03	4.4	0.83 ± 0.10	2.0	7.3 ± 0.2

[a] STO cleavage was measured in a saturating concentration of RNase P (360 nM - 4 μM), 10 nM Fl-pre-tRNA^{Asp} substrate, 50 mM Tris/MES, pH 5.5, 20-50 mM $MgCl_2$, 200-110 mM KCl and 20 mM DTT at 37°C. k_{obs} was calculated by a fit of single exponential (Equation 6) to the fraction cleavage of Fl-pre-tRNA^{Asp} substrate, which was calculated from the decrease in anisotropy using Equation 5 as described in Chapter 2.
[b] The k_{max} and pK_a were calculated from fitting a single ionization model (Equation 7) to the pH dependence of RNase P STO cleavage, as described in Chapter 2.

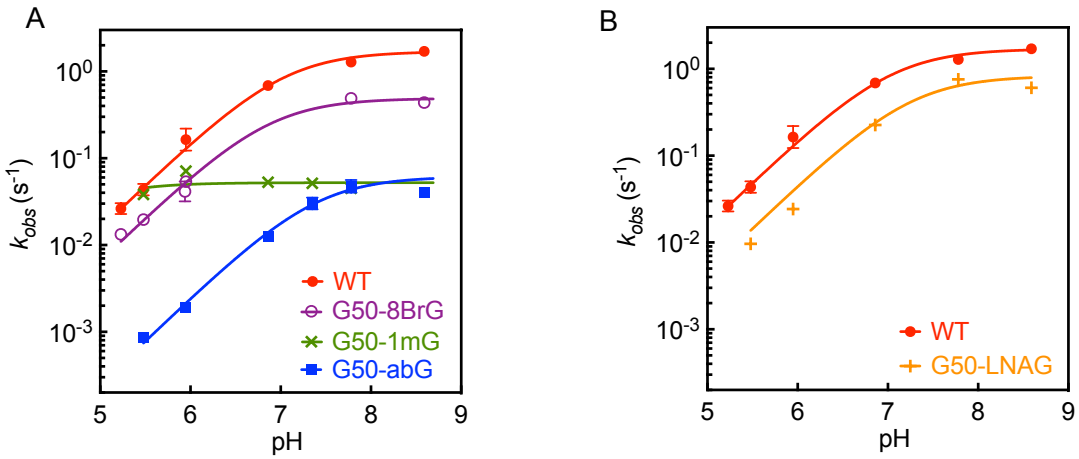

Figure 4-4: The structure of G50 affects pre-tRNA cleavage catalyzed for *B. subtilis* RNase P. The pH dependence of STO observed rate constants for **(A)** WT (●, red), G50-8BrG (**O**, purple), G50-1mG (×, green) and G50-abG (■, blue); and **(B)** WT (●, red) and G50-LNAG (+, orange) measured at 37°C in 50 mM Tris/MES, pH 5.2-8.6, 20-50 mM $MgCl_2$ and 20 mM DTT with KCl concentrations (~200-110 mM) adjusted to maintain constant ionic strength. 360 nM - 4 μM of RNase P holoenzyme and 10 nM of Fl-pre-tRNA^{Asp} were used and the reaction was measured by fluorescence polarization. A single ionization equation was fit to these data to calculate the apparent pK_a and k_{max} (solid lines).

4.3.4 Modifications in the A-tract and G50 alter Mg2+ affinity for pre-tRNA cleavage by RNase P

The Mg^{2+} titration of the NMR spectra and the G50-8BrG of the P4 stem-loop model lead to a TS model that predicts the formation of a kink formed suitable for metal ion binding. To investigate whether the residues involved in the conformational change of RNase P - pre-tRNA complex also affect Mg^{2+} binding to RNase P, I measured the Mg^{2+} dependence of pre-tRNA cleavage catalyzed by DelA48, G50-abG and G50-1mG modified RNase P under STO conditions. Compared with WT RNase P, all of three modifications lead to significant decrease in the apparent Mg^{2+} affinity for pre-tRNA cleavage. As shown before, the k_{obs} of WT holoenzyme is not affected by varying the Mg^{2+} concentration from 4 to 30 mM at low pH (pH 5.2 and pH 6.0) (Figure 4-5) [23].

However, DelA48 shows increased k_{obs} from 4 mM to 8 mM Mg^{2+} then reaches a plateau, and the k_{obs} value is not increased by additional Mg^{2+} (Figure 4-5). The high value of Hill coefficient indicates this mutant might also affect the metal ions associated with PRNA folding or substrate binding. And this defect cannot be rescued by additional metal ions. While, both the G50-abG and G50-1mG variants have similar activities to DelA48 at 20 mM of Mg^{2+}, the STO rate constants increase about 2-3-fold for G50-abG and G50-1mG upon future addition of Mg^{2+} (Figure 4-5). Both the apparent Mg^{2+} affinity ($K_{1/2,app}^{Mg^{2+}}$) and Hill coefficient of G50-abG and G50-1mG are similar with PRNA alone-catalyzed pre-tRNA cleavage (Chapter 2) suggesting the loss of Mg^{2+} ion or affecting the P protein affinity for PRNA. These results illustrate that modifications of the A-tract and G50 affect both the STO rate constant and the apparent Mg^{2+} affinity for activation of pre-tRNA cleavage. Other method, such as stopped-flow transient kinetics can be used to further test the effect of these modifications on substrate binding and conformational change.

Table 4-3: Mg^{2+} dependence of WT and modified *B. subtilis* PRNA catalyzed STO cleavage[a]

Holoenzyme	$K_{1/2,app}^{Mg^{2+}}$ [b]	n_H [b]
DelA48	4.9 ± 0.2	7.7 ± 2.4
G50-abG	23.6 ± 1.0	4.5 ± 0.7
G50-1mG	19.4 ± 0.7	4.6 ± 1.3

[a] The reaction was performed with 360 nM - 4 μM of RNase P holoenzyme and 10 nM of Fl-pre-$tRNA^{Asp}$ at 37°C in 50 mM Tris/MES, pH 7.8, 20 mM DTT and 4-50 mM $MgCl_2$ and varying KCl concentrations from ~240-110 mM. A single exponential was fit to the data to calculate the STO cleavage rate constants (k_{obs}).

[b] Hill equation was fit to the Mg^{2+} dependence of k_{obs} to calculate $K_{1/2,app}^{Mg^{2+}}$ and n_H of RNase P-catalyzed cleavage, as described in Chapter 2.

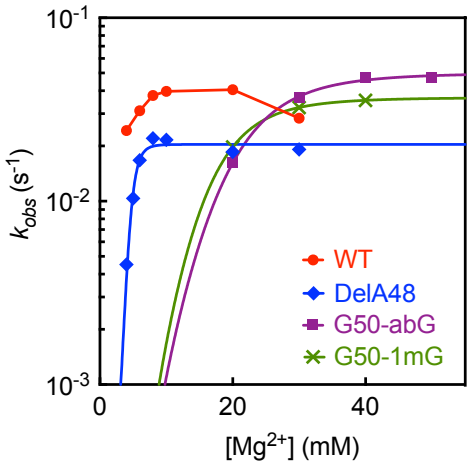

Figure 4-5: Deletion of one adenosine on A-tract and modifications on G50 affect Mg^{2+} affinity for pre-tRNA cleavage catalyzed by *B. subtilis* RNase P. The Mg^{2+} dependence of STO observed rate constants for WT (●, red), G50-abG (■, purple), G50-1mG (×, green) and DelA48 (◆, blue) measured at 37°C in 50 mM Tris/MES, pH 7.8 (pH 5.2 for WT), 20 mM DTT and 4-50 mM $MgCl_2$ with KCl concentrations (~240-110 mM) adjusted to maintain constant ionic strength. 360 nM - 4 μM of RNase P holoenzyme and 10 nM of Fl-pre-$tRNA^{Asp}$ were used and the reaction was measured by fluorescence polarization. Hill equation was fit to the Mg^{2+} dependence of k_{obs} (solid lines).

4.3.5 Modifications on Universal Conserved Uridine affect RNase P catalysis

The bulged U7 in the P4 helix mimic contributes to the TS with an independent process by oscillating in and out of the helix with a fast motion (picosecond-nanosecond time scale). To test if the movement of the universal conserved uridine also participates in the conformational change of RNase P - pre-tRNA complex, I removed U51 in *B. subtilis* PRNA and compared the STO rate constant with WT RNase P and other previous studied modifications.

For both deleting the entire nucleotide (DelU51) and just removing the base (U51-abU), the rate constants for hydrolytic cleavage decreased about 12-14-fold with modest decrease on the conformational change step (2.2-4.5-fold decrease) (Figure 4-6, Table 4-4). To examine if the bulged U51 forms a transient base pair in the

conformational change step, a methyl group was added at the N3 position (U51-3mU), which destabilizes the potential hydrogen bond formation. Differently, the U51-3mU variant k_{obs} shows little dependence on pH (pH 5.2-8.7) (Figure 4-6B), which is similar to the results for G50-1mG (Figure 4-4). Based on the comparable activity similarity of k_{obs} to WT RNase P at pH 5.2, it sugests that U51-3mU does not affect the cleavage of RNase P catalysis. However, at high pH k_{max} is 31-fold lower than WT RNase P (Table 4-4), which indicates a decrease in the rate constant of the conformational change step. These data illustrate the importance of the U51 nucleobase for both the cleavage and conformational change step of RNase P catalysis; removing the base decreases cleavage while addition of an extra methyl group destabilizes the conformational change.

Table 4-4: Single-turnover rate constants for cleavage of Fl-pre-tRNA^{Asp} catalyzed by *B. subtilis* WT and U51 modified RNase P

Holoenzyme	pH 5.2		High pH		pK_a[b]
	k_{obs} (s^{-1}) ($\times 10^{-2}$)[a]	$k_{obs}^{WT}/k_{obs}^{modified}$	k_{max} (s^{-1})[b]	$k_{max}^{WT}/k_{max}^{modified}$	
WT	2.6 ± 0.4	1	1.7 ± 0.1	1	7.0 ± 0.1
DelU51	0.18 ± 0.01	14	0.38 ± 0.05	4.5	7.6 ± 0.1
U51-abU[c]	0.21 ± 0.01	12	0.78 ± 0.12	2.2	7.9 ± 0.1
U51-3mU[c]	3.3 ± 0.2	0.8	0.054 ± 0.003	31	5.0 ± 0.2

[a] STO cleavage was measured in a saturating concentration of RNase P (360 nM - 4 μM), 10 nM Fl-pre-tRNA^{Asp} substrate, 50 mM Tris/MES, pH 5.2, 20 mM $MgCl_2$, 200 mM KCl and 20 mM DTT at 37°C. k_{obs} was calculated by a fit of single exponential (Equation 6) to the fraction cleavage of Fl-pre-tRNA^{Asp} substrate, which was calculated from the decrease in anisotropy using Equation 5 as described in Chapter 2.
[b] The k_{max} and pK_a were calculated from fitting a single ionization model (Equation 7) to the pH dependence of RNase P STO cleavage, as described in Chapter 2.
[c] Taker from Xin Liu [30].

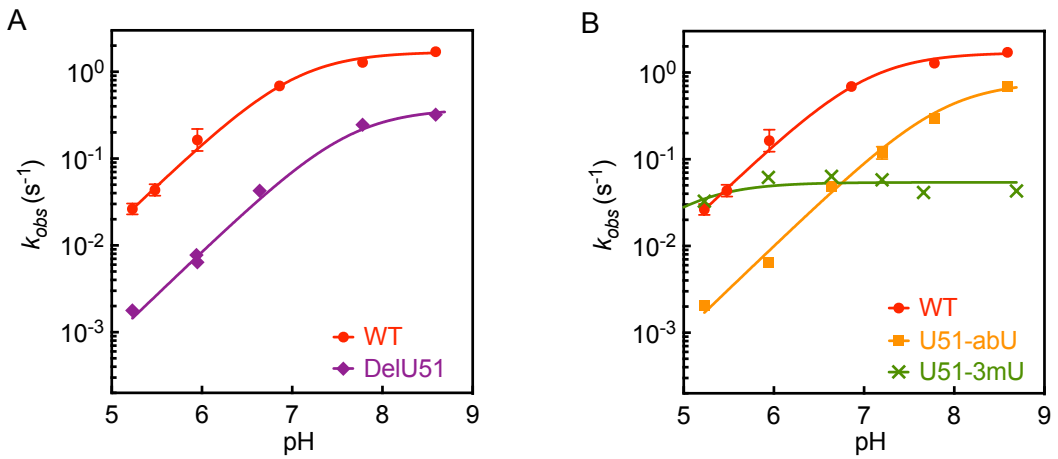

Figure 4-6: Modifications on the universal conserved U51 affect pre-tRNA cleavage catalyzed by *B. subtilis* RNase P. The pH dependence of STO observed rate constants for **(A)** WT (●, red) and DelU51 (◆, purple); and **(B)** WT (●, red), U51-abU (■, orange) and U51-3mU (, green) measured at 37°C in 50 mM Tris/MES, pH 5.2-8.6, 20 mM $MgCl_2$ and 20 mM DTT with KCl concentrations (~200 mM) adjusted to maintain constant ionic strength. 360-720 nM of RNase P holoenzyme and 10 nM of Fl-pre-tRNA^{Asp} were used and the reaction was measured by fluorescence polarization. A single ionization equation was fit to these data to calculate the apparent pK_a and k_{max} (solid lines). The data of U51-abU and U51-3mU are taken from Xin Liu [30].

4.3.6 Double Deletion Results in Inactive RNase P

The data above demonstrate that deletion of either A48 or U51 decrease RNase P activity. To determine if the effect is additive, I introduced a double deletion into the P4 helix (DelA48U51) and measured the pH dependence of the STO rate constants for pre-tRNA cleavage. After 3 hours incubation of reaction at 37°C, there was no product formation observed for all of the conditions. As shown in Figure 4-7, compared with substrate only control, the increased fluorescence anisotropy signal for the reactions containing RNase P indicates that the substrate binds to the enzyme. However, fluorescence anisotropy [29] does not decrease over time for DelA48U51, while WT RNase P cleaved Fl-pre-tRNA^{Asp} in 2 min (Figure 4-7). After separating the pre-tRNA substrate and 5' leader product from reactions by denaturing PAGE, no 5' leader was detected on the gel for DelA48U51 (data not shown). This result suggests DelA48U51

k_{obs} is less than 1×10^{-5} s^{-1} at both low and high pH. Compared with WT RNase P k_{obs}, which is 0.03 s^{-1} at pH 5.2 and 1.7 s^{-1} at pH 7.8, the decease caused by DelA48U51 is more than 3000-fold for cleavage and 170,000-fold for conformational change. It demonstrates that the double deletion in the P4 helix highly inactivates the RNase P for pre-tRNA cleavage.

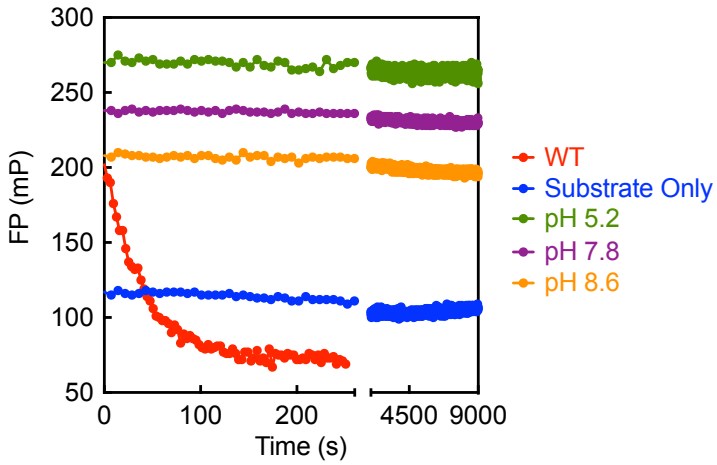

Figure 4-7: Double deletion of one adenosine in the A-tract and U51 results in inactive RNase P. Fluorescence polarization time course for the STO cleavage of Fl-pre-tRNA^{Asp} catalyzed by DelA48U51 at pH 5.2 (green), pH 7.8 (purple) and pH 8.6 (orange), The reactions were performed at 37°C in 50 mM Tris/MES, 20 mM $MgCl_2$ and 20 mM DTT with KCl concentrations (~200 mM) adjusted to maintain constant ionic strength. 360 nM of RNase P holoenzyme and 10 nM of Fl-pre-tRNA^{Asp} were used. WT RNase P control (pH 5.2) is shown in red and substrate only control is shown in blue.

4.3.7 Modifications on the 3' Side of the P4 Helix Have Little Effect on Pre-tRNA Cleavage by RNase P

These results demonstrate that residues from A47 to U51 in the P4 helix are all essential for pre-tRNA cleavage catalyzed by RNase P, stabilizing both the conformational change and phosphodiester bond hydrolysis steps. To test if the importance of those residues is due to base pairing, and to examine the function of the residues on the other side of the P4 helix, I substituted C380, U381 and U382 each with

an abasic modification, and measured STO pre-tRNA cleavage. The abasic substitution removes all of the potential functional groups on the nucleobase with minimal perturbation of the local structure of the helix. As shown in Figure 4-8, the pH profiles of all three modified RNase Ps are similar to WT RNase P and the values of k_{obs} are comparable to WT RNase P at both low and high pH (Table 4-5). These results demonstrate that the bases of C380, U381 and U312 are not crucial for RNase P activity. Formation of base pairs with residues on the other side of the P4 helix is not the reason that the A-tract, G50 and U51 are essential for RNase P catalysis.

Table 4-5: Single-turnover rate constants for cleavage of Fl-pre-tRNA^{Asp} catalyzed by *B. subtilis* WT and 3' side of the P4 helix modified RNase P

Holoenzyme	pH 5.2		High pH		pK_a[b]
	k_{obs} (s^{-1}) ($\times 10^{-2}$)[a]	$k_{obs}^{WT}/k_{obs}^{modified}$	k_{max} (s^{-1})[b]	$k_{max}^{WT}/k_{max}^{modified}$	
WT	2.6 ± 0.4	1	1.7 ± 0.1	1	7.0 ± 0.1
C380-abC	5.1 ± 0.3[c]	0.8[c]	0.61 ± 0.02	2.8	6.4 ± 0.1
U381-abU	4.2 ± 0.4	0.6	0.88 ± 0.16	1.9	6.7 ± 0.1
U382-abU	3.7 ± 0.5	0.7	1.35 ± 0.01	1.3	6.8 ± 0.2

[a] STO cleavage was measured in a saturating concentration of RNase P (360-720 nM), 10 nM Fl-pre-tRNA^{Asp} substrate, 50 mM Tris/MES, pH 5.2, 20 mM $MgCl_2$, 200 mM KCl and 20 mM DTT at 37°C. k_{obs} was calculated by a fit of single exponential (Equation 6) to the fraction cleavage of Fl-pre-tRNA^{Asp} substrate, which was calculated from the decrease in anisotropy using Equation 5 as described in Chapter 2.
[b] The k_{max} and pK_a were calculated from fitting a single ionization model (Equation 7) to the pH dependence of RNase P STO cleavage, as described in Chapter 2.
[c] STO cleavage was measured at pH 5.5.

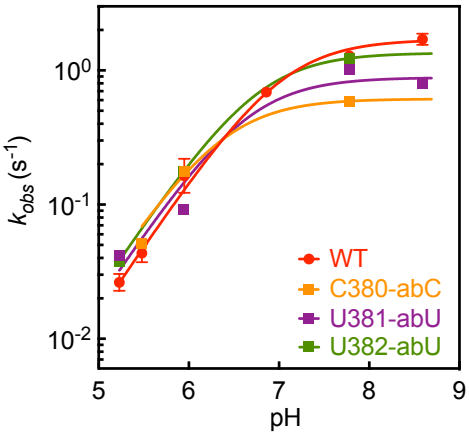

Figure 4-8: Modifications on the residues on 3' side of the P4 helix have minimal effect on pre-tRNA cleavage catalyzed by *B. subtilis* RNase P. The pH dependence of STO observed rate constants for WT (●, red), C380-abC (■, orange), U381-abU (■, purple) and U382-abU (■, green) measured at 37°C in 50 mM Tris/MES, pH 5.2-8.6, 20 mM $MgCl_2$ and 20 mM DTT with KCl concentrations (~200 mM) adjusted to maintain constant ionic strength. 360-720 nM of RNase P holoenzyme and 10 nM of Fl-pre-tRNA^{Asp} were used and the reaction was measured by fluorescence polarization. A single ionization equation was fit to these data to calculate the apparent pK_a and k_{max} (solid lines).

4.4 Discussion

The P4 helix is located in the core of the RNase P enzyme and is proposed to be the active site of this enzyme. NMR studies and 3D structure model prediction suggest a transient state of the P4 helix stem-loop mimic that includes movement of the A-tract region, G6 and bulged U7. To examine whether the P4 helix in full-length PRNA also undergoes a conformational change related to the TS observed in the P4 helix mimic and to uncover the function of this conformational change, I incorporated mutant and atom modification into the P4 helix of full-length PRNA and measured STO rate constants of pre-tRNA cleavage catalyzed by modified RNase Ps. The results show deletion of one adenosine in the A-tract (DelA48) or removal of the base on G50 (G50-abG) significantly decreases both the conformational change (30-100-fold) and cleavage steps (30-50-fold) in the RNase P catalytic cycle. Lack of a base on any

adenosine in the A-tract (A47-abG, A48-abG and A49-abG) or addition of methyl group on the N1 position of G50 (G50-1mG) or the N3 position of U51 (U51-3mU) decreases the rate constant for conformational change by 30-40-fold with minimal effect on hydrolytic cleavage. DelU51 or U51-abG modification decrease the cleavage rate constant by 12-14-fold while slightly lowering the conformational change step (2-5-fold). Double deletion of A48 and U51 (DelA48U51) results in an inactive enzyme at both low and high pHs. Additionally, DelA48, G50-abG and G50-1mG decrease the apparent Mg^{2+} affinity for activating pre-tRNA cleavage.

4.4.1 A-tract Facilitates the Conformational Change of RNase P - pre-tRNA Complex

In the P4 helix mimic, deletion of one adenosine (DelA4) in the A-tract eliminates or significantly diminishes the NMR relaxation dispersion observed in the P4 WT, therefore destabilizing the TS of the P4 helix mimic. In the TS model of the P4 helix mimic, the A-tract unwinds and opens up, so that the backbone conformation of A5 and G6 can form a kink. In this situation, a flexible helix stabilizes the TS more than a stable helix. In the DelA4 construct, two strong Watson-Crick base pairs were observed for A3-U26 (A47-U382 in *B. subtilis* PRNA) and A5-U25 (A49-U381 in *B. subtilis* PRNA) to form a stable helix. In contrast, in WT P4 helix mimic, the hydrogen bonds between three adenosines and two uridines are much weaker or unstable.

The structural and kinetics data suggest that the same scenario can be applied in full-length PRNA. Deleting one adenosine in A-tract (DelA48) in full-length PRNA decreases the cleavage rate constant by 30-fold and the conformational change by 100-fold (Table

4-1, Figure 4-3A). However, removing the base of U381 and U382 has no effect on RNase P activity (Table 4-5, Figure 4-8) indicating that there are no or weak hydrogen bonds formed between three adenosines and two uredines, or these base pairs do not contribute to RNase P catalysis. In the crystal structures of PRNA and RNase P tertiary complex, A48 (*B. subtilis* numbering) is bulged out while A47 and A49 are helical [24, 28] (Figure 4-9A). However, structure probing using 2'-hydroxyl acylation analyzed by primer extension (SHAPE) indicates that A48 is solvent exposed in *Agrobacterium tumefaciens*, but not in *Bacillus stearothermophilus* or *Escherichia coli* [35]. These results are consistent with the NMR model, where all three adenosines are in a helical conformation forming weak or unstable hydrogen bonds with the two uridines on the other strand of the P4 helix mimic (Figure 4-9B). Therefore there remains the uncertainty about whether the A48 conformation is in or loop out of the helix (Figure 4-9).

The data suggests that in full-length PRNA, the A-tract region of the P4 helix remains in a flexible helical conformation, as suggested by the insensitivity of activity to the loss of uridine bases (Table 4-5, Figure 4-8). In contrast, deletion of one adenosine (DelA48) leads to the formation of a stable base pair between A47-U382 and A49-U381, therefore stabilizing the helix. This helix with strong hydrogen bonds is not favorable for A-tract unwinding and restricts backbone conformation for A49 and G50 during the conformational change of RNase P - pre-tRNA complex, thereby explaining the decrease in the conformational change step. The non-bridging phosphoryl oxygens of A49 and G50 form inner-sphere coordination with catalytic metal ions [25, 26, 36]. Presumably, disrupting this site perturbs the catalytic metal ion binding site and

decreases the hydrolytic cleavage rate constant catalyzed by RNase P.

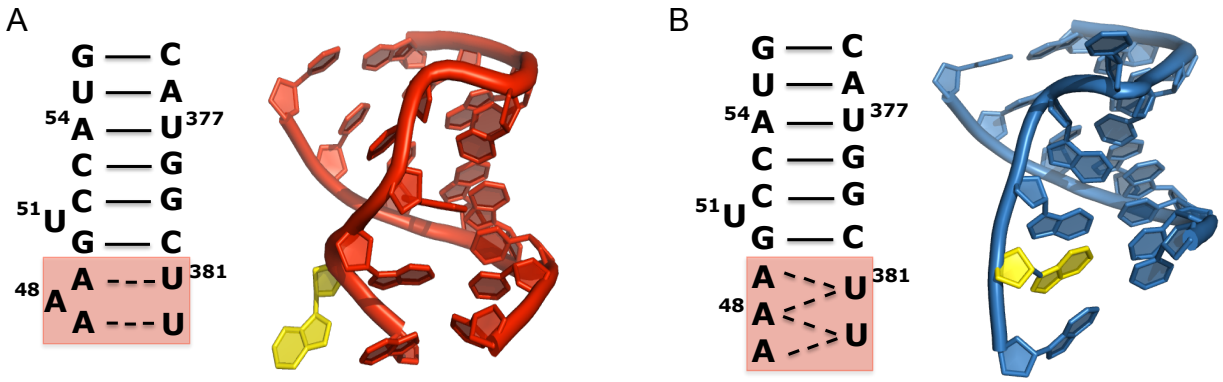

Figure 4-9: Two possible conformations of A-tract in the P4 helix of *B. subtilis* PRNA. **(A)** Based on the crystal structures [24, 28], A48 is bulged out and base stacking with J3/4 of the helix and A47-U382 and A49-U381 form weaker base pairs due to the presence of the bulge. The 3D structure shows the P4 helix region taken from the crystal structure of *T. maritima* RNase P ternary complex (PDB ID: 3Q1R, red) [24]. **(B)** Based on the structure probing of PRNA [35] and NMR data of the P4 helix mimic, all three adenosines are in helical conformation and form unstable hydrogen bonds with two uridines on the other strand of the helix. The 3D structure is the P4 helix stem-loop mimic predicted by MCSYM-LARMORD method [37]. A-tract regions are highlighted by squares in the secondary structures and A48 is highlighted in yellow in the 3D structures.

Additionally, removing any base of adenosines in this region causes a large decrease in conformational change rate constant but has little effect on cleavage (Table 2-3, Figure 2-8B). The high activity at low pH of the modified RNase Ps suggests that the abasic site do not lead to structural perturbations (Table 4-1, Figure 4-3B). One possible explanation for the decrease in conformational change rate constant for the abasic modification is that instead of forming unstable / exchangeable base pairs, removal of one base in the A-tract stabilizes the hydrogen bonds between the remaining two adenines and uredines' bases, therefore increasing the barrier for unwinding of the A-tract region and decreasing the rate constant of conformational change. This hypothesis argues against a bulged out A48 in the P4 helix since removal of the base at A48 also affects conformational change (Table 2-3, Figure 2-8B). But it can be explained by

deletion of the base on A48 affects the base stacking between A48 and G45 and G46 in J3/4. Another possibility is that the A-tract bases interact with cocatalytic metal ions that enhance the conformational change of the RNase P - pre-tRNA complex, but are not essential for hydrolysis. Harris and colleagues have previously suggested that metal ion interactions with nucleobases of the A-tract are important for catalytic function [38]. Furthermore, previous data indicate that there is a second class of metal ions that stabilize the conformation of the RNase P - pre-tRNA complex [21]. The double deletion of the bases on A-tract (A47/A49-abA) has greater effect on RNase P catalysis compared with single deletion, decreasing the rate constants of cleavage by 42-fold and conformational change by 189-fold (Table 2-3, Figure 2-8B). It is consistent with nucleobases coordinating with metal ions, but it could also be the double abasic sites perturb the local structure of the P4 helix.

Taken together, the kinetics data on alterations of the A-tract are consistent with the NMR results and predicted structural model. A flexible helix is preferred in the P4 helix mimic to stabilize the TS, and in full-length PRNA to facilitate the conformational change. The A-tract likely unwinds in the conformational change allowing the backbone of A49 and G50 to reposition to bind metal ions and to optimally cleave pre-tRNA to fulfill the structural requirement for catalysis.

4.4.2 Nucleobase of G50 Stabilizes the Active Conformation of RNase P - pre-tRNA Complex

In the TS of the P4 helix mimic, the base of G6 (G50 in *B. subtilis* PRNA) transits from *anti* to *syn* and this transition is proposed to allow the formation of a kink in the

backbone between A5 and G6. To examine whether the base of G50 is also crucial for the conformational change during RNase P catalysis, I introduced atom modifications on the G50 base. Adding a methyl group on N1 position of G50 base (G50-1mG) decreases the rate constant of conformational change by 33-fold, but does not affect the hydrolytic cleavage (Table 4-2, Figure 4-4A). The additional methyl group on N1 position can have two possible consequences: one is disrupting a Watson-Crick base pair between G50 and C380 [31, 39, 40]; and the other one is interfering with possible metal ion binding sites in the vicinity. The latter provides a better explanation of the effect on the conformational change caused by G50-1mG since the C380-abG modified RNase P has similar activity as WT RNase P (Table 4-5, Figure 4-8) precluding the G50-C380 base pairing as important for function. This result is consistent with a class of divalent metal ions stabilizing the conformational change that leads to an active RNase P - pre-tRNA complex [21].

Furthermore, removal of the base (G50-abG) reduces the rate constant of conformational change by 28-fold, and decreases cleavage by 50-fold (Table 4-2, Figure 4-4A). These changes are not due to disruption of the G50-C380 base pair. To test whether the orientation of the glycosidic bond, *syn* or *anti*, is important, I substituted 8BrG for G50. According to crystal structure G50 adopts an anti-conformation [24, 28], 8BrG is a conformationally restricted nucleoside that preferentially adopts the *syn* glycosidic torsion angle [32-34]. Strikingly, G50-8BrG has activity similar to WT RNase P (Table 4-2, Figure 4-4A) indicating that RNase P can tolerate a *syn* conformation at G50 during catalysis. This result is consistent with the model of the TS in the P4 helix mimic where the base of G6 is *syn*. The small difference (2.2-3.5-fold decrease) in

activity between G50-8BrG and WT (Table 4-2) could be explained by G50 preferring the *syn* conformation but the bulky bromine interferes with local structure. This small decrease is inconsistent with a catalytic requirement for an *anti* conformation at G50. If *anti* is required for the catalysis, a greater decrease [41], similar to the G50-abG modification, would be predicted for G50-8BrG.

In a typical A-form RNA helix, nucleotides have standard Watson-Crick base pairs and are in the *anti* conformation [42]. *Syn* conformation of nucleobases is less common and strongly disfavored owing to helix disruption [43]. Therefore, the occurrence of *syn* geometries in RNA are usually present in more complex structures, such as bulges, loops, kinks, stacking interactions and tertiary base pairs [44-51]. The importance of *syn* nucleobases in functional RNAs has been studied by structural and biochemical methods [41, 43, 50, 52-54], demonstrating that *syn* conformations are common in the active site of functional RNAs and participate in tertiary structure packing, ligand binding (metal ion, small molecule) and orientating atoms for catalysis [41, 44, 49, 54-58]. For example, almost all riboswitch structures and 75% of unique aptamer structures in the PDB have at least one *syn* nucleobase [44]. In the malachite green aptamer, three *syn* nucleobases form essential portions of the binding pocket [47]. In the guanine riboswitch, *syn* adenosines not only form binding pocket, but also mediate loop / loop interaction to enhance the global folding [57]. Furthermore, a *syn* adenosine has been implicated as the general acid in the cleavage reaction catalyzed by the hairpin ribozyme, and a *syn* guanosine is the leaving group and stacks upon the *syn* adenosine [55, 58]. In the lead-dependent ribozyme, a *syn* guanosine is in close proximity to two Pb^{2+} ions, positioning them to catalyze bond scission [41]. This result is consistent with

a computational structure in the lead-dependent ribozyme, where a *syn* guanosine at the core of the active site causes a kinked backbone and facilitates the lead binding at the oxygen on the backbone [45]. This restraint backbone in the lead-dependent ribozyme and its function are similar with the TS observed for the P4 helix mimic.

Therefore, based on the predicted structure of the P4 helix mimic and biochemical data discussed above, it is highly likely that a kinked backbone is also adopted by the P4 helix in full-length PRNA. As suggested previously, *syn* nucleobases allow alterations in the backbone structure to create clefts for ligand binding [41, 44, 49, 54]. During the conformational change of RNase P - pre-tRNA complex, the transition of G50 from *anti* to *syn* is coupled to the formation of kink in the backbone between A49 and G50, where catalytic metal ions are coordinated through inner-sphere interactions [25, 26, 36]. Phosphorothioate modification of non-bridging phosphodiester oxygens at A49 and G50 in the P4 helix of *B. subtilis* RNase P (A67 and G68 in *E. coli*) decreases the cleavage rate constant enormously (300- to 10^4-fold) without (or minimally) affecting the affinity of pre-tRNA [25, 26]. The G50-abG modification decreases the Mg^{2+} affinity for pre-tRNA cleavage (Figure 4-5), suggesting that the kink in the backbone enhances metal ion affinity. Removal of the G50 base inhibits the kink formation, thereby decreasing Mg^{2+} affinity. This theory also explains why G50-1mG does not affect the cleavage rate constant (Table 4-2, Figure 4-4A). The bulky methyl group impedes the conformational change step but does not perturb the structure of the kink therefore the catalytic metal ion binding site is intact.

Additionally, RNase P containing a guanosine with sugar locked at C3'-endo (G50-LNAG) at position 50 has comparable activity with WT RNase P (Table 4-2, Figure

4-4B). This result is consistent with the downfield chemical shift observed for G6C1' in the TS of the P4 helix mimic suggesting alteration of the sugar conformation. Howeve, the *syn/anti* switch could also cause the downfield-shift of G6C1'. Furthermore, there is no additional evidence to suggest the sugar pucker of G50 is critical for RNase P catalysis.

In summary, the kinetic data of atom modifications at G50 are consistent with the NMR results and the structure model predicted for the TS of the P4 helix mimic. During the conformational change of RNase P - pre-tRNA complex, G50 is proposed to change from *anti* to *syn* conformation which is coupled to a kink in the backbone that forms a metal ion binding pocket between A49 and G50, which allows the non-bridging phosphodiester oxygens to coordinate catalytic metal ions.

4.4.3 Bulged U51 Contributes to the Conformational Change of RNase P Catalysis

The universally conserved bulged uridine in RNase P has been widely studied. The existence and the identity of the bulged uridine in the P4 helix are important for enhancing the cleavage rate and pre-tRNA affinity in *E. coli* RNase P [59, 60]. A 4-thiouridine substitution for bulged uridine suggests an inner-sphere metal ion binding site at carbonyl O4 (Xin Liu, Yu Chen, and Carol A. Fierke, manuscript in preparation), which is consistent with the crystal structure [24]. This metal ion is proposed to stabilize the cleavage step during RNase P catalysis [30]. Similarly, deletion of the uridine or removal of the base on uridine in RNase P decreases the cleavage rate constant by 12-14-fold, while causing a small effect on the conformational change (2.2-4.5-fold) (Table

4-4, Figure 4-6) [30]. This result is consistent with removal of the base interrupting a metal ion binding site.

The methyl group addition on N3 position (U51-3mU) does not influence the cleavage step but significantly impedes the conformational change step, decreasing the rate constant by 31-fold (Table 4-4, Figure 4-6B) [30], which is comparable with the effect of G50-1mG modification (Table 4-2, Figure 4-4A). This decease seems not to be caused by the disruption to a potential base pair with U51 since removing the base or entire nucleotide does not result in the comparable hindrance as U51-3mU (Table 4-4, Figure 4-6). It is possible that U51 is associated with metal ions that enhance the conformational change of RNase P - pre-tRNA complex, same as G50. As discussed in Chapter 3, the crystal structure and NMR results are consistent with the bulged uridine adopting two different conformations [24, 28], oscillating in and out of the helix with a fast motion (picosecond-nanosecond). It is likely that the bulky methyl group on the uridine decreases the affinity of the metal ions that interacted with G50. The rapid base oscillation on U51 also contributes to the conformation change during RNaes P catalysis since lacking of the base causes small decrease (2.2-4.5-fold) on the rate constant (Table 4-4, Figure 4-6). It's probably due to the flexibility on the backbone supplied by the bulge and the existence of the base helping to restrain the backbone conformation accommodating the kink formation on G50 and A49.

4.4.4 Flexible Helix Is Required for RNase P catalysis

Bulged U51 and tandem adenosines (A47 and A48) in the A-tract are universally conserved in PRNAs [61]. Deletion of U51 or one of the adenosine impacts RNase P

activity at both the conformational change and cleavage steps, where DelA48 (30-100-fold) (Table 4-1, Figure 4-3A) has much greater effect than DelU51 (4.5-14-fold) (Table 4-4, Figure 4-6A). Strikingly, the double deletion of both U51 and A48 completely annihilates the catalytic activity of RNase P, resulting in an inactive enzyme (Figure 4-7).

Both U51 and A48 are located in the unstable regions of the P4 helix; U51 is bulged out and A48 is either bulged out or forming exchangeable weak hydrogen bond. The existence of these two residues allows a flexible helical structure for P4, while the DelA48U51 mutations establish a rigid double helix. According to the model proposed above, during the conformational change, transition of G50 from *anti* to *syn* is coupled to formation of a kinked backbone that forms a binding pocket between A49 and G50 for a catalytic metal ion. The kinked backbone requires the residues below and above to accommodate this structural change, therefore a flexible structure is more favorable than a rigid one. This model is consistent with the result that substitution of U51 with adenosine has only a minimal effect on PRNA activity (~5-fold decrease), while guanosine and cytidine substitutions reduce the activity 50-60-fold [59]. The adenosine substitution retains the bulge conformation, whereas the guanosine and cytidine move the bulge downward or upward by alternative base pairing. Furthermore, the bulge and the extra adenosine also create more space for the structural change than a compact helix. Therefore bulged U51 and A-tract reinforce the kink formation spatially and stabilize the conformational change. Moreover, the base is also crucial. The nucleobase plays a role in restricting the backbone conformation to allow the structural requirements to be dynamically satisfied by the kink formation and metal ion binding. Overall, a

flexible P4 helix, rather than a rigid conformation, is preferred by the conformational change in RNase P catalysis.

4.4.5 Implications of the Conformational Change

The transition of the ES complex to ES* active conformer is essential for RNase P catalysis, the ES* is stabilized by specific interactions between the pre-tRNA leader and the RNase P protein in the RNase P - pre-tRNA complex [20-22]. The global structural change in the ES complex could enhance the ability of RNase P to recognize the wide variety of pre-tRNAs and other substrates [21, 62, 63]. The data here suggest that the local structural rearrangement in the P4 helix after forming the ES complex enhances the binding affinity of the metal ions interacting with the non-bridging phosphodiester oxygens on the backbone of A49 and G50. These metal ions are proposed to supply a magnesium-hydroxide nucleophile to catalyze the hydrolysis of the phosphodiester backbone of the substrate [25, 26, 36, 64]. Thus, the conformational change in the P4 helix allows the formation of this highly reactive metal ion only after substrate binding to prevent self-cleavage or degradation of PRNA. Furthermore, the existence of active ES* is transient and changes back to inactive confermer after product formation, also limiting the catalysis only to the substrate.

4.5 Conclusion

Mutagenesis and atom modification combined with enzyme kinetics demonstrate that the P4 helix undergoes a structural alteration during the conformational change of RNase P catalysis. The data suggest that the structural changes mimic the TS observed

in the P4 helix stem-loop model by NMR relaxation dispersion, which includes a kink formation at the backbone between A49 and G50 facilitated by the transition of G50 flipping from *anti* to *syn*, bottom helix unwinding and oscillation of bulged U51. The kink forms a site that is favorable for Mg^{2+} ion binding. A flexible helix is preferred to stabilize this conformational change rather than a rigid double helix. This study also elucidates the possible ligands, base of G50 and A-tract, interact with a class of metal ions that stabilize the conformational change of RNase P.

This study provides structural insight into the dynamics of the P4 helix, the active site of RNase P, during the conformational change of RNase P and, for the first time, describes a model of the active conformation of the P4. The roles of the conformational change in the P4 are likely to position the active site residues and enhance the metal affinity to catalyze hydrolysis. These data also provides evidence for the presence of a transient, functionally important *syn* nucleotide in RNA.

4.6 Materials and Methods

4.6.1 Materials and Reagents

The chemicals, enzyme and buffers were prepared in the same way as described in Chapter 2. The ribo-oligonucleotide with rSpacer (abasic) modification was synthesized by the Keck Oligo Synthesis Resource (Yale School of Medicine), the one containing N1-methylated guanosine was purchased from GE Dharmacon, and the one with locked nucleic acid (LNA) was purchased from Exiqon. The ribooligonucleotide containing 8-bromoguanosine was synthesized by Kierzek's lab in the Polish Academy of Science.

4.6.2 Preparation of P Protein, Substrate, PRNA and PRNA mutant

B. subtilis RNase P protein, Fl-pre-tRNA^{Asp} substrate and WT PRNA were prepared as described in Chapter 2. DelA48, DelU51 and DelA48U51 plasmids were generated by deletion of A48 or (and) U51 by using QuikChange site-directed mutagenesis kit (Stratagene). The DelA48, DelU51 and DelA48U51 RNAs were then *in vitro* transcribed in the same way described in Chapter 2 by using a DNA template generated by digesting the plasmid with *Dra*I (New England Biolabs).

4.6.3 Preparation of Circularly Permuted RNA

The preparation of circularly permuted 386-365P (p386P) is described in Chapter 2. Plasmids containing the DNA template for transcribing circularly permuted 56-45P PRNAs (plasmids named as p56P) were cloned from the p2PRNA plasmid containing tandem repeats of RNase P, as described before [26, 65]. The p64P (64-45P RNA) plasmid was prepared by the deletion of nucleotides from G56 to C63 in p56P plasmid using QuikChange site-directed mutagenesis kit (Stratagene) (Primers: 5'-GGG CAT CTC AGC ACC TAT AGT GAG TCG TAT TAG AC-3'; 5'-GTC TAA TAC GAC TCA CTA TAG GTG CTG AGA TGC CC-3'). Following the linearization of the DNA templates by *Bsa*I (p56P and p64P) or *EcoR*V (p386) restriction enzymes (NEB), respectively, the circularly permuted P RNAs were transcribed *in vitro* to a 5′ guanosine monophosphate primed (5'-GMP) RNA, as previously reported [26].

4.6.4 Preparation of Modified PRNA by Ligation

For the 5' side of the P4 helix, the 10-mer (or 18-mer for 64-45P) ribo-oligonucelotide containing the same sequence as the 5' end strand of the P4 helix (5'-GA*^{47}A*^{48} A*^{49}G*^{50}U CCA U-3', or 5'-G GA*^{47}A*^{48} A*^{49}G*^{50}U CCA UGC UCG CAC-3' for 64-45P) with modifications (indicated by the asterisk sign and numbering) was ligated to the 5'-GMP transcribed 56-45P (or 64-45P) RNA in the presence of a DNA splint that is complementary to all 10-nt (or 18-nt) of the RNA oligo and the first 23 to 41 nt (or 23 to 33 nt for 64-45P) of 56-45P (or 64-45P) RNA (5'-GGG CAT CTC AGC ACC GTG CGA GCATGG ACT TTC A-3' or 5'-GCT AGG CAC GAA CACTAC GGG CAT CTC AGC ACC GTG CGA GCATGG ACT TTC-3') to create a 46P RNA [26]. The PRNA containing N1-methylguanosine and abasic modification of G50 were prepared with 64-45P and others were prepared with 56-45P. Modifications at the 3' side of the P4 helix were incorporated into PRNA same as described in Chapter 2.

The ligation protocol and determination of ligation efficiency were described in Chapter 2. The 6FAM labeled primer used to determine the ligation efficiency for 46P RNA anneals to nucleotide 114 to 95 of the 46P and the sequence is 5'-6FAM-GCC CTA GCT TAT GAC TTC GC-3' [26].

4.6.5 Single-turnover Kinetics Experiments

The experiments and data analysis were conducted in the same as described in Chapter 2. Both RNase P (360 nM - 4 μM) and Mg^{2+} (20-50 mM) were at saturating concentrations. For the Mg^{2+} dependence of RNase P STO cleavage, the concentration of $MgCl_2$ was 4-50 mM with varying KCl concentrations from ~250 to 110 mM.

4.7 References

1. Decatur, W.A. and Fournier, M.J., *RNA-guided nucleotide modification of ribosomal and other RNAs.* J Biol Chem, 2003. **278**(2): p. 695-8.
2. Serganov, A. and Patel, D.J., *Ribozymes, riboswitches and beyond: regulation of gene expression without proteins.* Nat Rev Genet, 2007. **8**(10): p. 776-90.
3. Diribarne, G. and Bensaude, O., *7SK RNA, a non-coding RNA regulating P-TEFb, a general transcription factor.* RNA Biol, 2009. **6**(2): p. 122-8.
4. Leeb, M., Steffen, P.A., and Wutz, A., *X chromosome inactivation sparked by non-coding RNAs.* RNA Biol, 2009. **6**(2): p. 94-9.
5. Tucker, B.J. and Breaker, R.R., *Riboswitches as versatile gene control elements.* Curr Opin Struct Biol, 2005. **15**(3): p. 342-8.
6. Nudler, E., *Flipping riboswitches.* Cell, 2006. **126**(1): p. 19-22.
7. Stone, M.D., et al., *Stepwise protein-mediated RNA folding directs assembly of telomerase ribonucleoprotein.* Nature, 2007. **446**(7134): p. 458-61.
8. Lilley, D.J., *Analysis of Global Conformational Transitions in Ribozymes*, in *Ribozymes and siRNA Protocols*, Sioud, M., Editor. 2004, Humana Press. p. 77-108.
9. Dunham, C.M., Murray, J.B., and Scott, W.G., *A helical twist-induced conformational switch activates cleavage in the hammerhead ribozyme.* J Mol Biol, 2003. **332**(2): p. 327-36.
10. Hoogstraten, C.G., Wank, J.R., and Pardi, A., *Active site dynamics in the lead-dependent ribozyme.* Biochemistry, 2000. **39**(32): p. 9951-8.
11. Zhuang, X., et al., *Correlating structural dynamics and function in single ribozyme molecules.* Science, 2002. **296**(5572): p. 1473-6.
12. Ke, A., et al., *A conformational switch controls hepatitis delta virus ribozyme catalysis.* Nature, 2004. **429**(6988): p. 201-5.
13. Kazantsev, A.V. and Pace, N.R., *Bacterial RNase P: a new view of an ancient enzyme.* Nat Rev Microbiol, 2006. **4**(10): p. 729-40.
14. Smith, J.K., Hsieh, J., and Fierke, C.A., *Importance of RNA-protein interactions in bacterial ribonuclease P structure and catalysis.* Biopolymers, 2007. **87**(5-6): p. 329-38.
15. Kirsebom, L.A., *RNase P RNA mediated cleavage: substrate recognition and catalysis.* Biochimie, 2007. **89**(10): p. 1183-94.
16. Walker, S.C. and Engelke, D.R., *Ribonuclease P: the evolution of an ancient RNA enzyme.* Crit Rev Biochem Mol Biol, 2006. **41**(2): p. 77-102.
17. Hartmann, E. and Hartmann, R.K., *The enigma of ribonuclease P evolution.* Trends Genet, 2003. **19**(10): p. 561-9.
18. Hall, T.A. and Brown, J.W., *The ribonuclease P family.* Methods Enzymol, 2001. **341**: p. 56-77.
19. Hsieh, J. and Fierke, C.A., *Conformational change in the Bacillus subtilis RNase P holoenzyme--pre-tRNA complex enhances substrate affinity and limits cleavage rate.* RNA, 2009. **15**(8): p. 1565-77.
20. Koutmou, K.S., Day-Storms, J.J., and Fierke, C.A., *The RNR motif of B. subtilis RNase P protein interacts with both PRNA and pre-tRNA to stabilize an active conformer.* RNA (New York, N.Y.), 2011. **17**(7): p. 1225-1235.
21. Hsieh, J., et al., *A divalent cation stabilizes the active conformation of the B. subtilis RNase P x pre-tRNA complex: a role for an inner-sphere metal ion in RNase P.* J Mol Biol, 2010. **400**(1): p. 38-51.
22. Crary, S.M., Niranjanakumari, S., and Fierke, C.A., *The Protein Component of Bacillus subtilis Ribonuclease P Increases Catalytic Efficiency by Enhancing Interactions with the 5,Äò Leader Sequence of Pre-tRNAAsp.* Biochemistry, 1998. **37**(26): p. 9409-9416.

23. Kurz, J.C. and Fierke, C.A., *The affinity of magnesium binding sites in the Bacillus subtilis RNase P x pre-tRNA complex is enhanced by the protein subunit.* Biochemistry, 2002. **41**(30): p. 9545-58.
24. Reiter, N.J., et al., *Structure of a bacterial ribonuclease P holoenzyme in complex with tRNA.* Nature, 2010. **468**(7325): p. 784-9.
25. Christian, E.L., Kaye, N.M., and Harris, M.E., *Helix P4 is a divalent metal ion binding site in the conserved core of the ribonuclease P ribozyme.* RNA, 2000. **6**(4): p. 511-9.
26. Crary, S.M., Kurz, J.C., and Fierke, C.A., *Specific phosphorothioate substitutions probe the active site of Bacillus subtilis ribonuclease P.* RNA, 2002. **8**(7): p. 933-47.
27. Christian, E.L., et al., *The P4 metal binding site in RNase P RNA affects active site metal affinity through substrate positioning.* RNA, 2006. **12**(8): p. 1463-7.
28. Kazantsev, A.V., et al., *Crystal structure of a bacterial ribonuclease P RNA.* Proceedings of the National Academy of Sciences of the United States of America, 2005. **102**(38): p. 13392-13397.
29. Liu, X., Chen, Y., and Fierke, C.A., *A real-time fluorescence polarization activity assay to screen for inhibitors of bacterial ribonuclease P.* Nucleic Acids Res, 2014. **42**(20): p. e159.
30. Liu, X., *Molecular Recognition of Inhibitors, Metal Ions and Substrates by Ribonuclease P*. 2013, University of Michigan, Ann Arbor.
31. Nikolova, E.N., et al., *Transient Hoogsteen base pairs in canonical duplex DNA.* Nature, 2011. **470**(7335): p. 498-502.
32. Tavale, S.S. and Sobell, H.M., *Crystal and molecular structure of 8-bromoguanosine and 8-bromoadenosine, two purine nucleosides in the syn conformation.* Journal of Molecular Biology, 1970. **48**(1): p. 109-123.
33. Michelson, A.M., Monny, C., and Kapuler, A.M., *Poly 8-bromoguanylic acid.* Biochim Biophys Acta, 1970. **217**(1): p. 7-17.
34. Ikehara, M., Uesugi, S., and Yoshida, K., *Studies on the conformation of purine nucleosides and their 5'-phosphates.* Biochemistry, 1972. **11**(5): p. 830-6.
35. Kazantsev, A.V., et al., *Solution structure of RNase P RNA.* RNA, 2011. **17**(6): p. 1159-71.
36. Harris, M.E. and Christian, E.L., *Recent insights into the structure and function of the ribonucleoprotein enzyme ribonuclease P.* Current Opinion in Structural Biology, 2003. **13**(3): p. 325-333.
37. Frank, A.T., Law, S.M., and Brooks, C.L., *A Simple and Fast Approach for Predicting 1H and 13C Chemical Shifts: Toward Chemical Shift-Guided Simulations of RNA.* The Journal of Physical Chemistry B, 2014. **118**(42): p. 12168-12175.
38. Christian, E.L., Kaye, N.M., and Harris, M.E., *Evidence for a polynuclear metal ion binding site in the catalytic domain of ribonuclease P RNA.* EMBO J, 2002. **21**(9): p. 2253-62.
39. Yang, H., et al., *Effect of 1-methyladenine on double-helical DNA structures.* FEBS Lett, 2008. **582**(11): p. 1629-33.
40. Lu, L., et al., *Structure determination of DNA methylation lesions N1-meA and N3-meC in duplex DNA using a cross-linked protein-DNA system.* Nucleic Acids Res, 2010. **38**(13): p. 4415-25.
41. Yajima, R., et al., *A conformationally restricted guanosine analog reveals the catalytic relevance of three structures of an RNA enzyme.* Chem Biol, 2007. **14**(1): p. 23-30.
42. Bloomfield, V.A., Crothers, D.M., and Tinoco, I.J., *Nucleic acids: Structures, properties, and functions*. 2000, Sausalito, CA: University Science Books.
43. Proctor, D.J., et al., *Restricting the conformational heterogeneity of RNA by specific incorporation of 8-bromoguanosine.* J Am Chem Soc, 2003. **125**(9): p. 2390-1.
44. Sokoloski, J.E., et al., *Prevalence of syn nucleobases in the active sites of functional RNAs.* RNA, 2011. **17**(10): p. 1775-87.

45. Lemieux, S., et al., *Modeling active RNA structures using the intersection of conformational space: application to the lead-activated ribozyme.* RNA, 1998. **4**(7): p. 739-49.
46. Martick, M. and Scott, W.G., *Tertiary contacts distant from the active site prime a ribozyme for catalysis.* Cell, 2006. **126**(2): p. 309-20.
47. Baugh, C., Grate, D., and Wilson, C., *2.8 A crystal structure of the malachite green aptamer.* J Mol Biol, 2000. **301**(1): p. 117-28.
48. Yang, Y., et al., *Structural basis of ligand discrimination by two related RNA aptamers resolved by NMR spectroscopy.* Science, 1996. **272**(5266): p. 1343-7.
49. MacElrevey, C., et al., *Structural effects of nucleobase variations at key active site residue Ade38 in the hairpin ribozyme.* RNA, 2008. **14**(8): p. 1600-16.
50. Toor, N., et al., *Crystal structure of a self-spliced group II intron.* Science, 2008. **320**(5872): p. 77-82.
51. Shi, H. and Moore, P.B., *The crystal structure of yeast phenylalanine tRNA at 1.93 A resolution: a classic structure revisited.* RNA, 2000. **6**(8): p. 1091-105.
52. Battle, D.J. and Doudna, J.A., *Specificity of RNA-RNA helix recognition.* Proc Natl Acad Sci U S A, 2002. **99**(18): p. 11676-81.
53. Cheong, C., Varani, G., and Tinoco, I., Jr., *Solution structure of an unusually stable RNA hairpin, 5'GGAC(UUCG)GUCC.* Nature, 1990. **346**(6285): p. 680-2.
54. Veeraraghavan, N., et al., *Metal binding motif in the active site of the HDV ribozyme binds divalent and monovalent ions.* Biochemistry, 2011. **50**(13): p. 2672-82.
55. Bevilacqua, P.C., *Mechanistic considerations for general acid-base catalysis by RNA: revisiting the mechanism of the hairpin ribozyme.* Biochemistry, 2003. **42**(8): p. 2259-65.
56. Klein, D.J. and Ferre-D'Amare, A.R., *Structural basis of glmS ribozyme activation by glucosamine-6-phosphate.* Science, 2006. **313**(5794): p. 1752-6.
57. Batey, R.T., Gilbert, S.D., and Montange, R.K., *Structure of a natural guanine-responsive riboswitch complexed with the metabolite hypoxanthine.* Nature, 2004. **432**(7015): p. 411-5.
58. Wilson, T.J. and Lilley, D.M., *Do the hairpin and VS ribozymes share a common catalytic mechanism based on general acid-base catalysis? A critical assessment of available experimental data.* RNA, 2011. **17**(2): p. 213-21.
59. Kaye, N.M., et al., *Conservation of helical structure contributes to functional metal ion interactions in the catalytic domain of ribonuclease P RNA.* J Mol Biol, 2002. **324**(3): p. 429-42.
60. Reiter, N.J., Osterman, A.K., and Mondragon, A., *The bacterial ribonuclease P holoenzyme requires specific, conserved residues for efficient catalysis and substrate positioning.* Nucleic Acids Res, 2012. **40**(20): p. 10384-93.
61. Frank, D.N. and Pace, N.R., *Ribonuclease P: unity and diversity in a tRNA processing ribozyme.* Annu Rev Biochem, 1998. **67**: p. 153-80.
62. Sun, L., et al., *Evidence that substrate-specific effects of C5 protein lead to uniformity in binding and catalysis by RNase P.* The EMBO journal, 2006. **25**(17): p. 3998-4007.
63. Hernandez-Cid, A., et al., *Ribonucleases P/MRP and the expanding ribonucleoprotein world.* IUBMB Life, 2012. **64**(6): p. 521-8.
64. Cassano, A.G., Anderson, V.E., and Harris, M.E., *Analysis of solvent nucleophile isotope effects: evidence for concerted mechanisms and nucleophilic activation by metal coordination in nonenzymatic and ribozyme-catalyzed phosphodiester hydrolysis.* Biochemistry, 2004. **43**(32): p. 10547-59.
65. Nolan, J.M., et al., *Circularly Permuted tRNAs as Specific Photoaffinity Circularly Probes of Ribonuclease P RNA Structure.* Advancement Of Science, 1993. **261**(5122): p. 762-765.

CHAPTER 5
CONCLUSIONS AND FUTURE DIRECTIONS

5.1 Conclusions

This work investigated two important factors for RNase P catalysis, metal ion interactions and conformational dynamics, to understand how RNase P catalyzes an essential biological reaction. By combining nuclear magnetic resonance (NMR) spectroscopy and enzyme kinetics, a structural rearrangement was observed in the P4 helix, the active site of RNase P. The function of this conformational change in the P4 helix is proposed to enhance the binding affinity of the catalytic divalent metal ions on the backbone of A49 and G50 (*Bacillus subtilis* numbering). Other metal ion binding sites in the P4 helix were also identified, including an outer-sphere metal ion coordinated by O6 of G379 and a class of divalent metal ions important for stabilizing the conformational change of RNase P associated with G50 and U51. Additionally, this work first time identified a functionally important transient *syn* nucleotide in RNA.

5.1.1 An Outer-Sphere Metal Ion Binding Site in the P4 Helix Enhances RNase P Catalysis

Atom modifications were specifically substituted for G378 and G379 in the P4 helix of *B. subtilis* RNase P to evaluate the structure and function of the putative metal ion binding sites proposed by NMR spectroscopy and X-ray absorption spectroscopy (XAS)

using a P4 stem-loop mimic [1].

Modifications on G378 and G379 affect the pre-tRNA substrate binding affinity for RNase P at low concentrations of metal ion but not at high concentration suggesting G378 and G379 stabilizing pre-tRNA affinity in a divalent metal ion-dependent fashion. Under single turnover (STO) conditions, the rate limiting step of RNase P is hydrolytic cleavage of pre-tRNA at low pH (≤6), and conformational change at high pH (≥8) [2]. 2-aminopurine nucleotide and abasic substitution at G379 decreases the STO cleavage rate constant at low pH suggesting that the carbonyl oxygen at O6 position of G379 in RNase P RNA (PRNA) interacts with a metal ion that stabilizes hydrolytic cleavage of RNase P. The 6-thioguanosine substitution at G379 has similar activity to WT RNase P and the addition of Cd^{2+} does not activate pre-tRNA cleavage activity demonstrating that O6 of G379 does not form an inner sphere contact with the metal ion. Rather O6 of G379 likely forms an outer-sphere interaction with a water-metal ligand. Abasic modification on G379 decreases the rate constant of the conformational change suggesting that the guanosine base of this nucleotide is essential for both catalysis and stabilization of an active conformer of RNase P.

These results revise the model of the metal ion binding sites proposed from analysis of a P4 stem-loop mimic. An outer-sphere metal ion binding site at G379 in the P4 helix of RNase P is proposed in this study. This metal ion is involved in stabilizing substrate affinity, enhancing catalysis of pre-tRNA cleavage as well as participating in a conformational change in the RNase P kinetic pathway.

5.1.2 The Transient State of the P4 Helix Mimic

To identify structural insights into the conformational change on the P4 helix of RNase P, a stem-loop mimic was used as a model to study the dynamics of the P4 helix. A NMR structure study of the P4 helix mimic suggest that in the ground state (GS), U7 (U51 in *B. subtilis* PRNA) is bulged out of the helix, and the three adenosines tract (A-tract, A47, A48 and A49 in *B. subtilis* PRNA) are in a helical conformation and form weak hydrogen bonds with two uridines on the other strand of the helix.

^{13}C and ^{15}N $R_{1\rho}$ relaxation dispersion NMR experiments demonstrated significant relaxation dispersion, indicative of chemical exchange, in and around the sugar C1' and base C2/6/8 of the bulged U7 (U51) and A-tract regions. A two-state off-resonance analysis of the data reveals a shared transient state (TS) for the helix and an independent TS for U7. Mutagenesis, chemical modification, ligand titration and thermodynamic studies were used to probe the structure of the TS. Using these data, a computational MCSYM-LARMORD approach [3] predicted a 3D model of the TS. In this model, the A-tract region unwinds and G6 (G50 in *B. subtilis* PRNA) changes from *anti* conformation to *syn* leading to a kink formation in the backbone between A5 (A49) and G6 (G50) that creates a favorable binding pocket for metal ion coordination. These data also suggest that the flexible helical conformation stabilizes the shared TS more than a rigid helix. Additionally, U7 (U51) flips in and out of the helix independently and with a relatively faster motion compared with the shared TS.

This study detected a transient *syn* base in an RNA double helix for the first time and identified a transient conformer of the P4 helix mimic, which may supply structural

information of metal ion binding sites and conformational change for the P4 helix during RNase P catalysis.

5.1.3 Conformational Change of the P4 Helix Facilitates the Binding Affinity of Catalytic Metal Ions

After probing the transient state of the P4 helix mimic, it is important to determine whether the TS of the P4 helix mimic observed by NMR is related to the conformational change step that occurs during the RNase P catalytic cycle. To test this hypothesis, mutants and modifications were incorporated into the residues in and around the conserved bulged U51, G50 and A-tract regions of the P4 helix in the full-length PRNA. By exploiting the same enzyme kinetics approach, the effect of the modifications on either the conformational change step or the hydrolytic step in RNase P catalysis was evaluated.

The kinetic data show strong correlations with the NMR results. The DelA4 eliminates the NMR relaxation dispersion and destabilizes the TS in the P4 helix mimic. Consistent with this, the DelA48 mutation in full-length PRNA significantly decreases the rate constants of both the conformational change and hydrolytic cleavage steps catalyzed by RNase P. Furthermore, the abasic modification on G50 (G50-abG) reduces RNase P activity to a level comparable to DelA48, indicating that the base of G50 is important for RNase P catalysis. The 8-bromoguanosine substitution for G50 has comparable activity to WT RNase P indicating that RNase P can tolerate a locked *syn* conformation on G50 during catalysis [4-6]. This result is consistent with the NMR result where G6 adopts a *syn* conformation in the TS of the P4 helix mimic. Both the DelA48

and G50-abG variants decrease the Mg^{2+} affinity for RNase P-catalyzed cleavage, suggesting that the observed defect in the conformational change caused by these modifications is related to metal ion binding. This result is consistent with the TS of the P4 helix proposed by the NMR data forming an electronegative patch for metal ion binding. The conserved bulged U51 contributes to the conformational change, consistent with the flexibility observed by U7 in the P4 helix mimic oscillating in and out of the helix in a fast motion.

The correlation between the RNase P kinetics data and the P4 stem-loop NMR results demonstrates that the TS observed in the P4 stem-loop model mimics the P4 helix conformational change in RNase P. These data indicate that in the conformational change of the RNase P - pre-tRNA complex, the P4 helix undergoes a structural rearrangement, including: formation of a kink at the backbone between A49 and G50 facilitated by the transition of G50 flipping from *anti* to *syn*; the A-tract region of the helix unwinds; and the bulged U51 oscillates between in and out conformations. A flexible helix stabilizes this conformational change more than a rigid double helix, as indicated by the DelA48 mutant. The backbone kink forms an electrostatic site favorable for Mg^{2+} ion binding to RNase P and activating catalysis. Additional data also suggest there is a class of metal ions, which stabilizes the conformational change of RNase P, interacting with the bases of G50 and U51.

This study supplies the evidence for the presence of a transient, functionally important *syn* nucleotide in RNA and provides the structural insights of the active conformation of the P4 helix. The function of the P4 structural rearrangement during conformational

change is to reposition the residues in the active site thereby enhancing the metal ion binding affinity for RNase P catalysis.

5.2 Future Directions

RNase P is an essential enzyme in all domains of life. Numerous fundamental questions remain on the mechanisms that RNase P uses to achieve precise and efficient catalysis. Discerning the position and structure of the divalent metal ions that site-specifically interact with the functional ligands is a major challenge to understanding the structure and mechanism of RNase P. The structural information of the RNase P conformational change and the precise roles that the conformational change is playing in the RNase P catalytic pathway have not been elucidated.

5.2.1 Probing the functional ligands associated with the metal ions stabilizing the conformational change of RNase P - pre-tRNA complex

This study identified modifications in the P4 helix that decrease the rate constant of the conformational change in RNase P catalysis without affecting the hydrolysis step. This effect on conformational change is divalent metal ion dependent. This finding is consistent with a class of metal ions enhancing the active conformer formation for enzyme-substrate complex [7]. The residues involved in interacting with these metal ions include G50 and the A-tract.

To further probe the sites on G50 and the A-tract that interact with metal ions related to conformational change, additional atom modifications could be incorporated into RNase P and the effect on catalysis could be examined. For example, as shown in

Figure 5-1, the 2-aminopurine substitution at G50 could be used to test for possible metal ion coordination at O6 of this position. The 7-deazaguanosine and 7-deazaadenosine modifications could be specifically substituted at G50 and A-tract, respectively, to probe for a potential metal ion interaction with N7. The N1-methyladenosine substitution could be used to detect interactions with the N1 position of the A-tract.

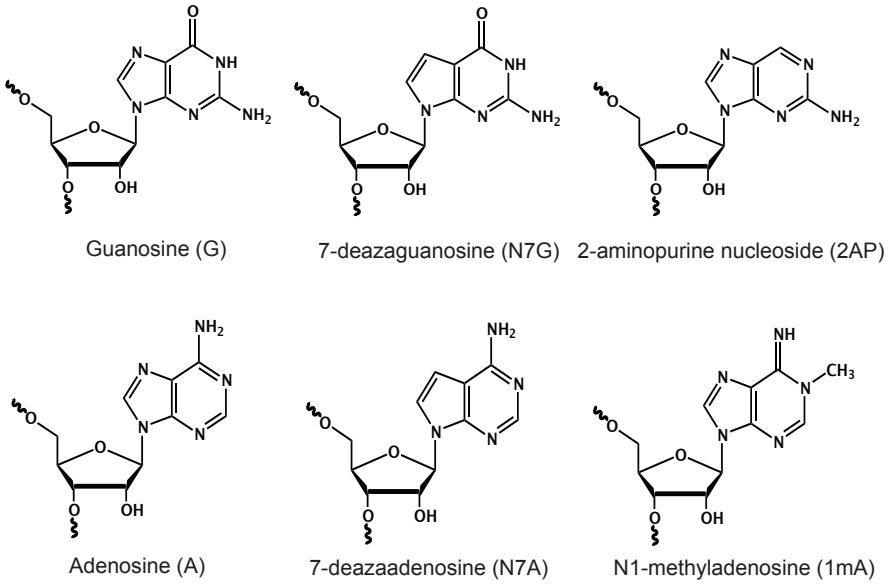

Figure 5-1: Chemical structures of adenosine, guanosine and substitutions

5.2.2 Examining the Conformational change of RNase P

The conformational change occurring in the P4 helix could be further probed with additional atom modifications. For example, the abasic substitutions at U381 and U382 in the P4 helix demonstrate that these based do not contribute to RNase P catalysis. Substitution of one or both of these uridines with the fluorescent analog, 4-thiouridine, could be used to monitor the conformational change step in the P4 helix (Figure 5-2). Alternatively, 4-thiouridine could be substituted for U51 to observe the conformation

transition since this substitution does not affect the rate constant of the conformational change (Xin Liu, Yu Chen, and Carol A. Fierke, manuscript in preparation). Alternatively, fluorescent analogs of guanosine at G378 or G379 could also serve as probes to detect the conformational change in the P4 helix, such as tricyclic cytidine analog tC^O or 6-methylisoxanthopterin (Figure 5-2) although the effect of those substitutions on RNase P activity need to be determined.

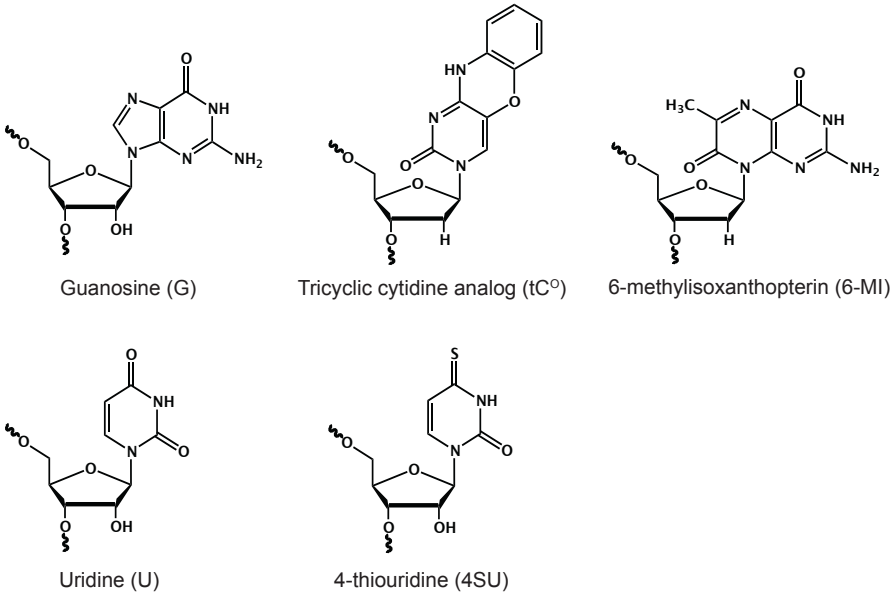

Figure 5-2: Chemical structures of guanosine, uridine and fluorescent analogs

In addition to the local conformational change in the P4 helix, time-resolved fluorescence energy transfer (trFRET) data have indicated that an inner-sphere metal ion-dependent conformational change step occurs upon substrate binding that leads to a ~ 40 Å movement between the catalytic- and specificity-domain of PRNA (John Hsieh and Carol A. Fierke, unpublished data). Since Del48 disrupts the local structural rearrangement in the P4 helix, similar trFRET experiments could be used to investigate whether the global conformational change is also disturbed by this mutation. These

data would test whether the long-range changes are linked to the local changes in the P4 helix.

5.2.3 Characterizing the P4 helix in Full-length PRNA by NMR spectroscopy

The NMR study on the P4 helix stem-loop mimic indicated small differences in the interhelical angle and the conformation of A48 compared to the crystal structure [8-10]. This difference was attributed to tertiary contacts between the upper stem of the P4 and L8, and the base stacking between A48 and J3/4 in the crystal structure [8] that are absent in the isolated P4 construct. Studying the P4 helix in the entire PRNA would be a better way to probe structural transitions in the P4 helix since the tertiary interactions and metal ion coordination would be retained.

5.2.3.1 Investigating the Structure P4 Helix

PRNA is a large molecule with about 400 nucleotides. The challenge of studying the full-length PRNA by NMR is that NMR signals of larger molecules relax faster, leading to line broadening and poor spectral sensitivity, and eventually to no NMR signals at all [11, 12]. Additionally, the large number of resonances from large molecules causes signal overlap, which can make analysis of the spectra very difficult. To alleviate these difficulties, selective labeling strategies can be applied. I developed a method to make a $^{13}C/^{15}N$ uniformly labeled single-strand RNA oligonucleotide with the sequence that same as nucleotides from G46 to U55 of the P4 helix (Chapter 3) (Figure 5-3A). A *B. subtilis* pre-tRNA^{Asp} where the leader sequence contains the ribooligonucleotide of interest (5'-GAA AGU CCA U-3') was designed and transcribed using uniformly $^{13}C/^{15}N$-

labeled nucleotide triphosphates (Figure 5-3B). Then this pre-tRNA^{Asp}-10 was cleaved by RNase P to produce a 10-mer oligonucleotide with a defined 3' hydroxyl end that contains $^{13}C/^{15}N$ labels (Figure 5-3B). This 10-mer containing the residues of the 5' side of the P4 helix can be ligated to 56P RNA and reconstitute a full-length, circularly permuted PRNA, 46P (Figure 5-3B) (Chapter 4) [13, 14]. Since this 46P is only segmentally $^{13}C/^{15}N$ labeled at half of the P4 helix, the signal sensitivity will be significantly increased. The $^{13}C/^{15}N$ uniformly labeled mature tRNA can be used for other studies.

Instead of using Mg^{2+}, Ca^{2+} will be used to fold the PRNA containing labeled P4 to limit self-cleavage and degradation. By comparing the 2D aromatic ^{13}C-^{1}H, aliphatic ^{13}C-^{1}H and imino ^{15}N-^{1}H of the P4 in PRNA with the ground state of the P4 helix mimic, the secondary structure of the P4 helix can be reevaluated. The discrepancy of the A48 and U51 conformations, whether they are bulged out or in helical conformation, between the crystal structures and the NMR study on the P4 helix mimic can be examined [8-10]. A similar method could also be used to selectively label the residues on the 3' side of the P4 helix and study the structure in the context of full-length PRNA. These experiments can supply direct structural information of the P4 helix in the full-length PRNA.

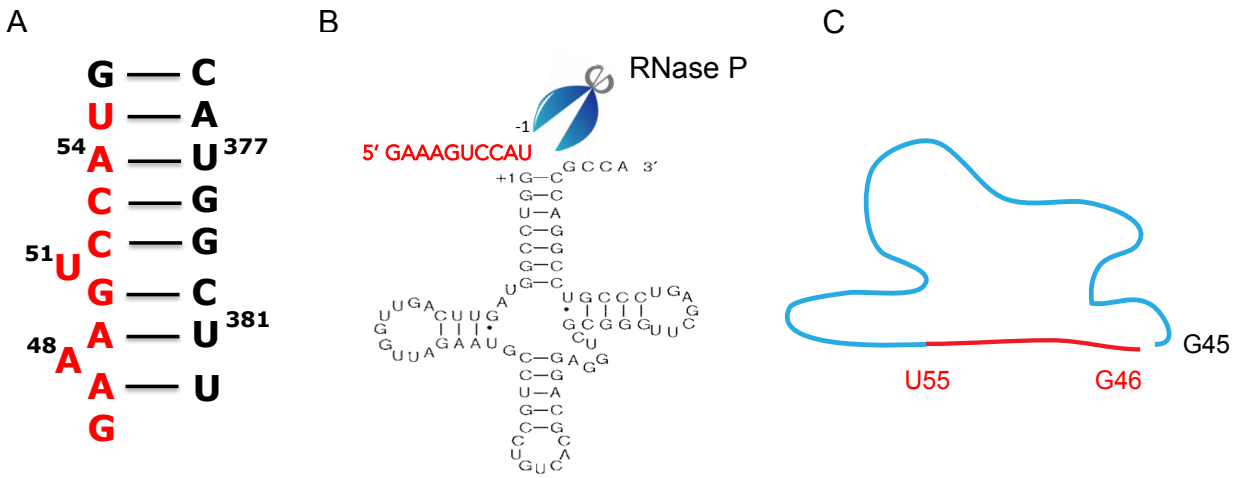

Figure 5-3: The strategy of selectively labeling half of the P4 helix in *B. subtilis* PRNA. **(A)** The secondary structure of the P4 helix. The residues $^{13}C/^{15}N$ labeled in PRNA are indicated in red. **(B)** A cartoon showing pre-tRNA^{Asp}-10 substrate cleaved by RNase P to generate the 10-mer identical to the 5' side of the P4 helix (in red). **(C)** A cartoon showing the 46P with $^{13}C/^{15}N$ enriched P4 region (in red).

5.2.3.2 Visualizing the Conformational Change of the P4 Helix

By studying a P4 helix stem-loop mimic using ^{13}C and ^{15}N $R_{1\rho}$ relaxation dispersion NMR experiments, a transient state of the P4 helix mimic is identified and it mimics the conformational change of the P4 helix in the full-length PRNA. Due to the secondary structure difference between the P4 helix mimic and the P4 helix in the context of the full-length PRNA, the isolated stem-loop mimic may not accurately reflect the PRNA structure. Therefore, investigating the conformational change of the P4 helix in the full-length PRNA is a direct solution.

After examining the structure of the P4 helix by using the segmentally labeled PRNA, addition of pre-tRNA substrate into PRNA can induce the conformational change of RNase P - pre-tRNA complex. The structure of the P4 helix can be reexamined in the presence of pre-tRNA and compared with the one without pre-tRNA, as well as the

transient state detected by relaxation dispersion using the stem-loop mimic, to probe the structural rearrangement after substrate binding. This experiment will be performed in Ca^{2+} to avoid cleavage of the pre-tRNA substrate. Similar experiments can also be conducted with mature tRNA to investigate the structure of the P4 helix after hydrolytic cleavage. By performing these experiments, the structural insights of the P4 helix during conformational change can be directly obtained.

5.2.4 Characterizing RNase P and Pre-tRNA Interaction by NMR spectroscopy

The conformational change that occurs during RNase P catalysis is stabilized by binding pre-tRNA and divalent metal ions. trFRET measurements indicate that the 5' leader of pre-tRNA moves 4 to 6 Å closer to the PRNA - P protein interface during the conformational change [7]. The study here provides evidence that the P4 helix in RNase P undergoes structural rearrangement, but it is unclear whether the structure of pre-tRNA also changes to dynamically fulfill a requirement for efficient RNase P catalysis. Characterizing a $^{13}C/^{15}N$ uniformly labeled pre-tRNA or mature tRNA by NMR spectroscopy could be a way to answer this question.

In collaboration with Dr. Sathyamoorthy and Dr. Salmon in the Al-Hashimi lab, we have already measured the 2D aromatic ^{13}C-^{1}H, aliphatic ^{13}C-^{1}H and imino ^{15}N-^{1}H spectra of a mature tRNA (Figure 5-4). One way to investigate the dynamics of the pre-tRNA / mature tRNA is by applying ^{13}C and ^{15}N $R_{1\rho}$ relaxation dispersion to probe the existence of transient state(s) and possible alternative conformers. Another way is titrating PRNA into pre-tRNA or mature tRNA to observe the peak perturbation reflecting PRNA - pre-tRNA interactions. The nucleotides that have differing chemical shifts

(proton, carbon or nitrogen) are proposed to be near the interaction surface, which can be mapped by identifying shifted resonances on the pre-tRNA [15, 16]. The peak perturbation on the 5' leader of pre-tRNA could provide structural information about the substrate bound to the active site of RNase P. This experiment could also be performed using protein-only RNase P to determine whether the conformation of the bound pre-tRNA is altered compared to RNA-based RNase Ps [17-19].

Taken together, the studies proposed here would address fundamental questions in the structure and mechanism of RNase P, including positions and functions of divlant metal ions, active conformation of RNase P, and the precise roles that the conformational change is playing in the RNase P catalytic pathway. These studies will also provide insights of enzyme - substrate interaction for both RNA-based and protein-only RNase P.

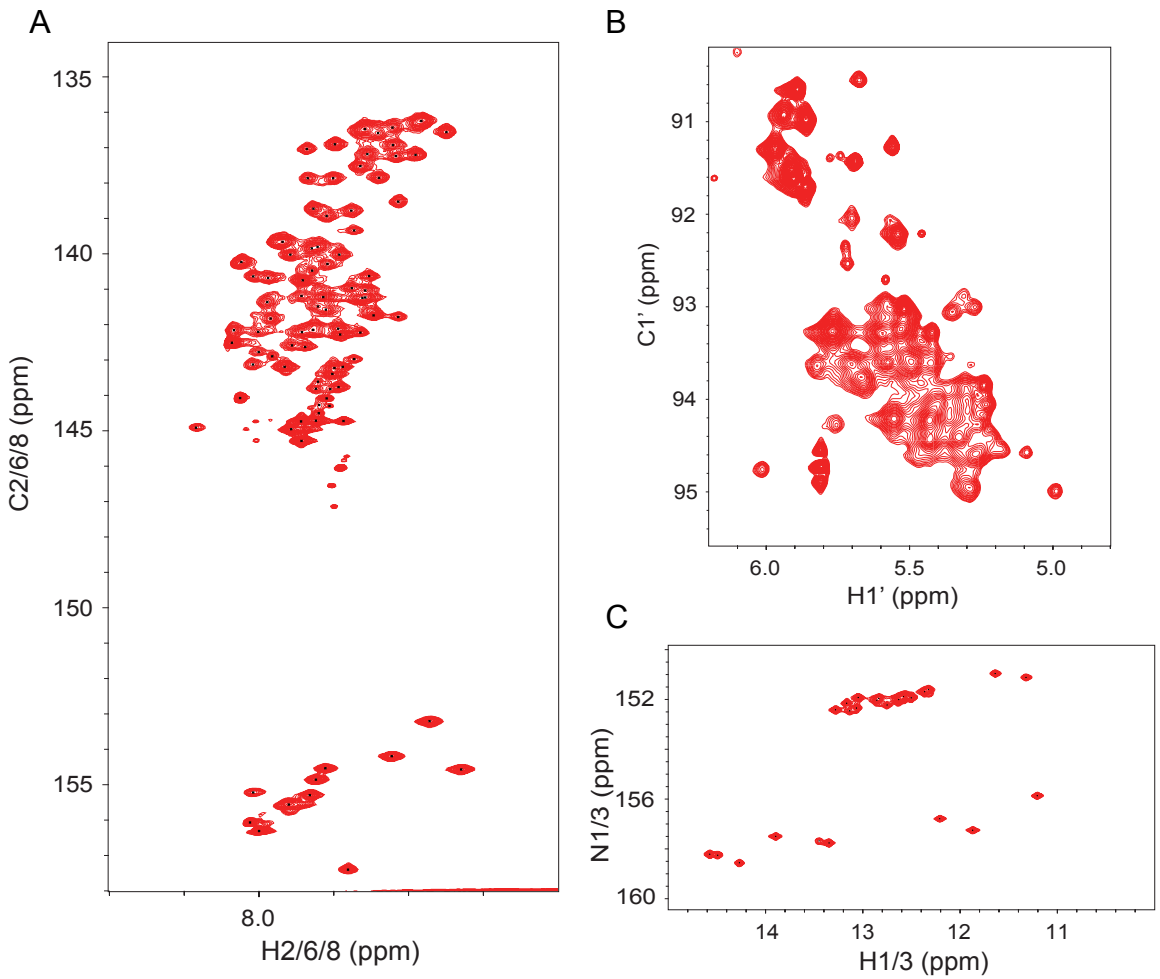

Figure 5-4: 2D ^{13}C-^{1}H and ^{15}N-^{1}H spectra of $^{13}C/^{15}N$ uniformly labeled *B. subtilis* $tRNA^{Asp}$. The data were collected in the buffer condition of 10 mM Na_3PO_4, 100 mM NaCl and 10 mM $MgCl_2$ under pH 6.5 at 37°C with 1 mM of $tRNA^{Asp}$. **(A)** $tRNA^{Asp}$ 2D ^{13}C-^{1}H spectra showing nucleobase C2/6/8-H2/6/8 correlation. **(B)** $tRNA^{Asp}$ 2D ^{13}C-^{1}H spectra showing sugar C1'-H1'correlation. **(C)** $tRNA^{Asp}$ 2D ^{15}N-^{1}H imino spectra showing nitrogen/proton (N1/3-H1/3) correlation[5].

[5] The *B. subtilis* $tRNA^{Asp}$ sample was prepared by Yu Chen and the NMR spectra were acquired by Bharathwaj Sathyamoorthy and Loïc Salmon in the Al-Hashimi lab

5.3 References

1. Koutmou, K.S., et al., *NMR and XAS reveal an inner-sphere metal binding site in the P4 helix of the metallo-ribozyme ribonuclease P.* Proceedings of the National Academy of Sciences, 2010. **107**(6): p. 2479-2484.
2. Hsieh, J. and Fierke, C.A., *Conformational change in the Bacillus subtilis RNase P holoenzyme--pre-tRNA complex enhances substrate affinity and limits cleavage rate.* RNA, 2009. **15**(8): p. 1565-77.
3. Frank, A.T., Law, S.M., and Brooks, C.L., *A Simple and Fast Approach for Predicting 1H and 13C Chemical Shifts: Toward Chemical Shift-Guided Simulations of RNA.* The Journal of Physical Chemistry B, 2014. **118**(42): p. 12168-12175.
4. Tavale, S.S. and Sobell, H.M., *Crystal and molecular structure of 8-bromoguanosine and 8-bromoadenosine, two purine nucleosides in the syn conformation.* Journal of Molecular Biology, 1970. **48**(1): p. 109-123.
5. Michelson, A.M., Monny, C., and Kapuler, A.M., *Poly 8-bromoguanylic acid.* Biochim Biophys Acta, 1970. **217**(1): p. 7-17.
6. Ikehara, M., Uesugi, S., and Yoshida, K., *Studies on the conformation of purine nucleosides and their 5'-phosphates.* Biochemistry, 1972. **11**(5): p. 830-6.
7. Hsieh, J., et al., *A divalent cation stabilizes the active conformation of the B. subtilis RNase P x pre-tRNA complex: a role for an inner-sphere metal ion in RNase P.* J Mol Biol, 2010. **400**(1): p. 38-51.
8. Kazantsev, A.V., et al., *Crystal structure of a bacterial ribonuclease P RNA.* Proceedings of the National Academy of Sciences of the United States of America, 2005. **102**(38): p. 13392-13397.
9. Reiter, N.J., et al., *Structure of a bacterial ribonuclease P holoenzyme in complex with tRNA.* Nature, 2010. **468**(7325): p. 784-9.
10. Getz, M.M., et al., *Structural plasticity and Mg2+ binding properties of RNase P P4 from combined analysis of NMR residual dipolar couplings and motionally decoupled spin relaxation.* RNA, 2006. **13**(2): p. 251-266.
11. Tzakos, A.G., et al., *NMR techniques for very large proteins and rnas in solution.* Annual review of biophysics and biomolecular structure, 2006. **35**: p. 319-342.
12. Fernández, C. and Wider, G., *TROSY in NMR studies of the structure and function of large biological macromolecules.* Current Opinion in Structural Biology, 2003. **13**(5): p. 570-580.
13. Crary, S.M., Kurz, J.C., and Fierke, C.A., *Specific phosphorothioate substitutions probe the active site of Bacillus subtilis ribonuclease P.* RNA, 2002. **8**(7): p. 933-47.
14. Liu, X., *Molecular Recognition of Inhibitors, Metal Ions and Substrates by Ribonuclease P*. 2013, University of Michigan, Ann Arbor.
15. Görlach, M., et al., *Interaction of the RNA-binding domain of the hnRNP C proteins with RNA.* The EMBO Journal, 1992. **11**(9): p. 3289-95.
16. Howe, P.W., et al., *NMR studies of U1 snRNA recognition by the N-terminal RNP domain of the human U1A protein.* The EMBO Journal, 1994. **13**(16): p. 3873-81.
17. Holzmann, J., et al., *RNase P without RNA: Identification and Functional Reconstitution of the Human Mitochondrial tRNA Processing Enzyme.* Cell, 2008. **135**(3): p. 462-474.
18. Gobert, A., et al., *A single Arabidopsis organellar protein has RNase P activity.* Nature Structural and Molecular Biology, 2010. **17**(6): p. 740-744.
19. Gutmann, B., Gobert, A., and Giegé, P., *PRORP proteins support RNase P activity in both organelles and the nucleus in Arabidopsis.* Genes & Development, 2012. **26**(10): p. 1022-1027.

APPENDIX A

A.1 Ligation Efficiency Determination by Primer Extension

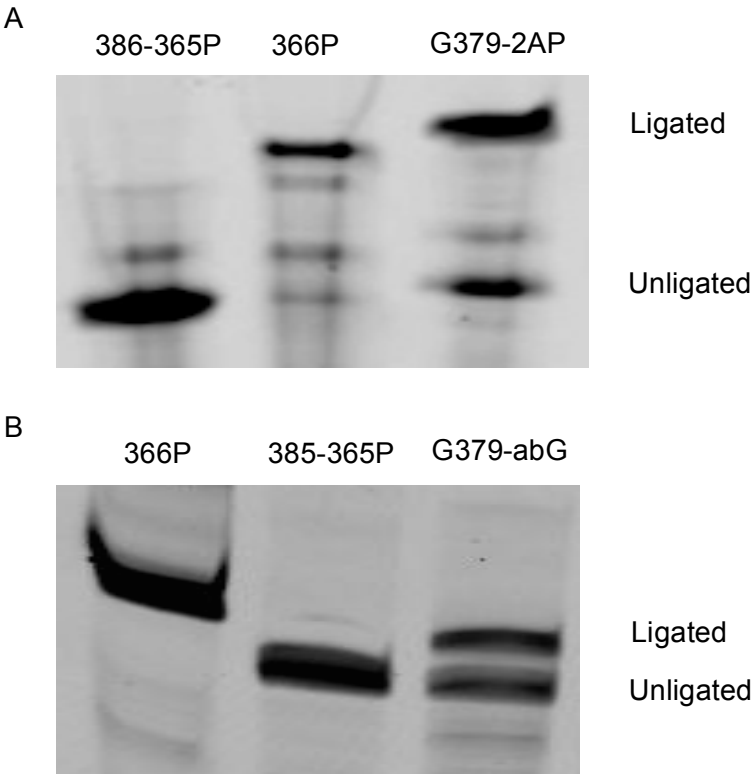

Figure A-1: Examples of ligation efficiency of 20-mer ribo-oligonucleotides containing (A) 2-amonipurine (2AP) and (B) abasic (abG) of G379 determined by primer extension analysis. The primer extension reaction by 6FAM labeled primer was visualized by a 6% denaturing PAGE. The ligation efficiency is calculated by the ratio of the intensity (I) of the bands corresponding to primer extension products of 366P and 386-365P RNA: $\%=I_{ligated}/(I_{ligated}+I_{unligated})$. For G379-abG, due to the lacking of the base, the primer extension was stopped and resulted in a shorter band.

A.2 Both RNase P Holoenzyme and PRNA with Modifications at G378/G379 Catalyze Cleavage of Fl-pre-tRNA^{Asp} at Correct Site

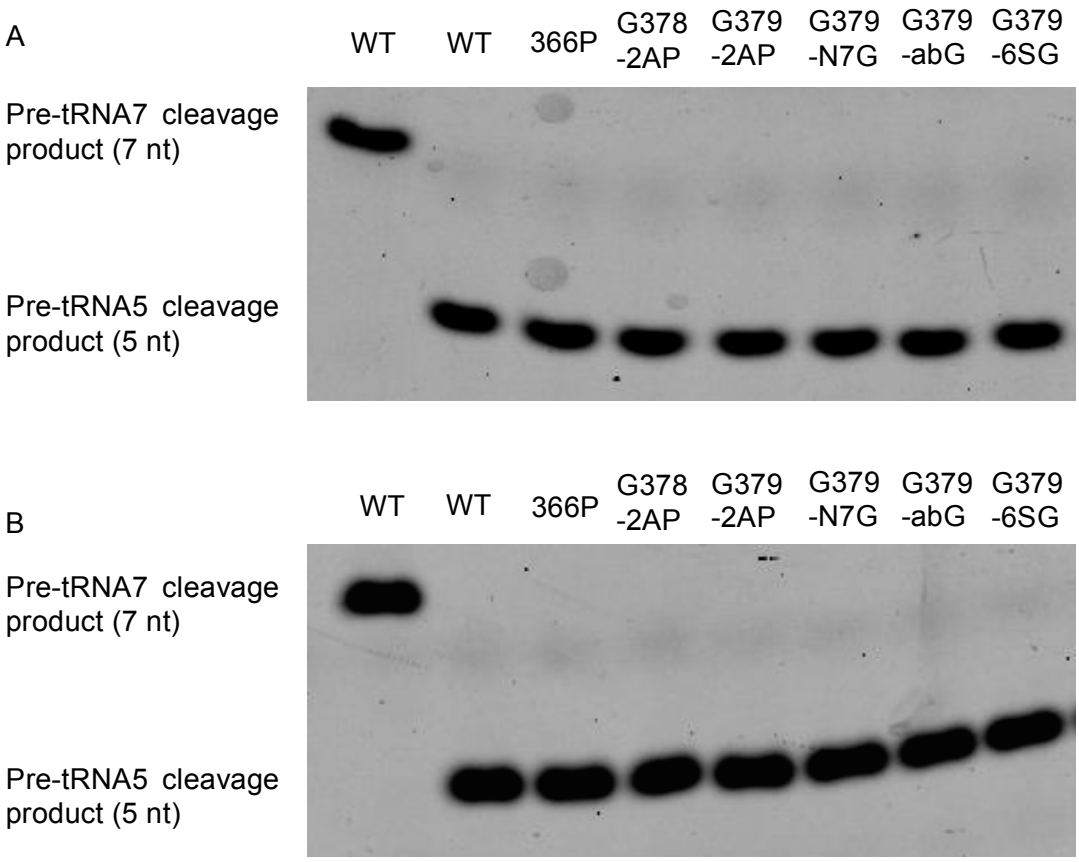

Figure A-2: Modified *B. subtilis* RNase P enzymes catalyze cleavage of Fl-pre-tRNA^{Asp} substrate at correct site. The reactions were performed with 10 nM Fl-pre-tRNA^{Asp} with either 7-nt 5' leader (pre-tRNA7) or 5-nt 5' leader (pre-tRNA5) and 360 nM **(A)** RNase P holoenzyme or **(B)** PRNA alone in 50 mM Tris/MES, pH 5.9, 20 mM $MgCl_2$ and 20 mM DTT with KCl concentrations (~200 mM). The reactions were incubated at 37°C for 10 min. The cleavage products are resolved by a 22% denaturing PAGE.

APPENDIX B

B.1 Parameter Sets for On- and Off-Resonance $R_{1\rho}$ Relaxation Dispersion Profiles of P4 WT and DelA4 Measured at Different Conditions

Table B-1: Parameter sets for P4 WT in 15 mM NaH_2PO_4, 25 mM NaCl and 0.1 mM EDTA

Residue (Spin)	T (°C)	On-resonance spinlock power (ω)/Off-resonance spinlock power (ω) & ± {offset (Ω)}
G2/A3 /A5/G23/U25 (C1') & A4 (C8)	15 & 37 (pH 6.8)	150, 200, 250, 300, 350, 400, 500, 600, 700, 800, 1000, 1500, 2000, 2500, 3000, 3500 Hz/ 150 Hz & ± {25, 50, 75, 100, 125, 150, 175, 200, 225, 250, 275, 300, 350, 400, 500, 600}
	25 (pH 5.4, 6.8 & 7.6)	300 Hz & ± {25, 50, 75, 100, 125, 150, 175, 200, 225, 250, 275, 300, 325, 350, 400, 600, 650, 700, 750, 800, 850, 900, 1200,1500} 600 Hz & ± {50, 100, 150, 200, 300, 500, 800, 1200, 1700, 2200} 1500 Hz & ± {50, 100, 250, 500, 750, 1000, 1500, 2000, 3000, 4500}
G2/A3 (C8)	25 (pH 6.8 & 7.6)	150, 200, 250, 300, 350, 400, 500, 600, 700, 800, 1000, 1500, 2000, 2500, 3000, 3500 Hz/ 100 Hz & ± {25, 50, 75, 100, 125, 150, 175, 200, 250, 300, 350, 400} 150 Hz & ± {25, 50, 75, 100, 125, 150, 175, 200, 225, 250, 275, 300, 350, 400, 500, 600} 300 Hz & ± {25, 50, 75, 100, 125, 150, 175, 200, 225, 250, 275, 300, 325, 350, 400, 600, 650, 700, 750, 800, 850, 900,1200,1500} 600 Hz & ± {50, 100, 150, 200, 300, 500, 800, 1200, 1700, 2200} 1500 Hz & ± {50, 100, 250, 500, 750, 1000, 1500, 2000, 3000, 4500}
	37 (pH 6.8)	150, 200, 250, 300, 350, 400, 500, 600, 700, 800, 1000, 1500, 2000, 2500, 3000, 3500 Hz/ 600 Hz & ± {50, 100, 150, 200, 300, 500, 800, 1200, 1700, 2200} 1500, 2000 Hz & ± {50, 100, 250, 500, 750, 1000, 1500, 2000, 3000, 4500} 3000, 3500 Hz & ± {50, 100, 250, 500, 750, 1000, 1500, 2000, 3000, 4500, 5000, 6000, 7000, 8000, 9000}
G2/G6 (NH)	15 (pH 6.8)	100, 150, 200, 250, 300, 350, 400, 450, 500, 550, 600, 700, 800, 900, 1000, 1200, 1400, 1600, 1800, 2000 Hz/ 150 Hz & ± {20, 40, 60, 80, 100,120, 140, 160, 180, 200, 220, 240, 260, 280, 300, 320, 400, 500, 600} 400 Hz & ± {30, 60, 90, 120, 150, 180, 210, 250, 300, 350, 400, 500, 600, 700, 800, 1000} 600 Hz & ± {40, 80, 120, 160, 200, 240, 300, 400, 500, 600, 800, 1000, 1200, 1400, 1600, 2000} 1000 Hz & ± {100, 200, 300, 400, 500, 600, 700, 900, 1100, 1300, 1500, 2000, 2500, 3000, 3500, 4000}
	25	100, 150, 200, 250, 300, 350, 400, 450, 500, 550, 600, 700, 800, 900, 1000, 1200, 1400, 1600, 1800, 2000 Hz/

	(pH 5.4, 6.8 & 7.6)	200 Hz & ± {20, 40, 60, 80, 100,120, 140, 160, 180, 200, 225, 250, 300, 350, 400, 500} 400 Hz & ± {30, 60, 90, 120, 150, 180, 210, 250, 300, 350, 400, 500, 600, 700, 800, 1000} 600 Hz & ± {40, 80, 120, 160, 200, 240, 300, 400, 500, 600, 800, 1000, 1200, 1400, 1600, 2000} 1000 Hz & ± {100, 200, 300, 400, 500, 600, 700, 900, 1100, 1300, 1500, 2000, 2500, 3000, 3500, 4000}
A3/A4/A5 (C2) & A5/G23 (C8)	15 (pH 6.8)	150, 200, 250, 300, 350, 400, 500, 600, 700, 800, 1000, 1500, 2000, 2500, 3000, 3500 Hz/ 100 Hz & ± {25, 50, 75, 100, 125, 150, 175, 200, 250, 300, 350, 400} 150 Hz & ± {25, 50, 75, 100, 125, 150, 175, 200, 225, 250, 275, 300, 350, 400, 500, 600}
	25 (pH 5.4, 6.8 & 7.6)	300 Hz & ± {25, 50, 75, 100, 125, 150, 175, 200, 225, 250, 275, 300, 325, 350, 400, 600, 650, 700, 750, 800, 850, 900,1200,1500} 600 Hz & ± {50, 100, 150, 200, 300, 500, 800, 1200, 1700, 2200} 1500 Hz & ± {50, 100, 250, 500, 750, 1000, 1500, 2000, 3000, 4500}
	37 (pH 6.8)	150, 200, 250, 300, 350, 400, 500, 600, 700, 800, 1000, 1500, 2000, 2500, 3000, 3500 Hz/ 300 Hz & ± {25, 50, 75, 100, 125, 150, 175, 200, 225, 250, 275, 300, 325, 350, 400, 600, 650, 700, 750, 800, 850, 900,1200,1500} 600 Hz & ± {50, 100, 150, 200, 300, 500, 800, 1200, 1700, 2200} 1500, 2000 Hz & ± {50, 100, 250, 500, 750, 1000, 1500, 2000, 3000, 4500} 3000, 3500 Hz & ± {50, 100, 250, 500, 750, 1000, 1500, 2000, 3000, 4500, 5000, 6000, 7000, 8000, 9000}
G6 (C1')	15 (pH 6.8)	150, 200, 250, 300, 350, 400, 500, 600, 700, 800, 1000, 1500, 2000, 2500, 3000, 3500 Hz/ 150 Hz & ± {25, 50, 75, 100, 125, 150, 175, 200, 225, 250, 275, 300, 350, 400, 500, 600}
	25 (pH 5.4, 6.8 & 7.6)	300 Hz & ± {25, 50, 75, 100, 125, 150, 175, 200, 225, 250, 275, 300, 325, 350, 400, 600, 650, 700, 750, 800, 850, 900,1200,1500} 600 Hz & ± {50, 100, 150, 200, 300, 500, 800, 1200, 1700, 2200} 1500 Hz & ± {50, 100, 250, 500, 750, 1000, 1500, 2000, 3000, 4500}
	37 (pH 6.8)	150, 200, 250, 300, 350, 400, 500, 600, 700, 800, 1000, 1500, 2000, 2500, 3000, 3500 Hz/ 150 Hz & ± {25, 50, 75, 100, 125, 150, 175, 200, 225, 250, 275, 300, 350, 400, 500, 600} 300 Hz & ± {25, 50, 75, 100, 125, 150, 175, 200, 225, 250, 275, 300, 325, 350, 400, 600, 650, 700, 750, 800, 850, 900,1200,1500} 600 Hz & ± {50, 100, 150, 200, 300, 500, 800, 1200, 1700, 2200} 1500, 2000 Hz & ± {50, 100, 250, 500, 750, 1000, 1500, 2000, 3000, 4500} 3000, 3500 Hz & ± {50, 100, 250, 500, 750, 1000, 1500, 2000, 3000, 4500, 5000, 6000, 7000, 8000, 9000}
G6 (C8)	15 (pH 6.8)	150, 200, 250, 300, 350, 400, 500, 600, 700, 800, 1000, 1500, 2000, 2500, 3000, 3500 Hz/ 100 Hz & ± {25, 50, 75, 100, 125, 150, 175, 200, 250, 300, 350, 400} 150 Hz & ± {25, 50, 75, 100, 125, 150, 175, 200, 225, 250, 275, 300, 350, 400, 500, 600}
	25 (pH 5.4, 6.8 & 7.6)	300 Hz & ± {25, 50, 75, 100, 125, 150, 175, 200, 225, 250, 275, 300, 325, 350, 400, 600, 650, 700, 750, 800, 850, 900,1200,1500} 600 Hz & ± {50, 100, 150, 200, 300, 500, 800, 1200, 1700, 2200} 1500, 2000, 3000 Hz & ± {50, 100, 250, 500, 750, 1000, 1500, 2000, 3000, 4500}
	37 (pH 6.8)	150, 200, 250, 300, 350, 400, 500, 600, 700, 800, 1000, 1500, 2000, 2500, 3000, 3500 Hz/ 100 Hz & ± {25, 50, 75, 100, 125, 150, 175, 200, 250, 300, 350, 400} 150 Hz & ± {25, 50, 75, 100, 125, 150, 175, 200, 225, 250, 275, 300, 350, 400, 500, 600} 300 Hz & ± {25, 50, 75, 100, 125, 150, 175, 200, 225, 250, 275, 300, 325, 350, 400, 600, 650, 700, 750, 800, 850, 900,1200,1500} 600 Hz & ± {50, 100, 150, 200, 300, 500, 800, 1200, 1700, 2200} 1500, 2000 Hz & ± {50, 100, 250, 500, 750, 1000, 1500, 2000, 3000, 4500} 3000, 3500 Hz & ± {50, 100, 250, 500, 750, 1000, 1500, 2000, 3000, 4500, 5000, 6000, 7000, 8000, 9000}
U7 (C1')	15 (pH 6.8)	150, 200, 250, 300, 350, 400, 500, 600, 700, 800, 1000, 1500, 2000, 2500, 3000, 3500 Hz/ 150 Hz & ± {25, 50, 75, 100, 125, 150, 175, 200, 225, 250, 275, 300, 350, 400, 500, 600}
	25 (pH 5.4, 6.8 & 7.6)	300 Hz & ± {25, 50, 75, 100, 125, 150, 175, 200, 225, 250, 275, 300, 325, 350, 400, 600, 650, 700, 750, 800, 850, 900,1200,1500} 600 Hz & ± {50, 100, 150, 200, 300, 500, 800, 1200, 1700, 2200} 1500 Hz & ± {50, 100, 250, 500, 750, 1000, 1500, 2000, 3000, 4500}

	37 (pH 6.8)	150, 200, 250, 300, 350, 400, 500, 600, 700, 800, 1000, 1500, 2000, 2500, 3000, 3500 Hz/ 300 Hz & ± {25, 50, 75, 100, 125, 150, 175, 200, 225, 250, 275, 300, 325, 350, 400, 600, 650, 700, 750, 800, 850, 900,1200,1500} 600 Hz & ± {50, 100, 150, 200, 300, 500, 800, 1200, 1700, 2200} 1500, 2000 Hz & ± {50, 100, 250, 500, 750, 1000, 1500, 2000, 3000, 4500} 3000, 3500 Hz & ± {50, 100, 250, 500, 750, 1000, 1500, 2000, 3000, 4500, 5000, 6000, 7000, 8000, 9000}
U7/C8 (C6)	15 & 37 (pH 6.8)	150, 200, 250, 300, 350, 400, 500, 600, 700, 800, 1000, 1500, 2000, 2500, 3000, 3500 Hz/ 200 Hz & ± {25, 50, 75, 100, 125, 150, 175, 200, 225, 250, 275, 300, 350, 400, 500, 600}
	25 (pH 5.4, 6.8 & 7.6)	300 Hz & ± {25, 50, 75, 100, 125, 150, 175, 200, 225, 250, 275, 300, 325, 350, 400, 600, 650, 700, 750, 800, 850, 900,1200,1500} 600 Hz & ± {50, 100, 150, 200, 300, 500, 800, 1200, 1700, 2200}
C8/C9 (C1')	25 (pH 6.8)	150, 200, 250, 300, 350, 400, 500, 600, 700, 800, 1000, 1500, 2000, 2500, 3000, 3500 Hz/ 150 Hz & ± {25, 50, 75, 100, 125, 150, 175, 200, 225, 250, 275, 300, 350, 400, 500, 600} 300 Hz & ± {25, 50, 75, 100, 125, 150, 175, 200, 225, 250, 275, 300, 325, 350, 400, 600, 650, 700, 750, 800, 850, 900,1200,1500} 600 Hz & ± {50, 100, 150, 200, 300, 500, 800, 1200, 1700, 2200}
C9/U25/ U27/C28 (C6)	15 & 37 (pH 6.8)	150, 200, 250, 300, 350, 400, 500, 600, 700, 800, 1000, 1500, 2000, 2500, 3000, 3500 Hz/ 200 Hz & ± {25, 50, 75, 100, 125, 150, 175, 200, 225, 250, 275, 300, 350, 400, 500, 600}
	25 (pH 5.4, 6.8 & 7.6)	300 Hz & ± {25, 50, 75, 100, 125, 150, 175, 200, 225, 250, 275, 300, 325, 350, 400, 600, 650, 700, 750, 800, 850, 900,1200,1500} 600 Hz & ± {50, 100, 150, 200, 300, 500, 800, 1200, 1700, 2200} 1500 Hz & ± {50, 100, 250, 500, 750, 1000, 1500, 2000, 3000, 4500}
A10/A20 (C2) & C24/C28 (C1')	25 (pH 5.4 & 6.8)	150, 200, 250, 300, 350, 400, 500, 600, 700, 800, 1000, 1500, 2000, 2500, 3000, 3500 Hz/ 150 Hz & ± {25, 50, 75, 100, 125, 150, 175, 200, 225, 250, 275, 300, 350, 400, 500, 600} 600 Hz & ± {50, 100, 150, 200, 300, 500, 800, 1200, 1700, 2200}
U11/U21/G 22/G23 (NH)	15 & 37 (pH 6.8)	100, 150, 200, 250, 300, 350, 400, 450, 500, 550, 600, 700, 800, 900, 1000, 1200, 1400, 1600, 1800, 2000 Hz/ 150 Hz & ± {20, 40, 60, 80, 100,120, 140, 160, 180, 200, 220, 240, 260, 280, 300, 320, 400, 500, 600} 1000 Hz & ± {100, 200, 300, 400, 500, 600, 700, 900, 1100, 1300, 1500, 2000, 2500, 3000, 3500, 4000}
	25 (pH 6.8)	100, 150, 200, 250, 300, 350, 400, 450, 500, 550, 600, 700, 800, 900, 1000, 1200, 1400, 1600, 1800, 2000 Hz/ 150 Hz & ± {20, 40, 60, 80, 100,120, 140, 160, 180, 200, 220, 240, 260, 280, 300, 320, 400, 500, 600} 200 Hz & ± {20, 40, 60, 80, 100,120, 140, 160, 180, 200, 225, 250, 300, 350, 400, 500} 1000 Hz & ± {100, 200, 300, 400, 500, 600, 700, 900, 1100, 1300, 1500, 2000, 2500, 3000, 3500, 4000}
G22 (C8)	25 (pH 6.8)	150, 200, 250, 300, 350, 400, 500, 600, 700, 800, 1000, 1500, 2000, 2500, 3000, 3500 Hz/ 150 Hz & ± {25, 50, 75, 100, 125, 150, 175, 200, 225, 250, 275, 300, 350, 400, 500, 600} 1500 Hz & ± {50, 100, 250, 500, 750, 1000, 1500, 2000, 3000, 4500}
U27 (C1')	15 (pH 6.8)	150, 200, 250, 300, 350, 400, 500, 600, 700, 800, 1000, 1500, 2000, 2500, 3000, 3500 Hz/ 150 Hz & ± {25, 50, 75, 100, 125, 150, 175, 200, 225, 250, 275, 300, 350, 400, 500, 600}
	25 (pH 6.8 & 7.6)	300 Hz & ± {25, 50, 75, 100, 125, 150, 175, 200, 225, 250, 275, 300, 325, 350, 400, 600, 650, 700, 750, 800, 850, 900,1200,1500} 600 Hz & ± {50, 100, 150, 200, 300, 500, 800, 1200, 1700, 2200} 1500 Hz & ± {50, 100, 250, 500, 750, 1000, 1500, 2000, 3000, 4500}
	37 (pH 6.8)	150, 200, 250, 300, 350, 400, 500, 600, 700, 800, 1000, 1500, 2000, 2500, 3000, 3500 Hz/ 600 Hz & ± {50, 100, 150, 200, 300, 500, 800, 1200, 1700, 2200} 1500, 2000 Hz & ± {50, 100, 250, 500, 750, 1000, 1500, 2000, 3000, 4500} 3000, 3500 Hz & ± {50, 100, 250, 500, 750, 1000, 1500, 2000, 3000, 4500, 5000, 6000, 7000, 8000, 9000}

Table B-2: Parameter sets for DelA4 in 15 mM NaH_2PO_4, 25 mM NaCl and 0.1 mM EDTA at pH 6.8

Residue (Spin)	T (°C)	On-resonance spinlock power (ω)/Off-resonance spinlock power (ω) & ± {offset (Ω)}
G2/A3/A5 A10/A20 (C8)	15 & 37	150, 200, 250, 300, 350, 400, 500, 600, 700, 800, 1000, 1500, 2000, 2500, 3000, 3500 Hz/ 150 Hz & ± {25, 50, 75, 100, 125, 150, 175, 200, 225, 250, 275, 300, 350, 400, 500, 600} 600 Hz & ± {50, 100, 150, 200, 300, 500, 800, 1200, 1700, 2200}
	25	150, 200, 250, 300, 350, 400, 500, 600, 700, 800, 1000, 1500, 2000, 2500, 3000, 3500 Hz/ 150 Hz & ± {25, 50, 75, 100, 125, 150, 175, 200, 225, 250, 275, 300, 350, 400, 500, 600} 300 Hz & ± {25, 50, 75, 100, 125, 150, 175, 200, 225, 250, 275, 300, 325, 350, 400, 600, 650, 700, 750, 800, 850, 900,1200,1500} 600 Hz & ± {50, 100, 150, 200, 300, 500, 800, 1200, 1700, 2200} 1500 Hz & ± {50, 100, 250, 500, 750, 1000, 1500, 2000, 3000, 4500}
A3/A5/ A10/A20 (C2)	25	150, 200, 250, 300, 350, 400, 500, 600, 700, 800, 1000, 1500, 2000, 2500, 3000, 3500 Hz/ 100 Hz & ± {25, 50, 75, 100, 125, 150, 175, 200, 250, 300, 350, 400} 150 Hz & ± {25, 50, 75, 100, 125, 150, 175, 200, 225, 250, 275, 300, 350, 400, 500, 600} 300 Hz & ± {25, 50, 75, 100, 125, 150, 175, 200, 225, 250, 275, 300, 325, 350, 400, 600, 650, 700, 750, 800, 850, 900,1200,1500}
G2/G6/ U11/U21/G 22/G23/U25 /U27 (NH)	15, 25 & 37	100, 150, 200, 250, 300, 350, 400, 450, 500, 550, 600, 700, 800, 900, 1000, 1200, 1400, 1600, 1800, 2000 Hz/ 150 Hz & ± {20, 40, 60, 80, 100,120, 140, 160, 180, 200, 220, 240, 260, 280, 300, 320, 400, 500, 600} 1000 Hz & ± {100, 200, 300, 400, 500, 600, 700, 900, 1100, 1300, 1500, 2000, 2500, 3000, 3500, 4000}
A5/U25/ U27 (C1')	15 & 37	150, 200, 250, 300, 350, 400, 500, 600, 700, 800, 1000, 1500, 2000, 2500, 3000, 3500 Hz/ 150 Hz & ± {25, 50, 75, 100, 125, 150, 175, 200, 225, 250, 275, 300, 350, 400, 500, 600} 600 Hz & ± {50, 100, 150, 200, 300, 500, 800, 1200, 1700, 2200}
	25	150, 200, 250, 300, 350, 400, 500, 600, 700, 800, 1000, 1500, 2000, 2500, 3000, 3500 Hz/ 150 Hz & ± {25, 50, 75, 100, 125, 150, 175, 200, 225, 250, 275, 300, 350, 400, 500, 600} 1500 Hz & ± {50, 100, 250, 500, 750, 1000, 1500, 2000, 3000, 4500}
G6 (C1')	15	150, 200, 250, 300, 350, 400, 500, 600, 700, 800, 1000, 1500, 2000, 2500, 3000, 3500 Hz/ 150 Hz & ± {25, 50, 75, 100, 125, 150, 175, 200, 225, 250, 275, 300, 350, 400, 500, 600} 300 Hz & ± {25, 50, 75, 100, 125, 150, 175, 200, 225, 250, 275, 300, 325, 350, 400, 600, 650, 700, 750, 800, 850, 900,1200,1500} 600 Hz & ± {50, 100, 150, 200, 300, 500, 800, 1200, 1700, 2200} 1500 Hz & ± {50, 100, 250, 500, 750, 1000, 1500, 2000, 3000, 4500}
	25	150, 200, 250, 300, 350, 400, 500, 600, 700, 800, 1000, 1500, 2000, 2500, 3000, 3500 Hz/ 150 Hz & ± {25, 50, 75, 100, 125, 150, 175, 200, 225, 250, 275, 300, 350, 400, 500, 600} 200 Hz & ± {25, 50, 75, 100, 125, 150, 175, 200, 225, 250, 275, 300, 350, 400, 500, 600} 300 Hz & ± {25, 50, 75, 100, 125, 150, 175, 200, 225, 250, 275, 300, 325, 350, 400, 600, 650, 700, 750, 800, 850, 900,1200,1500} 600 Hz & ± {50, 100, 150, 200, 300, 500, 800, 1200, 1700, 2200}
	37	150, 200, 250, 300, 350, 400, 500, 600, 700, 800, 1000, 1500, 2000, 2500, 3000, 3500 Hz/ 150 Hz & ± {25, 50, 75, 100, 125, 150, 175, 200, 225, 250, 275, 300, 350, 400, 500, 600} 200 Hz & ± {25, 50, 75, 100, 125, 150, 175, 200, 225, 250, 275, 300, 350, 400, 500, 600} 300 Hz & ± {25, 50, 75, 100, 125, 150, 175, 200, 225, 250, 275, 300, 325, 350, 400, 600, 650, 700, 750, 800, 850, 900,1200,1500}

		600 Hz & ± {50, 100, 150, 200, 300, 500, 800, 1200, 1700, 2200} 1500 Hz & ± {50, 100, 250, 500, 750, 1000, 1500, 2000, 3000, 4500}
G6 (C8)	15 & 25	150, 200, 250, 300, 350, 400, 500, 600, 700, 800, 1000, 1500, 2000, 2500, 3000, 3500 Hz/ 150 Hz & ± {25, 50, 75, 100, 125, 150, 175, 200, 225, 250, 275, 300, 350, 400, 500, 600} 600 Hz & ± {50, 100, 150, 200, 300, 500, 800, 1200, 1700, 2200}
	37	150, 200, 250, 300, 350, 400, 500, 600, 700, 800, 1000, 1500, 2000, 2500, 3000, 3500 Hz/ 100 Hz & ± {25, 50, 75, 100, 125, 150, 175, 200, 250, 300, 350, 400} 150 Hz & ± {25, 50, 75, 100, 125, 150, 175, 200, 225, 250, 275, 300, 350, 400, 500, 600} 300 Hz & ± {25, 50, 75, 100, 125, 150, 175, 200, 225, 250, 275, 300, 325, 350, 400, 600, 650, 700, 750, 800, 850, 900,1200,1500} 600 Hz & ± {50, 100, 150, 200, 300, 500, 800, 1200, 1700, 2200} 1500 Hz & ± {50, 100, 250, 500, 750, 1000, 1500, 2000, 3000, 4500}
U7/G23 (C1')	15, 25 & 37	150, 200, 250, 300, 350, 400, 500, 600, 700, 800, 1000, 1500, 2000, 2500, 3000, 3500 Hz/ 150 Hz & ± {25, 50, 75, 100, 125, 150, 175, 200, 225, 250, 275, 300, 350, 400, 500, 600} 300 Hz & ± {25, 50, 75, 100, 125, 150, 175, 200, 225, 250, 275, 300, 325, 350, 400, 600, 650, 700, 750, 800, 850, 900,1200,1500} 600 Hz & ± {50, 100, 150, 200, 300, 500, 800, 1200, 1700, 2200} 1500 Hz & ± {50, 100, 250, 500, 750, 1000, 1500, 2000, 3000, 4500
U7/C8/ U25/U27 (C6)	15 & 37	150, 200, 250, 300, 350, 400, 500, 600, 700, 800, 1000, 1500, 2000, 2500, 3000, 3500 Hz/ 200 Hz & ± {25, 50, 75, 100, 125, 150, 175, 200, 225, 250, 275, 300, 350, 400, 500, 600} 600 Hz & ± {50, 100, 150, 200, 300, 500, 800, 1200, 1700, 2200}
	25	150, 200, 250, 300, 350, 400, 500, 600, 700, 800, 1000, 1500, 2000, 2500, 3000, 3500 Hz/ 200 Hz & ± {25, 50, 75, 100, 125, 150, 175, 200, 225, 250, 275, 300, 350, 400, 500, 600} 300 Hz & ± {25, 50, 75, 100, 125, 150, 175, 200, 225, 250, 275, 300, 325, 350, 400, 600, 650, 700, 750, 800, 850, 900,1200,1500} 600 Hz & ± {50, 100, 150, 200, 300, 500, 800, 1200, 1700, 2200}
C8 (C1')	15 & 37	150, 200, 250, 300, 350, 400, 500, 600, 700, 800, 1000, 1500, 2000, 2500, 3000, 3500 Hz/ 150 Hz & ± {25, 50, 75, 100, 125, 150, 175, 200, 225, 250, 275, 300, 350, 400, 500, 600} 600 Hz & ± {50, 100, 150, 200, 300, 500, 800, 1200, 1700, 2200}
	25	150, 200, 250, 300, 350, 400, 500, 600, 700, 800, 1000, 1500, 2000, 2500, 3000, 3500 Hz/ 150 Hz & ± {25, 50, 75, 100, 125, 150, 175, 200, 225, 250, 275, 300, 350, 400, 500, 600} 300 Hz & ± {25, 50, 75, 100, 125, 150, 175, 200, 225, 250, 275, 300, 325, 350, 400, 600, 650, 700, 750, 800, 850, 900,1200,1500} 600 Hz & ± {50, 100, 150, 200, 300, 500, 800, 1200, 1700, 2200}
G22/G23 (C8)	25	150, 200, 250, 300, 350, 400, 500, 600, 700, 800, 1000, 1500, 2000, 2500, 3000, 3500 Hz/ 150 Hz & ± {25, 50, 75, 100, 125, 150, 175, 200, 225, 250, 275, 300, 350, 400, 500, 600} 600 Hz & ± {50, 100, 150, 200, 300, 500, 800, 1200, 1700, 2200}

Table B-3: Parameter sets for WT in 15 mM NaH_2PO_4, 25 mM NaCl, 5 mM or 44 mM $MgCl_2$ and 0.1 mM EDTA under pH 6.8 at 25 °C

Residue (Spin)	$[Mg^{2+}]$ (mM)	On-resonance spinlock power (ω)/Off-resonance spinlock power (ω) & ± {offset (Ω)}
A3/G6/ C8 (C1')	5	150, 200, 250, 300, 350, 400, 500, 600, 700, 800, 1000, 1500, 2000, 2500, 3000, 3500 Hz/ 150 Hz & ± {25, 50, 75, 100, 125, 150, 175, 200, 225, 250, 275, 300, 350, 400, 500, 600} 300 Hz & ± {25, 50, 75, 100, 125, 150, 175, 200, 225, 250, 275, 300, 325, 350, 400, 600, 650, 700, 750, 800, 850, 900,1200,1500} 600 Hz & ± {50, 100, 150, 200, 300, 500, 800, 1200, 1700, 2200} 1500 Hz & ± {50, 100, 250, 500, 750, 1000, 1500, 2000, 3000, 4500}
	44	150, 200, 250, 300, 350, 400, 500, 600, 700, 800, 1000, 1500, 2000, 2500, 3000, 3500 Hz/ 150 Hz & ± {25, 50, 75, 100, 125, 150, 175, 200, 225, 250, 275, 300, 350, 400, 500, 600} 300 Hz & ± {25, 50, 75, 100, 125, 150, 175, 200, 225, 250, 275, 300, 325, 350, 400, 600, 650, 700, 750, 800, 850, 900,1200,1500} 600 Hz & ± {50, 100, 150, 200, 300, 500, 800, 1200, 1700, 2200} 1500, 2000 Hz & ± {50, 100, 250, 500, 750, 1000, 1500, 2000, 3000, 4500} 3000, 3500 Hz & ± {50, 100, 250, 500, 750, 1000, 1500, 2000, 3000, 4500, 5000, 6000, 7000, 8000, 9000}
A3/A4/ A5/A10/A20 /G22/G23 (C2/C8)	5	150, 200, 250, 300, 350, 400, 500, 600, 700, 800, 1000, 1500, 2000, 2500, 3000, 3500 Hz/ 100 Hz & ± {25, 50, 75, 100, 125, 150, 175, 200, 250, 300, 350, 400} 150 Hz & ± {25, 50, 75, 100, 125, 150, 175, 200, 225, 250, 275, 300, 350, 400, 500, 600} 300 Hz & ± {25, 50, 75, 100, 125, 150, 175, 200, 225, 250, 275, 300, 325, 350, 400, 600, 650, 700, 750, 800, 850, 900,1200,1500} 600 Hz & ± {50, 100, 150, 200, 300, 500, 800, 1200, 1700, 2200} 1500 Hz & ± {50, 100, 250, 500, 750, 1000, 1500, 2000, 3000, 4500}
	44	150, 200, 250, 300, 350, 400, 500, 600, 700, 800, 1000, 1500, 2000, 2500, 3000, 3500 Hz/ 150 Hz & ± {25, 50, 75, 100, 125, 150, 175, 200, 225, 250, 275, 300, 350, 400, 500, 600} 600 Hz & ± {50, 100, 150, 200, 300, 500, 800, 1200, 1700, 2200}
G6 (C8)	5	150, 200, 250, 300, 350, 400, 500, 600, 700, 800, 1000, 1500, 2000, 2500, 3000, 3500 Hz/ 100 Hz & ± {25, 50, 75, 100, 125, 150, 175, 200, 250, 300, 350, 400} 150 Hz & ± {25, 50, 75, 100, 125, 150, 175, 200, 225, 250, 275, 300, 350, 400, 500, 600} 300 Hz & ± {25, 50, 75, 100, 125, 150, 175, 200, 225, 250, 275, 300, 325, 350, 400, 600, 650, 700, 750, 800, 850, 900,1200,1500} 600 Hz & ± {50, 100, 150, 200, 300, 500, 800, 1200, 1700, 2200} 1500, 2000, 3000 Hz & ± {50, 100, 250, 500, 750, 1000, 1500, 2000, 3000, 4500}
	44	150, 200, 250, 300, 350, 400, 500, 600, 700, 800, 1000, 1500, 2000, 2500, 3000, 3500 Hz/ 300 Hz & ± {25, 50, 75, 100, 125, 150, 175, 200, 225, 250, 275, 300, 325, 350, 400, 600, 650, 700, 750, 800, 850, 900,1200,1500} 1500 Hz & ± {50, 100, 250, 500, 750, 1000, 1500, 2000, 3000, 4500}
U7/U27 (C1')	5	150, 200, 250, 300, 350, 400, 500, 600, 700, 800, 1000, 1500, 2000, 2500, 3000, 3500 Hz/ 150 Hz & ± {25, 50, 75, 100, 125, 150, 175, 200, 225, 250, 275, 300, 350, 400, 500, 600} 300 Hz & ± {25, 50, 75, 100, 125, 150, 175, 200, 225, 250, 275, 300, 325, 350, 400, 600, 650, 700, 750, 800, 850, 900,1200,1500} 600 Hz & ± {50, 100, 150, 200, 300, 500, 800, 1200, 1700, 2200} 1500 Hz & ± {50, 100, 250, 500, 750, 1000, 1500, 2000, 3000, 4500}
	44	150, 200, 250, 300, 350, 400, 500, 600, 700, 800, 1000, 1500, 2000, 2500, 3000, 3500 Hz/

		300 Hz & ± {25, 50, 75, 100, 125, 150, 175, 200, 225, 250, 275, 300, 325, 350, 400, 600, 650, 700, 750, 800, 850, 900,1200,1500} 600 Hz & ± {50, 100, 150, 200, 300, 500, 800, 1200, 1700, 2200} 1500, 2000 Hz & ± {50, 100, 250, 500, 750, 1000, 1500, 2000, 3000, 4500} 3000, 3500 Hz & ± {50, 100, 250, 500, 750, 1000, 1500, 2000, 3000, 4500, 5000, 6000, 7000, 8000, 9000}
U7 (C6)	5	150, 200, 250, 300, 350, 400, 500, 600, 700, 800, 1000, 1500, 2000, 2500, 3000, 3500 Hz/ 200 Hz & ± {25, 50, 75, 100, 125, 150, 175, 200, 225, 250, 275, 300, 350, 400, 500, 600} 300 Hz & ± {25, 50, 75, 100, 125, 150, 175, 200, 225, 250, 275, 300, 325, 350, 400, 600, 650, 700, 750, 800, 850, 900,1200,1500} 600 Hz & ± {50, 100, 150, 200, 300, 500, 800, 1200, 1700, 2200} 1500 Hz & ± {50, 100, 250, 500, 750, 1000, 1500, 2000, 3000, 4500}
	44	150, 200, 250, 300, 350, 400, 500, 600, 700, 800, 1000, 1500, 2000, 2500, 3000, 3500 Hz/ 200 Hz & ± {25, 50, 75, 100, 125, 150, 175, 200, 225, 250, 275, 300, 350, 400, 500, 600} 300 Hz & ± {25, 50, 75, 100, 125, 150, 175, 200, 225, 250, 275, 300, 325, 350, 400, 600, 650, 700, 750, 800, 850, 900,1200,1500} 600 Hz & ± {50, 100, 150, 200, 300, 500, 800, 1200, 1700, 2200} 1500, 2000 Hz & ± {50, 100, 250, 500, 750, 1000, 1500, 2000, 3000, 4500} 3000 Hz & ± {50, 100, 250, 500, 750, 1000, 1500, 2000, 3000, 4500, 5000, 6000, 7000, 8000, 9000}
C8 (C6)	5	150, 200, 250, 300, 350, 400, 500, 600, 700, 800, 1000, 1500, 2000, 2500, 3000, 3500 Hz/ 200 Hz & ± {25, 50, 75, 100, 125, 150, 175, 200, 225, 250, 275, 300, 350, 400, 500, 600} 300 Hz & ± {25, 50, 75, 100, 125, 150, 175, 200, 225, 250, 275, 300, 325, 350, 400, 600, 650, 700, 750, 800, 850, 900,1200,1500} 600 Hz & ± {50, 100, 150, 200, 300, 500, 800, 1200, 1700, 2200} 1500 Hz & ± {50, 100, 250, 500, 750, 1000, 1500, 2000, 3000, 4500}
	44	150, 200, 250, 300, 350, 400, 500, 600, 700, 800, 1000, 1500, 2000, 2500, 3000, 3500 Hz/ 200 Hz & ± {25, 50, 75, 100, 125, 150, 175, 200, 225, 250, 275, 300, 350, 400, 500, 600} 300 Hz & ± {25, 50, 75, 100, 125, 150, 175, 200, 225, 250, 275, 300, 325, 350, 400, 600, 650, 700, 750, 800, 850, 900,1200,1500} 600 Hz & ± {50, 100, 150, 200, 300, 500, 800, 1200, 1700, 2200} 1500, 2000 Hz & ± {50, 100, 250, 500, 750, 1000, 1500, 2000, 3000, 4500} 3000, 3500 Hz & ± {50, 100, 250, 500, 750, 1000, 1500, 2000, 3000, 4500, 5000, 6000, 7000, 8000, 9000}
G6/U11/U2 1/G22/G23 (NH)	5	100, 150, 200, 250, 300, 350, 400, 450, 500, 550, 600, 700, 800, 900, 1000, 1200, 1400, 1600, 1800, 2000 Hz/ 200 Hz & ± {20, 40, 60, 80, 100,120, 140, 160, 180, 200, 225, 250, 300, 350, 400, 500} 400 Hz & ± {30, 60, 90, 120, 150, 180, 210, 250, 300, 350, 400, 500, 600, 700, 800, 1000} 600 Hz & ± {40, 80, 120, 160, 200, 240, 300, 400, 500, 600, 800, 1000, 1200, 1400, 1600, 2000} 1000 Hz & ± {100, 200, 300, 400, 500, 600, 700, 900, 1100, 1300, 1500, 2000, 2500, 3000, 3500, 4000}
	44	100, 150, 200, 250, 300, 350, 400, 450, 500, 550, 600, 700, 800, 900, 1000, 1200, 1400, 1600, 1800, 2000 150 Hz & ± {20, 40, 60, 80, 100,120, 140, 160, 180, 200, 220, 240, 260, 280, 300, 320, 400, 500, 600} 1000 Hz & ± {100, 200, 300, 400, 500, 600, 700, 900, 1100, 1300, 1500, 2000, 2500, 3000, 3500, 4000}

Table B-4: Parameter sets for DelA4 in 15 mM NaH_2PO_4, 25 mM NaCl, 44 mM of $MgCl_2$ and 0.1 mM EDTA under pH 6.8 at 25 °C

Residue (Spin)	On-resonance spinlock power (ω)/Off-resonance spinlock power (ω) & ± {offset (Ω)}
A3/A5 (C1'/C8)	150, 200, 250, 300, 350, 400, 500, 600, 700, 800, 1000, 1500, 2000, 2500, 3000, 3500 Hz/ 150 Hz & ± {25, 50, 75, 100, 125, 150, 175, 200, 225, 250, 275, 300, 350, 400, 500, 600} 600 Hz & ± {50, 100, 150, 200, 300, 500, 800, 1200, 1700, 2200}
G6/U7/C8 (C1')	150, 200, 250, 300, 350, 400, 500, 600, 700, 800, 1000, 1500, 2000, 2500, 3000, 3500 Hz/ 150 Hz & ± {25, 50, 75, 100, 125, 150, 175, 200, 225, 250, 275, 300, 350, 400, 500, 600} 300 Hz & ± {25, 50, 75, 100, 125, 150, 175, 200, 225, 250, 275, 300, 325, 350, 400, 600, 650, 700, 750, 800, 850, 900,1200,1500} 600 Hz & ± {50, 100, 150, 200, 300, 500, 800, 1200, 1700, 2200} 1500, 2000 Hz & ± {50, 100, 250, 500, 750, 1000, 1500, 2000, 3000, 4500} 3000, 3500 Hz & ± {50, 100, 250, 500, 750, 1000, 1500, 2000, 3000, 4500, 5000, 6000, 7000, 8000, 9000}
G6/G23 (C8)	150, 200, 250, 300, 350, 400, 500, 600, 700, 800, 1000, 1500, 2000, 2500, 3000, 3500 Hz/ 100 Hz & ± {25, 50, 75, 100, 125, 150, 175, 200, 250, 300, 350, 400} 150 Hz & ± {25, 50, 75, 100, 125, 150, 175, 200, 225, 250, 275, 300, 350, 400, 500, 600} 300 Hz & ± {25, 50, 75, 100, 125, 150, 175, 200, 225, 250, 275, 300, 325, 350, 400, 600, 650, 700, 750, 800, 850, 900,1200,1500} 600 Hz & ± {50, 100, 150, 200, 300, 500, 800, 1200, 1700, 2200} 1500 Hz & ± {50, 100, 250, 500, 750, 1000, 1500, 2000, 3000, 4500}
G6/G23/U25/U27 (NH)	100, 150, 200, 250, 300, 350, 400, 450, 500, 550, 600, 700, 800, 900, 1000, 1200, 1400, 1600, 1800, 2000 150 Hz & ± {20, 40, 60, 80, 100,120, 140, 160, 180, 200, 220, 240, 260, 280, 300, 320, 400, 500, 600} 1000 Hz & ± {100, 200, 300, 400, 500, 600, 700, 900, 1100, 1300, 1500, 2000, 2500, 3000, 3500, 4000}
U7/U25/U27 (C6)	150, 200, 250, 300, 350, 400, 500, 600, 700, 800, 1000, 1500, 2000, 2500, 3000, 3500 Hz/ 200 Hz & ± {25, 50, 75, 100, 125, 150, 175, 200, 225, 250, 275, 300, 350, 400, 500, 600} 300 Hz & ± {25, 50, 75, 100, 125, 150, 175, 200, 225, 250, 275, 300, 325, 350, 400, 600, 650, 700, 750, 800, 850, 900,1200,1500} 600 Hz & ± {50, 100, 150, 200, 300, 500, 800, 1200, 1700, 2200} 1500, 2000 Hz & ± {50, 100, 250, 500, 750, 1000, 1500, 2000, 3000, 4500} 3000, 3500 Hz & ± {50, 100, 250, 500, 750, 1000, 1500, 2000, 3000, 4500, 5000, 6000, 7000, 8000, 9000}
C8 (C6)	150, 200, 250, 300, 350, 400, 500, 600, 700, 800, 1000, 1500, 2000, 2500, 3000, 3500 Hz/ 200 Hz & ± {25, 50, 75, 100, 125, 150, 175, 200, 225, 250, 275, 300, 350, 400, 500, 600} 300 Hz & ± {25, 50, 75, 100, 125, 150, 175, 200, 225, 250, 275, 300, 325, 350, 400, 600, 650, 700, 750, 800, 850, 900,1200,1500} 600 Hz & ± {50, 100, 150, 200, 300, 500, 800, 1200, 1700, 2200} 1500 Hz & ± {50, 100, 250, 500, 750, 1000, 1500, 2000, 3000, 4500}

B.2 U7 Is the Only Bulged Residue in the P4 Helix Mimic

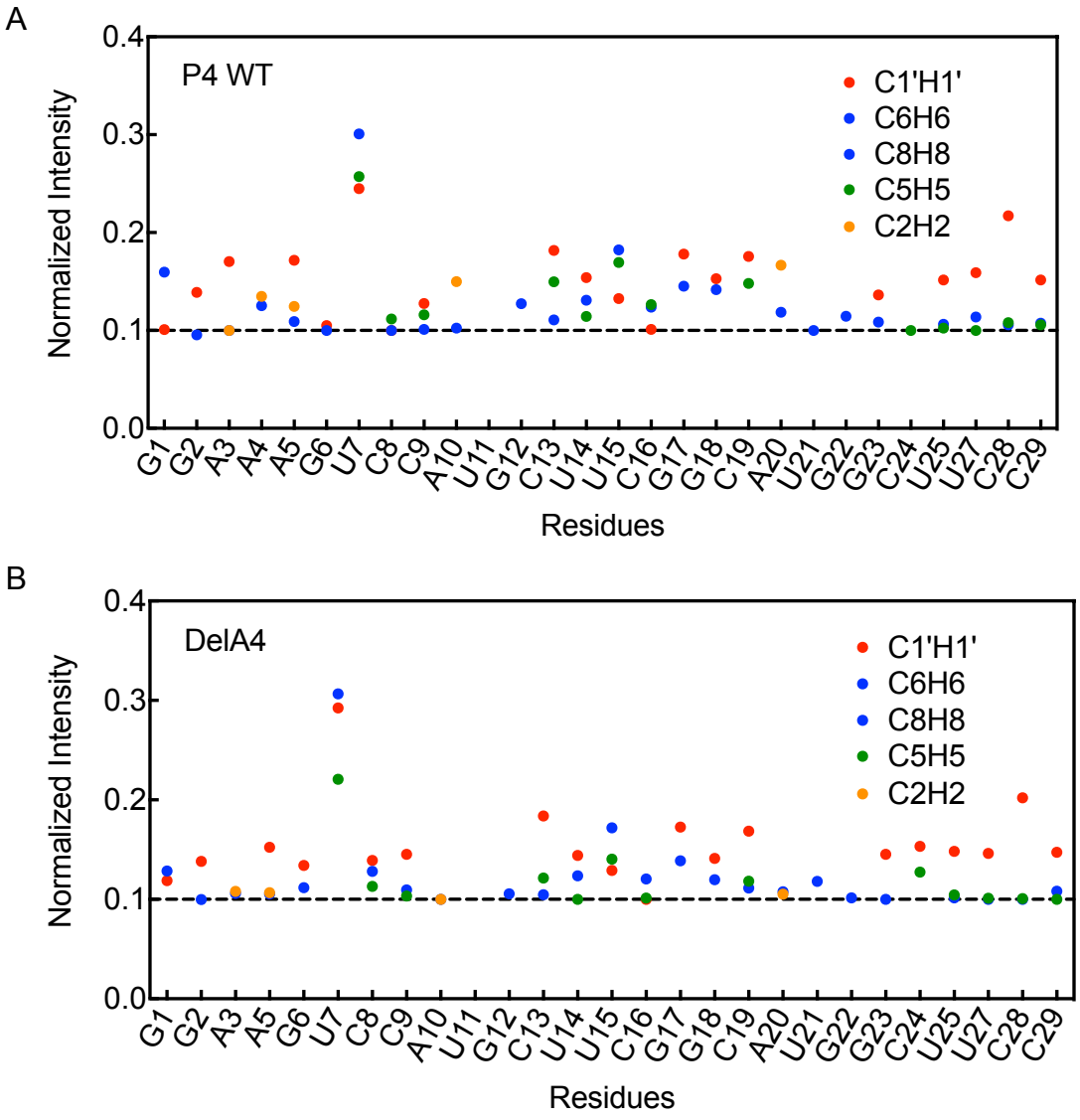

Figure B-1: Normalized resonance intensities as a function of residue in P4 WT **(A)** and DelA4 mutant **(B)** from *B. subtilis* PRNA. The data were collected at the condition of 15 mM NaH_2PO_4, 25 mM NaCl and 0.1 mM EDTA under pH 6.8 at 25°C with 2.3 mM of the P4 WT and 2.5 mM of DelA4. Intensities for a given type of C-H vector are normalized relative to a minimum value of 0.1 indicated by a horizontal line [1].

B.3 On- and Off-Resonance of $R_{1\rho}$ Relaxation Dispersion Profiles

B.3.1 $R_{1\rho}$ relaxation dispersion profiles of P4 WT under different conditions

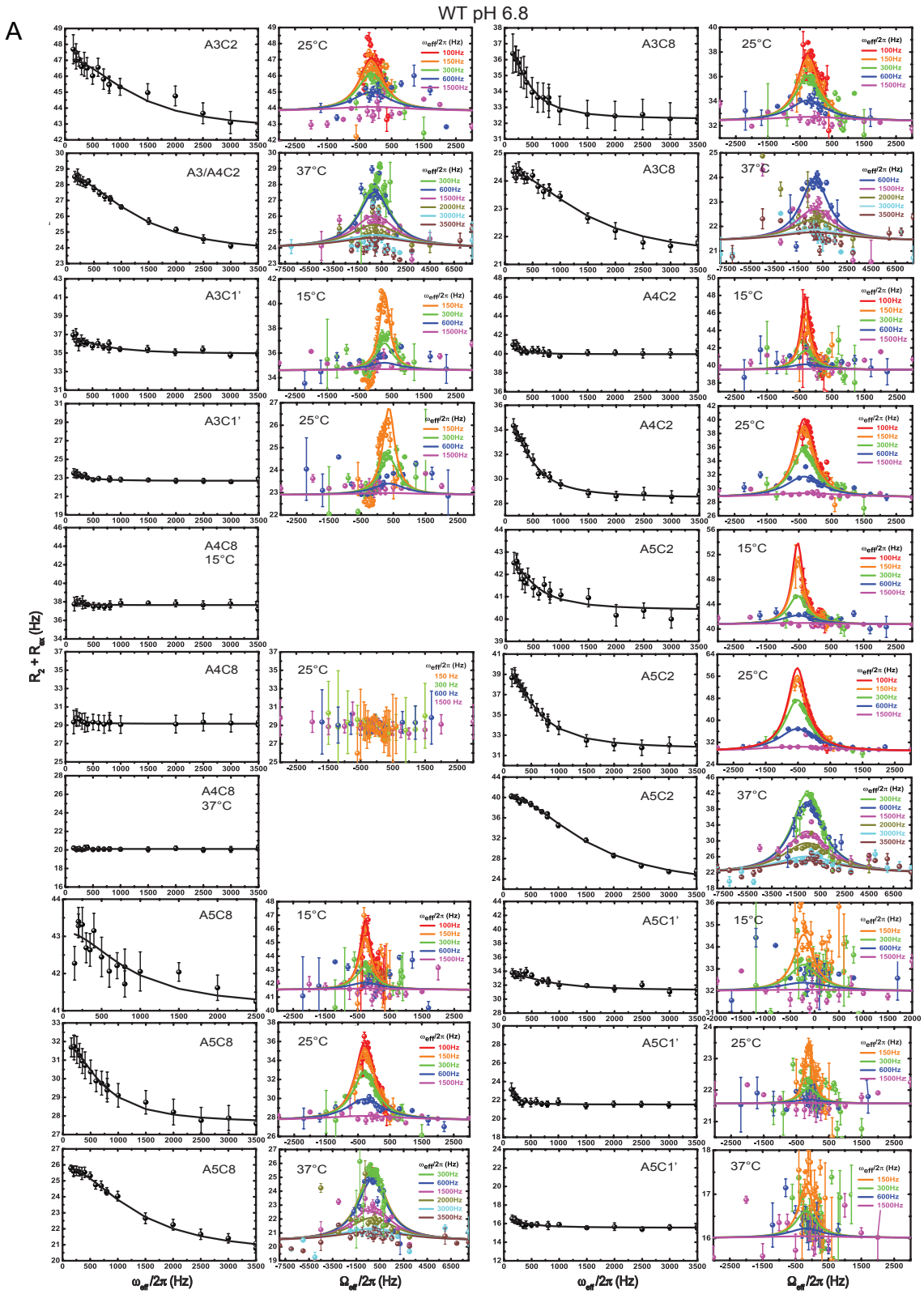

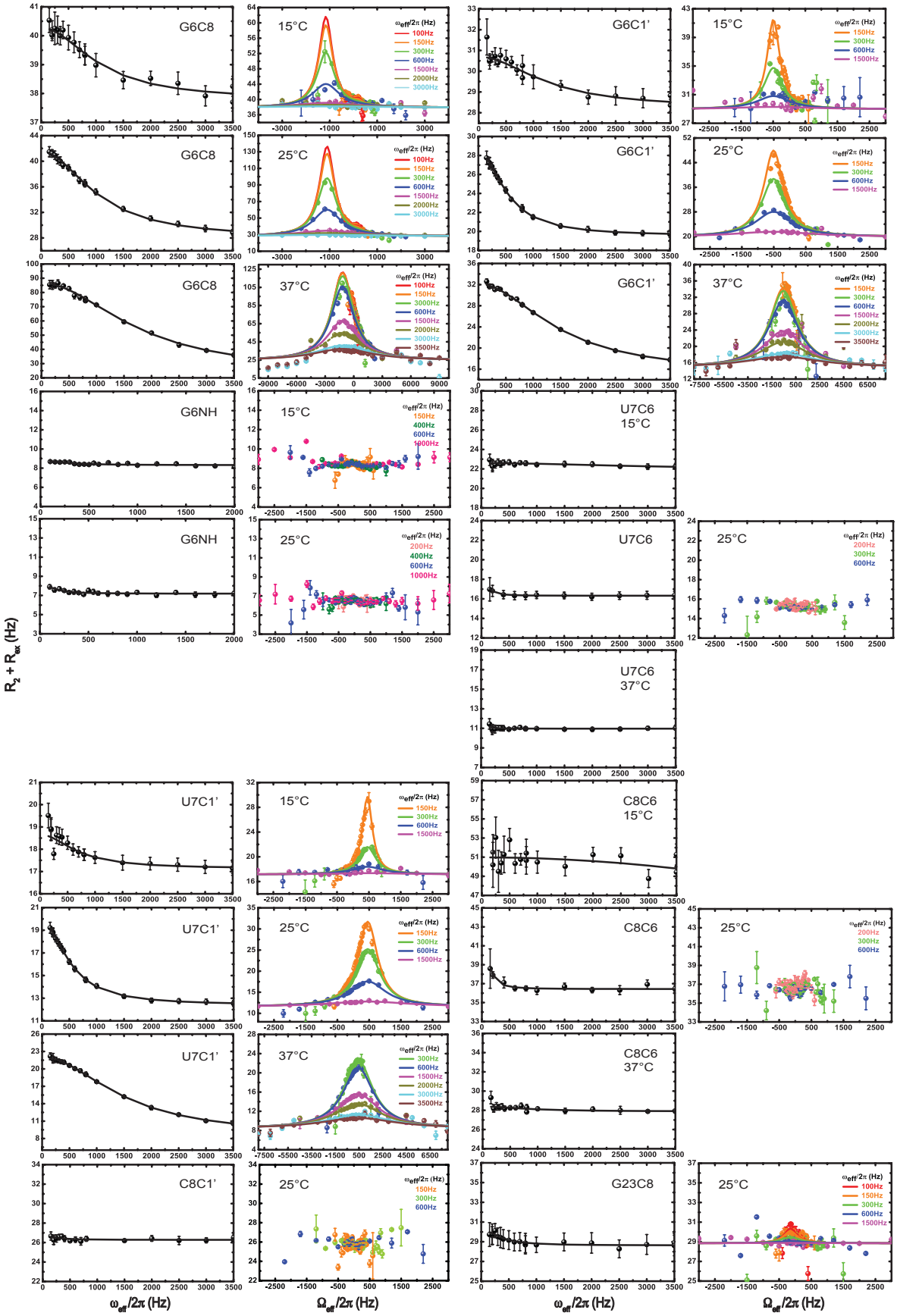
G6C8
15°C
25°C
37°C
G6C1'
G6NH
U7C6
U7C1'
C8C6
C8C1'
G23C8
$R_2 + R_{ex}$ (Hz)
$\omega_{eff}/2\pi$ (Hz)
$\Omega_{eff}/2\pi$ (Hz)

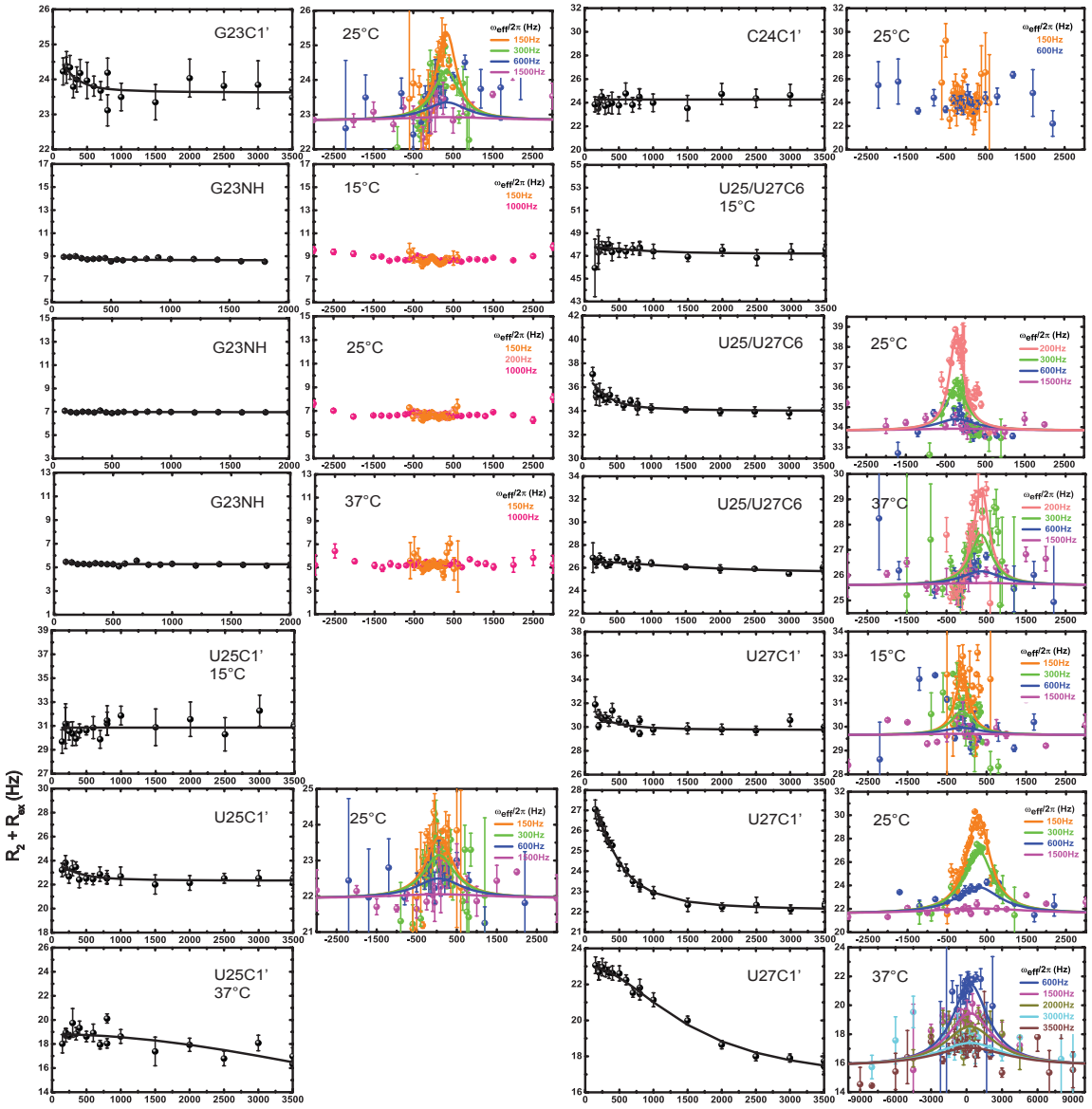
G23C1'
25°C
C24C1'
25°C
G23NH
15°C
U25/U27C6
15°C
G23NH
25°C
U25/U27C6
25°C
G23NH
37°C
U25/U27C6
37°C
U25C1'
15°C
U27C1'
15°C
U25C1'
25°C
U27C1'
25°C
U25C1'
37°C
U27C1'
37°C
WT pH 5.4
A3C2
25°C
A4C8
25°C
A5C2
25°C
G6C8
25°C
G6C1'
25°C
G6NH
25°C
R2 + Rex (Hz)
ωeff/2π (Hz)
Ωeff/2π (Hz)
ωeff/2π (Hz)
Ωeff/2π (Hz)

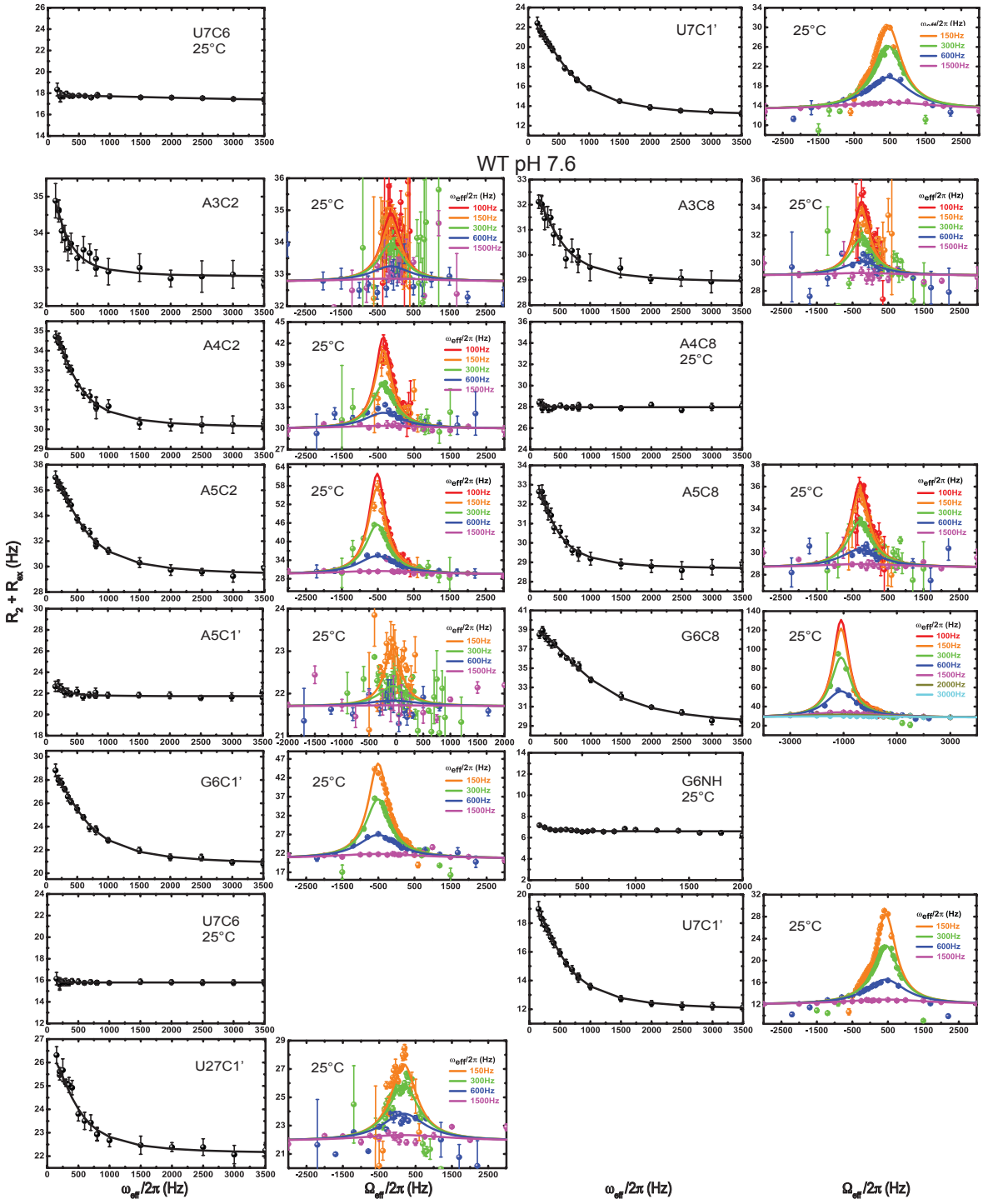
WT pH 7.6
U7C6
25°C
U7C1'
25°C
150Hz
300Hz
600Hz
1500Hz
A3C2
25°C
100Hz
150Hz
300Hz
600Hz
1500Hz
A3C8
25°C
A4C2
25°C
A4C8
25°C
A5C2
25°C
A5C8
25°C
A5C1'
25°C
G6C8
25°C
3000Hz
G6C1'
25°C
G6NH
25°C
U7C6
25°C
U7C1'
25°C
U27C1'
25°C
R2 + Rex (Hz)
ωeff/2π (Hz)
Ωeff/2π (Hz)

B

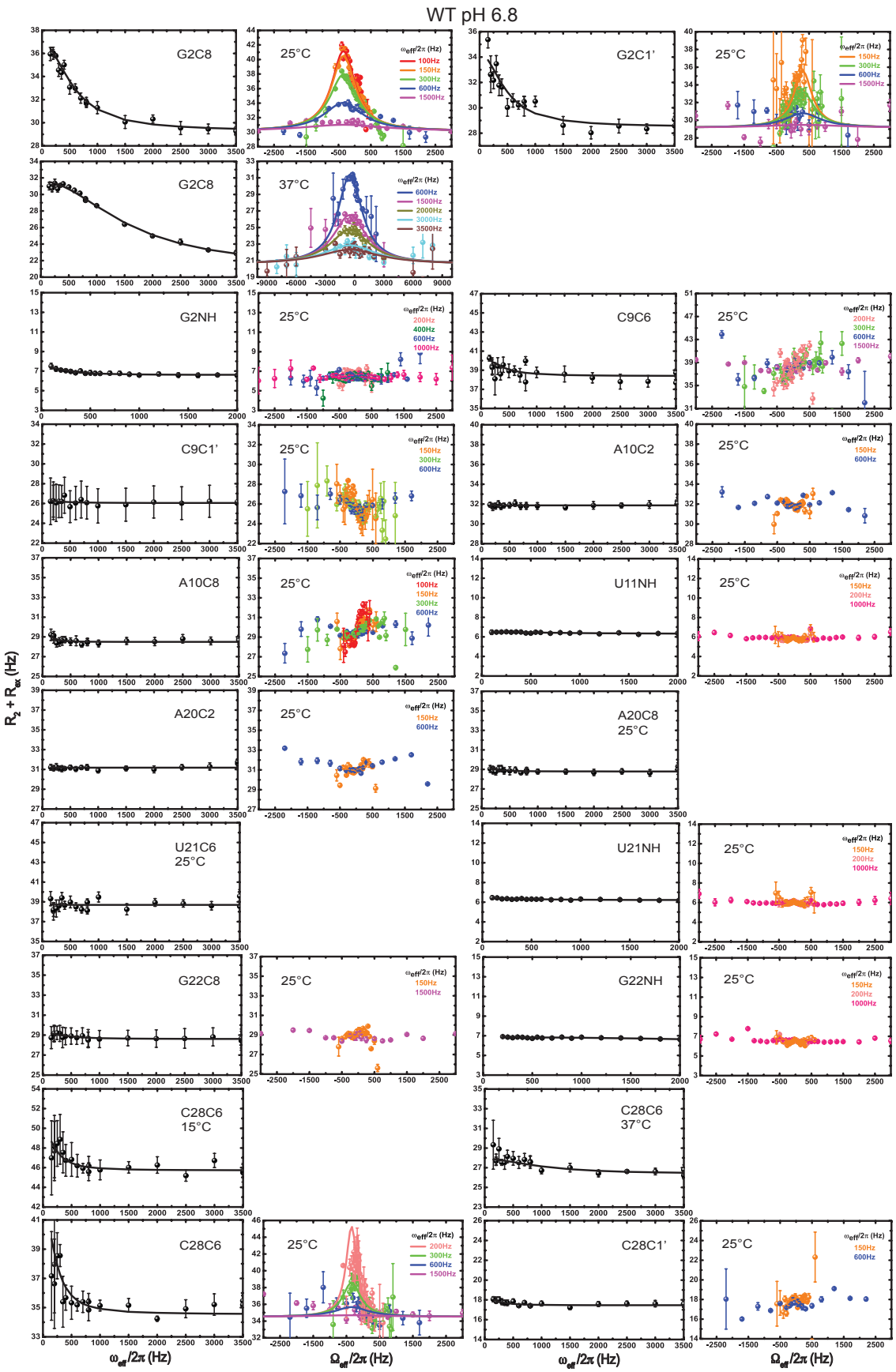
WT pH 6.8
G2C8
25°C
G2C1'
25°C
G2C8
37°C
G2NH
25°C
C9C6
25°C
C9C1'
25°C
A10C2
25°C
A10C8
25°C
U11NH
25°C
A20C2
25°C
A20C8
25°C
U21C6
25°C
U21NH
25°C
G22C8
25°C
G22NH
25°C
C28C6
15°C
C28C6
37°C
C28C6
25°C
C28C1'
25°C
R2 + Rex (Hz)
ωeff/2π (Hz)
Ωeff/2π (Hz)

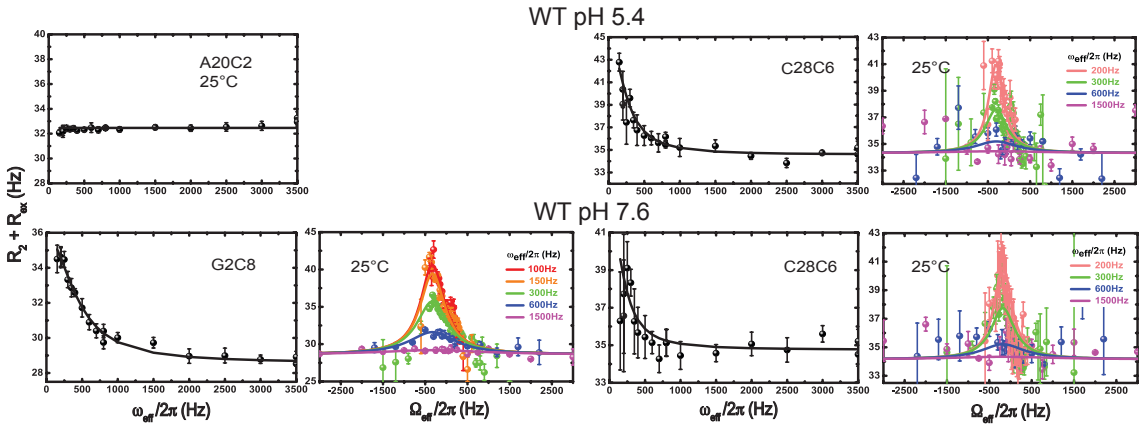
WT pH 5.4
A20C2
25°C
C28C6
25°C
WT pH 7.6
G2C8
25°C
C28C6
25°C
R2 + Rex (Hz)
ωeff/2π (Hz)
Ωeff/2π (Hz)

C

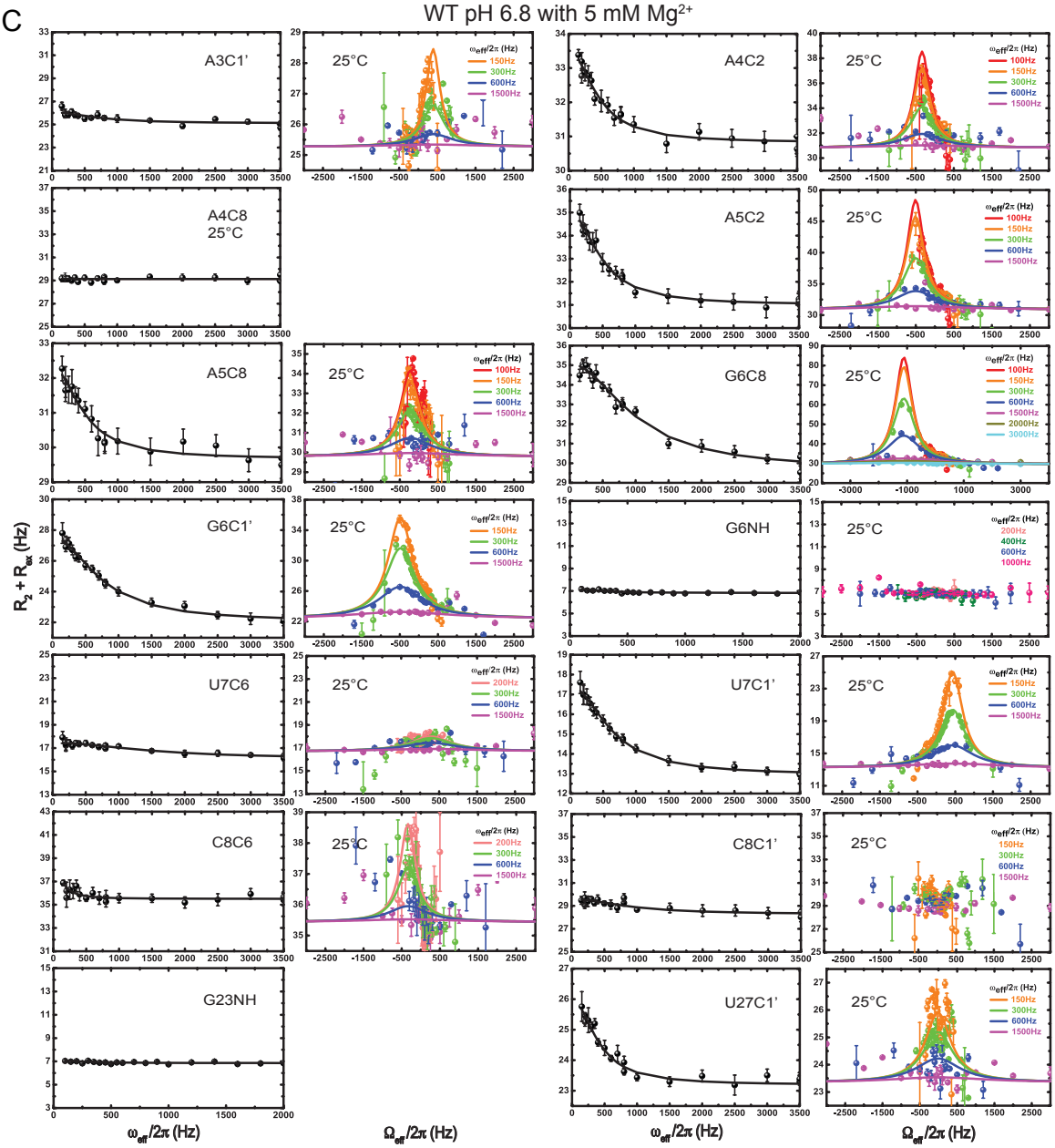
WT pH 6.8 with 5 mM Mg2+
A3C1'
A4C2
A4C8
25°C
A5C2
A5C8
G6C8
G6C1'
G6NH
U7C6
U7C1'
C8C6
C8C1'
G23NH
U27C1'
25°C
R2 + Rex (Hz)
ωeff/2π (Hz)
Ωeff/2π (Hz)

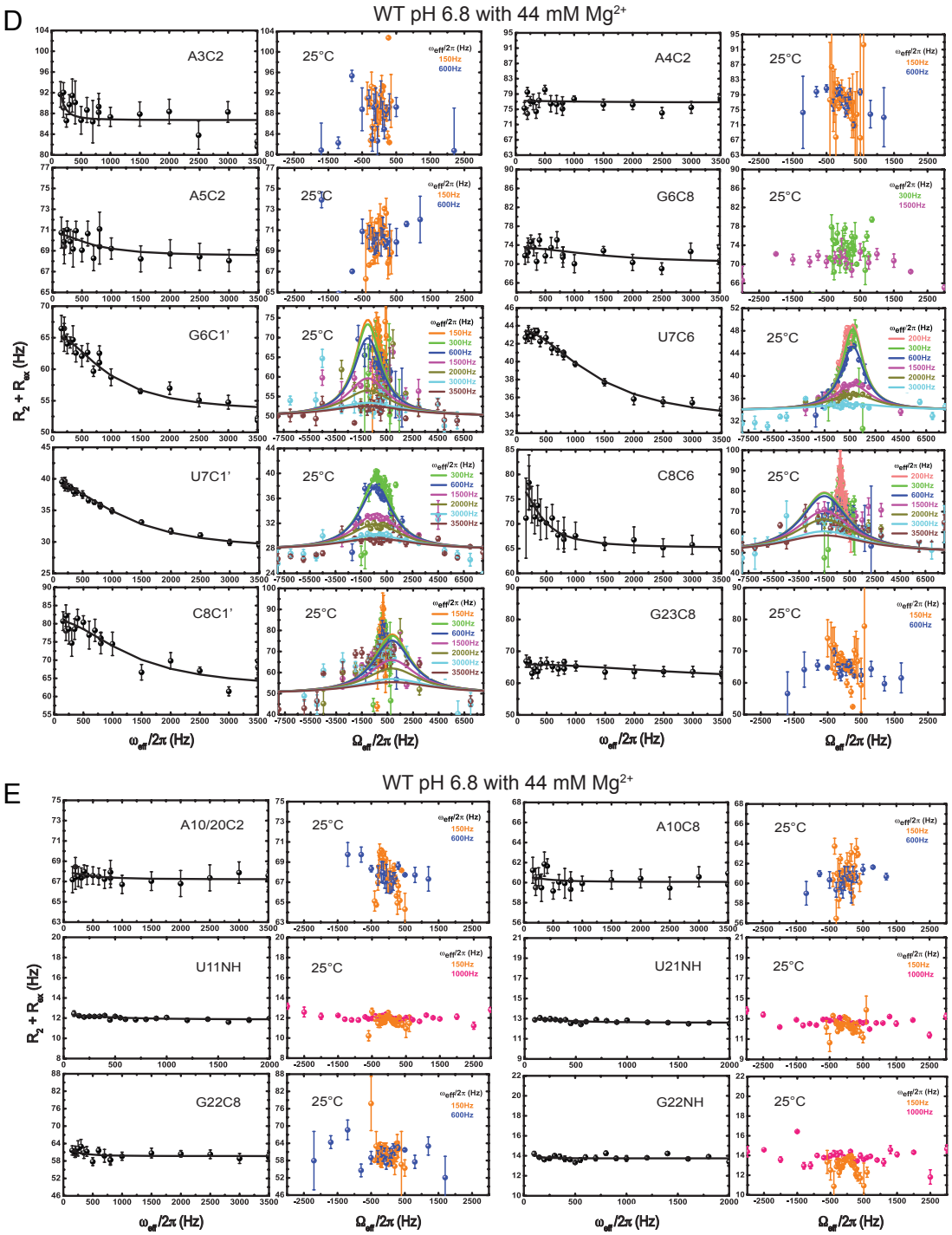

Figure B-2: Observation of the TS in and around U7 and A-tract of the P4 helix mimic from *B. subtilis* PRNA at the condition of 15 mM NaH_2PO_4, 25 mM NaCl and 0.1 mM EDTA under pH 5.4, 6.8 and 7.6 at 15°C, 25°C and 37°C with 2.3 mM of the P4 WT. **(A)** $R_{1\rho}$ relaxation dispersion profiles in and around U7 and A-tract and best fits (solid lines) to a two-state exchange model. **(B)** $R_{1\rho}$ relaxation dispersion profiles of other residues in the P4 helix mimic. **(C)** $R_{1\rho}$ relaxation dispersion profiles in the presence of 5 mM of $MgCl_2$. **(D)** $R_{1\rho}$ relaxation dispersion profiles in and around U7 and A-tract in the presence of 44 mM of $MgCl_2$. **(E)** $R_{1\rho}$ relaxation dispersion profiles of other residues in the P4 helix mimic in the presence of 44 mM of $MgCl_2$.

B.3.2 $R_{1\rho}$ relaxation dispersion profiles of DelA4 under different conditions

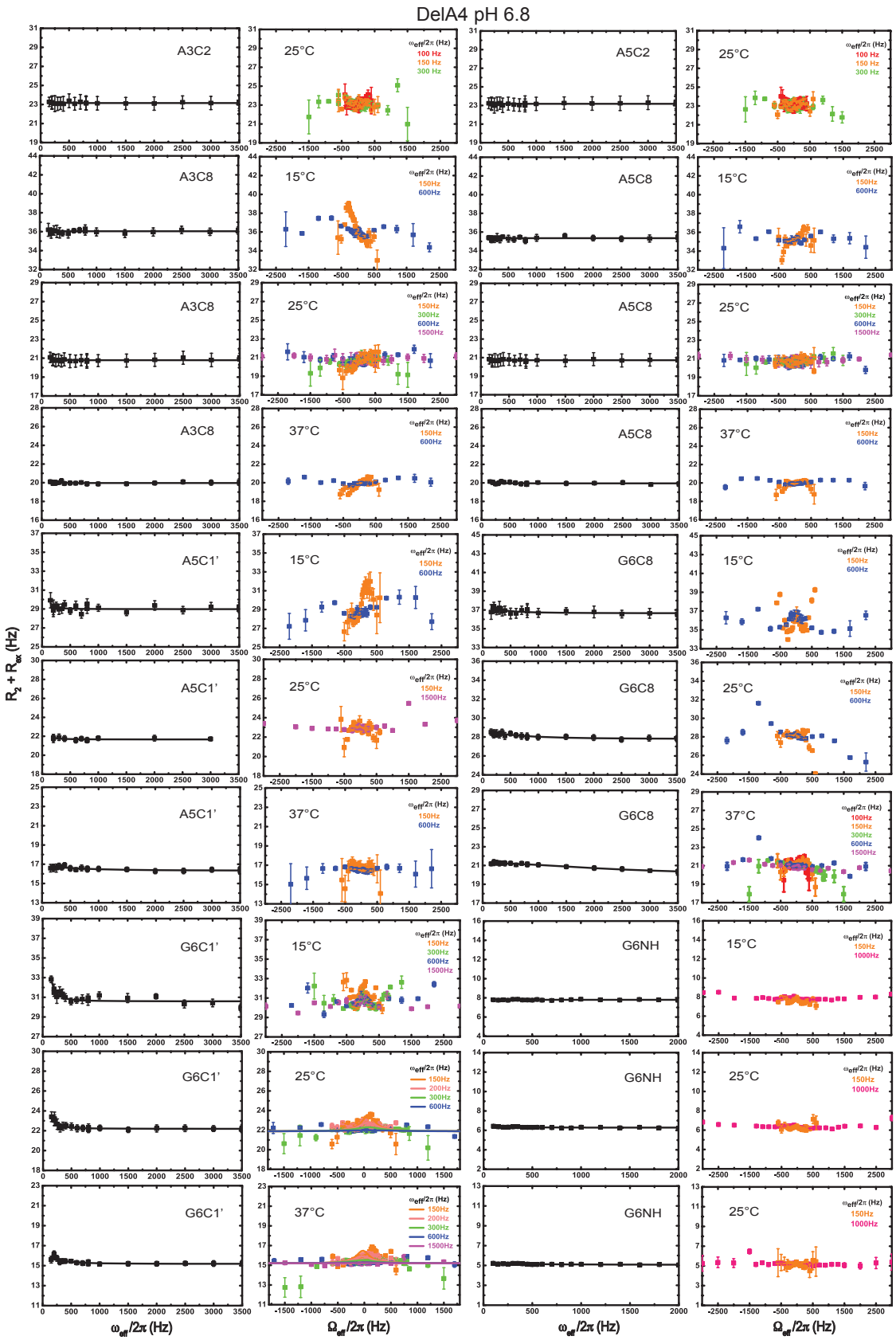

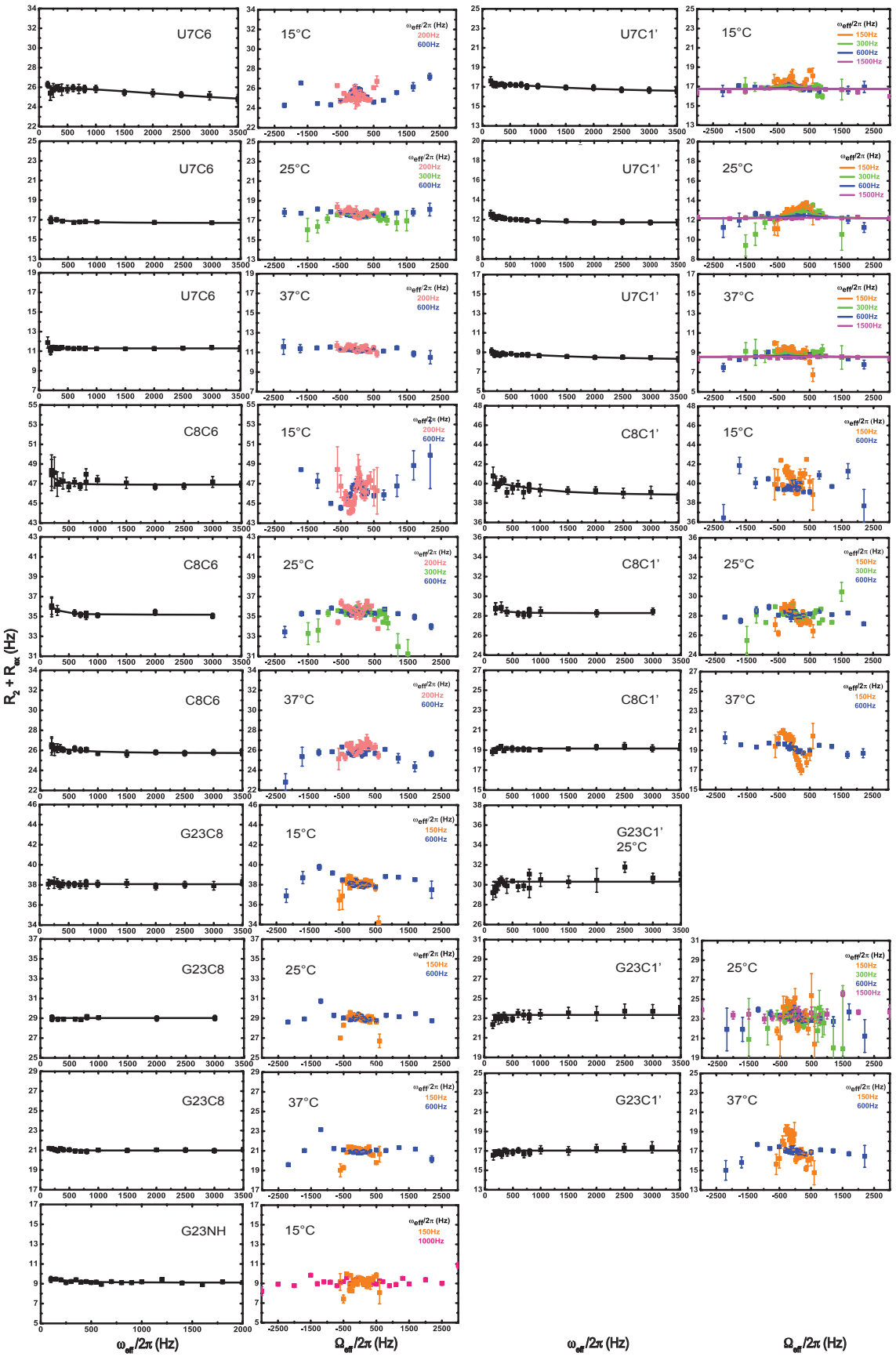
U7C6
15°C
25°C
37°C
U7C1'
C8C6
C8C1'
G23C8
G23C1'
25°C
G23NH
$\omega_{eff}/2\pi$ (Hz)
200Hz
300Hz
600Hz
150Hz
1500Hz
1000Hz
$R_2 + R_{ex}$ (Hz)
$\omega_{eff}/2\pi$ (Hz)
$\Omega_{eff}/2\pi$ (Hz)

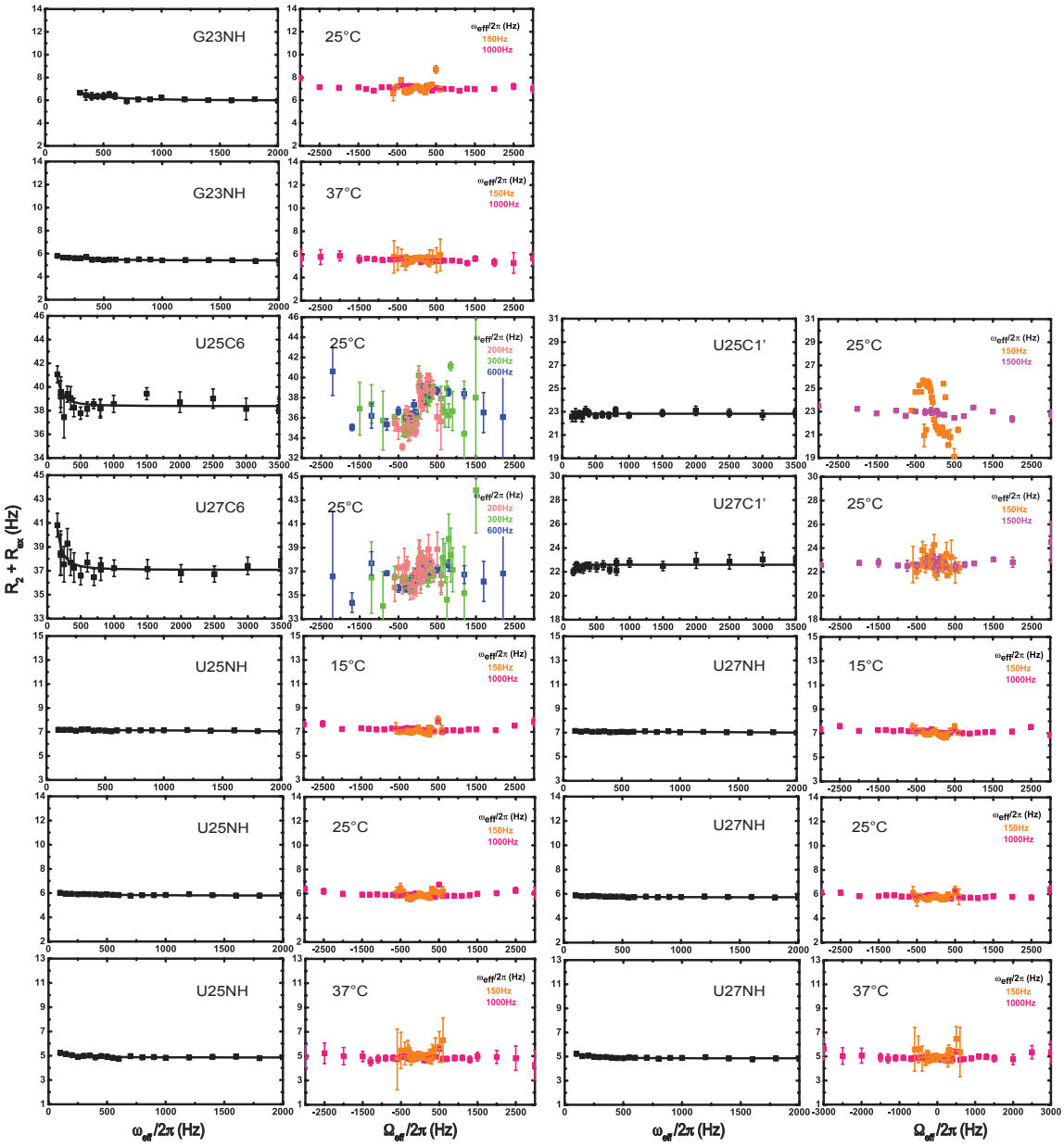
G23NH
25°C
37°C
U25C6
U27C6
U25C1'
U27C1'
U25NH
U27NH
15°C
ω_eff/2π (Hz)
150Hz
1000Hz
200Hz
300Hz
600Hz
1500Hz
R2 + Rex (Hz)
ω_eff/2π (Hz)
Ω_eff/2π (Hz)

B

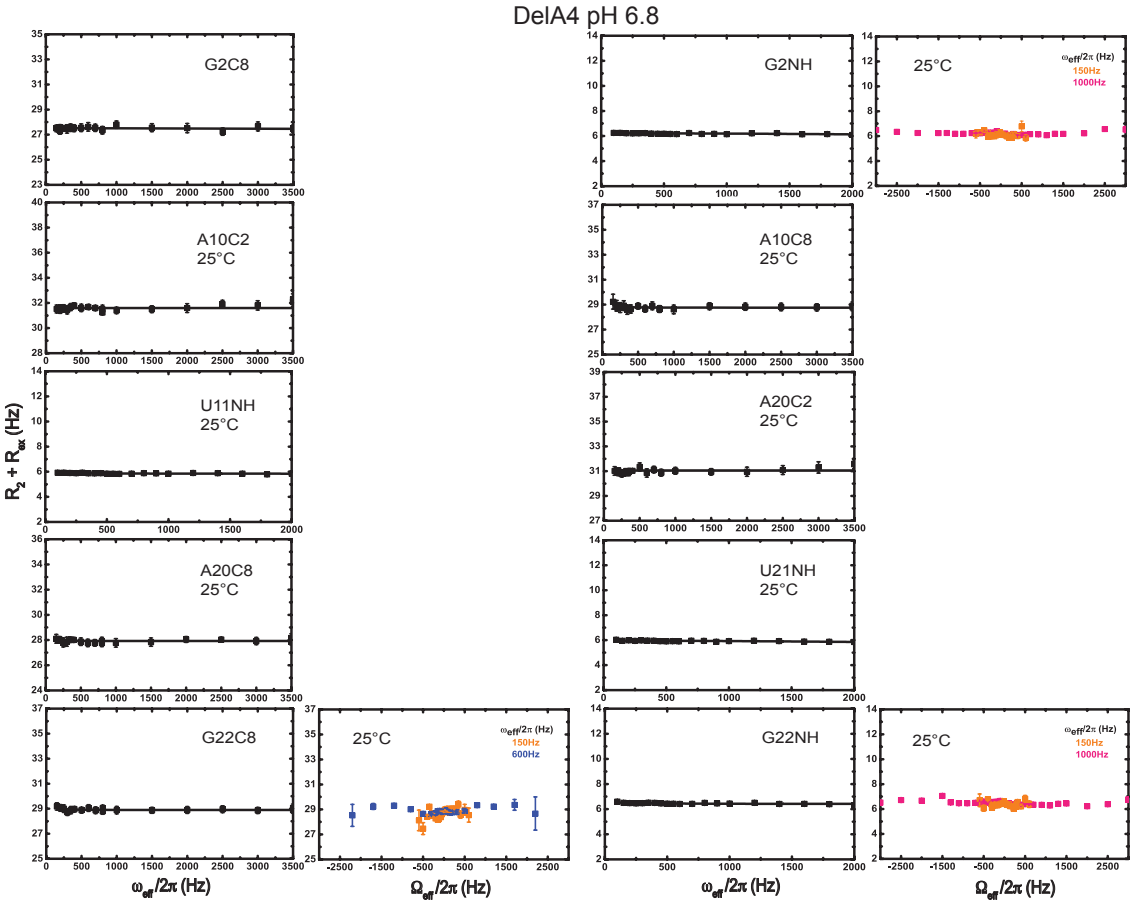
DelA4 pH 6.8
G2C8
A10C2
25°C
U11NH
25°C
A20C8
25°C
G22C8
25°C
150Hz
600Hz
G2NH
25°C
150Hz
1000Hz
A10C8
25°C
A20C2
25°C
U21NH
25°C
G22NH
25°C
150Hz
1000Hz
R2 + Rex (Hz)
ωeff/2π (Hz)
Ωeff/2π (Hz)

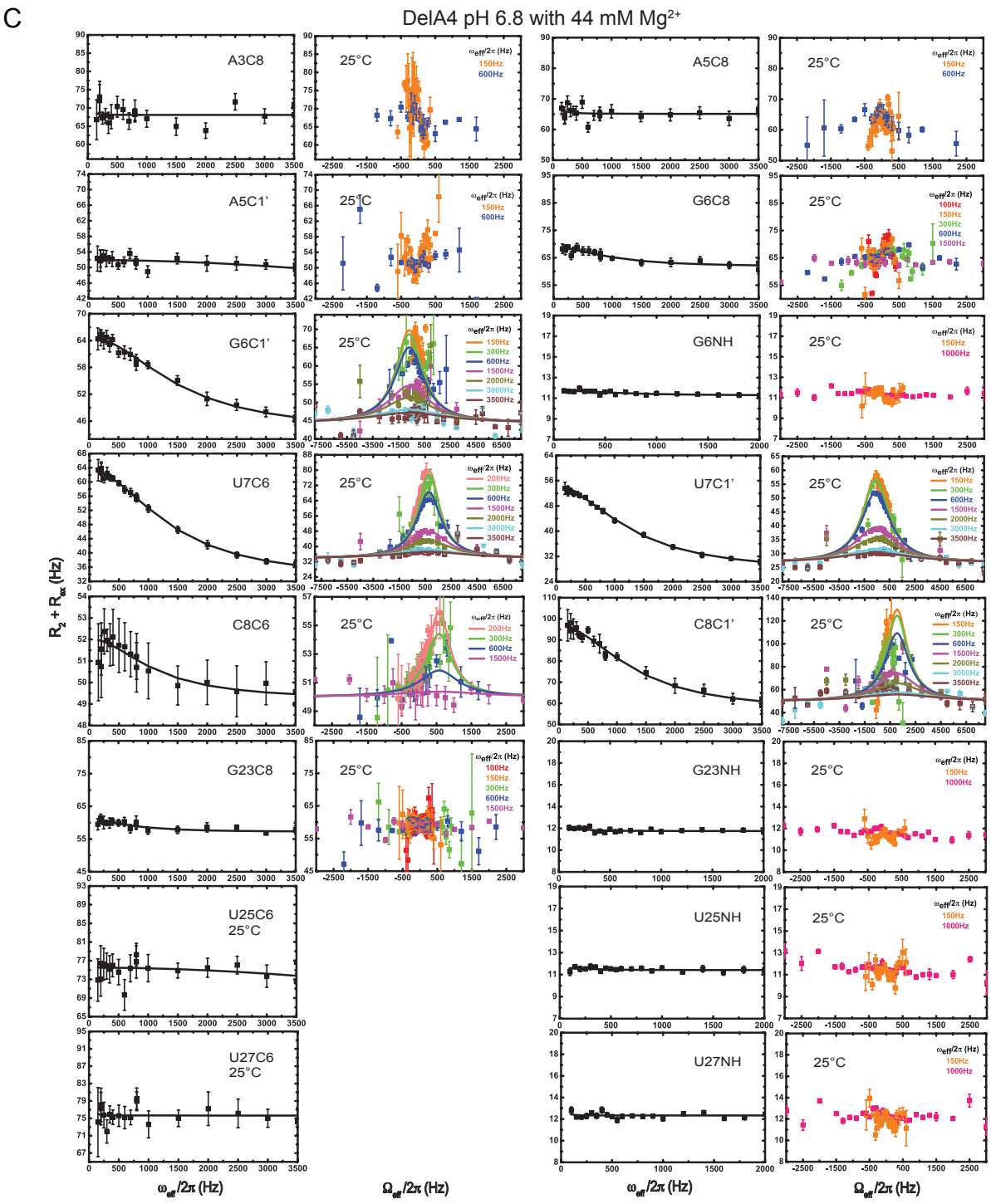

Figure B-3: DelA4 mutant eliminates the shared TS observed for the P4 WT in and around U7 and A-tract regions but retains the separated TS at U7. The experiments were performed under the condition of 15 mM NaH_2PO_4, 25 mM NaCl and 0.1 mM EDTA under pH 6.8 at 15°C, 25°C and 37°C with 2.5 mM of DelA4. **(A)** $R_{1\rho}$ relaxation dispersion profiles in and around U7 and A-tract and best fits (solid lines) to a two-state exchange model. **(B)** $R_{1\rho}$ relaxation dispersion profiles of other residues in DelA4. **(C)** $R_{1\rho}$ relaxation dispersion profiles in and around U7 and A-tract in the presence of 44 mM of $MgCl_2$.

B.4 Individual Fits of P4 WT Off-Resonance $R_{1\rho}$ Relaxation Dispersion under Different Conditions

Table B-5: Temperature dependence of P4 WT off-resonance $R_{1\rho}$ relaxation dispersion in 15 mM NaH_2PO_4, 25 mM NaCl and 0.1 mM EDTA at pH 6.8

Residue	T (°C)	R_1 (Hz)[a]	R_2 (Hz)[a]	p_B (%)[a]	k_{ex} (s^{-1})[a]	Δω (ppm)[a]
G2C8	**25**	1.95 ± 0.03	30.4 ± 0.09	0.44 ± 0.02	2267 ± 111	2.8 ± 0.97
	37	2.25 ± 0.08	20.6 ± 0.19	1.18 ± 0.22	8766 ± 410	3.3 ± 0.33
A3C8	**25**	1.91 ± 0.02	32.4 ± 0.17	0.58 ± 0.06	2388 ± 158	1.6 ± 0.08
	37	2.43 ± 0.08	21.4 ± 0.20	1.89 ± 4.41	8000 ± 1637	1.2 ± 1.42
A4C2	**15**	1.63 ± 0.07	39.5 ± 0.13	0.28 ± 0.04	846 ± 207	2.1 ± 0.16
	25	1.94 ± 0.03	28.7 ± 0.09	0.55 ± 0.02	2133 ± 75	2.3 ± 0.06
A5C8	**15**	1.68 ± 0.05	41.5 ± 0.11	0.28 ± 0.03	1103 ± 184	1.7 ± 0.14
	25	2.07 ± 0.02	27.7 ± 0.07	0.58 ± 0.03	2182 ± 74	1.9 ± 0.05
	37	2.59 ± 0.12	20.5 ± 0.29	2.15 ± 2.79	8506 ± 738	1.5 ± 0.98
A5C2	**15**	1.59 ± 0.06	40.7 ± 0.13	0.17 ± 0.03	1146 ± 289	3.6 ± 0.27
	25	2.00 ± 0.02	28.8 ± 0.09	0.66 ± 0.01	2169 ± 48	3.5 ± 0.04
	37	2.04 ± 0.07	21.7 ± 0.27	1.38 ± 0.16	9646 ± 312	4.1 ± 0.25
G6C1'	**15**	1.55 ± 0.06	29.0 ± 0.12	0.25 ± 0.02	1178 ± 191	3.3 ± 0.15
	25	1.93 ± 0.04	19.9 ± 0.18	0.70 ± 0.02	2132 ± 91	3.4 ± 0.08
	37	2.12 ± 0.04	14.8 ± 0.14	1.46 ± 0.11	8545 ± 175	3.6 ± 0.15
G6C8	**15**	1.55 ± 0.04	37.9 ± 0.09	0.10 ± 0.02	2105 ± 491	7.7 ± 0.36
	25	1.82 ± 0.03	28.0 ± 0.08	0.55 ± 0.02	2325 ± 99	7.4 ± 0.07
	37	2.67 ± 0.71	24.6 ± 1.28	1.53 ± 0.10	8456 ± 527	7.9 ± 0.49
U7C1'	**15**	2.01 ± 0.02	17.2 ± 0.05	0.30 ± 0.03	757 ± 101	-3.0 ± 0.06
	25	2.16 ± 0.02	11.6 ± 0.06	0.63 ± 0.01	2174 ± 34	-3.0 ± 0.03
	37	2.29 ± 0.03	8.44 ± 0.11	1.75 ± 0.17	9092 ± 189	-2.9 ± 0.14
U27C1'	**15**	1.44 ± 0.06	29.6 ± 0.13	0.83 ± 0.46	1015 ± 352	-0.8 ± 0.23
	25	1.82 ± 0.02	21.6 ± 0.07	0.65 ± 0.03	2009 ± 66	-1.9 ± 0.05
	37	2.12 ± 0.08	15.8 ± 0.28	1.81 ± 0.02	10991 ± 1133	-2.1 ± 0.94

[a] The data were fit to a two-state Laguerre equation (Equation 12) to obtain the values of all the parameters.

Table B-6: pH dependence of P4 WT off-resonance $R_{1\rho}$ relaxation dispersion in 15 mM NaH_2PO_4, 25 mM NaCl and 0.1 mM EDTA at 25 °C

pH	Residue	R_1 (Hz)[a]	R_2 (Hz)[a]	p_B (%)[a]	k_{ex} (s^{-1})[a]	Δω (ppm)[a]
5.4	**A3C2**	2.07 ± 0.06	33.8 ± 0.20	3.38 ± 0.90	2822 ± 188	0.90 ± 0.12
	A5C2	1.67 ± 0.06	37.7 ± 0.14	0.73 ± 0.01	2543 ± 91	3.8 ± 0.07
	G6C1'	1.73 ± 0.05	27.6 ± 0.17	1.07 ± 0.03	2211 ± 64	2.7 ± 0.06
	G6C8	1.67 ± 0.06	32.1 ± 0.15	0.74 ± 0.01	3867 ± 107	7.4 ± 0.08
	U7C1'	2.18 ± 0.03	13.2 ± 0.10	0.66 ± 0.02	2725 ± 80	-3.0 ± 0.07
	C27C6	2.02 ± 0.09	34.3 ± 0.15	0.61 ± 0.41	573 ± 436	2.0 ± 0.21
7.6	**G2C8**	1.93 ± 0.04	28.6 ± 0.11	0.63 ± 0.03	2048 ± 89	2.2 ± 0.08
	A3C2	1.92 ± 0.03	32.8 ± 0.07	0.79 ± 0.30	1894 ± 197	0.80 ± 0.16
	A3C8	1.85 ± 0.03	29.1 ± 0.09	0.43 ± 0.04	1655 ± 109	1.6 ± 0.09
	A4C2	1.68 ± 0.05	29.9 ± 0.11	0.49 ± 0.02	1582 ± 95	2.3 ± 0.07
	A5C1'	1.70 ± 0.03	21.7 ± 0.07	1.90 ± 1.91	728 ± 459	0.40 ± 0.18
	A5C2	1.52 ± 0.06	29.4 ± 0.16	0.58 ± 0.02	1642 ± 108	3.5 ± 0.08
	A5C8	1.97 ± 0.02	28.7 ± 0.06	0.53 ± 0.02	1821 ± 63	1.8 ± 0.05
	G6C1'	1.85 ± 0.04	20.7 ± 0.14	0.58 ± 0.01	1876 ± 83	3.4 ± 0.06
	G6C8	1.98 ± 0.04	28.4 ± 0.11	0.51 ± 0.02	2167 ± 110	7.3 ± 0.10
	U7C1'	2.11 ± 0.04	12.0 ± 0.10	0.54 ± 0.02	2040 ± 85	-2.9 ± 0.07
	U26C1'	1.70 ± 0.05	21.9 ± 0.11	1.30 ± 0.28	2549 ± 175	-1.2 ± 0.13
	C27C6	1.96 ± 0.06	34.2 ± 0.14	0.52 ± 0.19	941 ± 392	1.9 ± 0.21

[a] The data were fit to a two-state Laguerre equation (Equation 12) to obtain the values of all the parameters.

Table B-7: P4 WT off-resonance $R_{1\rho}$ relaxation dispersion in 15 mM NaH_2PO_4, 25 mM NaCl, 5 mM $MgCl_2$ and 0.1 mM EDTA under pH 6.8 at 25 °C

Residue	R_1 (Hz)[a]	R_2 (Hz)[a]	p_B (%)[a]	k_{ex} (s^{-1})[a]	Δω (ppm)[a]
A3C1'	1.51 ± 0.04	25.3 ± 0.07	0.10 ± 0.02	1039 ± 290	-2.6 ± 0.28
A4C2	1.94 ± 0.03	30.8 ± 0.07	0.29 ± 0.01	1388 ± 109	2.2 ± 0.08
A5C2	1.85 ± 0.05	30.9 ± 0.14	0.31 ± 0.02	1552 ± 169	3.4 ± 0.13
A5C8	2.10 ± 0.03	29.8 ± 0.08	0.44 ± 0.05	1853 ± 135	1.5 ± 0.10
G6C1'	2.02 ± 0.05	22.4 ± 0.13	0.38 ± 0.02	2280 ± 148	3.2 ± 0.13
G6C8	1.93 ± 0.04	29.5 ± 0.08	0.25 ± 0.02	2331 ± 198	7.3 ± 0.15
U7C1'	2.19 ± 0.03	13.2 ± 0.10	0.37 ± 0.02	1789 ± 123	-2.9 ± 0.10

[a] The data were fit to a two-state Laguerre equation (Equation 12) to obtain the values of all the parameters.

B.5 G6-8BrG sample has high purity and without contaminations

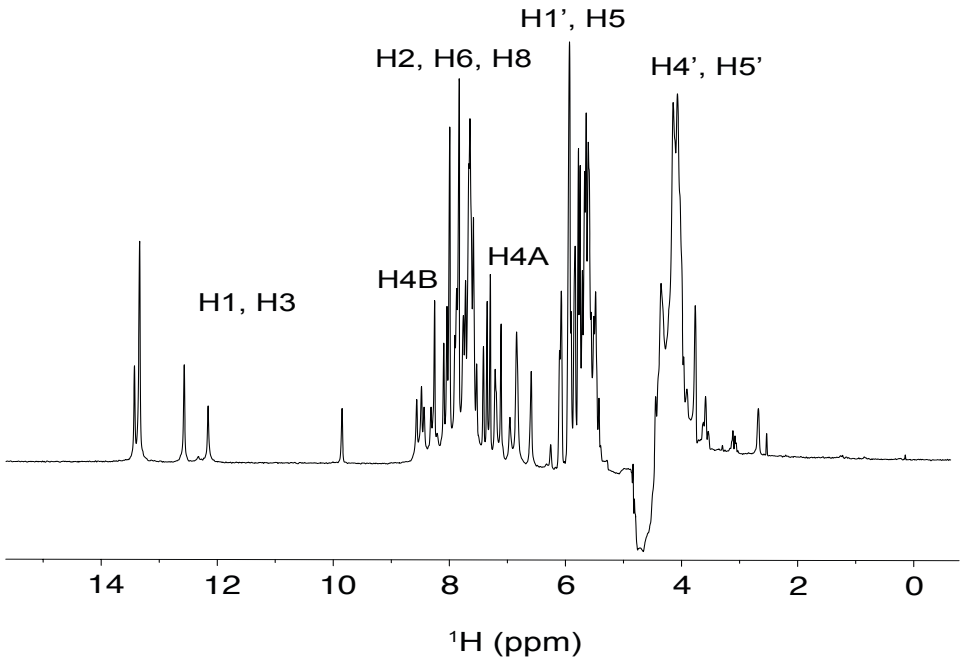

Figure B-4: ^{1}H NMR chemical shift of G6-1mG P4 helix mimic construct from *B. subtilis* PRNA. The data were collected in the buffer condition of 15 mM NaH_2PO_4, 25 mM NaCl and 0.1 mM EDTA under pH 5.4 at 25°C with 1 mM of unlabeled G6-8BrG.

B.6 G6-m1G Modification Is Unable to Provide Evidence for Hoogsteen Base Pair in the TS of the P4 Helix Mimic

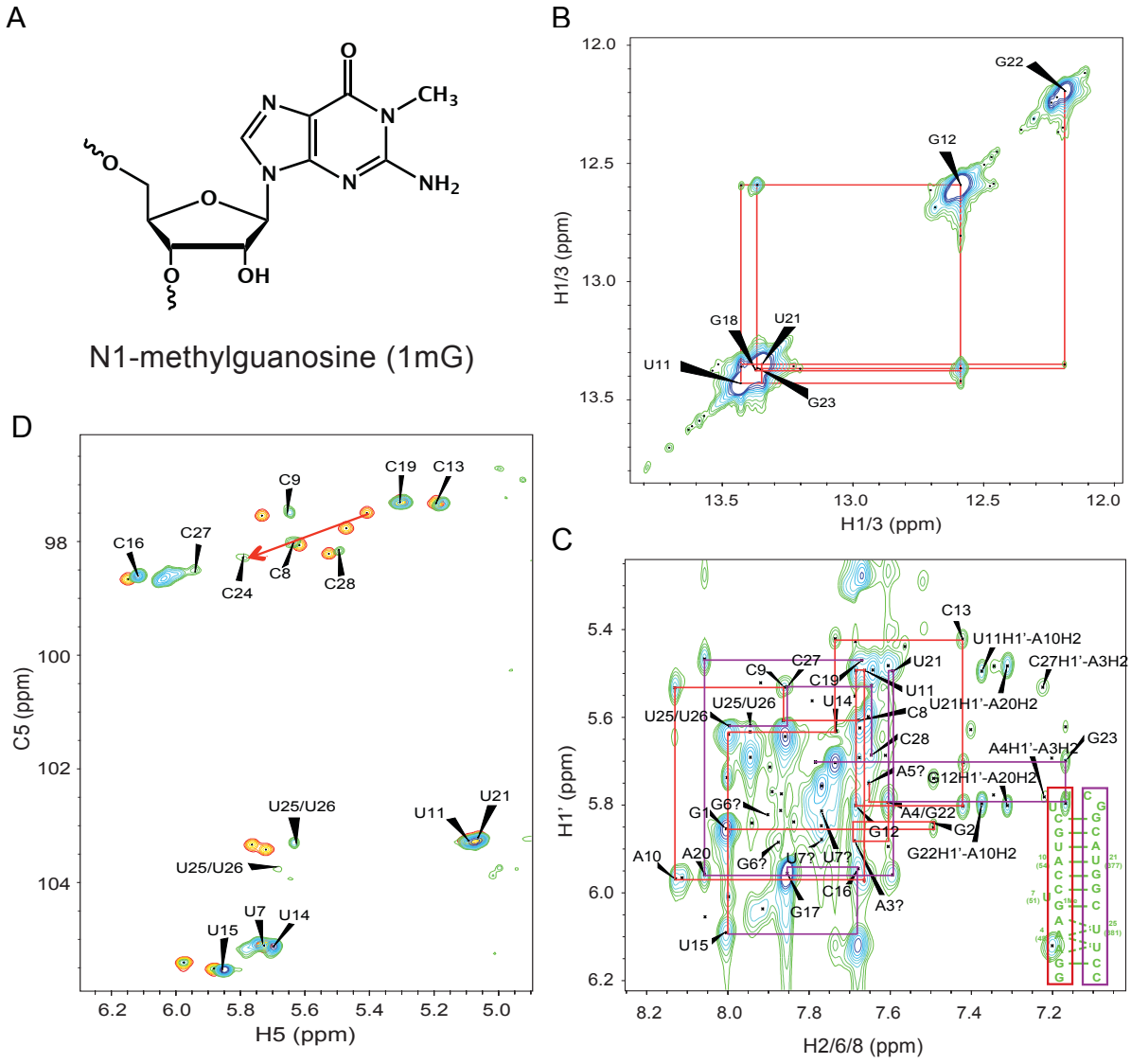

E

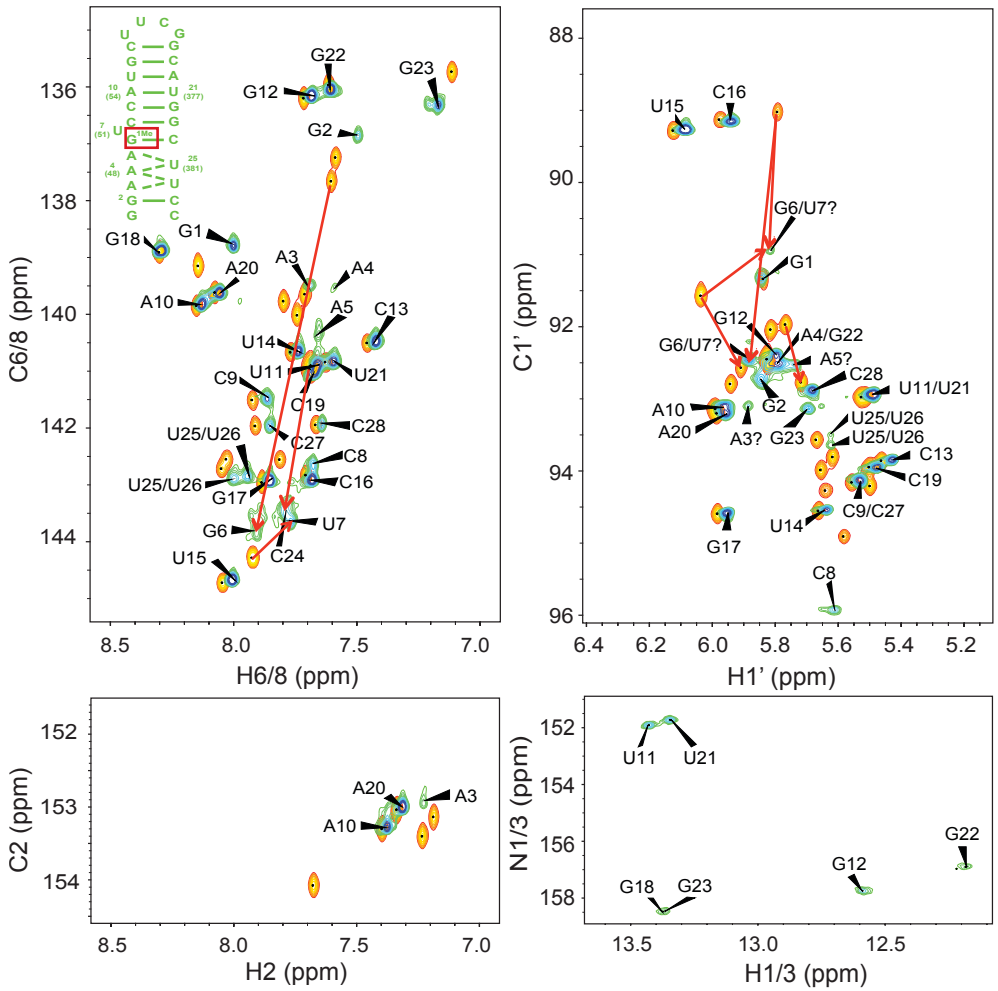

Figure B-5: Resonance assignments of G6-1mG P4 helix mimic construct from *B. subtilis* PRNA. The data were collected in the buffer condition of 15 mM NaH_2PO_4, 25 mM NaCl and 0.1 mM EDTA under pH 5.4 at 25°C with 1 mM of unlabeled G6-8BrG. **(A)** Chemical structure of N1-methylguanosine. **(B)** Exchangeable ^{1}H-^{1}H NOESY correlation of G6-1mG showing imino walk from residue G23 to G18. **(C)** Non-exchangeable ^{1}H-^{1}H NOESY correlation of G6-1mG showing nucleobase H2/6/8 to sugar H1' NOE walk. The connectivity from residue G1 to U15 is shown in red and U15 to C28 is in purple. **(D)** 2D ^{13}C-^{1}H natural abundance HSQC spectra showing C5 and H5 correlation for P4 WT (orange) and G6-1mG (green). **(D)** 2D ^{13}C-^{1}H natural abundance HSQC/HMQC spectra showing nucleobase C2/6/8-H2/6/8 and sugar C1'-H1' correlation for P4 WT (orange) and G6-1mG (green); ^{15}N-^{1}H natural abundance imino HMQC spectra showing nitrogen/proton (N1/3-H1/3) correlation. The guanosine substituted with 1mG is indicated in the secondary structure of the P4 helix mimic as inset. Chemical shift perturbation of G6C8, U7C6, C24C6, A5C1', G6C1' and U7C1' are shown in red arrows. Questions marks are indicated uncertainty of resonance assignments.

B.7 Structural Comparison between the TS and the ES

Table B-8: Sugar pucker and glycosidic angle designation for residues from G2 to U11 and C19 to C27 in the GS and the TS of the P4 helix mimic from *B. subtilis* PRNA[a]

Residue	GS		TS	
	Sugar pucker	**Glycosidic angle**	**Sugar pucker**	**Glycosidic angle**
G2	C2'-exo	*anti*	C3'-endo	*anti*
A3	C3'-endo	*anti*	C3'-endo	*anti*
A4	C3'-endo	*anti*	C3'-endo	*anti*
A5	C3'-endo	*anti*	C3'-endo	*anti*
G6	C2'-endo	*anti*	C4'-exo	*syn*
U7	C1'-exo	*syn*	C2'-endo	*anti*
C8	C3'-endo	*anti*	C2'-exo	*anti*
C9	C3'-endo	*anti*	C3'-endo	*anti*
A10	C3'-endo	*anti*	C3'-endo	*anti*
U11	C3'-exo	*anti*	C3'-endo	*anti*
C19	C2'-exo	*anti*	C3'-endo	*anti*
A20	C3'-endo	*anti*	C3'-endo	*anti*
U21	C3'-endo	*anti*	C3'-endo	*anti*
G22	C3'-endo	*anti*	C3'-endo	*anti*
G23	C3'-endo	*anti*	C3'-endo	*anti*
C24	C2'-exo	*anti*	C3'-endo	*anti*
U25	C3'-endo	*anti*	C3'-endo	*anti*
U26	C2'-exo	*anti*	C3'-endo	*anti*
C27	C3'-endo	*anti*	C3'-endo	*anti*

[a] Structure parameters were extracted from the corresponding chemical shift-selected MC-Sym models using the program MC-Annotate [2].

B.8 References

1. Zhang, Q., et al., *Resolving the Motional Modes That Code for RNA Adaptation.* Science, 2006. **311**(5761): p. 653-656.
2. Gendron, P., Lemieux, S., and Major, F., *Quantitative analysis of nucleic acid three-dimensional structures.* J Mol Biol, 2001. **308**(5): p. 919-36.

APPENDIX C

C.1 Table C-1: STO rate constants for cleavage of Fl-pre-tRNA^{Asp} catalyzed by *B. subtilis* WT and modified RNase Ps

Holoenzyme		WT	U51C	U51U50	U51U52	ΔC52	Inserstion A (G379/C380)
Structure		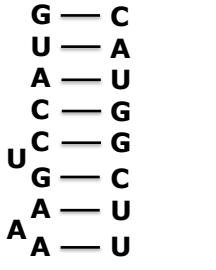	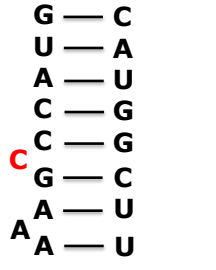	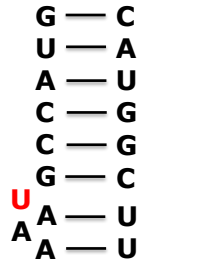	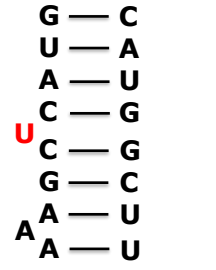	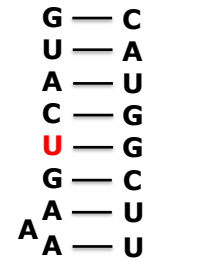	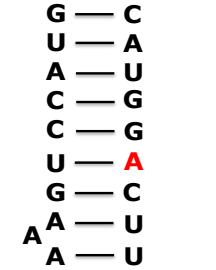
pH 5.2	k_{obs} (s^{-1}) ($\times 10^{-2}$)[a]	2.6 ± 0.4	0.14 ± 0.01	0.28 ± 0.09	0.084 ± 0.024	0.31 ± 0.01	ND
	$k_{obs}^{WT}/k_{obs}^{modified}$	1	19	9.3	31	8.4	ND
pH 5.9	k_{obs} (s^{-1}) ($\times 10^{-2}$)[a]	16 ± 2	ND[c]	ND	ND	ND	0.025 ± 0.001
	$k_{obs}^{WT}/k_{obs}^{modified}$	1	ND	ND	ND	ND	640
pH 7.7	k_{obs} (s^{-1}) ($\times 10^{-2}$)[a]	1.3 ± 0.2	0.11 ± 0.01	0.45 ± 0.04	0.062 ± 0.008	0.17 ± 0.03	0.003 ± 0.001
	$k_{obs}^{WT}/k_{obs}^{modified}$	1	12	2.9	21	7.6	433
High pH	k_{max} (s^{-1})[b]	1.7 ± 0.1	0.15 ± 0.01	ND	0.086 ± 0.001	0.19 ± 0.01	0.018 ± 0.001
	$k_{obs}^{WT}/k_{obs}^{modified}$	1	11	ND	20	8.9	94
	pK_a[b]	7.0 ± 0.1	7.2 ± 0.1	ND	7.2 ± 0.1	6.7 ± 0.1	8.3 ± 0.1

Holoenzyme		WT	C52U	C52-abC[d]	C52-3mU[d]	C52-tC[Od]
Structure		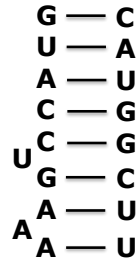	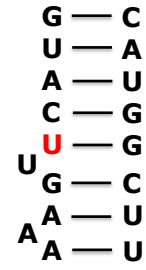	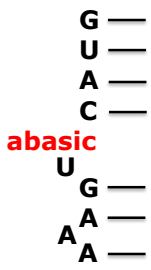	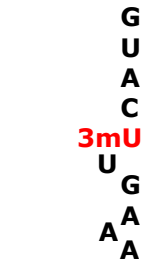	
pH 5.2	k_{obs} (s^{-1}) ($\times 10^{-2}$)[a]	2.6 ± 0.4	0.23 ± 0.01	0.31 ± 0.01	0.43 ± 0.01	0.065 ± 0.001
	$k_{obs}^{WT}/k_{obs}^{modified}$	1	11	8.4	6.0	40
pH 7.7	k_{obs} (s^{-1}) ($\times 10^{-2}$)[a]	1.3 ± 0.2	0.27 ± 0.04	0.052 ± 0.006	0.063 ± 0.001	0.011 ± 0.001
	$k_{obs}^{WT}/k_{obs}^{modified}$	1	4.8	25	21	118
High pH	k_{max} (s^{-1})[b]	1.7 ± 0.1	ND	0.048 ± 0.005	0.061 ± 0.005	0.010 ± 0.001
	$k_{obs}^{WT}/k_{obs}^{modified}$	1	ND	35	28	170
	pK_a[b]	7.0 ± 0.1	ND	6.1 ± 0.3	6.2 ± 0.2	6.4 ± 0.1

Holoenzyme		WT	G379A	U51C-G379A	C52U-G379A	C52A-G379U	C52G-G379C	C52/53G-G379/378G
Structure		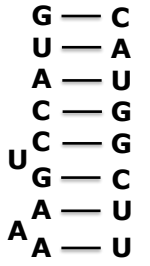	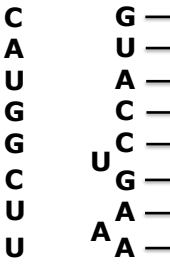		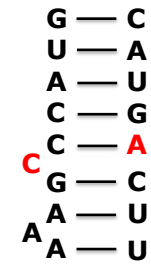	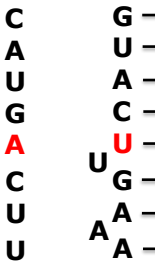	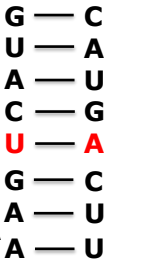	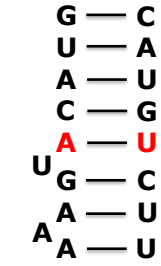
pH 5.2	k_{obs} (s^{-1}) ($\times 10^{-2}$)[a]	2.6 ± 0.4	0.12 ± 0.01	0.09 ± 0.03	0.99 ± 0.01	0.76 ± 0.01	0.46 ± 0.01	0.87 ± 0.01
	$k_{obs}^{WT}/k_{obs}^{modified}$	1	22	29	2.6	3.4	5.7	3.0
pH 7.7	k_{obs} (s^{-1}) ($\times 10^{-2}$)[a]	1.3 ± 0.2	0.14 ± 0.02	0.10 ± 0.01	ND	ND	ND	ND
	$k_{obs}^{WT}/k_{obs}^{modified}$	1	9.3	13	ND	ND	ND	ND
High pH	k_{max} (s^{-1})[b]	1.7 ± 0.1	0.28 ± 0.01	0.17 ± 0.01	ND	ND	ND	ND
	$k_{obs}^{WT}/k_{obs}^{modified}$	1	6.1	10	ND	ND	ND	ND
	pK_a[b]	7.0 ± 0.1	7.8 ± 0.1	7.5 ± 0.1	ND	ND	ND	ND

Holoenzyme		WT	G50-dG[d]	G50-8BrdG[d]	G50C-C380G
Structure		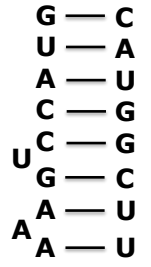	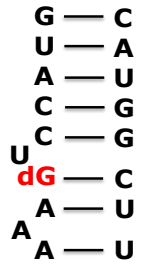	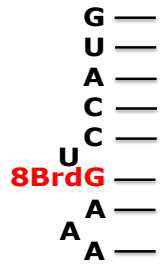	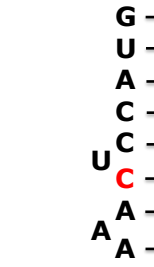
pH 5.5	k_{obs} (s^{-1}) ($\times 10^{-2}$)[a]	4.3 ± 0.7	6.4 ± 0.4	7.2 ± 1.5	4.6 ± 0.5
	$k_{obs}^{WT}/k_{obs}^{modified}$	1	0.7	0.6	0.9

Holoenzyme		WT	A49-dA[d]	A49-8BrdA[d]	A47/A49/U51-abasic[d]	U381C	U381/U382-abU[d]	Inserstion U (U381/U382)
Structure		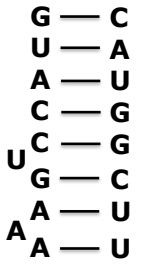	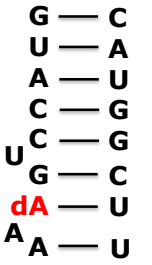	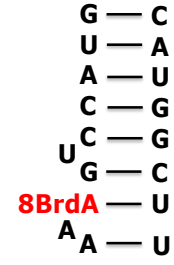	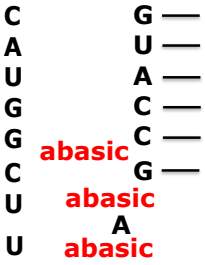	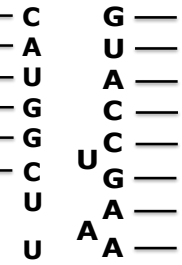	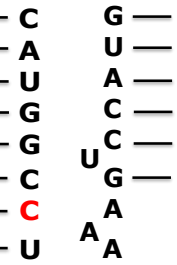	
pH 5.2	k_{obs} (s^{-1}) ($\times 10^{-2}$)[a]	2.6 ± 0.4	ND	ND	0.014 ± 0.004	3.0 ± 0.1	4.6 ± 0.3	2.8 ± 0.2
	$k_{obs}^{WT}/k_{obs}^{modified}$	1	ND	ND	186	0.9	0.6	0.9
pH 5.5	k_{obs} (s^{-1}) ($\times 10^{-2}$)[a]	4.3 ± 0.7	4.0 ± 0.3	1.8 ± 0.1	ND	ND	ND	ND
	$k_{obs}^{WT}/k_{obs}^{modified}$	1	1.1	2.4	ND	ND	ND	ND
pH 7.7	k_{obs} (s^{-1}) ($\times 10^{-2}$)[a]	1.3 ± 0.2	ND	ND	0.039 ± 0.001	ND	0.073 ± 0.006	ND
	$k_{obs}^{WT}/k_{obs}^{modified}$	1	ND	ND	33	ND	18	ND
High pH	k_{max} (s^{-1})[b]	1.7 ± 0.1	ND	ND	0.041 ± 0.001	ND	0.10 ± 0.02	ND
	$k_{obs}^{WT}/k_{obs}^{modified}$	1	ND	ND	41	ND	17	ND
	pK_a[b]	7.0 ± 0.1	ND	ND	6.7 ± 0.1	ND	5.1 ± 0.6	ND

[a] STO cleavage was measured in a saturating concentration of RNase P (360 nM - 4 μM), 10 nM Fl-pre-tRNA^{Asp} substrate, 50 mM Tris/MES, 20-50 mM $MgCl_2$ and 20 mM DTT with KCl concentrations adjusted to maintain constant ionic strength (~2 00-110 mM) at 37°C. k_{obs} was calculated by a fit of single exponential (Equation 6) to the fraction cleavage of Fl-pre-tRNA^{Asp} substrate, which was calculated from the decrease in anisotropy using Equation 5 as described in Chapter 2.

[b] The k_{max} and pK_a were calculated from fitting a single ionization model (Equation 7) to the pH dependence of RNase P STO cleavage, as described in Chapter 2.

[c] ND: Not determined.

[d] Abasic: rSpacer modification; 3mU: N3-methyluridine; tC^O: Tricyclic cytidine analog; dG: Deoxyguanosine; dA: Deoxyadenosine; 8BrdG: 8-bromo-deoxyguanosine; 8BrdA: 8-bromo-deoxyadenosine.

C.2 Table C-2: Mg^{2+} dependence of WT and modified *B. subtilis* PRNA catalyzed STO cleavage[a]

Holoenzyme	WT	ΔU51[c]	U51C[c]	U51U50	U51U52[c]	ΔC52[c]	C52U[c]	C52-abC[d]
Structure								
k_{max}^{PRNA} (s^{-1})[b] (×10^{-2})[b]	2.5 ± 0.1	0.15 ± 0.01	0.17 ± 0.01	0.14 ± 0.02	0.047 ± 0.002	0.44 ± 0.06	0.20 ± 0.01	0.51 ± 0.02
$K_{1/2,app}^{Mg^{2+}}$ (mM)[b]	13.0 ± 0.5	62.5 ± 13.2	16.5 ± 0.7	279 ± 64	23.5 ± 2.6	60.2 ± 23.5	41.8 ± 4.9	62.1 ± 7.0
n_H[b]	4.0 ± 0.5	1.1 ± 0.2	2.5 ± 0.2	1.2 ± 0.1	2.3 ± 0.7	1.0 ± 0.2	1.2 ± 0.2	1.5 ± 0.2
$k_{max}^{PRNA,\ WT}/k_{max}^{PRNA,\ modified}$	1	17	15	18	53	5.7	13	4.9

Holoenzyme	WT	G379A[c]	U51C-G379A[c]	C52U-G379A	C52A-G379U	C52G-G379C	C52/53G-G379/378G
Structure							
k_{max}^{PRNA} (s^{-1})[b] (×10^{-2})[b]	2.5 ± 0.1	0.15 ± 0.01	0.17 ± 0.01	0.50 ± 0.01	0.28 ± 0.02	0.36 ± 0.01	1.0 ± 0.1
$K_{1/2,app}^{Mg^{2+}}$ (mM)[b]	13.0 ± 0.5	11.7 ± 0.2	17.2 ± 0.5	14.8 ± 0.6	55.3 ± 12.6	103 ± 9	11.4 ± 0.7
n_H[b]	4.0 ± 0.5	2.7 ± 0.1	2.7 ± 0.2	4.5 ± 0.7	1.0 ± 0.2	1.1 ± 0.1	4.6 ± 1.0
$k_{max}^{PRNA,\ WT}/k_{max}^{PRNA,\ modified}$	1	17	15	5.0	8.9	6.9	2.5

Holoenzyme	WT	A47-abA[d]	A48-abA[c, d]	A49-abA[d]	U381-abU[d]	U382-abU[d]
Structure	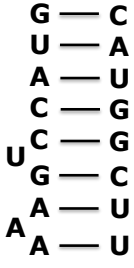					
k_{max}^{PRNA} (s^{-1})[b] ($\times 10^{-2}$)[b]	2.5 ± 0.1	0.036 ± 0.002	0.027 ± 0.001	0.080 ± 0.008	1.4 ± 0.1	2.6 ± 0.2
$K_{1/2,app}^{Mg^{2+}}$ (mM)[b]	13.0 ± 0.5	42.3 ± 5.1	25.9 ± 2.4	52.3 ± 11.6	20.7 ± 2.8	117 ± 19
n_H[b]	4.0 ± 0.5	4.2 ± 1.9	2.1 ± 0.4	2.1 ± 0.9	1.6 ± 0.5	1.3 ± 0.2
$k_{max}^{PRNA, WT}/k_{max}^{PRNA, modified}$	1	69	93	31	1.8	1

[a] The reaction was performed with 360 nM PRNA and 10 nM Fl-pre-tRNA^{Asp} at 37°C in 50 mM Tris/MES, pH 5.9, 20 mM DTT with 4 - 700 mM $MgCl_2$, and varying KCl concentrations from 118 to 10 mM. At higher Mg^{2+} concentration KCl was maintained at 10 mM. k_{obs} was calculated by a fit of single exponential (Equation 6) to the fraction cleavage of Fl-pre-tRNA^{Asp} substrate, which was calculated from the decrease in anisotropy using Equation 5 as described in Chapter 2.

[b] Equation 8 was fit to the Mg^{2+} dependence of k_{obs} to calculate k_{max}^{PRNA}, $K_{1/2,app}^{Mg^{2+}}$ and n_H of PRNA-catalyzed cleavage.

[c] Two phases were observed for Mg^{2+} dependence of STO cleavage. k_{max}^{PRNA}, $K_{1/2,app}^{Mg^{2+}}$ and n_H were obtained by fitting the data of the first phase ($MgCl_2$ concentration from 0 to 100~400 mM). STO cleavage rate constant increases in the second phase depending on the Mg^{2+} concentration ($MgCl_2$ concentration up to 700 mM).

[d] Abasic: rSpacer modification.